UNIVERSITY OF CRETE
DEPARTMENT OF CHEMISTRY

Doctoral Thesis

DEVELOPMENT OF GRAPHENE-BASED MATERIALS AND THEIR APPLICATION IN ORGANIC SOLAR CELLS

DIMITRIOS KONIOS

Thesis Supervisor: Athanasios G. Coutsolelos

HERAKLION 2016

Dedicated to my family

and my wife

DOCTORAL COMMITTEE

Athanasios G. Coutsolelos

Professor, Dept. of Chemistry, University of Crete

Emmanuel Kymakis

Associate Professor, Dept. of Electrical Engineering, Technological Educational Institute of Crete

Spiros Anastasiadis

Professor, Dept. of Chemistry, University of Crete

Demetrios Anglos

Associate Professor, Dept. of Chemistry, University of Crete

Nikolaos Katsarakis

Professor, Dept. of Electrical Engineering, Technological Educational Institute of Crete

Constantinos Petridis

Assistant Professor, Dept. of Electronic Engineering, Technological Educational Institute of Crete

Panagiotis Argitis

Director of Research, Department of Microelectronics, NCSR Demokritos

ACKNOWLEDGMENTS

CURICULUM VITAE

Dimitrios Konios

Research assistant

Chemistry Department, University of Crete,

Heraklion, 71003 Crete, Greece.

Center of Materials Technology & Photonics,

Technological Educational Institute (TEI) of Crete,

Heraklion, 71004 Crete, Greece.

Tel./Fax: +30-2810-379732

Mob: +30-6937732802

E-mail: konios@staff.teicrete.gr

Website: http://nano.teicrete.gr/

1. EDUCATION

Ph. D. Candidate in Chemistry, **2013-2016 (expected)**
Chemistry Department, University of Crete (UOC), Greece
Thesis Title: Novel graphene-based materials and their application in Organic Solar Cells (OPVs)
Advisor: Professor Athanassios G Coutsolelos

Master in Business Adminstration (MBA), 2012-2017 (expected)
School of Social Science, Hellenic Open University (HOU), Patras, Greece

M.Sc. Renewable Energy (REFLEX), 2007-2008
Faculties of Science, Agriculture & Engineering, University of Newcastle upon Tyne, Newcastle, United Kingdom
Thesis Title: An experimental study for the application of Refuse Derived Fuel (RDF) to cement industry
Advisor: Dr. Yaodong Wang

B.Sc. in Chemistry, **2002-2007**
Chemistry Department, University of Athens (UOA), Athens, Greece
Thesis Title: Refuse Derived Fuel – Calorific value and chlorine concentration in RDF samples from the Factory of Mechanical Recycling and Compost Production in Athens
Advisor: Professor Michael Scoullos

2. <u>WORK EXPERIENCE</u>

Research and laboratory assistant, Dept. of Sciences, TEI of Crete, Heraklion, Greece (11/2012-today)
<u>Teaching duties</u>: Laboratory courses in Advanced Materials

Customer Service Officer, Bank of Cyprus, Heraklion, Greece (10/2010-07/2012)

Chemist Assistant, Viofoods Food & Fruit Industry LTD, Nicosia, Cyprus (08/2008-10/2008)

Chemist, Factory of Mechanical Recycling and Compost Production, Athens, Greece (10/2006-02/2007)

3. <u>QUALIFICATIONS & SKILLS</u>

Certificate of Attendance "Basic steps in starting and organizing Businesses", 2010, University of Athens (UOA), Athens, Greece

Certificate Auditor/Lead Auditor for Environmental Management Systems (ISO 14001:2004), 2010, TUV Austria Hellas

Enology Certificate, 2002-2007, Chemistry Department, University of Athens (UOA), Athens, Greece

4. <u>FELLOWSHIPS</u>

Scholarship for Renewable Energy Flexible Training Programme (REFLEX), Engineering and Physical Sciences Research Council (EPSRC)

5. <u>AREAS OF INTEREST</u>

Research Topics
Photovoltaic materials and devices
Synthesis and fabrication of nanocomposites and nanomaterials
Graphene and Carbon nanotubes
Plasmonics
Organic Photovoltaics (OPVs)
2D Materials

6. <u>PUBLICATIONS – PRESENTATIONS – OTHER ACHIEVEMENTS (Synopsis)</u>

Mr. Konios has published 16 scientific articles in international peer-reviewed journals, 1 in conference proceedings, 1 laboratory manual and performed 21 oral and poster presentations in international meetings. He has received 206 citations, h-index: 6 (Google Scholar, 04/2016) He is also referee in high impact international scientific journals including Applied Physics Letters, Chemical Physics Letters, RSC Advances, New Journal of Chemistry, Organic Electronics, Carbon, Journal of Physical Chemistry, Solar Energy Materials & Solar Cells, Materials Science and Engineering B. Finally, during his research and laboratory experience, he had the opportunity to supervise 5 undergraduate and 1 MSc students to the successful completion of their degrees.

7. <u>PUBLISHED WORK</u>

7.1 PUBLICATIONS IN INTERNATIONAL PEER-REVIEWED JOURNALS

1. **Dispersion behavior of graphene oxide and reduced graphene oxide**
   Journal of Colloid & Interface Science (2014), 430, 108-112
   Konios D., Stylianakis M. M., Stratakis E., Kymakis E.

2. **Improving the efficiency of organic photovoltaics by tuning the work-function of graphene oxide hole transporting layers**
   Nanoscale (2014), 6, 6925-6931
   Stratakis E., Savva K., **Konios D.**, Petridis C., Kymakis E.

3. **Enhancement of the Efficiency and Stability of Organic Photovoltaic Devices via the Addition of a Lithium-Neutralized Graphene Oxide Electron-Transporting Layer**
   Chemistry of Materials (2014), 26, 5988-5993
   Kakavelakis G.*, **Konios D.** *, Stratakis E., Kymakis E.
   *[Equal contribution]

4. **Direct laser writing of flexible graphene field emitters**
   Applied Physics Letters (2014), 105, 203104
   Viskadouros G., **Konios D.**, Kymakis E, Stratakis E.

5. **Reduced graphene oxide micromesh electrodes for large area, flexible organic photovoltaic devices**
   Advanced Functional Materials (2015), 25, 15, 2213-2221
   Konios D., Petridis C., Kakavelakis G., Sygletou M., Savva K., Stratakis E., Kymakis E.
   [Chosen for the inside front cover of Adv. Funct. Mater]

6. **Ternary organic solar cells with reduced graphene oxide-Sb$_2$S$_3$ hybrid nanosheets as the cascade material**
ChemNanoMat (2015), 5, 346-352
Balis N., **Konios D.,** Stratakis E., Kymakis E.
[Chosen for the back cover of ChemNanoMat]

7. **Efficient ternary organic photovoltaics incorporating graphene-based porphyrin molecule as a universal electron cascade material**
Nanoscale (2015), 7, 17827-17835
Stylianakis M. M., **Konios D.**, Kakavelakis G., Charalambidis G., Stratakis E., Coutsolelos A. G., Kymakis E., Anastasiadis S. H.

8. **Rational Design of Graphene/Polymer Photovoltaic Interfaces from Atoms to Devices**
2D Materials (2015), 3, 015003
Noori K., **Konios D.,** Stylianakis M. M., Kymakis E., Giustino F.

9. **High efficient organic photovoltaic devices utilizing work-function tuned graphene oxide derivatives as the anode and cathode charge extraction layer**
Journal of Materials Chemistry A (2015), 4, 1612-1623
Konios D., Kakavelakis G., Stratakis E., Kymakis E.

10. **Stability enhancement of organic photovoltaic devices utilizing partially reduced graphene oxide as the hole transport layer: nanoscale insight into structural/interfaces properties and aging effects**
RSC Advances (2015), 5, 106930-106940
Paci B., Kakavelakis G., Generosi A., Albertini V., Wright J., Ferrero C**., Konios D.**, Stratakis E., Kymakis E.

11. **Laser induced assembly of plasmonic nanoparticles on two dimensional nanosheets for organic photovoltaics**
Journal of Materials Chemistry A (2015), 4, 1020-1027
Sygletou M., Tzourmpakis P., Petridis C., **Konios D**., Fotakis C., Kymakis E., Stratakis E.

12. **Slow photocharging and reduced hysteresis in low-temperature processed planar perovskite solar cells**
RSC Advances (2015), 5, 107771
Vaenas N., **Konios D.,** Stergiopoulos T., Kymakis E.

13. **Electron Field Emission from Graphene Oxide Wrinkles**
RSC Advances (2015), 6, 2768-2773

Viskadouros G., **Konios D.**, Kymakis E, Stratakis E

14. **Pulsed Laser Processing of Graphene and related Two-Dimensional Materials**
European Conference on Lasers and Electro-Optics - European Quantum Electronics Conference, Optical Society of America, paper CM_7_3 (2015)
Savva K., Kakavelakis G., Sigletou M., **Konios D.**, Paradissanos I., Stylianakis M. M., Petridis C., Kioseoglou G., Fotakis C., Kymakis E., Stratakis E.

15. **Solution-Processed Reduced Graphene Oxide Electrodes for Organic Photovoltaics**
Nanoscale Horizons (2016), DOI: 10.1039/C5NH00089K
Petridis C., **Konios D.**, Stylianakis M. M., Kakavelakis G., Sygletou M., Savva K., Tzourbakis P., Krassas M., Vaenas N., Stratakis E., Kymakis E.

16. **Efficiency and stability enhancement in perovskite solar cells by inserting lithium-neutralized graphene oxide as the electron transporting layer**
Advanced Functional Materials (2016), DOI: 10.1002/adfm.201504949
Agresti A., Pescetelli S., Cina L., **Konios D.**, Kakavelakis G., Kymakis E., Di Carlo A.

7.2 EDUCATIONAL/LABORATORY MANUALS

Laboratory manual for Advanced Materials & Microelectronics 1st edition (2014), Department of Electrical Engineering, School of Engineering, Technological Educational Institute (TEI) of Crete

8. CONFERENCE PRESENTATIONS

1. **D. Konios**, M. M. Stylianakis, E. Stratakis, E. Kymakis, "Nanomaterials and Organic Electronics Group" COST Action MP1202 HINT 2013, 1-4 April, Bordeaux, France.

2. **D. Konios**, G. Viskadouros, N. Kornilios, P. Tzanetakis, E. Stratakis, E. Kymakis, "Reduction of Graphene Oxide and the application of Reduced Graphene Oxide-polymer composites as Field-electron Emitter" 9th Panhellenic Scientific Conference of Chemical Engineering 2013, 23-25 May, Athens, Greece.

3. **D. Konios**, G. Viskadouros, C. Petridis, P. Tzanetakis, E. Stratakis, E. Kymakis, "Field emission properties of polymer-graphene nanocomposites",

Erlangen International Symposium Flexible Electronics, 19-21 June 2013, Erlangen, Germany.

4. **D. Konios**, M. M. Stylianakis, E. Stratakis, E. Kymakis, "Reduced graphene oxide as transparent conductive electrode", COST MP0902, 14-16 October 2013, Heraklion, Crete, Greece.

5. M. M. Stylianakis, **D. Konios**, E. Stratakis, E. Kymakis, "Stability and efficiency enhancement of bulk heterojunction plasmonic organic photovoltaics with graphene based buffer layers and surfactant free Au nanoparticles (NPs)", COST MP0902, 14-16 October 2013, Heraklion, Crete, Greece.

6. **D. Konios**, G. Viskadouros, C. Petridis, M. M. Stylianakis, E. Stratakis, E. Kymakis, "Polymer-graphene hybrids for 3D field emission elements" EMRS Spring Meeting, 26-30 May 2014, Lille, France.

7. G. Kakavelakis, **D. Konios**, E. Stratakis, E. Koudoumas, E. Kymakis, "Plasmonic engineering for performance and stability enhancement of air processed organic photovoltaics" EMRS Spring Meeting, 26-30 May 2014, Lille, France.

8. **D. Konios**, G. Kakavelakis, K. Savva, C. Petridis, E. Stratakis, E. Kymakis, "Graphene-based buffer layers for improved Bulk Heterojunction Solar Cell" Graphene Week, 23-27 June 2014, Gothenburg, Sweden

9. **D. Konios**, G. Viskadouros, M. M. Stylianakis, E. Stratakis, E. Kymakis, "The effect of different reduction methods in the Field Emission properties of Reduced Graphene Oxide Polymer composites" 11th International Conference on Nanosciences & Nanotechnologies (NN14), 8-11 July 2014, Thessaloniki, Greece.

10. **D. Konios**, K. Savva, G. Kakavelakis, C. Petridis, E. Stratakis, E. Kymakis, "Work-function tuned Graphene oxide as a cathode/anode interfacial layer in organic photovoltaics with high efficiency and stability" 11th International Conference on Nanosciences & Nanotechnologies (NN14), 8-11 July 2014, Thessaloniki, Greece.

11. G. Viskadouros, **D. Konios**, M. M. Stylianakis, E. Kymakis, E. Stratakis, "Graphitic Cathodes for 3D Field emission elements" HINT Annual general meeting, 15-17 September 2014, Istanbul, Turkey.

12. E. Vasilaki, M. Kaliva, D. Vernardou, I. Georgaki, **D. Konios**, E. Kymakis, M. Vamvakaki, N. Katsarakis. "Ag loaded TiO_2 coupled onto reduced

graphene oxide for enhanced visible-light photocatalytic activity" 30th Pan-hellenic conference on Solid-State Physics and Materials Science, 21-24 September 2014, Heraklion, Crete, Greece.

13. **D. Konios**, K. Savva, G. Kakavelakis, C. Petridis, E. Stratakis, E. Kymakis, "Laser Patterning of rGO thin films and their application as transparent conductive electrodes in organic photovoltaic solar cells", 5th International Symposium on Transparent Conductive Materials, 12-17 October 2014, Platanias, Chania, Crete, Greece.

14. M. M. Stylianakis, **D. Konios**, G. Kakavelakis, A. Orfanoudaki, C. Petridis, E. Stratakis, E. Kymakis, "Graphene-based Organic Photovoltaic Applications", HINT Annual Meeting: Nanostructured Hybrid Materials II: reinforced 3D structures, smart composites, self-healing, 22-24 April 2015, Heraklion Crete, Greece.

15. C. Petridis, **D. Konios**, E. Kymakis, E. Stratakis, "Decoration of 2D materials with plasmonic nanoparticles and their application as buffer layers in organic photovoltaics", E-MRS Spring Meeting, 11-15 May 2015, Lille, France.

16. C. Petridis, **D. Konios**, K. Savva, G. Kakavelakis, M. Sygletou, M. Stylianakis, C. Fotakis, E. Stratakis, E. Kymakis, "Pulsed Laser Processing of Grapehene for Organic Photovoltaic Applications", E-MRS Spring Meeting, 11-15 May 2015, Lille, France.

17. **D. Konios**, C. Petridis, G. Kakavelakis, M. Sygletou, K. Savva, E. Stratakis, E. Kymakis, "Reduced Graphene Oxide Micromesh electrodes for Large Area, Flexible, Organic Photovoltaic Devices" Graphene Week, 22-26 June 2015, Manchester, UK.

18. C. Petridis, **D. Konios**, G. Kakavelakis, M. Sygletou, K. Savva, E. Kymakis, E. Stratakis, "Reduced Graphene Oxide Micromesh Electrodes Decorated with Metal Nanoparticles for Large, Area, Flexible, Organic Photovoltaic Devices" 12th International Conference on Nanosciences & Nanotechnologies (NN15), 7-10 July 2015, Thessaloniki, Greece.

19. C. Petridis, **D. Konios**, G. Kakavelakis, N. Wijeyasinghe, T. Anthopoulos, E. Stratakis, E. Kymakis, "Solution processed Copper (I) Thiocyanate (CuSCN) with metal nanoparticles as a hole transport layer in BHJ organic photovoltaics", 12th International Conference on Nanosciences & Nanotechnologies (NN15), 7-10 July 2015, Thessaloniki, Greece.

20. E. Kymakis, E. Stratakis, C. Petridis, M. M. Stylianakis, N. Balis, N. Vaenas, **D. Konios**, G. Kakavelakis, M. Krassas, P. Tzourmpakis, "Activities of TEI

of Crete in Graphene flagship-Graphene-based photovoltaics", 12th International Conference on Nanosciences & Nanotechnologies (NN15), 7-10 July 2015, Thessaloniki, Greece.

21. K. Petridis, **D. Konios**, M. M. Stylianakis, G. Kakavelakis, M. Sygletou, K. Savva, E. Stratakis, E. Kymakis, "Flexible, printable organic photovoltaic cells using reduced graphene electrodes", International Conference Science in Technology (SCinTE), 5-7 November 2015, Athens, Greece.

9. <u>PERSONAL</u>

Date of Birth: September 1, 1984
Nationality: Greek
Place of Birth: Athens, Greece
Marital Status: Married

ABSTRACT

Ever since the isolation of free standing graphene in 2004, graphene research has experienced a phenomenal growth. Its exceptional electronic, optical and mechanical properties make graphene highly attractive, believed to be the next wonder material and thus triggering the application of graphene-based materials in the different layers of optoelectronics and especially organic photovoltaics (OPVs). In this thesis, novel graphene derivatives have been developed towards all graphene-based photovoltaics.

First of all, aiming to improve the processability of graphene oxide (GO) and reduced graphene oxide (rGO), the solubility of GO and rGO in a large number of common organic solvents was investigated. Their dispersions were prepared and compared, with respect to the long-term stability and dispersion quality. The effect of reduction process on the solubility of GO was investigated considering the solvent polarity and the surface tension. This work contribution mainly lies in the fact that for the first time, the solubility values of both GO and rGO were calculated and the data was analyzed to identify the Hansen and Hildebrand solubility parameters for the two graphene derivatives, facilitating the application of graphene derivatives to printed flexible electronics.

To contribute to the existing research on the use of graphene as transparent conductive electrode in OPVs, a novel, one step laser-based method to pattern previously prepared rGO thin films was presented. In more detail, the micromesh (MM) patterning of the rGO films with fs UV laser pulses, resulted in a significant increase of the transparency, retaining at the same time their conductivity at high levels, thereby improving the tradeoff between rGO layers transparency and sheet resistance. In particular, rGO films with initial transparency of ~20% were patterned, resulting in rGOMMs films with ~59% transmittance and sheet resistance of ~565 Ωsq^{-1}, significantly lower than the pristine rGO films resistance (~780 Ωsq^{-1}), exhibited at the same transparency. As a proof-of-concept application, rGOMMs were used as the transparent electrodes in flexible OPV devices, achieving power conversion efficiency (PCE) of 3.05%, the highest ever reported for flexible OPV devices incorporating solution-processed graphene-based electrodes.

The interface between the active layer and the electrodes plays an important role in the overall device performance of organic electronics. In this context, the effective utilization of work function (WF) tuned solution processable graphene-based derivatives as buffer layer in OPV devices was also demonstrated. The systematic tuning of functionalized GO WF was performed by either photochlorination for WF increase, or lithium neutralization for WF decrease. In this way, the WF of the photochlorinated GO (GO-Cl) layer perfectly matched with the HOMO level of two different polymer donors, enabling excellent hole transport. On top of that, the WF of the lithium functionalized GO (GO-Li) perfectly matched with the LUMO level of the fullerene acceptor, enabling excellent electron transport. The utilization of these graphene-based hole and electron transport layers in OPV devices, led to significant PCE improvement (+19.5% compared to PEDOT:PSS HTL, +14.2% compared to devices without the GO-Li interfacial layer, +19% in combo devices with GO-Cl HTL and GO-Li interfacial ETL).

Finally, the synthesis of graphene-inorganic nanocrystal derivatives as a way of designing energetically favorable materials for solar cells applications was also demonstrated. In particular, the synthesis and the application of reduced graphene oxide-antimony sulfide ($rGO-Sb_2S_3$) hybrid nanosheets as the cascade material in ternary PCDTBT:$PC_{71}BM$-based OPV led to PCE of 6.81%. The $rGO-Sb_2S_3$ hybrids combine the advantages of the individual materials, and could potentially enhance the electron cascade transfer into the active layer.

Keywords: Graphene derivatives, Organic photovoltaic, Work function, Transparent conductive electrode, Buffer layers, Additive

ΠΕΡΙΛΗΨΗ

Μετά την απομόνωσή του το 2004, το γραφένιο έχει συγκεντρώσει το ενδιαφέρον της επιστημονικής κοινότητας. Οι εξαιρετικές ηλεκτρονικές, οπτικές και μηχανικές του ιδιότητες, το καθιστούν ως το πιο ελπιδοφόρο υλικό, ιδανικό για ηλεκτρονικές εφαρμογές και ιδιαίτερα για τον τομέα των Οργανικών Φωτοβολταϊκών (OPVs). Στην παρούσα διατριβή, αναπτύχθηκαν καινοτόμα υλικά με βάση το γραφένιο και διερευνήθηκε η εφαρμογή τους στα δομικά στοιχεία των OPVs.

Αρχικά, διερευνήθηκε η διασπορά παραγώγων γραφενίου και συγκεκριμένα του οξειδίου του γραφενίου (GO) και του ανηγμένου οξειδίου του γραφενίου (rGO) σε διάφορους διαλύτες, με σκοπό την ανάπτυξη ενός πρωτοκόλλου για τη διευκόλυνση της επεξεργασίας τους. Συγκεκριμένα, τα εν λόγω διαλύματα συγκρίθηκαν όσον αφορά τη συγκέντρωση και τη σταθερότητα τους σε σχέση με το χρόνο, ενώ επιπλέον εξετάστηκε η επίδραση της αναγωγής στη διασπορά του GO σε σχέση με την πολικότητα και την επιφανειακή τάση των διαλυτών. Λαμβάνοντας υπόψη τους παράγοντες διαλυτότητας Hansen and Hildebrand των διαλυτών που χρησιμοποιήθηκαν, καθώς και τις συγκεντρώσεις του GO και του rGO σε αυτούς, προσδιορίστηκαν οι αντίστοιχοι παράγοντες διαλυτότητας για τις εξεταζόμενες γραφενικές δομές.

Εκμεταλλευόμενοι τη δυνατότητα επεξεργασίας υπό μορφή διαλύματος των παραγώγων του γραφενίου όπως του οξειδίου του γραφενίου, γραφενικές δομές ενσωματώθηκαν στα διάφορα δομικά στοιχεία ενός φωτοβολταϊκού κελιού, ενισχύοντας σημαντικά την απόδοσή και τις προοπτικές για την γρήγορη εμπορική αξιοποίηση τους. Αρχικά ακολουθώντας μια οπτική τεχνική που βασίζεται στη χρήση βραχέων παλμών λέιζερ, επετεύχθη η βελτίωση και ταυτόχρονα ο έλεγχος των οπτοηλεκτρονικών ιδιοτήτων λεπτών αγώγιμων ημενίων ανηγμένου οξειδίου του γραφενίου πάνω σε εύκαμπτα υποστρώματα. Η ελεγχόμενη ακτινοβόληση επέτρεψε την μερική, επιφανειακή αποδόμηση του rGO και το σχηματισμό μικροσκοπικών πηγαδιών σε απόλυτα ελεγχόμενες και διατεταγμένες θέσεις πάνω στην επιφάνεια των γραφενικών ημενίων. Συγκεκριμένα, ακτινοβολήθηκαν ημένια rGO με αρχικές τιμές διαπερατότητας ~20% οδηγώντας σε αύξηση σε τιμές ~59%, ενώ παράλληλα η επιφανειακή αντίσταση κυμάνθηκε σε χαμηλότερες τιμές (~565 Ωsq^{-1}) σε σχέση με την

αντίστοιχη (~780 Ωsq⁻¹) των μη ακτινοβοληθέντων ημενίων, στο ίδιο επίπεδο διαπερατότητας. Τα παραγόμενα ημένια παρουσίασαν εξαιρετική μηχανική σταθερότητα, ηλεκτρική αγωγιμότητα και οπτική διαπερατότητα επιτρέποντας τη χρήση τους ως διαφανή αγώγιμα ηλεκτρόδια σε εύκαμπτα OPVs, επιτυγχάνοντας απόδοση της τάξης του 3%, η υψηλότερη που έχει αναφερθεί ποτέ για εύκαμπτες διατάξεις βασισμένες σε παραχθέντα από διάλυμα γραφενικά ηλεκτρόδια.

Στη συνέχεια, γνωρίζοντας ότι οι διεπιφάνειες μεταξύ του φωτοενεργού στρώματος και των ηλεκτροδίων επηρεάζουν σημαντικά την απόδοση των OPVs, μελετήθηκε η χρήση παραγώγων γραφενίου ως ενδιάμεσα στρώματα. Αρχικά, πραγματοποιήθηκε φωτοχημικός εμπλουτισμός του GO με χλώριο και χρήση του ως στρώμα μεταφοράς οπών σε οργανικές φωτοβολταϊκές διατάξεις, Συγκεκριμένα, υποστρώματα GO ακτινοβολήθηκαν με laser, με αποτέλεσμα να πραγματοποιηθεί ταυτόχρονη αναγωγή και πρόσδεση χλωρίου στο γραφενιακό πλέγμα. Ο σχηματισμός δίπολων $C^{δ+}$-$Cl^{δ-}$ είχε ως αποτέλεσμα τη μετακίνηση της ενέργειας Fermi προς τη ζώνη σθένους του GO και τροποποίηση του έργου εξόδου (WF) από 4.9 eV σε μέγιστη τιμή 5.23 eV. Παράλληλα, πραγματοποιήθηκε τροποποίηση του GO με λίθιο, και μεταβολή του WF από 5.0 eV στο GO σε 4.3 (±0.1) eV στο GO-Li, ώστε να χρησιμοποιηθεί ως ενδιάμεσο στρώμα μεταφοράς ηλεκτρονίων. Η ενσωμάτωση των παραγόμενων γραφενικών δομών ως ενδιάμεσα στρώματα σε OPVs βελτίωσε σημαντικά την απόδοσή τους (+19.5% σε σχέση με διατάξεις όπου χρησιμοποιήθηκε το PEDOT:PSS ως στρώμα μεταφοράς οπών, +14.2% σε σύγκριση με διατάξεις όπου δεν χρησιμοποιήθηκε το GO-Li, +19% όταν ενσωματώθηκαν ταυτόχρονα τα GO-Cl και GO-Li).

Τέλος, μελετήθηκαν γραφενικές δομές εμπλουτισμένες με ανόργανους νανοκρύσταλλους ως υποσχόμενα υλικά για φωτοβολταϊκές εφαρμογές. Πραγματοποιήθηκε σύνθεση ανηγμένου οξειδίου του γραφενίου-θειούχου αντιμονίου (rGO-Sb_2S_3) και χρήση του ως πρόσθετο στο φωτοενεργό στρώμα PCDTBT:PC_{71}BM οργανικών κυψελίδων, επιτυγχάνοντας απόδοση 6.81%.

Λέξεις κλειδιά: Παράγωγα γραφενίου, Οργανικές φωτοβολταϊκές διατάξεις, Έργο εξόδου, Διάφανο αγώγιμο ηλεκτρόδιο, Ενδιάμεσα στρώματα, Πρόσθετο

TABLE OF CONTENTS

ABBREVIATIONS

AFM: Atomic Force Microscopy

2D: Two-Dimensional

TCEs: Transparent Conductive Electrodes

OPVs: Organic Photovoltaics

PC$_{61}$BM: (6,6)-phenyl-C61-butyric acid methyl ester)

SWCNT: Single-Walled Carbon Nanotubes

MWCNT: Multi-Walled Carbon Nanotubes

CVD: Chemical Vapor Deposition

SiC: Silicon Carbide

LPE: Liquid-Phase-Exfoliation

SBS: Sedimentation Based-Separation

DGU: Density Gradient Ultracentrifugation

YM: Yield by SLG percentage

NMP: N-Methyl-2-pyrrolidone

GO: Graphene Oxide

UHV: Ultra-High Vacuum

CCS: Confinement Controlled Sublimation

PVD: Physical Vapor Deposition

SLG: Single Layer Graphene

FLG: Few Layer Graphene

CBE: Chemical Beam Epitaxy

PAHs: Polycyclic Aromatic Hydrocarbons

GNRs: Graphene Nanorods

GQDs: Graphene Quantum Dots

C/O: Carbon/Oxygen

MAS NMR: Magic-Angle Spinning Nuclear Magnetic Resonance

rGO: Reduced Graphene Oxide

HI: Hydroiodic Acid

NaBH$_4$: Sodium Borohydride

PV: Photovoltaic

PET: Polyethylene Terephthalate

DSSCs: Dye-Sensitized Solar Cells

PeSCs: Perovskite Solar Cells

TiO$_2$: Titanium Dioxide

r2r: Roll-To-Roll

HOMO: Highest Occupied Molecular Orbital

LUMO: Lowest Unoccupied Molecular Orbital

PEDOT:PSS: Poly(3,4-ethylenedioxythiophene) poly(styrenesulfonate)

HTL: Hole Transport Layer

WF: Work Function

ITO: Indium Tin Oxide

TiO$_x$: Titanium Suboxide

ETL: Electron Transport Layer

PCE: Power Conversion Efficiency

J$_{sc}$: Short-Circuit Current Density

V$_{oc}$: Open-Circuit Voltage

FF: Fill Factor

V$_{MPP}$: Maximum Power Point Voltage

I$_{MPP}$: Maximum Power Point Current

T$_r$: Transparency

R$_s$: Sheet Resistance

P3HT: Poly(3-hexylthiophene-2,5-diyl)

PCDTBT: Poly [N-9'-heptadecanyl-2,7-carbazole-alt-5,5-(4',7'-di-2-thienyl 2',1',3'benzothiazole)]

PTB7: Poly ({4,8-bis[(2-ethylhexyl)oxy]benzo[1,2-b:4,5-b']dithiophene-2,6-diyl}{3-fluoro-2-[(2-ethylhexyl) carbonyl]thieno [3,4-b]thiophenediyl} (PTB7)

PMMA: Poly(methyl methacrylate)

TCNQ: Tetracyanoquinodimethane

NWs: Metal Nanowires

P3OT: Poly(3-octylthiophene-2,5-diyl)

GO-EDNB: GO-ethylene-dinitro-benzoyl

ICBA: Indene-C_{60} bisadduct

ICL: Interconnection layer

GO-Cs: Cesium-functionalized Graphene Oxide

prGO: Partially Reduced GO

PBDTTT-CF: poly[1-(6-{4,8-bis[(2-ethylhexyl)oxy]-6-methylbenzo[1,2-b:4,5-b'] dithiophen-2-yl}-3-fluoro-4-methylthieno [3,4-b]thiophen-2-yl)-1-octanone]

FrGO: fluorinated rGO

THF: Tetrahydrofuran

DMF: N,N-dimethylformamide

DCM: Dichloromethane

CB: Dhlorobenzene

o-DCB: o-dichlorobenzene

CN: 1-chloronaphthalene

FT-IR: Fourier transform infrared spectroscopy

XRD: X-ray diffraction

TGA: Thermogravimetric Analysis

$δ_D$: Dispersion cohesion parameter

$δ_P$: Polarity cohesion parameter

$δ_H$: Hydrogen bonding cohesion parameter

δ$_T$: Hildebrand solubility parameter

rGOMM: Reduced Graphene Oxide Micromesh

rms: Root-mean-square

SEM: Scanning Electron Microscopy

P: Laser power

N$_P$: Number of pulses

UPS: Ultraviolet Photoelectron Spectroscopy

XPS: X-ray Photoelectron Spectroscopy

SKPM: Scanning Kelvin Probe Microscopy

GO-Cl: Photochlorinated GO

OSC: Organic Solar Cells

ICBA: Indene-C60 bisadduct

PTFE: Polytetrafluoroethylene

EQE: External quantum efficiencies

EDX: Energy Dispersive X-Ray spectroscopy

CV: Cyclic Voltammetry

CH$_3$CN: Acetonitrile

TBAPF6: Tetrabutylammonium Hexafluorophosphate

IPCE: Incident Photon-to-Current Efficiency

J$_{ph}$: Photocurrent Density

V$_{eff}$: Effective Voltage

G$_{max}$: Maximum Exciton Generation Rate

GO-Li: Lithium-neutralized Graphene Oxide

SCLC: Space-Charge-Limited Current Density

DIO: 1,8-diiodooctane

IQE: Internal Quantum Efficiency

Chapter 1

1.1 Introduction to carbon allotropes

Carbon forms the key component of all organic molecules, making it the most important element of life. Being one of the most abundant element in nature, it is present in over 95% of the known chemical compounds.[1] The unique electronic structure of carbon allows the hybridization between 2s and 2p orbitals, forming sp^n state, where n refers to the number of 2p orbitals mixed with the 2s orbital. The presence of sp^n hybridization gives rise to the development of a wide variety of molecular and crystalline structures.[2] In this way, carbon forms allotropes of any possible dimensionality ranging from 3D diamond (carbon atoms are bonded in a tetrahedral lattice arrangement) and graphite (carbon atoms are bonded in hexagonal lattice sheets) to 2D graphene, 1D nanotube (single-walled carbon nanotubes - SWCNT), multi-walled carbon nanotubes - MWCNT) and 0D fullerenes (carbon atoms are bonded in spherical, tubular, or ellipsoidal formations) (**Figure 1.1**).[3,4] These materials exhibit unique and extraordinary optical, thermoelectrical and mechanical properties rising from their structure and dimensionality.
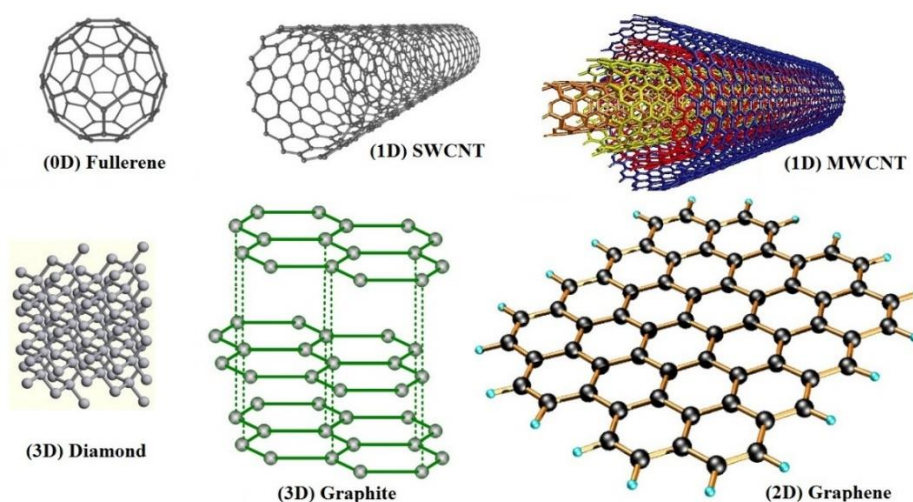
Figure 1.1. The different carbon allotropes and the respective dimension. Reproduced from reference 4.

Graphite, which became widely known after the invention of pencil in 1564, consists of atomic layers of sp^2 hybridized carbons, stacked together by weak

van der Waals forces.[5] Within a layer, each carbon atom is bonded to three other forming a planar array of fused hexagons, while the un-hybridized $2p_z$ orbital where the fourth electron is accommodated, forms a delocalized orbital of π symmetry that further stabilizes the in-plane bonds.[1] Its use as writing tool or lubricant originates from the fact that it consists of stacks of graphene layers with weak interlayer interaction between them. Owing to the delocalized π band and σ bonds, graphite exhibits good electrical conductivity in the plane directions, while it is an insulator in the stacking direction.[6] Diamond consists of carbon atoms bonded in a tetrahedral lattice (each sp^3-hybridized carbon atom covalently bonds to four others), arranged in a three-dimensional structure. It is the hardest known natural mineral, suitable for cutting and grinding of metals and other materials.[7] In contrast to graphite, diamond is not a good electrical conductor but the mineral is an excellent thermal conductor.[7]

Laser spectroscopy experiments at Rice University in 1985 led to the discovery of fullerenes.[8] These molecules, which were named after Richard Buckminster Fuller, an architect known for the design of geodesic domes, are molecules where carbon atoms are arranged spherically. Fullerenes can be thought as wrapped-up graphene, since they can be obtained from graphene by replacing some hexagon rings with pentagons in order to form a spherical structure.[1] Much attention have been paid to investigate the chemistry and physical properties of fullerenes, with many functionalized derivatives being reported in several applications, with the C_{60} derivative, (6,6)-phenyl-C61-butyric acid methyl ester) (PCBM), being the state-of-the-art electron acceptor in organic photovoltaics (OPVs).[9,10,11] By rolling graphene sheets along a specific direction, carbon nanotubes can be obtained. Prof. Sumio Iijima discovered the first nanotube, a MWCNT, in 1991 in Tsukuba, Japan, while in 1993 he produced the first SWCNT.[12,13] Depending on how graphene sheet is rolled to form the nanotube, metallic or semiconducting properties arise.[1] Nanotubes can be of different diameters, open-ended or closed-ended and either of these parameters will affect their properties. Except diamond, the rest carbon allotropes (fullerenes, nanotubes, and graphite) can be thought as different structures built from the same hexagonal array of sp^2 carbon atoms, the graphene.

1.2 An overview of graphene

Graphene is a one-atom-thick planar sheet of sp^2-bonded carbon atoms stacked in a two-dimensional (2D) honeycomb lattice (**Figure 1.2a**), and it is the basic building block for carbon allotropes of any dimensionality.[14] It can be viewed as both a solid and a macromolecule with molecular weights of more than 10^6-10^7 gmol^{-1}.[15] Although it has been previously thought to be physically unstable, Geim and Novoselov et al. were able to isolate and characterize mono and few-layer graphene in 2004,[16] a work which earned them the 2010 Nobel Prize in physics "for groundbreaking experiments regarding the two-dimensional material graphene". Due to its unique optical, electronic, mechanical, and thermal properties, the research on graphene and its derivatives represent an emerging field of interdisciplinary science.

1.2.1 Optical properties

It has been theoretically calculated and experimentally verified that graphene can absorb ~2.3% of white light and reflects <0.1% of the incident (**Figure 1.2b**).[17] In addition, the optical absorption of graphene layers is linearly proportional to the number of layers. The absorption of monolayer graphene exhibits a flat behavior over a long range, presenting a peak in the UV region (~250 nm), owing to π-π* transition.[18]
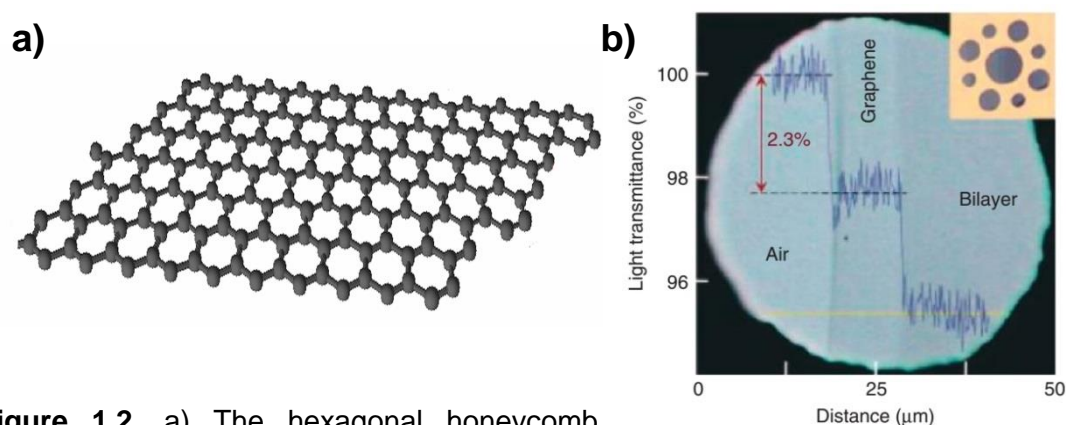
Figure 1.2. a) The hexagonal honeycomb crystal lattice of graphene. b) Photograph of a 50-mm aperture partially covered by graphene and its bilayer. Reproduced from reference 17.

1.2.2 Electronic properties

In graphene 2D plane, each carbon atom is connected to three other, leaving an electron freely available in the third dimension for electronic conduction. These electrons called π (pi) electrons exhibit high mobility and are located above and below the graphene sheet.[19] In this way, carbon atoms in the graphene layer form three σ-bonds, constituted by p_x and p_y orbitals and one π (pi)-bond, constituted by the p_z ones. The electronic properties of graphene are governed by the bonding and anti-bonding (the valence and conduction bands) of the π (pi) orbitals.[19]
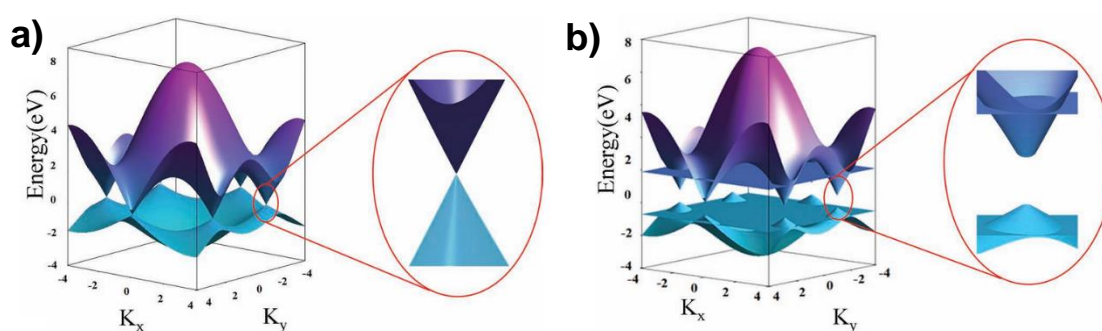
Figure 1.3. a) The band structure of graphene in the honeycomb lattice. The energy bands at the Dirac points are demonstrated in the enlarged picture. b) Chemically functionalized graphene band structure. The functionalization can open up the band gap and introduce new energy levels. Reproduced from reference 20.

Graphene conduction and valence bands meet at the isolated points (K and K') in the Brillouin zone corners (so-called Dirac points).[20] As a result it can be considered as zero-band-gap semiconductor, while measurements have demonstrated that graphene exhibits very high electronic mobility (>15,000 $cm^2V^{-1}s^{-1}$).[19] The low resistivity and extremely thin nature make it a very promising material as transparent conductive electrode (TCE) in a variety of applications (from touch screens to solar cells). However, for some optoelectronic applications, graphene zero bandgap property can be an important drawback and it is necessary to open its energy band gap and extend the lifetime of photo-generated carriers (**Figure 1.3b**).[20]

1.2.3 Mechanical properties

Carbon allotropes have their own record in terms of mechanical strength, hardness, or Young's modulus. Graphene is no exception, considered as one of the strongest materials ever tested, owing to the 0.142 nm-long carbon bonds strength.[19] It exhibits a tensile strength of 130 GPa, which it is approximately 100 times stronger than steel, while a Young's modulus of 0.5 TPa has been verified by Atomic Force Microscopy (AFM).[21] Finally, despite of its strength, graphene is very light, since 0.77 mg per square meter is 1000 times lighter than a square meter of paper, with one gram of graphene being large enough to cover a football field.[19]

1.2.4 Thermal properties

Apart from its excellent optoelectrical and mechanical properties, graphene is a unique thermal conductor. Its thermal conductivity exceeds 5000 $Wm^{-1}K^{-1}$, significantly higher compared to other carbon structures and even graphite (1000 $Wm^{-1}K^{-1}$).[22]

1.3 Graphene production

It is clear that graphene is a material with unique properties, which correspond to free-standing or suspended graphene monolayers. However, for most applications and for real commercialization, graphene production in higher quantities is necessary. Today, graphene is typically prepared through Chemical Vapor Deposition (CVD),[23,24] micromechanical exfoliation of graphite,[25] epitaxial growth on electrical insulating surfaces as silicon carbide (SiC) and finally through colloidal suspensions made from graphite. The latter has been described in many studies as the liquid phase exfoliation of graphite to graphene. The main graphene production approaches are demonstrated in **Figure 1.4** and can be distinguished in dry and liquid exfoliation, as well as in growing and deposition techniques.[26]
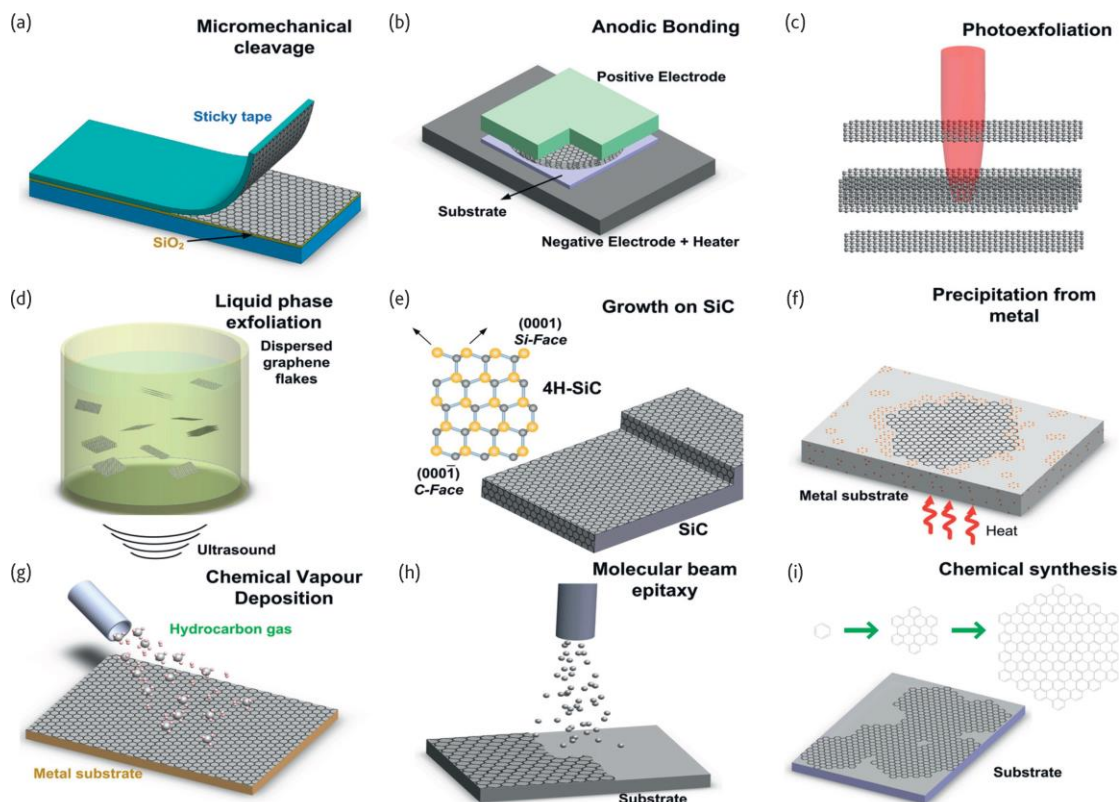
Figure 1.4. Schematic illustration of the main graphene production techniques. a) Micromechanical cleavage, b) Anodic bonding, c) Photoexfoliation, d) Liquid phase exfoliation, e) Growth on SiC. Gold and grey spheres represent Si and C atoms, respectively. At elevated T, Si atoms evaporate (arrows), leaving a carbon-rich surface that forms graphene sheets, f) Segregation/precipitation from carbon containing metal substrate, g) Chemical vapor deposition, h) Molecular Beam epitaxy, i) Chemical synthesis using benzene as building block. Reproduced from reference 26.

1.3.1 Dry exfoliation

Dry exfoliation is the splitting of layered materials into atomically thin sheets via mechanical, electrostatic, or electromagnetic forces in air, vacuum or inert environments.

1.3.1.1 Micromechanical cleavage

Micromechanical cleavage, also known as micromechanical exfoliation, has been used for decades by crystal growers and crystallographers.[27,28] In 1999, Ruoff et al. reported a controlled method of cleaving graphite,[29] yielding films consisting of several layers of graphene.[26] It was also suggested that "more extensive rubbing of the graphite surface against other flat surfaces might be a

way to get multiple or even single atomic layers of graphite plates." This technique was then used by Novoselov et al., succeeding to characterize single layer graphene (SLG), isolated using a scotch tape (**Figure 1.4a**).[16] Micromechanical cleavage has been improved to yield high quality layers, with size of the order of millimeters, depending on the single crystal grains of the pristine graphite.[26,30] Elastic[31] and inelastic[32] light scattering can be used to identify the number of layers. Raman spectroscopy can be also used as a fast and non-destructive technique to monitor the doping,[33,34] defects,[35,36] strain,[37] disorder,[38] chemical modifications[39] and edges.[40]

Although, micromechanical exfoliation is infeasible for large scale production, it is still used for fundamental studies. Indeed, the majority of basic results and prototype devices were obtained by investigating micromechanical exfoliated flakes.[26] Thus, the aforementioned method remains the best production technique in terms of electrical and structural quality of the obtained graphene, owing to the high quality of the starting single crystalline graphite source. The size of the deposit is also important, and nowadays can be purchased on supporting substrate in the fraction of square millimeter.

1.3.1.2 Anodic bonding

Anodic bonding is extensively used in the microelectronics industry to bond silicon wafers to glass,[41] and protect them from humidity or contaminations.[42] To use this technique to produce SLGs,[43,44] firstly graphite is pressed onto a glass substrate. Afterwards, high voltage of few kVs (0.5-2 kV) is applied between the graphite and a metal back contact (**Figure 1.4b**), while the glass substrate is finally heated at ~200 °C for ~10-20 min).[26,44] The application of positive voltage to the top contact results in a negative charge accumulation in the glass side facing the positive electrode, causing the decomposition of sodium oxide (Na_2O) impurities of the glass into Na^+ and O^{2-} ions.[44] O^{2-} remain at the graphite-glass interface, while Na^+ are transferred to the back contact, creating a high electric field at the interface.[26] SLGs and few layers of graphite stick to the glass by electrostatic interaction and can then be cleaved off.[44] The number of layers as well as their sizes can be tuned by controlling the temperature or an applied voltage. In this way, flakes up to about a millimeter in width can be prepared.[43]

1.3.1.3 Laser ablation and photoexfoliation

The use of a laser beam to remove material from a solid surface is termed laser ablation.[45] If irradiation leads to the detachment of an entire or partial layer, photoexfoliation is conducted.[46] In this way, laser pulses can be used to ablate/exfoliate graphite flakes (**Figure 1.4c**). By tuning the laser energy density, graphene patterning can be conducted.[47] In particular, the ablation of a defined number of layers can be obtained exploiting the laser energy density window required for ablating a SLG and n-layer graphene.[47] Laser ablation is still in a premature stage[48] and further development is required. The process is best implemented in inert or vacuum conditions,[49,50] since ablation in air can result in oxidized graphene layers.[47] Promising results have been also presented in liquids.[51]

1.3.2 Liquid-phase exfoliation (LPE)

Liquid-phase exfoliation is considered as one of the most feasible approaches for industrial production of graphene owing to its scalability and low cost. This technique is based on the sonication of graphite or graphite oxide powders in different solvents. With respect to the graphite precursors, LPE has been demonstrated using (a) natural graphite, (b) graphite oxide and (c) graphite intercalation compound (GIC) as displayed in **Figure 1.4d**. The LPE generally includes three steps: 1) graphite dispersion in a solvent, 2) exfoliation and 3) "purification" (**Figure 1.5**).[52] The third step is important to separate exfoliated from un-exfoliated flakes, and is conducted via ultracentrifugation.[53]

a) Starting material   b) Dispersion in solvents   c) Ultrasonication   d) Dispersion after Ultracentrifugation
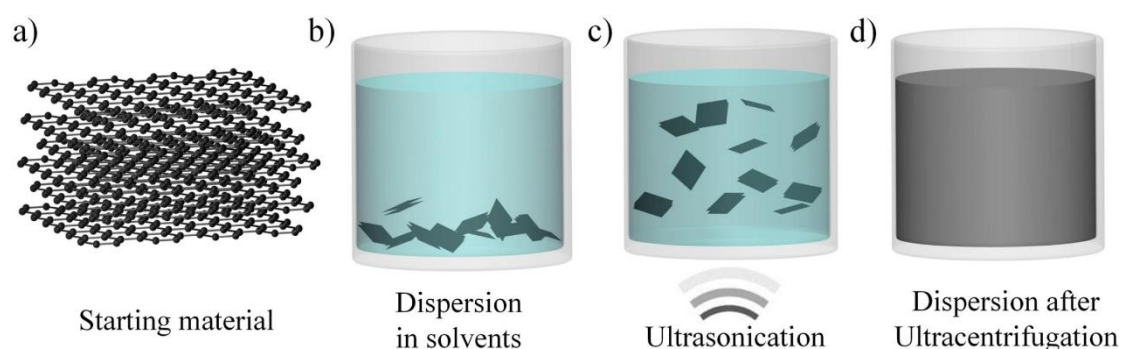
Figure 1.5. Liquid-phase exfoliation process. a) Starting material (e.g. graphite), b) chemical wet dispersion, c) ultrasonication and d) final dispersion after the ultracentrifugation process. Reproduced from reference 52.

1.3.2.1 LPE of graphite

Graphite exfoliation via chemical wet dispersion followed by ultrasonication in water[54,55] and organic solvents[56,57] has been demonstrated to be an efficient and low-cost method to produce oxide-free graphene flakes in solution. The exfoliation process is based on the strong interaction between the solvent and the composing layers of graphite. Ultrasound-assisted exfoliation is controlled by hydrodynamic shear-forces, associated with cavitation,[58] i.e. the formation, growth, and collapse of bubbles or voids in liquids due to pressure fluctuations.[58] After exfoliation, the interaction between the solvent and graphene needs to balance the inter-sheet attractive forces.

Polydispersity and flake size need to be taken into consideration when graphene is dispersed in organic solvents and/or surfactant solutions. The former is related to the nature of the flakes present in the solution, i.e. monolayers, bilayers, multilayers, which ideally must be separated before film formation. Due to the different buoyant densities of the multilayered graphene in comparison with mono or bilayer graphene, different approaches based on ultracentrifugation in a uniform medium,[59] or in a density gradient medium,[60] are utilized in order to remove the thick flakes. Differential ultracentrifugation (sedimentation based-separation, SBS)[59] and density gradient ultracentrifugation (DGU) are among the used techniques.[60] The SBS can separate various particles based on their sedimentation rate in response to centrifugal force acting on them.[59] SBS is the most common separation strategy, succeeding to isolate flakes ranging from few nanometers to few microns, with few mgml^{-1} concentrations.[61,62] For large scale production of composites[53] and inks, high concentration is important.[56] Yield by SLG percentage (Y_M) up to ~70% has been achieved by mild sonication in water with SDC, followed by SBS,[54] while Y_M~33% was reported in N-Methyl-2-pyrrolidone (NMP).[56] This Y_M difference is related to the difference in flake lateral size. The narrower the dispersivity of the graphene dispersions, the more homogeneous the films obtained, which leads to subsequent improvement in transmittance and sheet resistance.[63] Flake size is another important parameter on the film formation. In general, the small sized graphene sheets present improved

stability in a solution than the large ones. Thus, in terms of stability, long-time sonication is normally used to cut the large graphene sheet to small pieces.[64]

Solvents that minimize the interfacial tension (mNm^{-1}) between the liquid and graphene flakes (i.e. the force that minimizes the area of the surfaces in contact) are ideal to disperse graphene.[65] Generally, interfacial tension plays a key role when a solid surface is immersed in a liquid medium.[66,67] If the interfacial tension between solid and liquid is high, there is poor dispersibility of the solid in the liquid.[65] In the case of graphitic flakes in solution, if the interfacial tension is high, the flakes tend to adhere to each other, thereby the cohesion work between them is high (i.e. the energy per unit area required to separate two flat surfaces from contact),[65] hindering their dispersion in liquid. Liquids presenting γ~40 mNm^{-1} surface tension values (i.e. the property of the surface of a liquid that allows it to resist to an external force, due to the cohesive nature of its molecules),[53] are ideal solvents for the dispersion of graphene and graphitic flakes, since they minimize the interfacial tension between solvent and graphene.

1.3.2.2 LPE of graphite oxide

A low cost method of producing graphene on a large scale is to reduce graphene oxide (GO) to graphene. GO can be prepared by oxidizing graphite with strong acids followed by intercalation and exfoliation in water.[68,69] In 1859, Brodie oxidized graphite in the presence of potassium chlorate (KClO$_3$) and fuming nitric acid (HNO$_3$), while investigating the reactivity of graphite flakes.[70] This process involved successive oxidative treatments of graphite in different reactors. In 1898, Staudenmaier modified Brodie's method by using concentrated sulfuric acid (H$_2$SO$_4$) and adding KClO$_3$ in sequential steps during the reaction.[71] This allowed to carry out the reaction in a single vessel.[72] However, both techniques were both time consuming and hazardous, as they yielded chlorine dioxide (ClO$_2$) gas,[73] which can explosively decompose into oxygen and chlorine. Graphite oxide flakes were already investigated by Kohlschtter and Haenni in 1918,[74] and in 1948 Ruess and Vogt[75] demonstrated the presence of single GO sheets in the first TEM images. In 1958, Hummers modified the process using a mixture of sulfuric acid, sodium nitrate (NaNO$_3$) and potassium permanganate (KMnO$_4$).[68] The replacement of the KClO$_3$ made

the process safer and quicker with no explosive byproducts.[68] The downside of this approach is that, after reduction, some places in the sp^2 carbon network can be irreversibly destroyed leaving sp^3 carbons and vacancies which behave as electron traps.[76,77] Thus, hydroxyl or epoxide groups are introduced in the basal plane, while carbonyl and carboxylic groups, together with lactone, phenol and quinone are attached to the edges (**Figure 1.6**). However, the introduction of these functional groups is essential for the GO production and the subsequent liquid dispersion. GO flakes can be produced via sonication,[78,79] stirring,[80] thermal expansion,[81] etc. of graphite oxide. The aforementioned functional groups make GO flakes strongly hydrophilic, allowing their dispersion in pure water[78,82] organic solvents,[80,83] aqueous mixtures with methanol, acetone, acetonitrile or 1-propanol and ethylene glycol.[84,85]
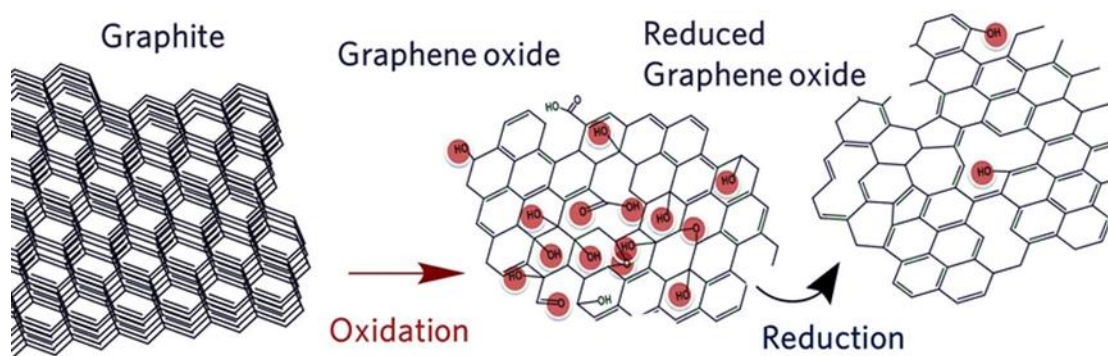
Figure 1.6. The process involves the oxidation of graphite to graphite oxide, the exfoliation of later to graphene oxide and subsequent reduction to reduced graphene oxide.

GO is electrically insulating material due to its disrupted sp^2 bonding networks. On the other hand, the reduction of the GO can recover the π-network and restore the electrical conductivity of graphene (**Figure 1.6**). Thus, GO sheets became one of the most promising starting materials in the mass production of solution processable graphene sheets through various reduction approaches, e.g. by chemical (using reducing agents), thermal and photochemical reduction methods. Reduction processes will be discussed later in this chapter.

1.3.2.3 LPE of intercalated graphite

LPE of graphite using intercalation compounds (**Figure 1.7**) for production of graphene was first reported by Viculis et al. and recently has attracted great interest.[86,87,88,89] The technique starts with the intercalation of graphite with molecules followed by its expansion via rapid rise in the vapor pressure of the volatile intercalated substance through microwave or thermal treatment. In this way, high-yield production of graphene with improved quality can be realized. For example, Qian et al. reported that, by solvothermal-assisted exfoliation of expanded graphite in acetonitrile, monolayer and bilayer graphene with 10-12 wt% yield and without significant structural defects could be obtained.[90] However, these recipes are limited by using either poisonous chemical agents[87] or dangerous chemical reactions.[88,89,91]
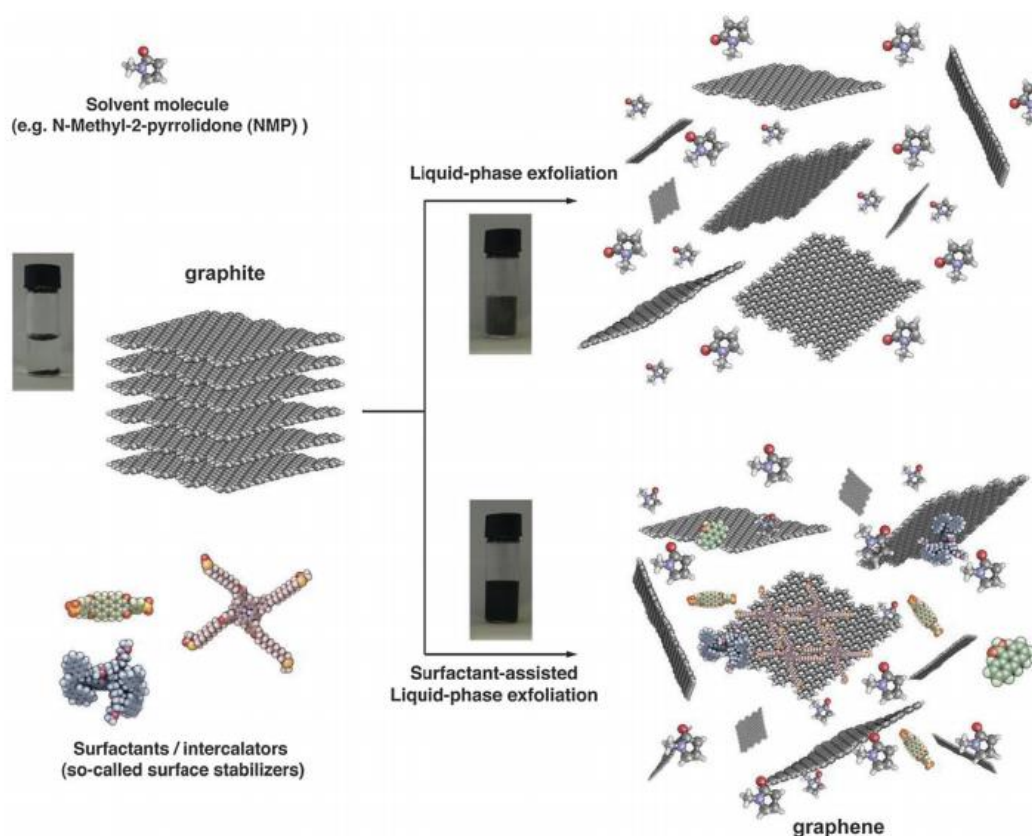
Figure 1.7. Schematic representation of the liquid-phase exfoliation process of graphite in the absence (top-right) and presence (bottom-right) of surfactant molecules. Reproduced from reference 91.

1.3.3 Growth on SiC

Graphene can also be produced through carbon segregation from SiC through high-temperature annealing.[92,93,94] Acheson reported the first method of producing graphite from SiC in 1896.[93] High-quality layers can now be produced on SiC under argon[95] and electronic decoupling from the underlying SiC substrate can be achieved by hydrogen treatment.[96]

The underling method in synthesizing graphene from SiC wafers is to sublime silicon from the wafer surface whereby the remaining carbon will reform into a graphene sheet (**Figure 1.4e**).[97] However, the use of high annealing temperatures (up to 1300 °C) and ultra-high vacuum (UHV) is needed to achieve silicon sublimation. In addition, the surface topography of SiC will affect the graphene growth as it is limited to the horizontal terraces with little growth occurring on vertical edges.

Epitaxial graphene synthesis from SiC was first presented by Von Bommel et al. in 1974.[98] The procedure was carried out in UHV, at >800 °C temperatures. The experiments showed that the orientation of the crystal plays a principal role in graphene growth, with carbon terminated faces presenting increased graphene growth rates compared to silicon terminated sides.

Studies into graphene synthesis on SiC by Emtsev et al.[95] demonstrated that graphene defects in sublimed SiC are caused by high silicon sublimation rates seen in UHV synthesis, and that sublimation can be facilitated by utilizing argon at atmospheric pressures. As a result, monolayer graphene can be synthesized on SiC terraces. The disadvantage of atmospheric annealing under argon is naturally the higher temperatures required (1600 °C) in order to initiate sublimation in ambient pressure argon.

Following the successful approach of controlling silicon sublimation, de Heer et al.[99] have recently presented a refined synthesis method referred to as confinement controlled sublimation (CCS). In this method SiC wafers are confined in a nonreactive graphite chamber with a small leakage aperture which maintains a higher silicon vapor pressure and thus limits the sublimation rate. The CCS method has be used with both UHV and argon atmospheres and can effectively grow graphene on both the SiC silicon and carbon terminated faces by controlling both the temperature and size of the leak aperture.

In addition, a variety of methods of graphene synthesis from SiC have been presented, one of which consists of growing SiC films on silicon via gas source molecular beam epitaxy, followed by an in situ UHV annealing.[100] This method is conducted under lower annealing temperatures (1200 °C) in UHV compared to the previously used 1250-1450 °C, while it also demonstrates the utility of SiC synthesis method avoiding the use of expensive SiC wafers.

1.3.4 Precipitation from metal[26]

The first reports on the synthetic growth of graphite on transition metals date back to the early 1940s.[101,102] However, it took thirty years to elucidate the details of the growth process, when Shelton et al. reported, using a combination of Auger and low energy electron diffraction, that SLG were formed from carbon precipitation, under high temperature annealing of Co, Pt, or Ni.[103] Graphite can be also prepared by carbon saturated molten Fe during the formation of steel.[104] During this process, Fe is supersaturated with carbon, with the excess carbon precipitating.[103] The amount of carbon that can be dissolved in most metals is up to a few atomic percent.[105] To limit the competition between forming a carbide and graphite/graphene growth, the use of non-carbide forming metals, e.g. Cu, Ni, Au, Pt, Ir, is favored.[106] Elements like Ti, Ta, Hf, Zr and Si form thermally stable carbides,[107,108] thereby they are not "ideal" for graphite/graphene growth.

Carbon can be deposited on a metal surface by a number of techniques: flash evaporation, physical vapor deposition (PVD), CVD, spin coating, etc. The carbon source can be solid,[109,110] liquid[111,112,113] or gas.[114] In the case of a pure carbon source, flash evaporation[115] or PVD,[116] can be utilized to deposit carbon directly on the desired substrate, before high temperature diffusion, followed by precipitation of graphite (graphene) upon cooling. The growth process using Ni substrate was first presented in 1974.[103] Shelton et al. identified SLG on Ni (111) at T>1000 K by Auger analysis, followed by graphite formation upon cooling. During high temperature annealing, carbon diffuses into the metal until it reaches the solubility limit. During cooling, carbon precipitates forming first graphene (**Figure 1.4f**), then graphite.[103] The thickness of the graphite film depends on the metal, the carbon solubility in that metal, the temperature at

which the introduction of carbon is conducted, the thickness of the metal and the cooling rate.

Growth of graphene on Ni,[117] Co,[118] Ru[119] was also reported by performing CVD method at high temperatures, using various hydrocarbon precursors. However, since graphene rather grows by carbon segregation from the metal bulk, as a result of carbon supersaturation in the solid and not directly prepared on the metal surface by the reaction and deposition of the precursor, the CVD process referred to in the aforementioned papers is a misnomer.[103]

Growth of graphene by precipitation requires careful control of metal thickness, annealing temperature and time, cooling rate, and metal microstructure. Yoshii eta al. reported the graphene growth on Ni, Co and Ru on sapphire, demonstrating uniform growth on Ru by a surface catalyzed reaction of hydrocarbons, but not on Ni and Co.[119] Both SLG and few layer graphene (FLG) were detected on Ni and Co, presumably due to the higher carbon solubility and incorporation kinetics compared to Ru at the same temperature.[119] An alternative strategy for SLG growth on high carbon solubility substrates was demonstrated by using a binary alloy (Ni-Mo).[120] The Mo component of the alloy traps all the dissolved excess carbon atoms, forming molybdenum carbides and limiting carbon precipitation.[120]

One of the shortcomings of graphene metal growing is that most applications require graphene on an insulating substrate. It is suggested that graphene can be grown directly on SiO_2 by the precipitation of carbon from a Ni film deposited on its surface.[121] This process although promised, needs further refinement.

1.3.5 Chemical vapor deposition (CVD)

CVD is a process widely used to deposit or grow thin films, crystalline or amorphous, from solid, liquid or gaseous precursors of many materials.[26] Although the mechanical exfoliation method can provide high quality graphene and liquid phase exfoliation can produce large quantities of graphene, the prepared graphene has too small average size to be suitable for applications in large optoelectronics. In this context, CVD is a promising technique for producing large-area and continuous graphene films on transition metal substrates **(Figure 1.4g)**.[122]

The main difference in the CVD equipment for the different precursor types is the gas delivery system. When solid precursors are used, the solid can be either vaporized and then transferred to the deposition chamber, or dissolved using an appropriate solvent, delivered to a vaporizer, and finally transported to the chamber.[123] The precursor transfer can also be facilitated by a carrier gas. Depending on the deposition temperature, precursor reactivity, or growth rate, it may be necessary to introduce an external energy source to aid precursor decomposition.[26]

Ni is one of the most commonly working catalysts in the prior synthesis of carbon nanotubes and the respective methods have been adapted in the production of graphene through the use of CVD.[124] Ni provides a very soluble media in which carbon can diffuse into, at high temperature. The first study on preparing large scale graphene on Ni using a CVD method was reported in 2006.[125] The authors obtained FLG film on Ni substrates from pyrolysis of camphor by thermal CVD. In particular, large amount of camphor yielded pyrolytic graphite films. Later, Yu et al. provided better understanding about the growth mechanism of graphene, after preparing three to four-layer graphene through a CVD process on Ni foils.[126] It was found that the formation of graphene on Ni occurred only under moderate cooling rates, while it was demolished at extreme cooling rates values. In another study, high-quality graphene were grown on patterned Ni films and then transferred on arbitrary substrates by using polydimethylsiloxane.[127] The obtained graphene exhibited 77% transmittance with sheet resistance as low as 280 Ωsq^{-1}, but the segregation rate of carbon from the metal carbide is heterogeneous at the Ni grains and grain boundaries, making difficult to control the layers and homology of graphene.

The growth process of graphene on Cu differs from that on Ni due to the different carbon solubilities in the two metals.[122] Cu exhibits ultralow carbon solubility, with the graphene growth mechanism on Cu being a catalytic process. After the deposition of one- or two-layer, the Cu catalytic properties of decomposing the hydrocarbon surface is decreased, thereby mainly single- or bi-layer graphene can be grown on polycrystalline Cu substrates.[122]

1.3.6 Molecular beam epitaxy (MBE)

MBE is widely used method for the deposition and growth of compound semiconductors.[128] It has been used to grow graphitic layers with high purity carbon sources (**Figure 1.4h**) on a variety of substrates such as SiC,[129] Al_2O_3,[130,131] Mica,[132,133] SiO_2,[132] Ni,[134] Si,[135] h-BN,[136] MgO,[137] etc., using 400-1100 °C temperature range. However, since MBE is not a self-limited process and relies on the reaction between the deposited species,[128] the prepared films have a large domain size distribution of defective crystals with lack of layer control.[134] Since MBE relies on atomic beams of elements impinging on the substrates, it is difficult to prevent the deposition of carbon on areas where graphene has already grown.[26] Therefore, since MBE is a thermal process, the carbon is probable being deposited in the amorphous or nanocrystalline phase. On the other hand, chemical beam epitaxy (CBE)[138] can be used to grow graphene in a catalytic mode, benefiting from the ability of CBE to grow multiple materials, such as dielectrics[139] or layered materials, on the top of graphene, to form heterostructures.

1.3.7 Chemical synthesis

A different graphene production method is based on chemical synthesis, by assembling polycyclic aromatic hydrocarbons (PAHs), through surface-mediated reactions (**Figure 1.4i**).[140,141] Zhi et al. exploited a dendritic precursor transformed in graphene by cyclodehydrogenation and planarization, producing small domains, called nanographene.[142] Another method includes the PAH pyrolysis.[143] PAHs can also be exploited to achieve atomically precise graphene nanorods (GNRs)[143] and graphene quantum dots (GQDs)[144].

1.4 An overview of graphene oxide (GO)

1.4.1 Chemical synthesis of graphite oxide

The discovery of graphite oxide was conducted much earlier than graphene. As already referred, the first report on graphite oxide goes back in 1859, when Prof. Brodie from the University of Oxford attempted to measure the molecular

weight of the graphite.[70] The preparation method was based on heating a mixture of graphite and fuming HNO_3 in the presence of $KClO_3$ at 60 °C for 3-4 days. After washing the product, the oxidation process was repeated four times, to finally produce a light yellow solid after drying at 100 °C. The product C:H:O was calculated to be 61.04:1.85:37.11 and since it was dispersed in pure or alkaline water, and not in acidic media, Brodie named the material ''graphic acid''.[70,145]

Later, in 1898, Staudenmaier altered the previous reported oxidation method by adding the $KClO_3$ quantity in small portions, while the mixture was further acidified with concentrated H_2SO_4.[71] Although, Staudenmaier method produced graphite oxide with almost similar carbon/oxygen (C/O) ratio compared to Brodie procedure, it was much more facile since it did not need further oxidation repetitions.[71]
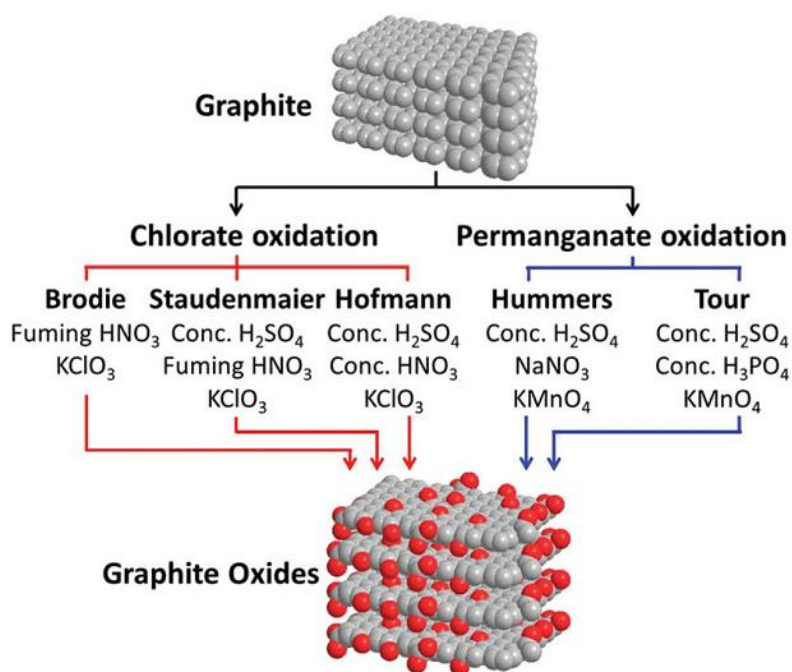
Figure 1.8. Schematic illustration of graphite oxidation methods based either on $KClO_3$ or $KMnO_4$ oxidation routes. Reproduced from reference146.

In 1958, Hummers and Offeman used $KMnO_4$ instead of $KClO_3$ in a mixture of concentrated H_2SO_4 and $KMnO_4$.[68] Since the nitric acid is produced in situ, the use of highly corrosive fuming nitric acid is avoided, making the proposed method safer. On top of that, the combination of $KMnO_4$ and $NaNO_3$ resulted in

a more oxidized form of graphite oxide, thereby Hummers method has been used by many researchers. However, all the aforementioned methods produce toxic gases, mainly NO_2, N_2O_4, as well as explosive ClO_2, in the case of Staudenmaier-Hofmann.

In 2010, Tour et al. used the less corrosive H_3PO_4 to replace the in situ production of nitric acid.[147] This method exhibits a variety of advantages, including the higher oxidation degree of graphite and the avoidance of large exotherm or toxic gases production, making it suitable for large scale production of graphite oxide.

1.4.2 Structure of graphite oxide

Understanding the graphite oxide structure is vital to propose any subsequent chemical modifications of the material.[145] Graphite oxide is primarily composed of carbon, oxygen and hydrogen atoms, with a C/O ratio of approximately 1.5 to 2.5.[145] Although a number of graphite oxide synthesis methods have been proposed during the last 150 years, its exact chemical structure is still under debate. **Figure 1.9** demonstrates the proposed graphite oxide structures, such as the Hofmann, Ruess, Scholz-Boehm, Nakajima-Matsuo, Lerf-Klinowski, Dekany and Ajayan models.
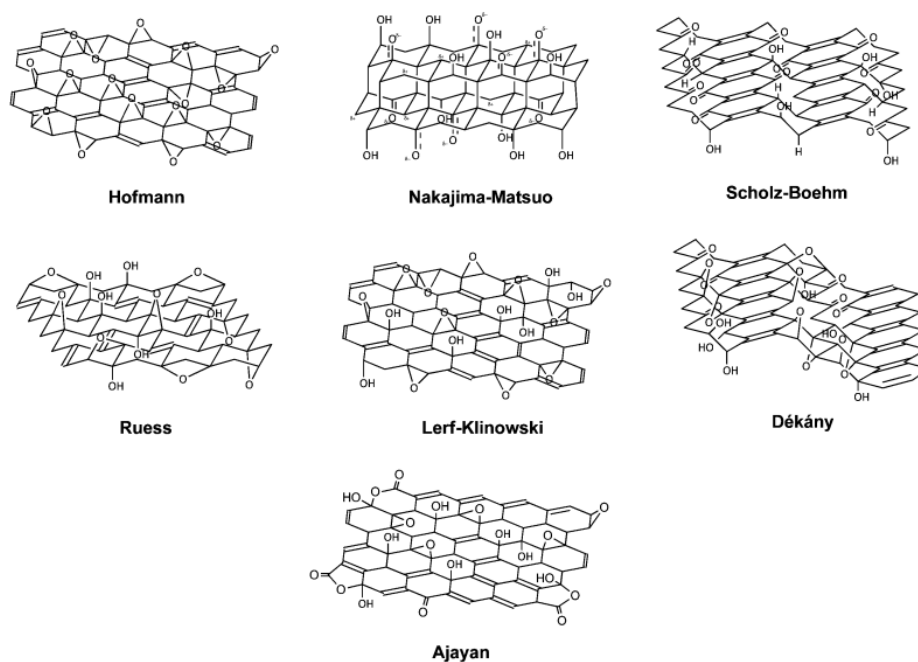
Figure 1.9. The proposed structures of graphite oxide. Reproduced from reference 145.

Hofmann and Holst proposed the first model for graphite oxide structure, which contained repeated units of 1,2-epoxides on the entire graphene basal-plane.[148] In 1946, Ruess presented a new model consisted of sp^3 hybridized basal-planes (1,3-epoxide and hydroxyl groups) in contrast to sp^2 hybridized system of Hofmann and Holst.[149] Twenty years later, a new graphite oxide model consisted of hydroxyl and ketone groups was proposed by Scholz and Boehm, while Nakajima and Matsuo presented a structure which was very analogous to a graphite intercalation compound.[150,151] Lerf and Klinowski, after performing ^{13}C and ^{1}H magic-angle spinning nuclear magnetic resonance (MAS NMR) studies, presented a graphite oxide model, containing an aromatic region with unoxidised benzene rings as well as an aliphatic six-membered rings region.[152,153] Oxygen functional groups including 1,2-epoxides occupied the basal-plane while carboxyl are located at the edge-plane. Hydroxyl groups can be found in both regions. Based on the Ruess and Scholz–Boehm models, De kany depicted a graphite oxide structure comprised of two distinct domains containing trans linked cyclohexane chairs and corrugated hexagon ribbons.[154] Finally, in 2009, Ajayan et al. detected the presence of lactols at peripheral edges, specifically 2-hydroxynaphthalic anhydrides or 1,3-dihydroxyxanthones.[155] **Figure 1.10** demonstrates a general model of graphite oxide including the proposed oxygen containing groups.
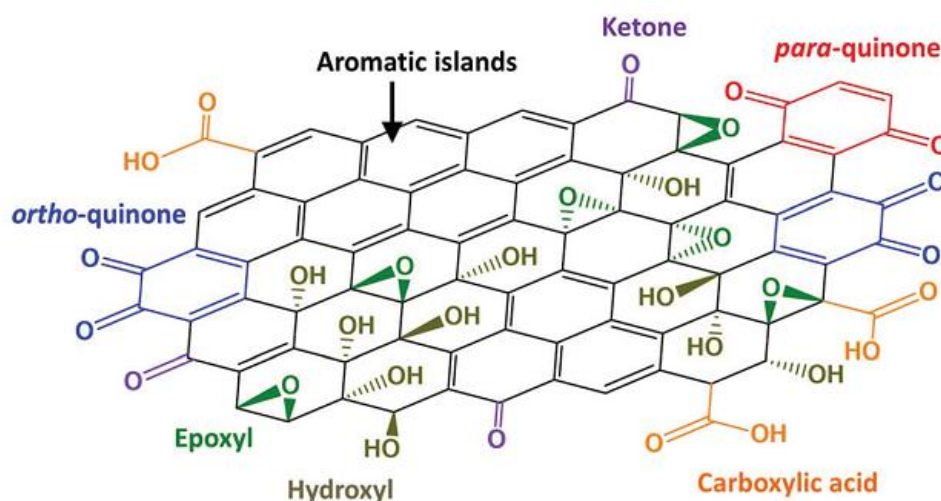
Figure 1.10. General model of graphite oxide demonstrating various oxygen functional group types distributed across aromatic regions. Reproduced from reference 146.

1.4.3 From graphite oxide to graphene

Graphite oxide is a very important intermediate material towards graphene production (**Figure 1.11**).[145] The introduction of oxygen functionalities on graphite layers assist in the increase of the interlayer distance between graphene sheets in graphite, with the subsequent weakening of van der Waals forces. In this way, the exfoliation of graphite oxide to GO is facilitated, providing the opportunity for the large scale production of graphene.[145] Graphite oxide can be thought as a highly oxidized graphite form, with the same multilayer structure of its precursor but with higher interlayer spacing. These oxygen functionalities are responsible for the structural defects that differentiate graphite oxide from the state of pristine graphene.
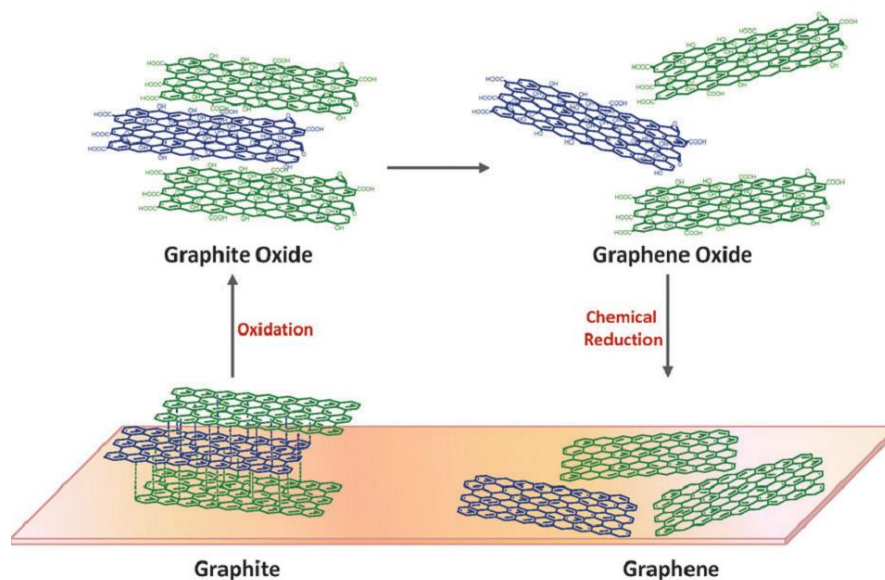
Figure 1.11. Production of graphene from graphite. Reproduced from reference 145.

The corresponding exfoliated GO, is the second intermediate material in the chemical exfoliation of graphene. GO is structurally different but chemically analogous to graphite oxide.[145] The oxygen containing groups of its precursor are present, but it consists of mono-, bi- or few-layer graphene layers. The aqueous dispersibility is attributed to the carboxylic acid groups which mainly decorate the flake edges, facilitating the assembly of macroscopic structures by simple and cheap solution processes.[77,156] The exfoliation of GO can be performed via mechanical stirring or ultrasonication methods in a polar organic

solvent or aqueous media.[145] Although ultrasonication results in a more efficient and faster exfoliation of the stacked graphite oxide sheets, it can lead to structural damages and breaking of GO sheets into smaller fragments.[157] Mechanical stirring can take more time to accomplish, but it is a much less heavy-handed method.

The final step in the chemical exfoliation of graphene includes the reduction of GO, which lead to removal of the majority of oxygen functionalities. The final product, termed reduced graphene oxide (rGO), is an attractive material, because it exhibits similar properties with graphene, but it also offers the opportunity for solution process.

1.4.4 Reduction of graphite oxide

An important aspect in the research and applications of GO is the reduction, through which the structure and properties of graphene are partially restored. Different methods have been proposed for the reduction of GO to rGO, using thermal, chemical and photochemical means. The different reduction methods would lead to rGO of varying performances in terms of electronic, structural, physical and surface morphological properties.[145] Although these graphene derivatives exhibit a sp^2 carbon network containing defects, they share close resemblance to pristine graphene and are highly suitable for applications that require a large quantity of graphene materials.[145]

1.4.4.1 Thermal reduction

GO can be reduced through heat treatment and the process is termed thermal annealing reduction.[156] In the early graphene research stages, the rapid heating (>2000 °Cmin^{-1}) was used to exfoliate graphite oxide to graphene.[81,158] The respective exfoliation mechanism is based on the sudden expansion of CO or CO_2 gases developed into the spaces between graphene sheets during the rapid temperature increase of the graphite oxide. The rapid heating result in the decomposing of the oxygen functional groups attached into gases that subsequently cause the generation of huge pressure between the stacked layers. Based on state equation, a pressure of 40 MPa and 130 MPa can be created at 300 °C and 1000 °C respectively.[159]

Although this thermal reduction is attractive due to its simplicity, ideal graphene is not prepared, even at temperatures higher than 1100 °C. Instead, a ruptured carbon framework is prepared, that exhibits s-hole defects functionalized with oxygen containing groups, such as carbonyl groups or ethers.[15,160] Defects negatively affect the rGO electronic properties by reducing the ballistic transport path length and introducing scattering centers. As a result, the electrical conductivity of the thermally rGO sheets equals to 10-23 Scm[-1] much lower than that of perfect graphene.[156] Complete deoxygenation of GO can be performed at temperatures >1500 °C, where also reorganization of the carbon framework is caused.[161] Such conditions are not favorable due to the high energy required as well as the incompatibility with temperature-sensitive substrates.[15] In addition, CVD methods are more effective for preparing higher quality graphene at lower temperatures.

1.4.4.2 Chemical reduction

While the first reports for graphite oxidation go back in 1859, efforts to remove the oxygen containing groups from graphite oxide did not occur until 1963. It was then, when Brauer demonstrated the reduction of graphite oxide with hydrazine, hydroxylamine, hydroiodic acid (HI), iron(II) and tin(II) ions.[162] This knowledge has been transferred to GO reduction.

Reduction using chemical means is performed based on their chemical reactions with GO. The reduction process can be conducted at room temperature or by moderate heating and it is clear that the requirement for specific equipment is not as crucial compared to thermal reduction. This makes chemical reduction much cheaper and facile technique for graphene mass production. The GO transformation to rGO is experimentally often indicated by a color change of the reaction mixture from brown to black as well as an increase of hydrophobicity/aggregation, owing to the removal of oxygen functional groups.[145] Elemental analysis has verified a decrease in oxygen contents and an increase in C/O ratio.[145]

Numerous methods of chemical reduction have been tested. The graphite oxide reduction with hydrazine was used before the discovery of graphene,[163] while Stankovich et al. first reported the use of hydrazine to prepare chemically derived graphene.[79] The reduction process using hydrazine and its derivatives

(hydrazine hydrate and dimethylhydrazine)[164] can be performed by adding the liquid reagents to an aqueous dispersion of GO, resulting in agglomerated graphene-based nanosheets owing to the hydrophobicity increase. An electrically conductive black powder with C/O ratio around 10 can be obtained, after drying.[79] Metal hydrides, such as sodium hydride, sodium borohydride (NaBH₄) and lithium aluminium hydride, have been reported as strong reducing reagents in organic chemistry.[165] Although these reducing agents are slowly hydrolyzed by water, their use is kinetically slow enough that the freshly-formed solution can effectively reduce GO.[156] NaBH₄ can be used as selective reducing agent, since it is most effective at reducing C=O groups and exhibits moderate reduction performance for epoxy groups and carboxylic acids.[166] Alcohol functional groups remain after reduction.[156] Recently, HI was reported as a strong reducing reagent for GO, resulting in rGO with C/O ratio of around 15,[167,168] and conductivity values of approximately 300 Scm^{-1}. The mechanisms of GO reduction by HI included the iodination of alcohols, cleavage of ether, reduction of aromatic iodides and partial reduction of the carbonyl moiety.[168]

1.4.4.3 Photochemical reduction

GO reduction can be also performed using appropriate photochemical means. Flash treatment can effectively reduce GO films when performed using a single, close-up (<1 cm) flash from a xenon lamp such as the one that exists on a camera.[169] In particular, a flash lamp can emit enough energy at a close distance (<2 mm: ~1 Jcm^{-2}) to induce deoxygenating reactions.[169] This energy equals nine times the thermal energy needed for heating GO over 100 °C, suggesting that flash irradiation could lead to a much higher degree of reduction of GO. Since the light can be easily shielded, rGO patterns can be developed using photomasks, which facilitates the direct fabrication of electronic devices based on rGO films.[156] Zhang et al. demonstrated GO photoreduction and fabrication of patterned film using femtosecond laser irradiation.[170] The focused laser beam has higher power density than a xenon lamp flash, while the heated area on a GO film is more localized. As a result, the laser reduction can prepare rGO films with higher conductivity (~256 Scm^{-1}), while a pre-programmed laser can form more complicated circuits on rGO film patterns, which can be directly used in electronic devices.

REFERENCES

1 Falcao, E.H.L.; Wudl, F. *J Chem Techn Biot*, **2007**, 82, 524-531.

2 Georgakilas, V. Functionalization of Graphene, Wiley-VCH Verlag GmbH & Co. KGaA, Weinheim, Germany, **2014**.

3 Saito, R.; Dresselhaus, G.; Dresselhaus, M.S. Physical Properties of Carbon Nanotubes Imperial College Press, London, **1998**.

4 Rinken, T. Biosensors - Micro and Nanoscale Applications, InTech, **2015**.

5 Petroski, H. The pencil: A History of design and circumstance, Knopf, New York, **1989**.

6 Chung, D.D.L. *J Mater Sci,* **2002**, 37, 1475-1489.

7 Mongillo, J.F. Nanotechnology 101. Greenwood Press, Westport, Connecticut, USA, **2007**.

8 Kroto, H.W.; Heath, J.R.; O'Brien, S.C.; Curl, R.F.; Smalley, R.E. *Nature,* **1985**, 318, 162-164.

9 Wudl, F. *Acc Chem Res*, **1992**, 25, 157–161.

10 Buhl, M.; Hirsch, A. *Chem Rev*, **2001**, 101, 1153–1183.

11 Segura, J.L.; Martin, N.; Guldi, D.M. *Chem Soc Rev,* **2005**, 34, 31–47.

12 Iijima, S. *Nature,* **1991**, 354, 56.

13 Iijima, S.; Ichihashi, T. *Nature*, **1993**, 363, 603.

14 Geim, A. K.; Novoselov, K. S. *Nat Mater*, **2007**, 6, 183–191.

15 Eigler, S.; Hirsch, A. *Angew Chem Int Ed Engl.*, **2014**, 53, 7720-38.

16 Novoselov, K. S.; Geim, A. K.; Morozov, S. V.; Jiang, D.; Zhang, Y.; Bubonos, S. V.; Grigorieva, I. V.; Firsov, A. A. *Science*, **2004**, 306, 666.

17 Nair, R. R.; Blake, P.; Grigorenko, A. N.; Novoselov, K. S.; Booth, T. J.;. Stauber, T.; Peres, N. M. R.; Geim, A. K. *Science*, **2008**, 320, 1308.

18 Weber, C. M.; Eisele, D. M.; Rabe, Y.; Liang, X.; Feng, L.; Zhi, K.; Müllen, J.; Lyon, L.; Williams, R.; Bout, D. A. V.; Stevenson, K. J. *Small*, **2010**, 6, 184.

19 Tiwari, A.; Syvajarvi, M. Graphene Materials: Fundamentals and Emerging Applications, Wiley, **2015**.

20 Wang, H. X.; Wang, Q.; Zhou, K.G.; Zhang, H. L. *Small,* **2013**, 9, 1266-1283.

21 Lee, C.; Wei, X. D.; Kysar, J. W.; Hone, J. *Science*, **2008**, 321, 385-388.

22 Balandin, A. A.; Ghosh, S.; Bao, W. Z.; Calizo, I.; Teweldebrhan, D.; Miao, F.; Lau, C. N., *Nano Lett*, **2008**, 8, 902-907.

23 Eizenberg, M.; Blakely, J. M. *Surf Sci*, **1970**, 82, 228–236.

24 Aizawa, T.; Souda, R.; Otani, S.; Ishizawa, Y.; Oshima, C.; *Phys Rev Lett*, **1990**, 64, 768–771.

25 Berger, C.; Song, Z.; Li X.; Wu X.; Brown, N.; Naud, C.; Mayou, D.; Li, T.; Hass, J.; Marchenkov, A.N.; Conrad, E.H.; First, P.N.; de Heer, W.A. *Science*, **2006**, 312, 1191–1196.

26 Bonaccorso, F.; Lombardo, A.; Hasan, T.; Sun, Z.; Colombo, L.; Ferrari, AC *Mater Today*, **2012**, 15, 564.

27 Schultz, R. A.; Jensen, M. C.; Bradt, R. C. *Int J Fracture*, **1994**, 65, 291.

28 Romero, R.; Robert, M.; Elsass, F.; Garcia, C. *Clay Minerals*, **1992**, 27, 21.

29 Lu, X.; Yu, M.; Huang, H.; Ruoff, R. S. *Nanotechnology*, **1999**, 10, 269.

30 Geim, A. K. *Science*, **2009**, 324, 1530.

31 Casiraghi, C.; Hartschuh, A.; Lidorikis, E.; Qian, H.; Harutyunyan, H.; Gokus, T.; Novoselov, K. S.; Ferrari, A. C. *Nano Lett*, **2007**, 7, 2711.

32 Ferrari, A. C.; Meyer, J. C.; Scardaci, V.; Casiraghi, C.; Lazzeri, M.; Mauri, F.; Piscanec, S.; Jiang, D.; Novoselov, K. S.; Roth, S.; Geim, A. K. *Phys Rev Lett*, **2006**, 97, 187401.

33 Casiraghi, C.; Pisana, S. *Appl Phys Lett*, **2007**, 91, 233108.

34 Das, A.; Pisana, S.; Chakraborty, B.; Piscanec, S.; Saha, S. K.; Waghmare, U. V.; Novoselov, K. S.; Krishnamurthy, H. R.; Geim, A. K.; Ferrari, A. C.; Sood, A. K. *Nat Nanotech*, **2008**, 3, 210.

35 Ferrari, A. C.; Robertson, J. *Phys Rev B*, **2000**, 61, 14095.

[36] Cancado, L. G.; Jorio, A.; Martins Ferreira, E. H.; Stavale, F.; Achete, C. A.; Capaz, R. B.; Moutinho, M. V. O.; Lombardo, A.; Kulmala T. S.; Ferrari, A. C. *Nano Lett*, **2011**, 11, 3190.

[37] Ferralis, N.; Maboudian, R.; Carraro, C. *Phys Rev Lett*, **2008**, 101, 156801.

[38] Ferrari, A. C. *Solid State Comm*, **2007**, 143, 47.

[39] Elias, D. C.; Nair, R. R.; Mohiuddin, T. M. G.; Morozov, S. V.; Blake, P.; Halsall, M. P.; Ferrari, A. C.; Boukhvalov, D. W.; Katsnelson, M. I.; Geim, A. K.; Novoselov, K. S. *Science*, **2009**, 323, 610.

[40] Basko, D. M.; Piscanec, S.; Ferrari, A. C. *Phys Rev B*, **2009**, 80, 165413.

[41] Albaugh, K. B. *J. Electrochem. Soc.*, **1991**, 138, 3089.

[42] Henmi, H.; Shoji, S.; Shoji, Y.; Yoshimi, K.; Esashi, M. *Sens Act A*, **1994**, 43, 243.

[43] Shukla, A.; Kumar, R.; Mazher, J.; Balan, A. *Solid State Commun*, **2009**, 149, 718.

[44] Moldt, T.; Eckmann, A.; Klar, P.; Morozov, S. V.; Zhukov, A. A.; Novoselov, K. S.; Casiraghi, C. *ACS Nano*, **2011**, 5, 7700.

[45] Chrisey, D. B.; Hubler, G. K. Pulsed Laser Deposition of Thin Films, 648 Wiley-VCH, **2003**.

[46] Miyamoto, Y.; Zhang, H.; Tomanek, D. *Phys Rev Lett*, **2010**, 104, 208302.

[47] Dhar, S.; Barman, A. R.; Ni, G. X.; Wang, X.; Xu, X. F.; Zheng, Y.; Tripathy S.; Ariando; Rusydi, A.; Loh, K.P.; Rubhausen, M.; Castro Neto, A. H.; Ozyilmaz, B.; Venkatesan, T. *AIP Adv*, **2011**, 1, 022109.

[48] Reininghaus, M.; Wortmann, D.; Finger, J.; Faley, O.; Poprawe, R.; Stampfer, C. *Appl Phys Lett*, **2012**, 100, 151606.

[49] Lee, S.; Toney, M. F.; Ko, W.; Randel, J. C.; Jung, H.J.; Munakata, K.; Lu, J.; Geballe, T. H.; Beasley, M. R.; Sinclair, R.; Manoharan, H. C.; Salleo, A. *ACS Nano*, **2010**, 4, 7524.

[50] Qian, M.; Zhou, Y. S.; Gao, Y.; Park, J.B.; Feng, T.; Huang, S. M.; Sun, Z.; Jiang, L.; Lu Y. F. *Appl Phys Lett*, **2011**, 98, 173108.

[51] Mortazavi, S. Z.; Parvin, P.; Reyhani, A. *Laser Phys. Lett.*, **2012**, 9, 547.

[52] Bonaccorso F.; Sun, Z. *Opt Mater Express*, **2014**, 4, 63–78.

[53] Hernandez, Y.; Nicolosi, V.; Lotya, M.; Blighe, F. M.; Sun, Z.; De, S.; Mc Govern, I. T.; Holland, B.; Byrne, M.; Gun'ko, Y. K.; Boland, J. J.; Niraj, P.; Duesberg, G.; Krishnamurthy, S.; Goodhue, R.; Hutchison, J.; Scardaci, V.; Ferrari, A. C.; Coleman, J. N. *Nat Nanotech*, **2008**, 3, 563.

[54] Lotya, M.; Hernandez, Y.; King, P. J.; Smith, R. J.; Nicolosi, V.; Karlsson, L. S.; Blighe, F. M.; De, S.; Wang, Z.; Mc Govern, I. T.; Duesberg, G. S.; Coleman, J. N. *J Am Chem Soc*, **2009**, 131, 3611.

[55] Maragó, O. M.; Bonaccorso, F.; Saija, R.; Privitera, G.; Gucciardi, P. G.; Iatı, M. A.; Calogero, G.; Jones, P. H.; Borghese, F.; Denti, P.; Nicolosi, V.; Ferrari, A. C. *ACS Nano*, **2010**, 4, 7515.

[56] Torrisi, F.; Hasan, T.; Wu, W.; Sun, Z.; Lombardo, A.; Kulmala, T. S.; Hsieh, G. W.; Jung, S.; Bonaccorso, F.; Paul, P. J.; Chu, D.; Ferrari, A. C. *ACS Nano*, **2012**, 6, 2992.

[57] Blake, P.; Brimicombe, P. D.; Nair, R. R.; Booth, T. J.; Jiang, D.; Schedin, F.; Ponomarenko, L. A.; Morozov, S. V.; Gleeson, H. F.; Hill, E. W.; Geim, A. K.; Novoselov, K. S. *Nano Lett.*, **2008**, 8, 1704.

[58] Mason, T. J. Sonochemistry, *Oxford*, **1999**.

[59] Svedberg, T.; Pedersen, K. O. The Ultracentrifuge, Oxford, **1940**.

[60] Behrens, M. Z.; Hoppe-Seyler's Z. *Physiol Chem*, **1939**, 258, 27.

[61] Khan, U.; O'Neill, A.; Lotya, M.; De, S.; Coleman, J. N. *Small*, **2010**, 6, 864.

[62] Alzari, V.; Nuvoli, D.; Scognamillo, S.; Piccinini, M.; Gioffredi, E.; Malucelli, G.; Marceddu, S.; Sechi, M.; Sanna, V.; Mariani, A. *J Mater Chem*, **2011**, 21, 8727.

[63] Green A. A.; Hersam, M. C. *Nano Lett*, **2009**, 9, 4031.

[64] Wu, Z. S.; Ren, W. C.; Gao, L. B.; Liu, B. L.; Zhao, J. P.; Cheng, H. M. *Nano Res*, **2010**, 3, 16.

[65] Israelachvili, J. Intermolecular and surface force. Boston: Academic Press 3rd edition, **2011**.

[66] Ghatee, M. H.; Pakdel, L. *Fluid Phase Equil*, **2005**, 234, 101.

[67] Lyklema, J. *Colloids Surf A*, **1999**, 156, 413.

[68] Hummers, W. S.; Offeman, R. *E. J Am Chem Soc*, **1958**, 80, 1339.

[69] Nakajima, T.; Matsuo, Y. *Carbon*, **1994**, 32, 469.

[70] Brodie, B. C. *Ann Chim Phys*, **1860**, 59, 466.

[71] Staudenmaier, L. V. *Ber Deut Chem Ges*, **1898**, 31, 1481.

[72] Dreyer, D. R.; Park, S.; Bielawski, C. W.; Ruoff, R. S. *Chem Soc Rev*, **2010**, 39, 1.

[73] Hyde, F. S. *J Soc Chem* Ind, **1904**, 23, 300.

[74] Kohlschtter, V.; Haenni, P. Z.; *Anorg Allg Chem*, **1918**, 105, 121

[75] Ruess, G.; Vogt, F.; *Monatsh für Chemie*, **1948**, 78, 222.

[76] Gomez-Navarro, C.; Meyer, J. C.; Sundaram, R. S.; Chuvilin, A.; Kurasch, S.; Burghard, M.; Kern, K.; Kaiser, U. *Nano Lett*, **2010**, 10, 1144

[77] Erickson, K.; Erni, R.; Lee, Z.; Alem, N.; Gannett, W.; Zettl, A. *Adv Mater*, **2010**, 22, 4467.

[78] Li, X.; Wang, X.; Zhang, L.; L. Lee, L.; Dai, H. *Science*, **2008**, 319, 1229.

[79] Stankovich, S.; Dikin, D. A.; Piner, R. D.; Kohlhaas, K. A.; Kleinhammes, A.; Jia, Y.; Wu, Y.; Nguyen, S. T.; Ruoff, R. S. *Carbon*, **2007**, 45, 1558.

[80] Lomeda, J. R.; Doyle, C. D.; Kosynkin, D. V.; Hwang, W. F.; Tour, J. M. *J Am Chem Soc*, **2008**, 130, 16201.

[81] Schniepp, H. C.; Li, J. L.; McAllister, M. J.; Sai, H.; Herrera-Alonso, M.; Adamson, D. H.; Prud'homme, R. K.; Car, R.; Saville, D. A.; Aksay, I. A. *J Phys Chem B*, **2006**, 110, 8535.

[82] Li, X. L.; Wang, H. L.; Robinson, J. T.; Sanchez, H.; Diankov, G.; Dai, H. J. *J Am Chem Soc*, **2009**, 131, 15939.

[83] Niyogi, S.; Bekyarova, E.; Itkis, M. E.; McWilliams, J. L.; Hamon, M. A.; Haddon, R. C. *J Am Chem Soc*, **2006**, 128, 7720.

[84] Konios, D.; Stylianakis, M. M.; Stratakis, E.; Kymakis, E. *J Col Interf Sci*, **2014**, 430, 108.

[85] Paredes, J. I.; Villar-Rodil, S.; Martınez-Alonso, A.; Tascon, J. M. D. *Langmuir*, **2008**, 24, 10560.

[86] Viculis, L. M.; Mack, J. J., Mayer, O. M.; Hahn, H. T.; Kaner, R.B. *J Mater Chem*, **2005**, 15, 974.

[87] Lee, J. H.; Shin, D. W.; Makotchenko, V. G.; Nazarov, A. S.; Fedorov, V. E.; Kim, Y. H.; Choi, J. Y.; Kim, J. M.; Yoo, J. B. *Adv Chem*, **2009**, 21, 4383.

[88] Gu, W. T.; Zhang, W.; Li, X. M.; Zhu, H. W.; Wei, J. Q.; Li, Z.; Shu, Q.; Wang, C.; Wang, K. L.; Shen, W.; Kang, F. Y.; Wu, D. H.; Mater, J. *Chem*, **2009**, 19, 3367.

[89] Falcao, E. H. L.; Blair, R. G.; Mack, J. J.; Viculis, L. M.; Kwon, C. W.; Bendikov, M.; Kaner, R. B.; Dunn, B. S. *Carbon*, **2007**, 45, 1367.

[90] Qian, W.; Hao, R.; Hou, Y. L.; Tian, Y.; Shen, C. M.; Gao, H. J.; Liang, X. L. *Nano Res*, **2009**, 2, 706.

[91] Ciesielski, A.; Samori, P. *Chem Soc Rev*, **2014**, 43, 381-398.

[92] Berger, C.; Song, Z.; Li, T.; Li, X.; Ogbazghi, A. Y.; Feng, R.; Dai, Z.; Marchenkov, A. N.; Conrad, E. H.; First, P. N.; de Heer, W. A. *J Phys Chem B*, **2004**, 108, 19912.

[93] Acheson, E. G. *US patent*, **1896**, 615, 648.

[94] Badami, D. V. *Nature*, **1962**, 193, 569.

[95] Emtsev, K. V.; Bostwick, A.; Horn, K.; Jobst, J.; Kellogg, G. L.; Ley, L.; McChesney, J. L.; Ohta, T.; Reshanov, S. A.; Röhrl, J.; Rotenberg, E.; Schmid, A. K.; Waldmann, D.; Weber, H. B.; Seyller, T. *Nat Mater*, **2009**, 8, 203.

[96] Riedl, C.; Coletti, C.; Iwasaki, T.; Zakharov, A. A.; Starke, U. *Phys Rev Lett*, **2009**, 103, 246804.

[97] Borsa C. J. Large Area Graphene Synthesis, M.Sc. in Nanotechnology, KTH Royal Institute of Technology, **2012**.

[98] Van Bommel, A. J.; Crombeen, J. E.; Van Tooren, A. *Surf Sci*, **1975**, 48, 463.

[99] de Heer, W. A.; Berger, C.; Ruan, M.; Sprinkle, M.; Li, X.; Hu, Y.; Zhang, B.; Hankinson, J.; Conrad, E. *PNAS*, **2011**, 108, 16900.

[100] Kang, H. C.; Karasawa, H.; Miyamoto, Y.; Handa, H.; Suemitsu, T. Suemitsu, M.; Otsuji, T. *Sol State Electron*, **2010**, 54, 1010.

[101] Lipson, H.; Stokes, A. R.; *Proc R Soc Lond A*, **1942**, 181, 101.

[102] Biscoe, J.; Warren, B. E. *J Appl Phys*, **1942**, 13, 364.

[103] Shelton, J. C.; Patil, H. R.; Blakely, J. M. *Surf Sci*, **1974**, 43, 493.

[104] Winder, S. M.; Liu, D.; Bender, J. W. *Carbon*, **2006**, 44, 3037.

[105] Massalski, T. B.; Okamoto, H.; Subramanian, P. R.; Kacprzak, L., Binary Alloy Phase Diagrams, *ASM International*, **1990**.

[106] Li, X.; Cai, W.; An, J.; Kim, S.; Nah, J.; Yang, D.; Piner, R.; Velamakanni, A.; Jung, I.; Tutuc, E.; Banerjee, S. K.; Colombo, L.; Ruoff, R. S. *Science*, **2009**, 324, 1312.

[107] Okamoto, H. C-Hf (Carbon-Hafnium), Binary Alloy Phase Diagrams, 2nd Ed., *Ed T B Massalski*, **1990**, 1, 849.

[108] Cadoff, I.; Nielsen, J. F. *Trans Am Inst Min Metal Pet Eng*, **1953**, 197, 248.

[109] Ruan, G.; Sun, Z.; Peng, Z.; Tour, J. M. *ACS Nano*, **2011**, 5, 7601.

[110] Sun, Z.; Yan, Z.; Yao, J.; Beitler, E.; Zhu, Y.; Tour, J. M. *Nature*, **2010**, 468, 549.

[111] Guermoune, A.; Chari, T.; Popescu, F.; Sabri, S. S.; Guillemette, J.; Skulason, H. S.; Szkopek, T.; Siaj, M. *Carbon*, **2011**, 49, 4204.

[112] Miyasaka, Y.; Nakamura, A.; Temmyo, J. *J Appl Phys*, **2011**, 50, 04DH12.

[113] Miyata, Y.; Kamon, K.; Ohashi, K.; Kitaura, R.; Yoshimura, M.; Shinohara, H. *Appl Phys Lett*, **2010**, 96, 263105.

[114] Karu, A. E.; Beer, M. *J Appl Phys*, **1966**, 37, 2179.

[115] Peters, K. R. *J Microsc*, **1984**, 133, 17.

[116] Powell, C. F.; Joseph, H. O.; John, M. B.; Blocher, M. *New York Wiley*, **1966**.

[117] Coraux, J.; N′Diaye, A. T.; Busse, C.; Michely, T. *Nano Lett*, **2008**, 8, 565.

[118] Ramon, M. E.; Gupta, A.; Corbet, C.; Ferrer, D. A.; Movva, H. C. P.; Carpenter, G.; Colombo, L.; Bourianoff, G.; Doczy, M.; Akinwande, D.; Tutuc, E.; Banerjee, S. K. *ACS Nano*, **2011**, 5, 7198.

[119] Yoshii, S.; Nozawa, K.; Toyoda, K.; Matsukawa, N.; Odagawa, A.; Tsujimura, A. *Nano Lett*, **2011**, 11, 2628.

[120] Dai, B.; Fu, L.; Zou, Z.; Wang, M.; Xu, H.; Wang, S.; Liu, Z. *Nat Comm*, **2011**, 2, 522.

[121] Peng, Z.; Yan, Z.; Sun, Z.; Tour, J. M. *ACS Nano*, **2011**, 5, 8241.

[122] Liu, A.; Lau, S. P.; Yan, F. *Chem Soc Rev*, **2015**, 44, 5638-5679

[123] Xu, Y.; Yan, X. T. Chemical Vapour Deposition: An Integrated Engineering Design for Advanced Materials Springer, **2009**.

[124] Reina, A.; Jia, X.; Ho, J.; Nezich, D.; Son, H.; Bulovic, V.; Dresselhaus, M. S.; Kong, J. *Nano Lett*, **2009**, 9, 30.

[125] Somani, P.R.; Somani, S. P.; Umeno, M. *Chem Phys Lett*, **2006**, 430, 56-59.

[126] Yu, Q.; Lian, J.; Siriponglert, S.; Li, H.; Chen Y. P.; Pei, S. S. *Appl Phys Lett*, **2008**, 93, 113103

[127] Kim, K. S.; Zhao, Y.; Jang, H.; Lee, S. Y.; Kim, J. M.; Ahn, J. H.; Kim, P; Choi, J. Y.; Hong, B. H. *Nature*, **2009**, 457, 706-710

[128] Cho, A. Y.; Arthur, J. R. *Prog Solid State Chem*, **1975**, 10, 157.

[129] Al-Temimy, A.; Riedl, C.; Starke, U. *Appl Phys Lett*, **2009**, 95, 231907.

[130] Jerng, S. K.; Yu, D. S.; Kim, Y. S.; Ryou, J.; Hong, S.; Kim, C.; Yoon, S.; Efetov, D. K.; Kim, P.; Chun, S.H. *J Phys Chem C*, **2011**, 115, 4491.

[131] Liu, Z.; Tang, J.; Kang, C.; Zou, C.; Yan, W.; Xu, P. *Solid State Commun*, **2012**, 152, 960.

[132] Seifarth, O.; Lippert, G.; Dabrowski, J.; Lupina, G.; Mehr, W.; Lemme, M. C. *IEEE*, **2011**, 12344834, 1.

[133] Lippert, G.; Dabrowski, J.; Lemme, M. C.; Marcus, C. M.; Seifarth, O.; Lupina, G. *Phys Stat Solidi B*, **2011**, 248, 2619.

[134] Garcia, J. M.; He, R.; Jiang, M. P.; Yan, J.; Pinczuk, A.; Zuev, Y. M.; Kim, K. S.; Kim, P.; Baldwin, K.; West, K. W.; Pfeiffer, L. N. *Solid State Commun*, **2010**, 150, 809.

[135] Hackley, J.; Ali, D.; Di Pasquale, J.; Demaree, J. D.; Richardson, C. J. K. *Appl Phys Lett*, **2009**, 95, 133114.

[136] Garcia, J. M.; Wurstbauer, U.; Levy, A.; Pfeiffer, L. N.; Pinczuk, A.; Plaut, A. S.; Wang, L.; Dean, C. R.; Buizza, R.; Van Der Zande, A. M.; Hone, J.; Watanabe, K.; Taniguchi, T. *Solid State Commun*, **2012**, 152, 975.

[137] Jerng, S. K.; Lee, J. H.; Yu, D. S.; Kim, Y. S.; Ryou, J.; Hong, S.; Kim, C.; Yoon, S.; Chun, S. H. *J Phys Chem C*, **2012**, 116, 7380.

[138] Tsang, W. T. *Appl Phys Lett*, **1984**, 45, 1234.

[139] Lee, K. Y.; Lee, W. C.; Lee, Y. J.; Huang, M. L.; Chang, C. H.; Wu, T. B.; Hong, M.; Kwo, J. *Appl Phys Lett*, **2006**, 89, 222906.

[140] Wu, J.; Pisula, W.; Muellen, K. *Chem Rev*, **2007**, 107, 718-743.

[141] Cai, J., Ruffieux, R.; Jaafar, R.; Bieri, M.; Braun, T.; Blankenburg, S.; Muoth, M.;Seitsonen, A. P.; Saleh, M.; Feng, X.; Müllen K.; Fasel R. *Nature*, **2010**, 466, 470-473.

[142] Zhi, L.; Mullen, K. A. *J Mater Chem*, **2008**, 18, 1472.

[143] Dossel, L.; Gherghel, L.; Feng, X.; Mullen, K. *Angew Chem*, **2011**, 50, 2540.

[144] Yan, X., Cui, X.; Li, B.; Li L. S. *Nano Lett*, **2010**, 10, 1869-1873.

[145] Chua, C. K.; Pumera, M. *Chem Soc Rev*, **2014**, 43, 291-312

[146] Eng, A. Y. S.; Chua, C. K; Pumera, M. *Nanoscale*, **2015**, 7, 20256

[147] Marcano, D. C.; Kosynkin, D. V.; Berlin, J. M.; Sinitskii, A.; Sun, Z. Z.; Slesarev, A.; Alemany, L. B.; Lu W.; Tour, J. M. *ACS Nano*, **2010**, 4, 4806-4814.

[148] Hofmann U.; Holst, R. *Ber Dtsch Chem Ges*, **1939**, 72, 754-771

[149] Ruess, G. *Monatsh Chem*, **1946**, 76, 381-417

[150] Scholz W.; Boehm, H. P. *Z Anorg Allg Chem*, **1969**, 369, 327-340

[151] Nakajima, T.; Matsuo, Y. *Carbon*, **1994**, 32, 469-475.

[152] He, H.; Riedl, T.; Lerf A.; Klinowski, J. *J Phys Chem*, **1996**, 100, 19954-19958.

[153] Lerf, A.; He, H. Y.; Forster, M.; Klinowski, J. *J Phys Chem B*, **1998**, 102, 4477-4482.

[154] Szabo T.; Berkesi, O.; Forgo, P.; Josepovits, K.; Sanakis, Y.; Petridis D.; Dekany, I. *Chem Mater*, **2006**, 18, 2740-2749.

[155] Gao, W.; Alemany, L. B.; Ci L. J.; Ajayan, P. M. *Nat Chem*, **2009**, 1, 403-408.

[156] Pei, S.; Cheng, H. M. *Carbon*, **2012**, 50, 3210-3228.

[157] Park S.; Ruoff, R. S. *Nat Nanotechnol*, **2009**, 4, 217-224.

[158] Wu, Z. S.; Ren, W.; Gao, L.; Liu, B.; Jiang, C.; Cheng, H. M. *Carbon* **2009**, 47, 493-499.

[159] McAllister M.J.; Li J. L.; Adamson, D. H.; Schniepp, H. C.; Abdala, A. A.; Liu, J.; Alonso, M. H.; Milius, D. L.; Car, R.; Prud'homme, R. K.; Aksay, I. A. *Chem Mater*, **2007**, 19, 4396-4404.

[160] Ganguly, A.; Sharma, S.; Papakonstantinou, P.; Hamilton, J. *J Phys Chem C*, **2011**, 115, 17009.

[161] Rozada, R.; Paredes, J. I.; Villar-Rodil, S.; Martnez-Alonso, A.; Tascn, J. M. D. *Nano Res*, **2013**, 6, 216-233.

[162] Brauer, G. Handbook of Preparative Inorganic Chemistry, Academic Press, **1963**.

[163] Kotov, N. A.; Dekany, I.; Fendler, J. H. *Adv Mater*, **1996**, 8, 637-641

[164] Stankovich, S.; Dikin, D. A.; Dommett, G. H. B.; Kohlhaas, K. M.; Zimney, E. J.; Stach, E. A.; Piner, R. D.; Nguyen, S. T.; Ruoff, R. S. *Nature*, **2006**, 442, 282-286.

[165] Chua, C. K.; Pumera, M. *J Mater Chem A*, **2013**, 1, 1892-1898.

[166] Periasamy, M.; Thirumalaikumar, M. *J OrganoMetallic Chem*, **2000**, 609, 137-151

[167] Pei, S.; Zhao, J.; Du, J.; Ren, W.; Cheng, H. M. *Carbon*, **2010**, 48, 4466-4474.

[168] Moon, K.; Lee, J.; Ruoff, R. S.; Lee, H. *Nat Comm*, **2010**, 1, 73-78.

[169] Cote, L. J.; Cruz-Silva, R.; Huang, J. *J Am Chem Soc*, **2009**, 131, 1027-1032.

[170] Zhang, Y.; Guo, L.; Wei, S.; He, Y.; Xia, H.; Chen, Q.; Sun, H. B.; Xiao, F. S. *Nanotoday*, **2010**, 5, 15-20.

Chapter 2

2.1 Introduction to solar energy

When the global warming and depletion of common used energy supplies, such as fossil fuels started threatening the balance of human life, great attention was driven towards the renewable energy sources. Among the different renewable energy sources, including wind energy, hydroelectric energy, biomass and geothermal energy, solar energy has the highest potential. A very small fraction of sun power (less than 0.02%) reaching the earth surface can satisfy the worldwide energy needs. However, by the end of year 2015, solar technology energy sources have been providing only 0.9% of all the energy consumed by humans according to Renewable Energy Policy Network (REN21) report.[1]

There are various solar technologies for harvesting the sun energy, which can be divided into two categories: passive solar and active solar. A passive technique example is the designing of a building in such a way that it efficiently harvests and stores the sun energy. Active solar technologies include the solar thermal collectors or photovoltaic (PV) devices. However, the fastest and most efficient direct conversion of sun light into electrical energy is possible only through PV devices. The PV effect, discovered by Becquerel is the fundamental physical process, by which the semiconductor material converts electromagnetic radiation (sun light) into electrical power.[2,3]

The paradox is that despite the fact that solar power is abundant, the PV technology is still too expensive to become a primary energy source. Therefore, the main task of the solar cell research community is to develop a technology, which can provide cheap PV products and make the photo-conversion of sun light into electrical power cost efficient.

2.2 Photovoltaic technology evolution

Nowadays, PV devices (solar cells) can be categorized in three technology generations according to their development.[4]

The first generation solar cells are large scale, already commercialized, single junction devices. Most of the production is based on silicon wafers including single crystal and multi-crystalline silicon. About 90% of the current photovoltaic production is based on 1st generation solar cells. The theoretical limit of the single junction cells efficiency is ~30% (the Shockley-Queisser limit).[5,6] Currently the common silicon wafer based devices exhibit nearly 20% efficiency, with the highest reported efficiencies reaching 25%.[7]

However, the cost per produced Watt is nearly four times higher than conventional energy sources prices due to the high cost of the materials used and high manufacturing and processing expenses. Although, the cost decreases along with the progress of the technology, the 1st generation products will probably reach their price limit before achieving the competitive level in the market.

The second generation solar cells were developed to address the cost issue, with the primary task being to decrease the amount of expensive material used in the production process while keeping the efficiency of the device high. The foremost approach is producing thin film solar cells on low cost substrates, such as glass and flexible substrates like polyethylene terephthalate (PET). Different techniques are utilized for production process such as solution deposition, vapor deposition, electroplating etc. Most efficient materials used are amorphous silicon, $CuIn(Ga)Se_2$ and CdTe/CdS deposited on thin substrates. The respective devices can reach lab efficiencies up to 19%, but the module efficiencies exhibit only 14% due to difficulties in producing large-scale uniform films (**Figure 2.1**).[7] Although thin film technology can significantly decrease the PVs fabrication budget, 2nd generation solar cells will be constrained by certain cost ceilings per watt due to efficiency limits and material costs.
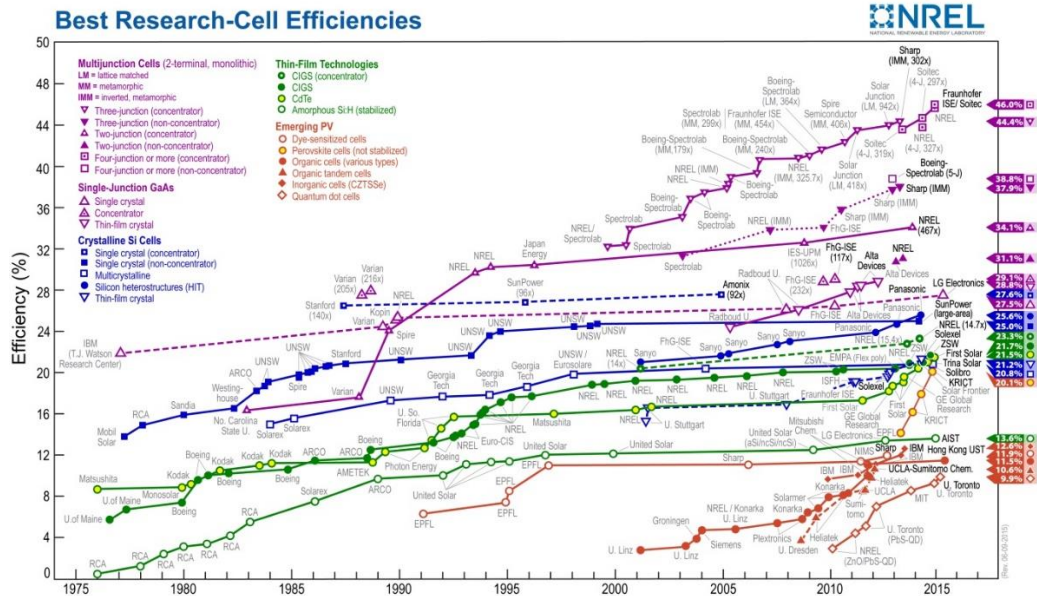
Figure 2.1. Best research-cell efficiencies for several technologies presented by the National Renewable Energy Laboratory. Reproduced from reference 8.

The third generation (3G) is an alternative way to get the cost down by increasing the efficiency through multiple stacking (sandwich) of solar cells. In this way, the idea of multi junction solar cells was introduced, which can significantly increase the device efficiency via harvesting improvement of photons and even overcome the theoretical limit of 30%. Currently the highest efficiencies reported for multi-junction solar cells are over 33% (**Figure 2.1**).[7]

In addition, 3rd generation technology utilizes completely new concepts in terms of device architectures and materials. Three typical approaches of photovoltaics are Dye-Sensitized Solar Cells (DSSCs),[9,10] Perovskite Solar Cells (PeSCs) and OPVs. DSSCs are based on a combination of dyes with metal oxides and electrolyte. The DSSC efficiencies reach 12% for small lab scale devices, while the lifetime of the devices is rather low compared to inorganic solar cells. Similar to DSSCs sensitization, in PeSCs the perovskite material is coated onto a charge-conducting mesoporous scaffold most commonly titanium dioxide (TiO_2) - as light absorber. The efficiencies of PeSCs have already exceeded 20%, with very promising future. On the other hand OPV technology in based on organic compounds such as conjugated polymers and fullerenes blended together to form heterojunctions in the nanoscale. The certified OPVs record performance has exceeded 10% using simple deposition

techniques and low cost fabrication materials. Anthracene was the first organic compound in which photoconductivity has been observed by Pochettino in 1906,[11] launching a new era for studying organic compounds for electronic applications. Particularly in the last decade the field of OPVs grew really fast, demonstrating promising potential for rather cheap PV technology. For that reason, in recent years OPVs became one of the most fascinating research fields.

2.3 An overview of Organic Photovoltaics

OPVs based on conjugated polymers offer the possibility of low cost, use of less toxic manufacturing methods and the option for large area, light weight, flexible PV panels. Conjugated polymers are organic molecules with alternating single and double carbon-carbon bonded atoms, with their electrical conductivity ranging from insulator to metal behavior. They combine both the optoelectronic properties of semiconductors, the excellent mechanical and processing properties of polymeric materials, while they can be fabricated easily and cheaply through different solution processing techniques such as printing, doctor-blading, slot die and roll-to-roll (r2r) on top of any selected substrate. These characteristics give a great advantage for the commercialization of OPVs compared to any other competitive technology.
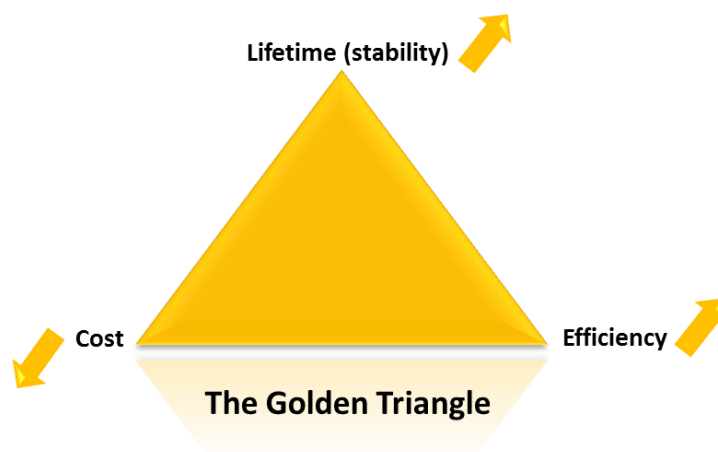
Figure 2.2. The critical triangle for photovoltaics demonstrating the three key factors. Reproduced from reference 12.

Despite their advantages, OPVs have to fulfill the basic requirements for renewable energy production. In the solar energy market the competitive

position of every PV technology is mainly determined by factors such as the efficiency, lifetime and cost regarding the electricity generation (per Wp). The potential of organic photovoltaics has to be judged by these key figures as well, and two of them are drawbacks at the present. **Figure 2.2** demonstrates the requirements that OPV technology should satisfy in order to be commercialized. A product development succeeding in only two aspects like, e.g. competitive costs and reasonable efficiency, will only be able to address niche markets unless the third parameter, in that case, life time, is also optimized.

2.3.1 Materials for Organic Photovoltaics

2.3.1.1 Conjugated Polymers

Heeger et al. demonstrated in 1977 that chemical doping of conjugated polymers results in an increase of the latter electronic conductivity by several orders of magnitude. This discovery was awarded with the Nobel Prize in chemistry in 2000.[13,14] Most organic semiconductor materials are conjugated polymers that essentially consist of a linear framework of alternating single and double bonds between the carbon atoms along the polymer backbone. Conjugated polymers are nowadays used in various organic electronic applications, like transistors, photodiodes, light emitting diodes, solar cells, etc. The origin of the conductivity and semi-conductivity behavior in conjugated polymers, e.g. polyacetylene, is due to alternation of single and double bonds across their molecular structure which comes as a result of chemical bonding behavior of the carbon atoms (**Figure 2.3a**).
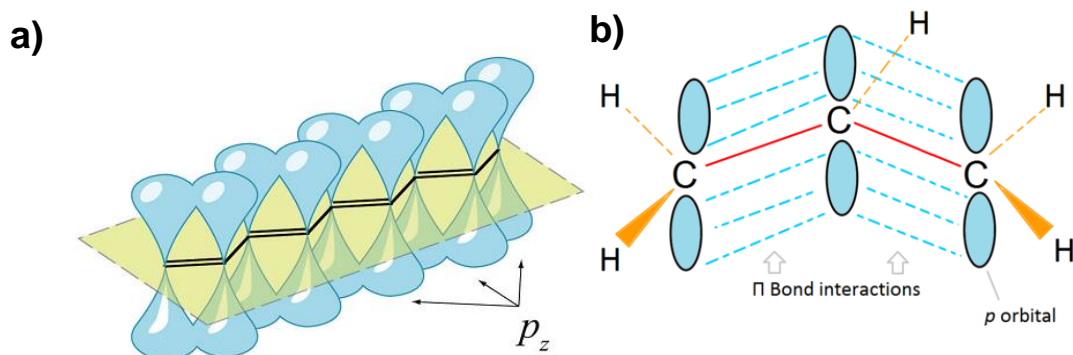
Figure 2.3. a) A conjugated backbone with overlapping p_z orbitals that point out of the molecular plain. Reproduced from reference 15. b) A conjugated π electron system. Reproduced from reference 16.

The carbon atom, in the ground state, has four valence electrons, two in 2s and two in 2p orbitals. In conjugated polymers carbon atoms are sp^2 hybridized. In the sp^2 hybridization the 2s orbital is hybridized with two 2p orbitals (2p$_x$, 2p$_y$) giving rise to three sp^2 orbitals and one 2p orbital (2p$_z$) unhybridized. Carbon can form two types of bonds: the σ-bond is formed by the overlap of the hybridized orbitals of the adjacent atoms which are oriented along the chain. So there are three coplanar sp^2 hybridized orbitals at 120° angle. Therefore three σ bonds are formed, two with neighbor carbon atoms and one with a hydrogen atom. The remaining out of plane p$_z$ orbitals, each occupied by one electron, overlap with neighboring p$_z$ orbitals to form bonds perpendicular to the chain (**Figure 2.3b**). These electrons are delocalized along the entire polymer backbone, which is the reason for the conducting properties of conjugated polymers.

The overlap of p$_z$ orbitals forms two molecular orbitals, a bonding π-orbital which is the highest occupied molecular orbital (HOMO) and an antibonding π*-orbital which is the lowest unoccupied molecular orbital (LUMO). The π-orbital and π*- orbital are equivalent to an inorganic semiconductor valence and conduction band, respectively. The difference between the HOMO and LUMO is called the energy band gap of the organic material. The optical and electrical properties of an organic material are determined by the band gap, while the gap is reduced when the polymer chain is longer. Commonly used polymer donor materials in OPV devices are the poly(3-hexylthiophene-2,5-diyl) (P3HT), poly [N-9'-heptadecanyl-2,7-carbazole-alt-5,5-(4',7'-di-2-thienyl 2',1',3'benzothiazo-le)] (PCDTBT) and poly ({4,8-bis[(2-ethylhexyl)oxy]benzo[1,2-b:4,5-b'] dithiophene-2,6-diyl}{3-fluoro-2-[(2-ethylhexyl) carbonyl]thieno [3,4-b]thiophe nediyl} (PTB7).

2.3.1.2 Fullerene derivatives

Organic materials with appropriate properties, such as conjugated polymers and small molecular compounds, can be used as electron donor materials in OPVs. On the other hand, many organic compounds exhibit potential properties to be tested as electron acceptor material, but very few electron acceptor materials can lead to high performance OPV devices. Fullerene and its derivatives are the most successful electron acceptor materials.

Fullerene C_{60} has well-symmetric structure and exhibits good electron mobility. Thereby, C_{60} and its derivatives can be ideal as electron acceptor materials. In 1992, Sariciftci et al. demonstrated the photoinduced ultrafast electron transfer between electron donor and acceptor by using C_{60} as electron acceptor.[17] However, C_{60} exhibits very low solubility in the most commonly used organic solvents. In this context, $PC_{61}BM$, a C_{60} derivative, was applied in OPVs, improving its solubility and also avoiding severe phase separation of donor:acceptor blend. Nowadays, $PC_{61}BM$ and its corresponding C_{70} derivative ($PC_{70}BM$) are the state-of-the-art OPVs electron acceptors. In contrast to $PC_{60}BM$, $PC_{70}BM$ possesses enhanced absorption in visible region, but C_{70} remains more expensive than C_{60} due to its complicated purification process, which limits its application.

2.3.1.3 Buffer layer materials

Poly(3,4-ethylenedioxythiophene) poly(styrenesulfonate) (PEDOT:PSS) is the state-of-the-art hole transport layer (HTL) in OPV devices. Part of the PSS sulfonyl groups are deprotonated and carry a negative charge, while PEDOT is a conjugated polymer and carries positive charges. In this way, the charged macromolecules form a macromolecular salt (**Figure 2.4**). Due to its solution processability, high work function (WF), sufficient conductivity, and high optical transparency in the visible-NIR regime.[18] However, there are several drawback issues leading to OPV failure, which are directly related to the PEDOT:PSS. The acidic and hygroscopic nature of PEDOT:PSS corrodes both the indium tin oxide (ITO) electrode[19] and the processing equipment at elevated temperatures,[20] and can introduce water into the active layer, degrading the performance and long-term stability of the OPV device.
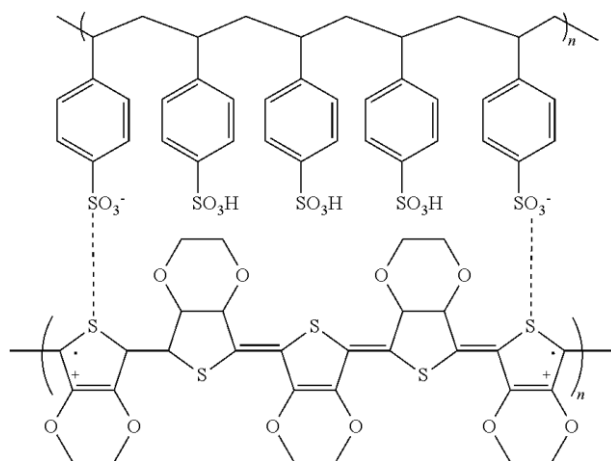
Figure 2.4. Chemical structure of PEDOT:PSS. Reproduced from reference 21.

Titanium suboxide (TiO_x) is introduced as an electron transport layer (ETL) between the active layer and bottom electrode in OPVs. It is one of the most studied metal oxide semiconductors, exhibiting high electron mobility, high transparency in visible wavelength region, excellent chemical and thermal stability. It is also non-toxic, inexpensive, and easy in processing. TiO_x can be deposited from various methods namely sputtering, pulsed laser deposition, metal organic CVD, electrochemical deposition and spin coating.

2.3.1.4 Electrodes

TCEs are widely used as electrodes in a large variety of optoelectronic devices due to their unique combination of optical and electrical properties (superior stability, high transparency in the visible range and high electrical conductivity). Currently, ITO is the dominant material used as TCE in rigid OPVs owing both to its high transparency in the visible spectrum, as well as to its good conductivity.[22] However, ITO suffers from considerable limitations. Firstly, it is expensive due to both the scarcity of indium reserves and the sputter deposition line expenses and secondly is not flexible, since its polycrystalline microstructure is brittle and cracks when the layer is bent or stretched repeatedly.[23] On top of that, indium is known to diffuse through the photoactive layer, leading to significant deterioration of the photovoltaic performance.[24]

The final step for OPV fabrication involves the deposition of a top metal contact.[25] In most cases, the top electrode is applied using vacuum deposition.

In general, the top contact metal is selected based on its WF to achieve Ohmic contact with the underlying active organic layer.[25] Efficient OPV back electrodes should have high electrical conductivity, appropriate energy level alignment with the fullerene acceptor and should not harm the photoactive layer during the fabrication process. Additionally, they should have high optical transparency when incorporated in semitransparent OPVs. Hence, more stable metals, such as aluminum, often form blocking contacts because of their higher WF.

2.3.2 Bulk Heterojunction OPVs

2.3.2.1 Device Structure

The device structure of OPV is different from traditional silicon wafer based solar cells. The photoactive layer is a blend of conjugated polymers as electron donors and fullerene derivatives as electron acceptors. This photoactive layer is sandwiched between two electrodes with proper work functions. **Figure 2.5** shows a schematic diagram of OPV device structure. In this device architecture, the light is transmitted through the glass substrate. The device is built on a transparent substrate which may be flexible. The substrates used are usually glass or PET. The anode consists of a semitransparent oxide layer, usually ITO. Its role is to allow light to pass through, and to collect holes from the device. A layer of the conductive polymer PEDOT:PSS is applied between the anode and the photoactive layer. This thin layer is spin coated on top of the ITO surface. The PEDOT:PSS layer serves as a HTL and exciton blocker. It smooths the ITO surface, seals the active layer from oxygen, and prevents the anode material from diffusing into the active layer, which can lead to trap sites.[26]
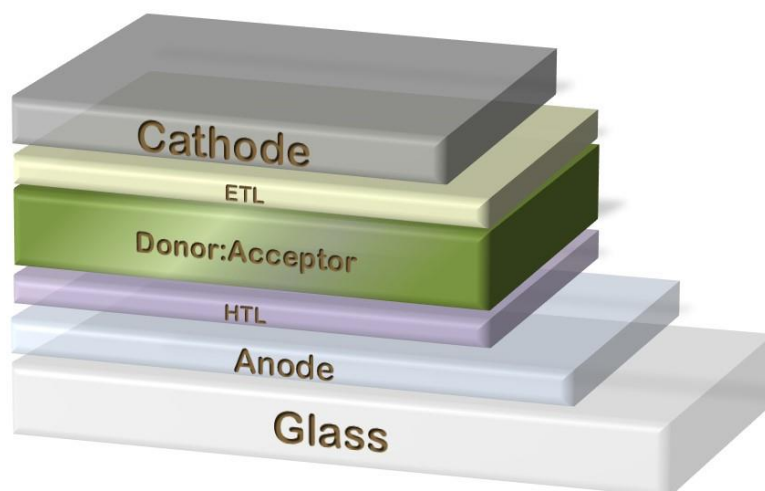
Figure 2.5. Schematic illustration of the BHJ OPV device.

The light absorbing photoactive layer containing the donor and acceptor material is sandwiched between two electrodes. For laboratory devices, this layer is spin coated from a common solution which contains the polymer donor and fullerene acceptor suspended in an appropriate solvent or mixture of solvents. The incorporation of an ETL between the photoactive layer and the cathode can lead to improved charge transport and charge extraction in the device, playing a key role in enhancing the power conversion efficiency (PCE). Additionally, the ETL improves the stability of the device by acting as a shield against the penetration of humidity into the active layer, retarding degradation of BHJ OPVs. The cathode is usually aluminum, although calcium or silver is sometimes used. The function of the cathode is to collect electrons from the device. This layer is deposited by thermal evaporation.

2.3.2.2 Operation Principles

As the fundamental properties of organic semiconductors are different to that of their inorganic counterparts, the operation of OPV devices is different to that of silicon solar cells. In a silicon solar cell, incident photons break the covalent bonds, which form electron-hole pairs. Due to the crystalline nature of silicon, generation of charge carriers requires only a small force of interaction. Therefore, absorption in silicon leads to effectively free charge carriers. As a result of the low dielectric constant (≈3) in semiconducting polymer materials, the columbic forces of attraction between electrons and holes are very high.[27,28]

This implies that unlike inorganic semiconductors, in which photo excitation generally forms a free electron and hole, excited states in semiconducting polymers form bound electron-hole pairs. This bound electron-hole pair is referred to as an 'exciton'. A driving force is required to overcome this excitonic binding energy so that free charge carriers can be produced and transported throughout the device. In organic solar cells, excitons formed in the donor material can be dissociated at the donor-acceptor (D-A) interface. The force required to overcome the exciton binding energy is provided by the energy level offset of the LUMO of the donor and the LUMO of the acceptor material.
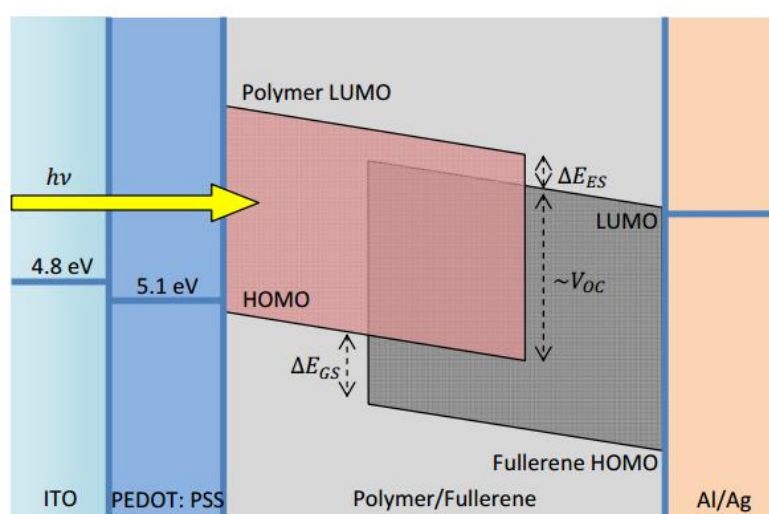
Figure 2.6. Energy band diagram of donor-acceptor materials in bulk heterojunction OPVs.

Figure 2.6 displays an energy band diagram of an OPV device. This energy offset used to dissociate excitons is illustrated as ΔE_{ES}, which is the excited state energy offset. In order to dissociate excitons formed in the acceptor material, the energy offset of the HOMO of the acceptor and the HOMO of the donor material is required. This energy offset used to dissociate excitons is illustrated as ΔE_{GS}, which is the ground state energy offset. Excitonic dissociation due to these energy offsets occurs at the interface between the donor and acceptor phase, therefore, the arrangement of the two materials in the active layer is crucial for the successful operation of the device.

Excitons can be created when photons are absorbed in the donor material. These excitons then can be dissociated at a D:A interface. Once separated, the electron can transfer to the acceptor material and be transported to the cathode for charge collection. The hole produced in the donor material travels throughout the polymer and is collected at the anode. This process is illustrated in **Figure 2.7**. A driving force is required to overcome this excitonic binding energy (Coulomb bonding) so that free charge carriers can be produced and transported throughout the device. The dissociated electrons and holes are driven by build-in electric field and then moved to negative and positive electrode, respectively, and then collected by the electrodes to realize the photon-to-electron conversion.
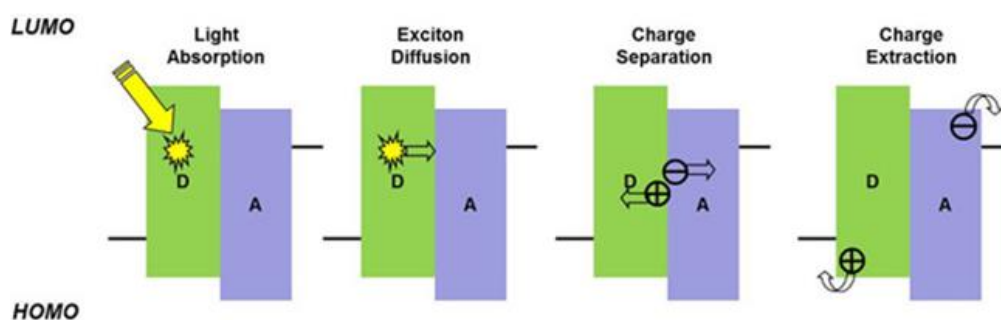
Figure 2.7. Energy band diagram of donor-acceptor materials in bulk heterojunction OPVs. Reproduced from reference 29.

2.3.2.3 Operation Principles

To evaluate the performance of photovoltaic devices the current-voltage (I-V) characteristic must be measured. **Figure 2.8** shows the typical shape and key elements of the I-V curve for a photovoltaic device under illumination. The power conversion efficiency, η, is the ratio of the electrical power generated by the device at its maximum power point to the input power from incident light.[30] The maximum power delivered to a load by a solar cell occurs when the product V*I is at its maximum, P_{max}, i.e. when the solar cell operates at its maximum power point voltage (V_{MPP}) and maximum power point current (I_{MPP}). The fraction of maximum power and the product of open-circuit voltage (V_{oc}) and

short-circuit current density (J_{sc}) is defined as the fill factor, FF (**Figure 2.8**), which further can be related to the efficiency, η.

$$\eta = \frac{P_{out}}{P_{in}} = \frac{V_{OC} * J_{SC} * FF}{P_{in}} * 100\%$$

where, P_{in} is the incident power density (sun power) = 100 mWcm^{-2}.

In photovoltaic devices, the V_{oc} is the maximum possible voltage, in sunlight or equivalent, across the device when no current is flowing.[30] This is also referred to as the no load condition.[30] The V_{oc} is a key parameter in determining the power conversion efficiency, as shown above. The J_{sc} is the current density when there is no potential across the photovoltaic device. The J_{sc} is a key parameter in determining the PCE. The light absorption and excitons generation provides a "baseline" for the number of potential charge carriers which may be harvested, and thus, J_{sc} will increase proportionally with the rise in irradiance and/or absorption of irradiance.[30] FF is a parameter which, in conjunction with V_{oc} and I_{sc}, determines the maximum power from a solar cell. The FF is defined as the ratio of the maximum power from the solar cell to the product of V_{oc} and I_{sc}.[30] Graphically, the FF is a measure of the "squareness" of the solar cell and is also the area of the largest rectangle fitted in the I-V curve.[30] Basically, with higher FF, the performance of a solar cell is better.
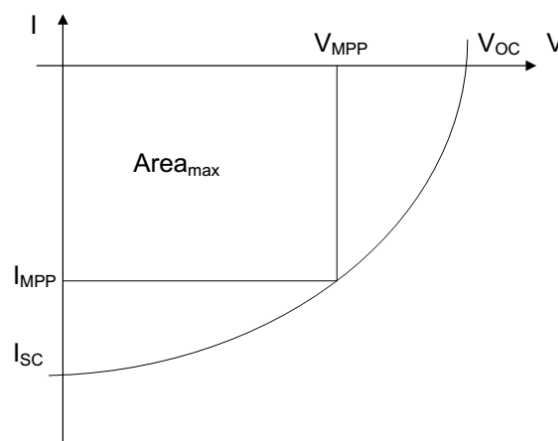
Figure 2.8. A characteristic current-voltage diagram of photovoltaic device. The maximum power point current (I_{MPP}), and the maximum power point voltage (V_{MPP}) are demonstrated. Reproduced from reference 30.

2.4 Graphene in Organic Photovoltaics

OPV devices based on donor-acceptor BHJ structure, hold tremendous potential for low cost, large-scale fabrication on flexible substrates, presenting great compatibility with r2r manufacturing. Over the last few years, there has been significant progress in the performance of polymer BHJ solar cells owing to the intensive effort on the development of new photoactive materials, morphological structures and fabrication techniques, that facilitated enhanced PCE exceeding 9% for single junction[31,32] and over 10% for tandem OPVs.[33,34]

Ever since the isolation of free standing graphene in 2004,[35] graphene research has experienced a phenomenal growth. Its exceptional electronic, optical and mechanical properties make graphene highly attractive, believed to be the next wonder material for optoelectronics and thus triggering the application of graphene-based materials in the different layers of photovoltaic devices.[36] Graphene and other 2D crystals can be either incorporated as an additional component in a typical OPV structure, or replace traditional materials, aiming at both performance and stability enhancement. In this context, the utilization of 2D crystals can simultaneously or individually optimize the PV parameters by taking advantage of their high charge mobility to provide additional percolated pathways for efficient exciton dissociation and charge transport in the photoactive layer, by adopting WF tuned interfacial layers, capable of providing a perfect energy match for either hole or electron transport, and to fabricate flexible TCEs with tailored optoelectronic properties.

In this context, graphene has been employed in all the major components of an OPV device (**Figure 2.9**) with a variety of functions, such as a) TCE or back electrode b) electron acceptors in binary OPVs or additives in ternary OPVs in the form of nanosheets or nanoflakes dispersed in the polymer or polymer:fullerene matrices, respectively c) WF tuned HT or ET layers in OPVs, or interfacial layers in tandem OPVs.
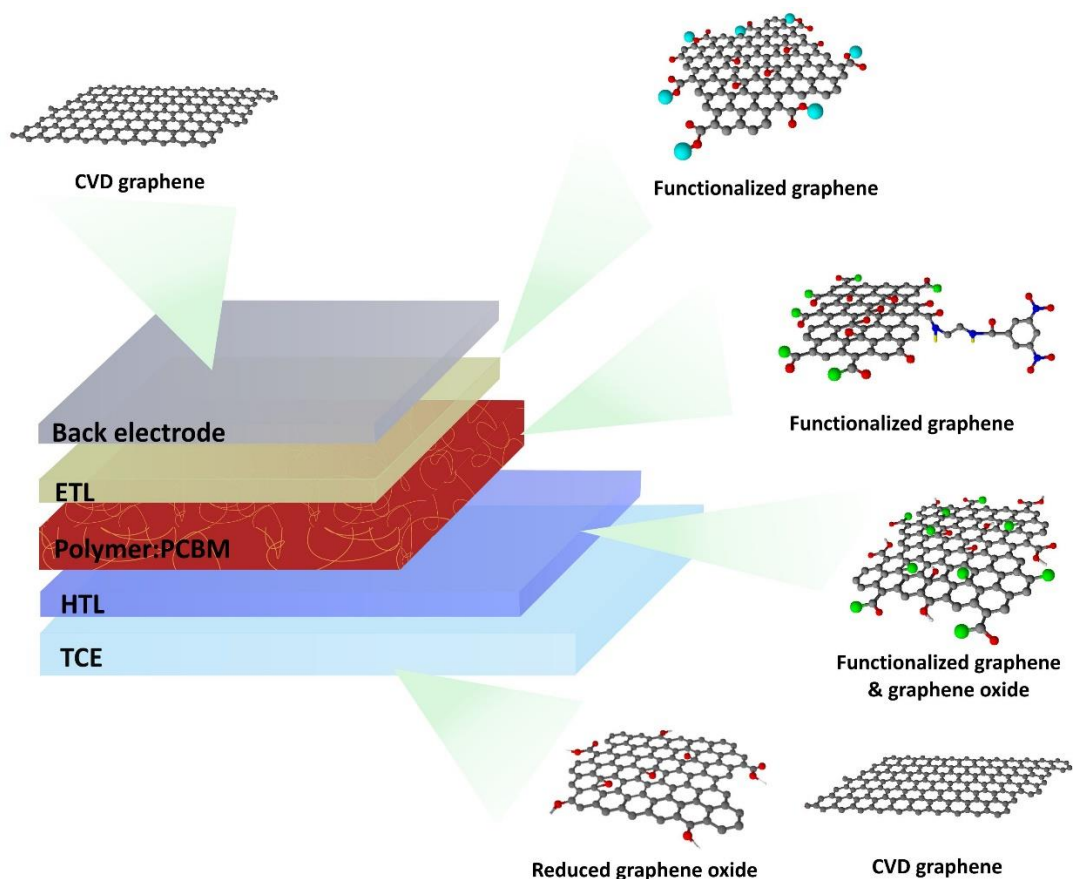
Figure 2.9. Graphene-based materials utilized in all the components of an OPV, including the electrodes, the buffer and the photoactive layers. Reduced graphene oxide and CVD graphene have been utilized as TCEs, functionalized graphene molecules, graphene oxide have been investigated as HTLs, while in the active layer graphene-based molecules have been used as electron acceptors in binary blends or additives in ternary OPVs. Finally, OPV devices incorporating functionalized graphene molecules as electron transport layers or interlayers and/or CVD graphene as back electrodes have been demonstrated.

2.4.1 As transparent conductive electrodes

Graphene has been widely investigated as TCE in OPVs to replace traditional ITO electrodes. Currently, ITO is the dominant material used as TCE in rigid OPVs owing both to its high transparency (T_r) in the visible spectrum, as well as to its good conductivity.[22] However, as already referred, ITO suffers from considerable limitations (expensive, brittleness, diffusion into the photoactive layer and performance deterioration).[23,24] Solution processed carbon nanotubes,[37,38] metallic nanowires[39] and conductive polymers[40] have

been utilized as alternative TCE in organic electronic devices. However, they exhibit relatively high surface roughness or large sheet resistance (R_s), thus reducing the reproducibility rate of the devices.

Wang et al. were the first to demonstrate a P3HT:PC$_{61}$BM device with 1.7% PCE using nickel-grown CVD few-layer graphene as the TCE.[41] Graphene was functionalized with pyrene buanoic acid succidymidyl ester to render the surface hydrophilic and to increase its WF from 4.2 to 4.7 eV (**Figure 2.10a)** However, the obtained PCE was noticeably lower than that of ITO reference device (3.1%).

Similarly, flexible OPVs were reported, in which the graphene TCE was synthesized through CVD on thermally annealed polycrystalline nickel surface and subsequently transferred on a PET substrate using poly(methyl methacrylate) (PMMA) as the supporting layer.[42] The CVD graphene films demonstrated very low R_s (230 Ωsq^{-1}) and a T_r of 72%. Moreover, a high mechanical flexibility was observed, as evidenced by only 7.9% decrease of R_s after 100 bending cycles. The as-prepared PET/graphene was utilized as the TCE in CuPc-C$_{60}$ OPVs, resulting in a PCE of 1.18%, comparable to the ITO reference PCE. More importantly, the graphene-based OPVs maintain their performance at bending angles up to 138º, while the ITO-based OPVs started to rapidly degrade at bending angles higher than 36º, due to the generation of cracks on ITO surface.

Meanwhile, several approaches have been implemented to improve the PCE of the devices by mainly decreasing the R_s of the graphene TCEs. Wang et al. reported P3HT:PC$_{61}$BM OPVs incorporating 4-layers HNO$_3$-doped graphene TCE prepared by a layer-by-layer transfer method.[43] PCEs of 2.5% were obtained by the additional evaporation of a thin layer of MoO$_3$, in order to improve its hydrophilic property, and to tune its WF from 4.36 to 5.37 eV.

In the same context, Hsu et al. reported P3HT:PC$_{61}$BM OPVs with CVD graphene stacked films, consisting of two tetracyanoquinodimethane (TCNQ) layers sandwiched by three graphene layers (R_s=140 Ωsq^{-1}, T_r=90%) as the TCE, demonstrating a PCE of 2.58%.[44] The TCNQ molecules were deposited onto the surface of each graphene layer resulting in doping of the graphene layers, while an Au assisted transfer process was employed. Also, significant R_s decrease of CVD-grown graphene films was demonstrated by p-type doping

through chemical treatment with HNO_3 and $SOCl_2$.[45] The doped graphene exhibited an R_s of 450 Ωsq^{-1} and T_r higher than 90%.
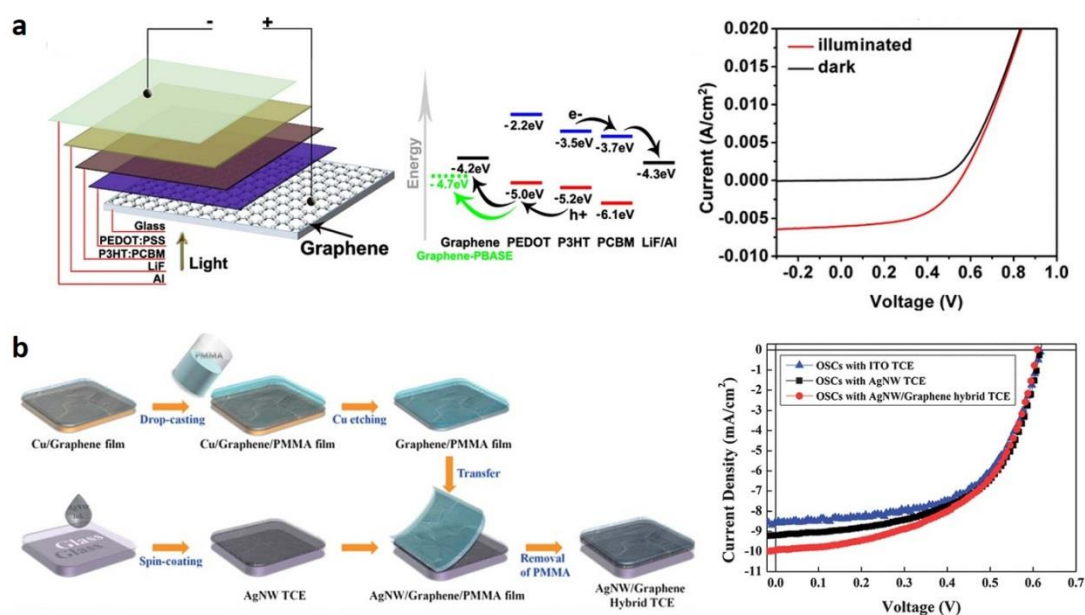
Figure 2.10. a) Energy diagram of the fabricated device with structure graphene/PEDOT:PSS/P3HT:PC_{61}BM/LiF/Al and J-V characteristics of the OPV based on graphene films in dark and under illumination, where graphene film modified by pyrene buanoic acid succidymidyl ester. Reproduced from reference 41. b) Schematic illustration of the fabrication of the AgNWs-graphene hybrid TCE on a glass substrate and J-V characteristics of inverted BHJ OPVs with ITO, AgNWs, and AgNWs-graphene hybrid TCEs. Reproduced from reference 46.

Moreover, hybrid materials of metal nanowires (NWs)-graphene were utilized as TCEs in flexible P3HT:PC_{61}BM OPVs, where CVD graphene was dry-transferred onto Ag NWs film (**Figure 2.10b**).[46] The OPVs incorporating the hybrid TCE, exhibited not only superior performance but also long-term stability under prolonged illumination. Another hybrid film based on inkjet printed Ag grid and CVD-graphene was employed as TCE in flexible OPVs.[47] A PCE of 2.9% was recorded for a TCE with a R_s of 12 Ωsq^{-1} and T_r of 73%. The hybrid TCE R_s remained unchanged even after 500 bending cycles, while the PET/ITO reference R_s increased rapidly to exceed 1 $k\Omega sq^{-1}$ after only a few bending cycles.

The R_s of the CVD grown graphene TCEs can also decrease by blending with a high surface WF polymer, like the PEDOT:PSS. In this way, graphene will be p-type doped, leading to significant R_s decrease.[48] As a proof of concept, a three layer graphene-modified PEDOT:PSS composite film were employed in flexible OPV devices, resulting in a 4.33% PCE. In this context, PEDOT:PSS was also used as both the supporting layer for the transfer and as a stable doping layer for the graphene, solving the polymer residue transfer problem.[49] OPVs with PCEs of 5.5% and 4.8% in rigid and flexible substrates respectively, were demonstrated. On top of that, excellent mechanical stability after 2000 bending cycles for the flexible OPVs was obtained.

To date, the highest PCE for flexible OPVs utilizing CVD graphene TCEs is at 6.1% and 7.1% for conventional and inverted OPV structures respectively.[50] This was accomplished by thermal annealing of the MoO_3 buffer layer on graphene TCE, which resolves the compatibility issue of pristine MoO_3 with the blend solvent of the polymer:fullerene when spin coated. It has very recently been demonstrated that a high PCE of 8.48% can be achieved in a tandem architecture by combining a wide-bandgap small molecule and a low-bandgap polymer using Au-doped single-layer graphene nanoribbons as the TCE.[51]

Hence, it can be concluded that CVD is the most successful approach to produce highly transparent and low R_s graphene TCEs.[52,53] Nonetheless, the grown graphene films have to be transferred onto a target substrate through a complicated process, increasing the manufacturing cost. An alternative low cost top-down approach compatible with r2r mass production is the chemical exfoliation of GO either by ultrasonic dispersion or rapid thermal expansion followed by reduction with proper chemical[54] or photo-assisted routes.[55] The rGO can be easily produced in bulk quantities as graphene ink,[56] taking advantage of its improved soluble character in common solvents.[57]

In this context, there was an extensive research effort on the utilization of rGO as the TCE in OPVs.[58,59,60] In particular, flexible P3HT:PC_{61}BM OPV devices were firstly fabricated by using a transferred rGO film as theTCE.[60] The GO was initially spin coated on a rigid SiO_2/Si substrate, subsequently reduced by thermal annealing and transferred on a PET substrate. The devices (area 1 mm^2) exhibited a PCE of 0.78% for a 16 nm thick rGO film, mainly due to the low T_r (65%) and high R_s of the rGO films (~3.2 kΩsq^{-1}), compared to the highly

commercialized ITO (90%, 15 Ωsq^{-1}). Remarkably, the rGO-based OPV can sustain a thousand bending cycles at 2.9% tensile strain.

In the same context, Kymakis et al. has recently demonstrated an efficient laser-based reduction method for fabricating flexible graphene TCEs that can be spin casted on temperature sensitive substrates.[61] The femtosecond laser treated rGO (LrGO) films with 70% T_r and R_s of 1.6 $k\Omega sq^{-1}$ were integrated as the TCE in P3HT:$PC_{61}BM$ OPVs, leading to PCE of 1.1%. Additionally, the graphene-based OPVs can be bend to angles up to 135° without PCE deterioration. In contrast, the reference ITO-based OPVs fail completely at bending angles higher than 65°. Therefore, it is evident that pristine rGO films cannot compete with ITO with respect to its conductivity, owing to their extremely high R_s (>1 $k\Omega sq^{-1}$) for high T_r values.

2.4.2 As active layer components

2.4.2.1 As electron acceptors

Solution processable functionalized GO derivatives have also utilized as the electron acceptor material, replacing PCBM, in OPVs.[62,63,64] Firstly, Liu et al. functionalized GO with phenyl isocyanate and used it as the electron acceptor in BHJ OPVs, incorporating poly(3-octylthiophene-2,5-diyl) (P3OT) as the polymer donor.[65] A PCE of 1.4% was obtained, mainly due to the absence of a bandgap. It should be notice that only after thermal annealing, the OPV device exhibited PCE higher than 0.4%. The same group blended the functionalized GO with P3HT, achieving a PCE of 1.1%.[62] Graphene quantum dots have also been electrochemically synthesized, functionalized with aniline and blended with P3HT, leading to OPVs with a PCE of 1.14% (**Figure 2.11a**).[66]

In addition, a GO-C_{60} hybrid was used as the electron acceptor in P3HT-based BHJ OPVs, resulting in a PCE of 1.22%.[67] The hybrid was realized by covalently attaching C_{60} on the GO surface using a simple lithiation method. A 2.5 fold enhancement in PCE was observed for OPVs using the hybrid electron acceptor compared to OPVs with only C_{60} (0.47%). This was attributed to the introduction of an additional percolation network for electron transport through the 2D graphene flakes.

Stylianakis et al. efficiently functionalized GO sheets by linking them with a small molecule via peptide bonds between the acylated COCl groups of GO and 3,5-dinitrobenzoyl chloride, with the amino groups of ethylenediamine.[68] The resulting GO-ethylene-dinitro-benzoyl (GO-EDNB) was mixed with P3HT resulted in a PCE of 0.96%. However, the utilization of the GO-EDNB as a universal electron acceptor is not possible, since its LUMO is at 3.4 eV, providing an energetic offset for excitons dissociation only in the P3HT case (LUMO$_{P3HT}$=3 eV), and not with the state-of-the-art polymer donors. Therefore, it became obvious that more efficient functionalization routes should be employed in order to improve the dispersity of the flakes in the polymer matrix and properly tune the band gap of the graphene derivatives, to achieve an ideal energy offset between the polymer and the graphene for enhanced OPV performance.

In this context, a photochemical functionalization of GO, through laser-induced covalent grafting of GO nanosheets with EDNB molecules, aiming at its bandgap tuning was recently demonstrated by the same group.[69] The resulted functionalized laser induced GO-EDNB showed excellent processability and dispersity in organic solvents, but most importantly, it was shown that its bandgap and therefore its HOMO-LUMO levels can be easily tuned through adjustment of the laser irradiation parameters. The utilization of the prepared molecule with a band gap of 1.7 eV, and a resultant LUMO level of 4.1 eV, as the electron acceptor in PCDTBT OPVs resulted in a V$_{oc}$ of 1.17 V and to a PCE of 2.41%, which is the highest PCE for graphene-based electron acceptors to date.

Most recently, pristine rGO sheets were incorporated in nanoarchitectural TiO$_2$ nanorod (NR)-ZnO nanoparticle (NP)/P3HT hybrid OPVs.[70] A PCE of 3.79% is achieved, using a 900 nm-thick TiO$_2$ NR array. It was postulated that the rGO acts as an energy-matched auxiliary electron acceptors in the hybrid connecting to the electron transport pathway constructed by the 3D ZnO network and TiO$_2$ NR array on the FTO substrate.
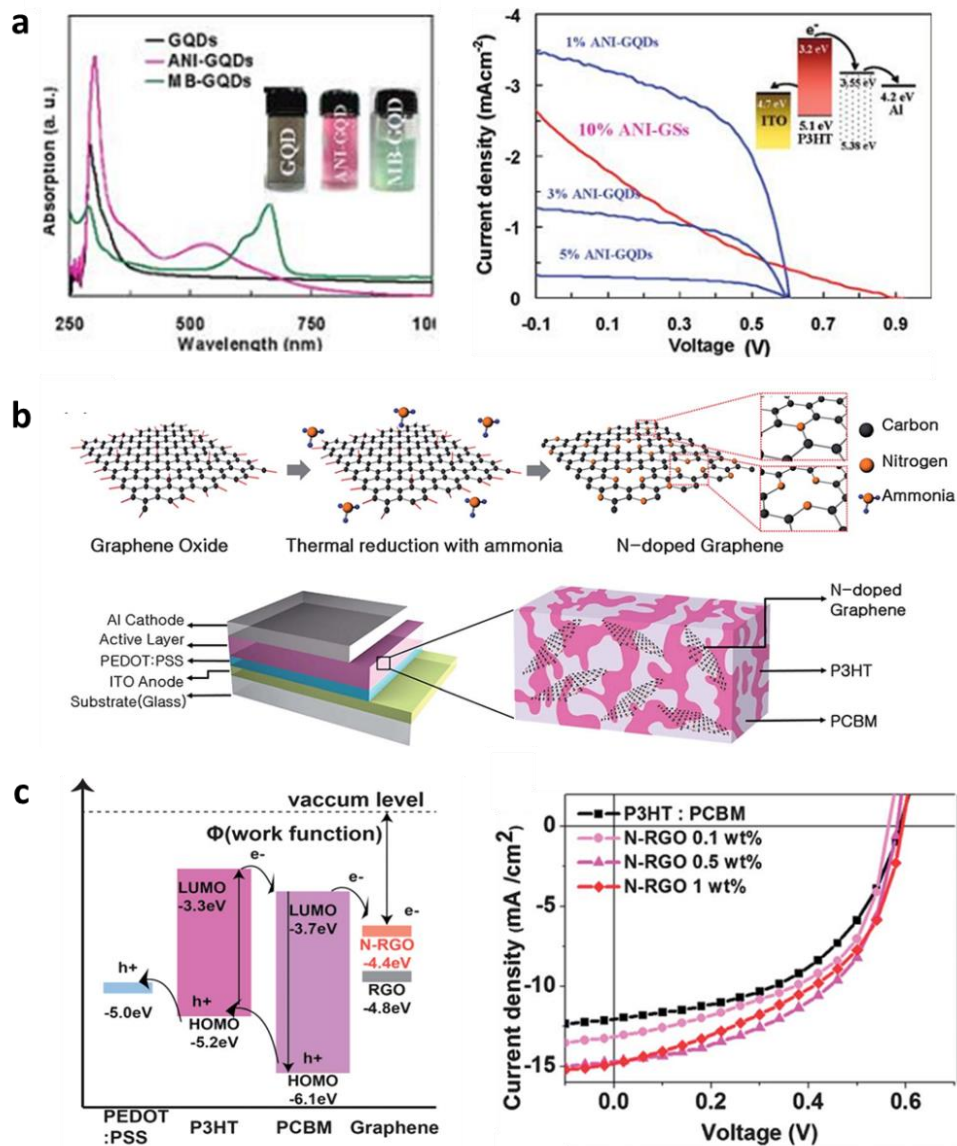
Figure 2.11. a) UV-vis absorption and J-V characteristics of the photovoltaic devices based on ANIGQDs with different GQDs content and ANI-GS. Reproduced from reference 66. b) Schematic of the nitrogen doping process of rGO and the respective BHJ solar cell using the N-doped graphene/P3HT:$PC_{61}BM$ active layer. Reproduced from reference 73. c) Energy-level diagram of a rGO and N-rGO/P3HT:$PC_{61}BM$ OPV showing the charge generation and transfer between the two organic components to the electrodes and I-V characteristics of devices as a function of N-rGO concentration. Reproduced from reference 73.

2.4.2.2 As electron acceptors

A fascinating way to further facilitate the energy cascade procedure and therefore enhance the performance of BHJ OPVs is through the addition of a third component into the polymer-fullerene binary blend, resulting in the formation of a ternary OPV device.[71] This approach requires that the HOMO and the LUMO levels of the additive to lie between the HOMO and LUMO levels of the polymer and the fullerene respectively, so proper energy offsets are presented at all interfaces. Among others, carbon derivatives such as Indene-C_{60} bisadduct (ICBA) have been successfully employed as the third component into ternary blends.[72] In this context, solution processable graphene derivatives would be ideal additives in OPVs, since a remarkable carrier mobility is expected via the graphene one-atom thick, honeycomb lattice. In particular, graphene as well as GO and rGO have been exploited as additives in OPVs aiming at PCE increase.

Jun et al. exploited n-doped rGO, doped with nitrogen, as the additive material in P3HT:PC_{61}BM OPVs and reported a PCE of 4.39%, 40% higher than the binary OPV, owing to enhanced charge carriers mobility (**Figure 2.11b**).[73] However, the employed rGO and n-rGO have WF value of 4.4 and 4.8 eV respectively, establishing an energetically favorable offset between the P3HT or the PC_{61}BM and the n-rGO only for electron transfer (**Figure 2.11c**). In contrast, the absence of appropriate bandgap makes the flakes to act as carrier traps in the BHJ, since an energy band offset is present only for electron transport. Therefore, n-doped graphene flakes cannot be considered as an energy cascade material but as a provider of additional charge pathways.

Similarly, Robaeys et al. used solution-processed graphene nanoflakes, obtained from the exfoliation of pristine graphite, as additive material in P3HT:PC_{61}BM OPVs.[74] It was shown that the graphene addition determines the formation of continuous active film with interpenetrating structure by improving the crystallinity of the P3HT. Nevertheless, similar to the n-RGO case, solution-processed graphene flakes cannot be considered as an energy cascade component in a ternary BHJ solar cell due to lack of a bandgap, and thus energy level matching. Contrary, solution-processed graphene flakes can be considered as an additive to improve the crystallization and morphology of

P3HT as well as the charge transport properties. The most efficient charge transport properties are ascribed to a better balancing between electron and hole mobilities with respect to the reference P3HT:PC_{61}BM OPV.

Most recently, graphene nanoflakes with controlled lateral size and functionalized with EDNB were demonstrated to act as an efficient electron cascade acceptor material in air processed PCDTBT:PC_{71}BM OPVs.[75] The functionalization process allowed the tuning of the HOMO and the LUMO levels of the graphene nanoflakes between the HOMOs and the LUMOs of the host polymer and fullerene components. Furthermore, the functionalized nanoflakes act as highly conductive bridge between polymer chains and fullerene balls and offer two additional interfaces for exciton dissociation as well as multiple routes for charge transfer at the donor:acceptor interfaces. The as prepared ternary OPV exhibited an increase of 18% in PCE, achieving a value of 6.59%, with respect to the binary device (PCE=5.59%). Kim et al. has incorporated GO QDs in PTB7:PC_{71}BM OPVs, and studied the effect of the reduction degree of GO in the PV characteristics.[76] It was found that the addition of prGO QDs in the active layer, led to the highest PCE increase from 6.7% to 7.6%, attributed to a balance in optical absorption and conductivity of the QDs.

2.4.3 As interconnection layers

Tandem OPVs incorporating two or more single-junction subcells with complementary bandgaps stacked together, aim at fully harvesting the whole solar spectrum.[77] The V_{oc} of the tandem devices ideally equals to the sum of the subcells, while the J_{sc} equals to the lower one of the subcell, resulting to a significant increase in the PCE. The most critical part of a tandem OPV is the interconnection layer (ICL), which connects the two subcells. The ICL collects electron and holes from the respective subcells, and more importantly acts as a recombination site. Therefore, an ideal ICL should be continuous, highly conductive, transparent, robust and solvent resistant.[78] To date PEDOT:PSS/ TiO_2,[79] PEDOT:PSS:ZnO[80] and LiF/Al/Au/PEDOT:PSS[81] are some of the most effective ICL structures. However, the presence of PEDOT:PSS is accompanied by important drawbacks derived from its acidic and aqueous nature.[82]

Due to its transparency and high conductivity, multilayer CVD graphene was utilized as ICL in both series and parallel-connected tandem OPVs.[83] The nickel grown graphene was transferred using a polydimethylsiloxane stamp and its WF was increased to 5.5 eV by coating it with a MoO_3 layer. It should be noted that the high WF MoO_3/graphene/MoO_3 layer served as an effective ICL in the parallel-connected tandem OPV, consisting of P3HT:PC_{61}BM and ZnPc:C_{60} subcells.

Likewise, the first solution processable graphene-based ICL in series-connected tandem OPVs was reported by Tung et al., who employed a GO:PEDOT:PSS nanocomposite as the ICL in a tandem OPV, consisting of two identical P3HT:PC_{61}BM subcells.[84] The tandem OPVs were fabricated by a direct adhesive lamination process enabled by the sticky GO:PEDOT film. A PCE of 4.14% for the tandem device was obtained, with high V_{oc} of 0.94 V, reaching the 84% of the sum of the two subcells. The presence of GO in the composite was crucial as it increased the conductivity of PEDOT:PSS and led to a dispersion with increased solution viscosity and subsequently high adhesive properties.

In addition, Yusoff et al. incorporated a GO/TiO_2 recombination layer, into a tandem OPV device comprising two subcells in series.[85] The total V_{oc} (1.62 V) was measured to be the sum of the V_{oc} values obtained for the subcells (0.94 V and 0.68 V), indicating that the realized interconnection was ideal, offering a resistance-free adhesion for the front and the rear cell. The tandem OPVs fabricated were all-solution processed and stable, while the TiO_2/GO ICL exhibited a large LUMO and HOMO contrast between its two interfaces with the bottom and top active layers, leading to low absorption losses. As a result the PCE attained reached 8.40%.

Lastly, cesium-functionalized (GO-Cs) was used in GO-Cs/Al/GO/MoO_3 ICL between two PCDTBT-based subcells.[86] The GO-based ICL provided an efficient recombination region for electrons and holes generated from the front and rear cells, due to excellent energy level alignment of the materials involved. In particular, the GO WF was increased to 5.3 eV after MoO_3 modification, matching the HOMO of the PCDTBT, while the GO-Cs WF was reduced to 4 eV by the addition of Al interlayer, matching the LUMO of the PCBM. The PCE obtained was 3.91% with a V_{oc} of 1.69 V, which was almost the sum of the V_{oc}

values of the respective subcells, indicating the beneficial role of the graphene-based recombination layer.

2.4.4 As buffer layers

The most successful application of graphene and other 2D crystals in OPVs is as buffer layers for either electron or hole transport (or blocking). For high efficient OPVs, buffer layers are placed between the photoactive layer and the anode and cathode respectively, to minimize the potential barriers at both interfaces and effectively supress their recombination rate and current leakage[87]. Ideally, the WF of the HTL should match the HOMO of the polymer donor, while the WF of the ETL should match the LUMO of the fullerene acceptor, ensuring perfect ohmic contacts at both interfaces[88].

A number of HTL materials for OPVs have been used, including transition metal oxides (e.g.V_2O_5, NiO_x)[89,90] and self-assembled organic molecules[91], with the PEDOT:PSS being the current state-of-art material. On the other hand, the most efficient materials are n-type inorganic semiconductors (ZnO, TiO_x)[92], and n-type organic semiconductors[93]. However, there are several drawbacks concerning the current state-of-the-art buffer layers, which are detrimental to both PCE and stability, arising from the strong acidic and hygroscopic character of PEDOT:PSS or the sensitiveness of sol-gel prepared TiO_x to moisture, and also the increased costly vacuum manufacturing[94]. In addition, the majority of the buffer materials do not allow their WF tuning, preventing the direct energy match by demand with the numerous active layer donors and acceptors and urging the need for universal, tuned WF buffer layer materials. In this context, graphene derivatives and other 2D crystals are extensively explored as buffer layers in order to exploit their great advantages including solution processability, low cost fabrication, astonishing stability and more importantly their WF tunability through several functionalization methods.

2.4.4.1 As HTLs

The first report on graphene based HTL was by Li et al., who spin-coated a 2 nm-thick GO films in order to replace the PEDOT:PSS in P3HT:PC_{61}BM OPVs.[95] It was found that the devices with GO exhibited slower recombination

rate, and better stability than the PEDOT:PSS-based OPVs. Yu et al. used a PEDOT:PSS-GO composite as the HTL in PTB7:PC$_{71}$BM OPVs.[96] The composite layer improved the hole mobility of the device due to the improved conductivity by benzoid-quinoid transitions and well matched WF between the GO and PEDOT:PSS. A PCE of 8.21% was achieved, 12% higher that the PEDOT:PSS only device. Also, Chao et al. sequentially spin coated two layers of GO and vanadium oxide, and utilized the hybrid as the HTL in inverted OPVs devices, reaching an improved PCE of 6.7%[97].

It should be also noted that the GO HTL is actually modified to a partially reduced GO (prGO), during either the subsequent fabrication steps by thermal annealing or during illumination by photoreduction.[98] Therefore, GO refers to the starting material and not the actual HTL, which is either a prGO or rGO and its insulating nature is not anymore an obstacle for hole collection. In this context, many research groups have switched their attention to rGO and not to GO derivatives. Yun et al. prepared rGO by using a novel p-toluenesulfonyl hydrazide reductant and subsequently incorporated it as the HTL in P3HT: PC$_{61}$BM OPVs achieving PCEs of 3.6%, highly comparable with the PEDOT: PSS devices.[99] Furthermore, the rGO devices exhibited much longer lifetimes compared with the PEDOT:PPS ones. Similarly, Murray et al. treated a GO HTL with UV irradiation in order to reduce it and at the same time to increase its WF in order to match the HOMO of the PTB7 donor (**Figure 2.12a**).[100] It was demonstrated that the resulting prGO layer templates more effectively the PTB7 π-stacking orientation, which is favorable for charge extraction. In addition, although the PCE (7.5%) of prGO-based device was comparable to the one with PEDOT:PSS, the long lifetime in air to remain prGO key advantage.

Following a different reduction method, Yeo et al. used rGO as the HTL by functionalizing GO using p-hydrazinobenzene sulfonic acid hemihydrate as the reducing agent.[101] The resulting srGO presented a very high dispersion concentration in pure water, without the assistance of insulating surfactants, as well as high conductivity. Most importantly, the WF of srGO exhibited a higher value (5.04 eV) compared to other graphene derivatives, rendering it compatible with the HOMO level of several donor polymers. The srGO was successfully employed in solar cells with P3HT, PTB7 and poly[1-(6-{4,8-bis[(2-ethylhexyl)oxy]-6-methylbenzo[1,2-b:4,5-b']dithiophen-2-yl}-3-fluoro-4-methyl

thieno [3,4-b] thiophen-2-yl)-1-octanone] (PBDTTT-CF) as polymer donors. PCEs of 7.18% were recorded for PTB7:PC$_{71}$BM, and PBDTTT-CF:PC$_{71}$BM OPVs, utilizing the srGO, values highly comparable to those of PEDOT:PSS-based OPVs. Another GO reduction method was proposed by Liu et al.,[102] who synthesized a highly soluble sulfated rGO, by introducing -OSO$_3$H groups to the carbon basal plane of GO (i.e. rGO-OSO$_3$H). The resulted rGO-OSO$_3$H HTL exhibited an significant high conductivity of 1.3 Sm^{-1} and a well matched WF with the HOMO of the P3HT, leading to a PCE of 4.37%, which was highly comparable to PEDOT:PSS (4.39%).

An alternative way to increase the GO conductivity is by mixing it with SWNTs, as proposed by Kim et al.[103] In this way, the HTL conductivity is increased, and a PCE of 4.1% was obtained for P3HT:PC$_{61}$BM OPVs. Also, surfactant free Au NPs were placed between the GO HTL and the photoactive layers, resulting in 30% PCE enhancement compared with the PEDOT:PSS devices.[104] Likewise, they preserved 50% of their initial PCE after 45 h of continuous illumination, contrary to the PEDOT:PSS-based ones that failed after 20 h. The PCE increase was attributed to enhanced exciton generation rate due to NP-induced plasmon absorption enhancement, while the stability enhancement to limited oxygen and/or indium diffusion from the ITO electrode into the active layer.

Li et al. utilized spin-coated GQDs as the HTL in P3HT:PC$_{61}$BM OPVs[105]. The GQD films exhibited homogenous morphology and high conductivity, resulting in a PCE of 3.51% for the P3HT:PC$_{61}$BM based devices, comparable with the PEDOT:PSS (3.52%). Importantly, The GQDs OPVs exhibited longer lifetime and more reproducible PCE. Another fascinating approach to enhance the performance of GO-based HTLs is via WF tuning through different functionalization routes. Kim et al. synthesized a fluorinated rGO (FrGO) with a WF of 4.9 eV by employing a phenylhydrazine-based reductant containing fluorine atoms, and used it as the HTL in PTB7:PC$_{71}$BM and P3HT:ICBA OPVs (**Figure 2.12b**).[106] The functionalization route effectively removes oxygen functional groups attached to GO while simultaneously dopes the basal plane and edges of the graphene sheets with the fuorine atoms. The resulted WF increase leads to OPV devices exhibiting similar performance to that of PEDOT:PSS and outperforming them in stability. Another route was proposed

by Li et al. who synthesized a series of GOs with precise oxidation via strictly controlling pre-oxidation steps, oxidant content and oxidation time, resulting in different values of the WF, ranging from 4.74 to 5.06 eV.[107] By fine tuning of the oxidation time, a PCE of 3.74% for a P3HT:PC$_{61}$BM device obtained, higher than the 3.60% reported with the PEDOT:PSS-based counterpart.
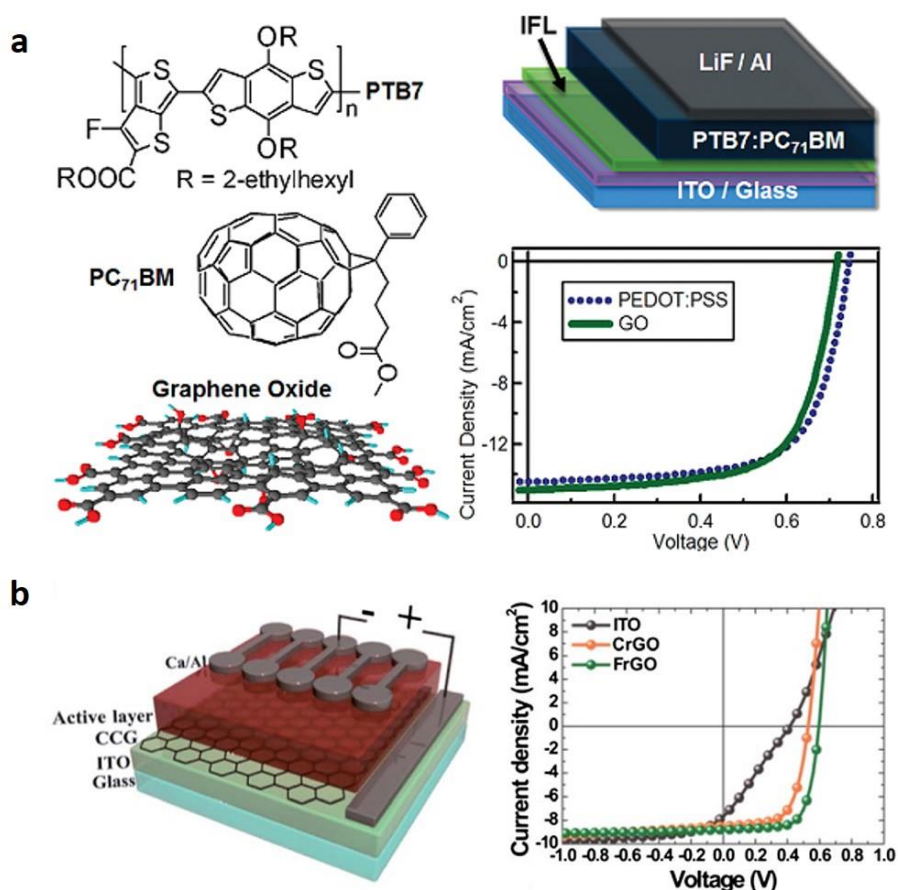
Figure 2.12. a) Chemical structures of the PTB7 donor polymer, PC$_{71}$BM acceptor, and GO IFL. Schematic of a standard OPV indicating the location of the IFLs. Comparative photovoltaic performance of PTB7:PC$_{71}$BM OPVs with PEDOT:PSS or GO IFLs. Reproduced from reference 100. b) Schematic illustration of the OPV structure. J-V curves of OPVs based on different anode interfacial layers. Reproduced from reference 106.

2.4.4.2 As ETLs

For the utilization of GO derivatives as the ETL, proper functionalization routes have been employed for the decrease of the WF to values close to the fullerene acceptor HOMO, to facilitate efficient electron transport. The first

report on graphene based ETLs was by Liu et al., who used Cs_2CO_3 functionalised GO as the ETL in P3HT:PC_{61}BM.[108] By replacing the periphery–COOH groups of the GO with the -COOCs groups through charge neutralization, the WF decreased from 4.7 to 4.0 eV, matching the LUMO level of the PC_{61}BM for efficient electron transport. PCEs of 3.67% and 2.97% were obtained, by employing normal and inverted OPV structures respectively, both comparable with OPVs using LiF as the ETL.

The same functionalization route was applied to GQDs, and the resulted GQDs-Cs_2CO_3 layer was used as the ETL in inverted P3HT:PC_{61}BM OPVs (**Figure 2.13a**).[109] The OPVs with the GQDs-Cs_2CO_3 ETL, exhibited a PCE of 3.23%, 56% higher than the OPVs with the pristine Cs_2CO_3 HTL. Moreover, the PCE of GQDs-Cs_2CO_3-based devices retained 50% of its original value after 1200 h of continuous exposure to ambient conditions, while the pristine Cs_2CO_3-based device PCE decreased to only 17% of its initial value. The observed performance stability enhancements were attributed to the better electron-extraction, suppression of leakage current, and inhibition of Cs^+ ion diffusion at the buffer/polymer interface by GQDs–Cs_2CO_3.

Jayawardena et al. proposed an alternative n-doping strategy by forming rGO-ZnO and rGO-TiO_2 nanocomposites, and used them as the ETLs in inverted PTB7:PC_{71}BM OPVs.[110] The PCE yielded was superior in both cases (7.50% for the rGO-ZnO and 7.46% for the rGO-TiO_2) against devices containing pristine ZnO (7.39%) and TiO_2 (7.22%) as ETLs. Moreover the researchers compared the OPVs containing rGO-metal oxide nanocomposites with devices containing thermal evaporated bathocuproine as the ETL. In the latter case, the PCE obtained (7.47%) was quite comparable to the rGO- metal oxide-based OPVs, as the presence of rGO played a key role in balancing the hole and electron mobilities of the devices. Also, rGO-metal oxide nanocomposites were utilized as the ETL in PCDTBT:PC_{71}BM,[111] P3HT:PC_{61}BM,[112] and low band gap quinoxaline based D-A copolymer:PC_{61}BM[113] OPVs.

Furthermore, Qu et al. utilized an rGO-PC_{61}BM composite, prepared by anchoring PC_{61}BM onto the GO lattice via a pyridine moiety, in P3HT:PC_{61}BM OPVs (**Figure 2.13b**).[114] The rGO-PC_{61}BM nanocomposite presented higher solubility compared to rGO, while the WF value, measured via kelvin probe

microscopy measurements, was low enough to match with the LUMO of the electron acceptor. The $PC_{61}BM$ modification resulted in OPVs with a PCE of 3.89%, significantly improved compared to OPVs, utilizing pristine rGO or pyrene-$PC_{61}BM$ ETLs.
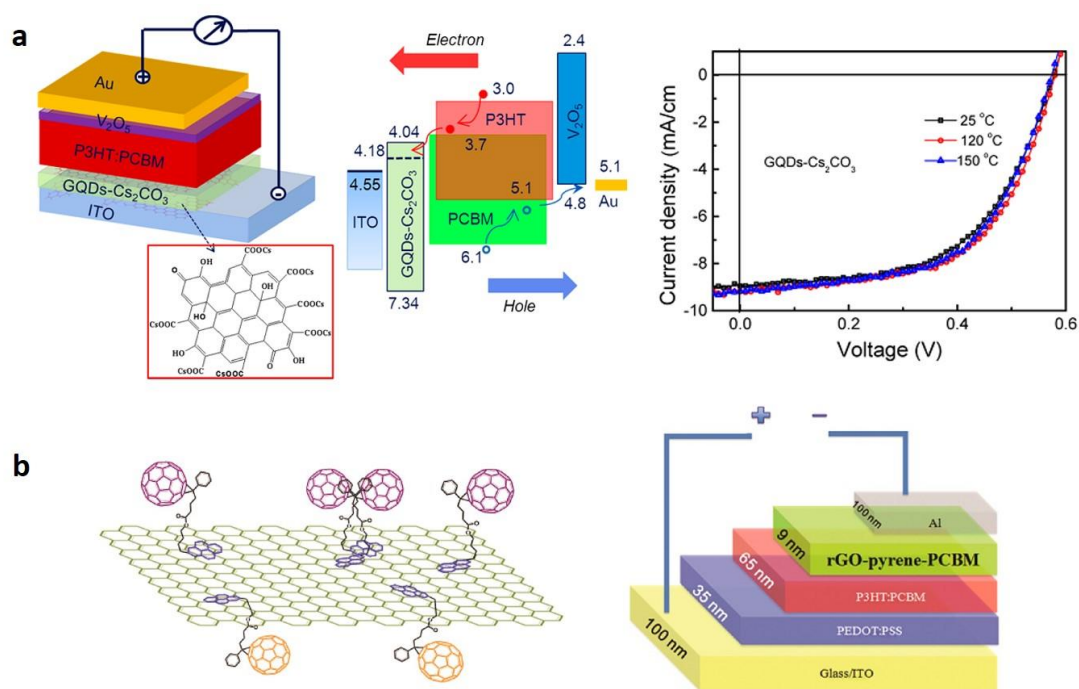
Figure 2.13. a) Schematic structure and energy band diagram of an inverted OPV device with GQDs-Cs_2CO_3 buffer layer and J-V curves of inverted P3HT:$PC_{61}BM$ devices with GQDs-Cs_2CO_3 buffer layer annealed at different temperatures. Reproduced from reference 109. b) Schematic illustration rGO-pyrene-$PC_{61}BM$ configuration and Schematic architecture of ITO/PEDOT:PSS/P3HT:$PC_{61}BM$/rGO-pyrene-$PC_{61}BM$/Al BHJ-PSC device with the incorporation of rGO-pyrene-$PC_{61}BM$ electron extraction layer. The thicknesses of each layer are also demonstrated. Reproduced from reference 114.

Another strategy was proposed by Wang et al., in which an oxidized CVD grown graphene film was directly transferred onto the active layer, through a stamping process, prior to the top cathode deposition.[115] The transferred GO was used as an interfacial layer between the PCDTBT:$PC_{71}BM$ active layer and the TiO_x ETL, resulting in a PCE of 7.5%, higher than both the devices with pristine GO (6.72%) and TiO_x (7.02%) ETLs. The observed enhancement was

attributed to a synergistic effect of improved charge transport and enhanced optical field amplitude.

Also, graphene based derivatives are simultaneously utilized as both the HT and the ETLs. As previously discussed, Liu et al. used Cs_2CO_3 functionalised GO as the ETL, and pristine GO as the HTL in P3HT:PC_{61}BM OPVs.[108] The HTL and ETL WFs were 4.7 and 4 eV, enabling hole and electron transport respectively. As a result, both the normal and inverted OPV devices with GO-based buffer layers outperformed the respective devices with PEDOT:PSS HTL and LiF ETL. Nevertheless, the lack of WF tunability of the produced GO derivatives limits its application on only the well-studied P3HT:PC_{61}BM device, since hole or electron transport is not energetically possible with the current cutting edge active layers, such as the PTB7:PC_{71}BM. Therefore low-cost, high-throughput, facile and r2r compatible methods for WF tuning of the GO buffer layers, which will allow their application in high efficient BHJ OPVs are highly desirable.

REFERENCES

[1] Renewables 2015 Global Status Report, Renewable Energy Policy Network for the 21st Century, Available online at http://www.ren21.net/wpcontent/uploads/2015/07/GSR2015_KeyFindings_lowres.pdf

[2] Becquerel, A. E. *Comptes Rendus De L'Académie Des Sciences*, **1839**, 9, 145.

[3] Becquerel, A. E. *Comptes Rendus De L'Académie Des Sciences*, **1839**, 9, 561.

[4] Bagnall, D. M.; Boreland, M. *Energy Policy*, **2008**, 36, 4390-4396.

[5] Shockley, W.; Queisser, H. J. *J Appl Phys*, **1961**, 32, 510-519.

[6] Hanna, M. C.; Nozik, A. Z. *J Appl Phys*, **2006**, 100, 074510.

[7] Green, M. A.; Emery, K.; Hishikawa, Y.; Warta, W. *Prog Photovolt: Re .Appl*, **2009**, 17, 320-326.

[8] Research Cell Efficiency Records, National Center for Photovoltaics (NCPV), Available online at http://www.nrel.gov/ncpv/

[9] Gratzel, M. *Nature*, **2001**, 414, 338-344.

[10] Nazeeruddin, M. K.; Kay, A.; Rodicio, I.; Humphry-Baker, R.; Mueller, E.; Liska, P.; Vlachopoulos, N.; Graetzel, M. *J Am Chem Soc*, **2002**, 115, 6382-6390.

[11] Pochettino, A. *Acad Lincei Rend*, **1906**, 15, 355.

[12] What is levelised cost of energy, **2012**, Dyesol, Available online at http://www.dyesol.com/posts/what-is-levelised-cost-of-energy-february-2012-enewsletter/#sthash.o8xR7sIK.dpuf

[13] Chiang, C. K.; Fincher, C. R.; Park, Y. W.; Heeger, A. J.; Shirakawa, H.; Louis, E. J.; Gau, S. C.; MacDiarmid, A. G. *Phys Rev Lett*, **1977**, 39, 1098.

[14] Shirakawa, H.; Louis, E. J.; Macdiarmid, A.G.; Chiang, C. K.; Heeger, A. J. *JCS Chem Comm*, **1977**, 16, 578-580.

[15] Mikhnenko O. V. Singlet and Triplet Excitons in Organic Semiconductors, PhD Thesis, University of Groningen, the Netherlands, **2011**.

[16] Hu, J. Overlap of Adjacent p Orbitals-Electron Delocalization, available onine at http://chemwiki.ucdavis.edu/Core/Organic_Chemistry/Conjugation/Overlap_of_Adjacent_p_Orbitals-Electron_Delocalization

[17] Sariciftci, N.S.; Smilowitz, L.; Heeger, A. J.; Wudl, F. *Science*, **1992**, 258, 1474–1476.

[18] Zhang, F.; Ceder, M.; Inganas, O. *Adv Mater*, **2007**, 19, 1835.

[19] Yan, H.; Lee, P.; Armstrong, N. R.; Graham, A.; Evmenenko, G. A.; Dutta, P.; Marks, T. J. *J Am Chem Soc*, **2005**, 127, 3172.

[20] Yang, X. H.; Jaiser, F.; Stiller, B.; Neher, D.; Galbrecht, F.; Scherf, U. *Adv Funct Mater*, **2006**, 16, 2156.

[21] Kaisha, C. N. Organic electroluminescent device and production method of the device, and display apparatus, Patent US 7990049 B2, **2011**.

[22] Park, S. H.; Roy, A.; Beaupre, S.; Cho, S.; Coates, N.; Moon, J. S.; Moses, D.; Leclerc, M.; Lee, K.; Heeger, A.J. *Nat. Photonics,* **2010**, 3, 297.

[23] Hecht, D. S.; Hu, L.; Irvin, G. *Adv Mater,* **2011**, 23, 1482.

[24] Wu, J. B.; Agrawal, M.; Becerril, H. A.; Bao, Z. N.; Liu, Z. F.; Chen, Y. S.; Peumans, P. *ACS Nano*, **2010**, 4, 43.

[25] Richter, C.; Lincot, D.; Gueymard, C. A. Solar Energy, Springer, **2013**.

[26] Saunders, B. R. *Journal Colloid and Interface Science*, **2012**, 369, 1-15.

[27] Cai, W.; Gong, X.; Cao, Y. *Solar Energy Materials and Solar Cells*, **2010**, 94, 114-127.

[28] Garcia-Belmonte, G.; Munar, A.; Barea, E. M.; Bisquert, J.; Ugarte, I.; Pacios, R. *Organic Electronics*, **2008**, 9, 847-851.

[29] Organic Photovoltaics, OPV Tutorial, Sigma-Aldrich, Available online at http://www.sigmaaldrich.com/materials-science/organic-electronics/opv-tutorial.html

[30] Miller S. L. PhD thesis, Graduate School, New Brunswick Rutgers, The State University of New Jersey, **2011**.

[31] He, Z.; Zhong, C.; Huang, X.; Wong, W. Y.; Wu, H.; Chen, L.; Su, S.; Cao, Y. *Adv Mater,* **2011**, 23, 4636.

[32] Liu, S. J.; Zhang, K.; Lu, J. M.; Zhang, Z.; Yip, H. L.; Huang, F.; Cao, Y. *J Am Chem Soc*, **2013,** 135, 15326.

[33] You, J. B.; Dou, L. T.; Yoshimura, K.; Kato, T.; Ohya, K.; Moriarty, T.; Emery, K.; Chen, C. C.; Gao, J.; Li, G.; Yang, Y. *Nat Commun*, **2013**, 4, 1446–1455.

[34] Dou, L. T.; You, J. B.; Yang, J.; Chen, C. C.; He, Y. J.; Murase, S.; Moriarty, T.; Emery, K.; Li, G.; Yang, Y. *Nat Photonics,* **2012**, 6, 180.

[35] Novoselov, K. S.; Geim, A. K.; Morozov, S. V.; Jiang, D.; Zhang, Y.; Dubonos, S. V.; Grigorieva, I. V.; Firsov, A. A. *Science* **2004**, *306*, 666.

[36] Yin, Z.; Zhu, J.; He, Q.; Cao, X.; Tan, C ; Chen, H.; Yan, Q.; Zhang, H. *Adv Energy Mater,* **2014**, *4*, 1300574.

[37] Tyler, T. P.; Brock, R. E.; Karmel, H. J.; Marks, T. J.; Hersam, M. C. *Adv Energy Mater*, **2011**, 1, 785.

[38] Kymakis, E.; Stratakis, E.; Koudoumas, E.; Fotakis, C. *IEEE Trans Electron Devices,* **2011**, 58, 860.

[39] De, S.; Higgins, T. M.; Lyons, P. E.; Doherty, M.E.; Nirmalraj, P.N.; Blau, W. J.; Boland, J. J.; Coleman, J. N. *ACS Nano,* **2009**, 3, 1767.

[40] Na, S. I.; Kim, S. S.; Jo, J.; Kim, D. Y. *Adv Mater,* **2008**, 20, 4061.

[41] Wang, Y.; Chen, X. H.; Zhong, Y. L.; Zhu, F. R.; Loh, K. P. *Appl Phys Lett*, **2009**, 95, 063302.

[42] Arco, L. G. D.; Zhang, Y.; Schlenker, C. W.; Ryu, K.; Thompson, M. E.; Zhou, C. *ACS Nano*, **2010**, 4, 2865-2873.

[43] Wang, Y.; Tong, S. W.; Xu, X. F.; Ozyimaz, B.; Loh, K. P. *Adv Mater*, **2011**, 23, 1514.

[44] Hsu, C. L.; Lin, C. T.; Huang, J. H.; Chu, C. W.; Wei, K. H.; Li, L. J. *ACS Nano*, **2012**, 6, 5031.

[45] Lee, *S.;* Yeo*, J. S.;* Cho*,* Kim*, D. Y.;* Na S. I.; Lee, B. H.; Lee*, T. Nanotechnology*, *2012,* 23, 344013.

[46] Lee, D.; Lee, H.; Ahn, Y.; Jeong, Y.; Lee, D. Y.; Lee, Y. *Nanoscale*, **2013**, 5, 7750-7755.

[47] Kahng, Y. H.; Kim, M. L.; Lee, J. H.; Kim, Y. J.; Kim, N.; Park, D. W.; Lee, K. *Sol Energ Mat Sol C*, **2014**, 124, 86-91.

[48] Kim, H.; Bae, S. H.; Han, T. H.; Lim, K. G.; Ahn, J. H.; Lee, T. W. *Nanotechnology*, **2014**, 25, 014012

[49] Lee, B. H.; Lee, J. H.; Kahng, Y. H.; Kim, N.; Kim, Y. J.; Lee, J.; Lee, T.; Lee, K. *Adv Funct Mater*, **2014**, 24, 1847–1856

[50] Park, H.; Chang, S.; Zhou, X.; Kong, J.; Palacios, T.; Gradečak, S. *Nano Lett,* **2014**, 14, 5148-5154.

[51] Yusoff*, A. R. M.;* Kim*, D.;* Schneider*, F. K.;* da Silva, W. J.; Jang*, J. Energy Environ Sci,* **2015***,* 8, 1523-1537.

[52] Li, X.; Zhu, Y.; Cai, W.; Borysiak, M.; Han, B.; Chen, D.; Piner, R. D.; Colombo, L.; Ruoff, R. S. *Nano Lett,* **2009**, 9, 4359.

[53] Bae, B.; Kim, H.; Lee, Y.; Xu, X. F.; Park, J. S.; Zheng, Y.; Balakrishnan, J.; Lei, T.; Kim, H. R.; Song, Y. I.; Kim, Y. J.; Kim, K. S.; Ozyilmaz, B.; Ahn, J. H.; Hong, B. H.; Iijima, S. *Nat Nanotechno.,* **2010**, 5, 574.

[54] Park, S.; An, J.; Potts, J. R.; Velamakanni, A.; Murali, S.; Ruoff, R. S. *Carbon*, **2011**, 49, 3019.

[55] Kymakis, E.; Petridis, C.; Anthopoulos, T. D.; Stratakis, E. *IEEE Journal of Selected Topics in Quantum Electronics,* **2014**, 20, 6573325.

[56] Bonaccorso, F.; Lombardo, A.; Hasan, T.; Sun, Z.; Colombo, L.; Ferrari, A. C. *Mater Today,* **2012***,* 15*,* 564.

[57] Konios, D.; Stylianakis, M. M.; Stratakis, E.; Kymakis, E. *J Col Interf Sci,* **2014**, 430, 108.

[58] Xu, Y.; Long, G.; Huang, L.; Huang, Y.; Wan, X.; Ma, Y.; Chen, Y. *Carbon,* **2010**, 48, 3308.

59 Kymakis, E.; Stratakis, E.; Stylianakis, M. M.; Koudoumas, E.; Fotakis, C. *Thin Solid Films,* **2011**, 520, 1238.

60 Yin, Z.; Sun, S.; Salim, T.; Wu, S.; Huang, X.; He, Q.; Lam, Y. M.; Zhang, H. *ACS Nano,* **2010**, *4*, 5263.

61 Kymakis, E.; Savva, K.; Stylianakis, M. M.; Fotakis, C.; Stratakis, E *Adv Funct Mater*, **2013**, *23*, 2742.

62 Liu, Q.; Liu, Z. F.; Zhang, X. Y.; Yang, L. Y.; Zhang, N.; Pan, G. P.; Yin, S. G.; Chen, Y. S.; Wei, J. *Adv Funct Mater,* **2009**, 19**,** 894-904.

63 Yu, D.; Yang, Y.; Durstock, M.; Baek, J. B.; Dai, L. *ACS Nano,* **2010**, 4, 5633-5640.

64 Hill, C. M.; Zhu, Y.; Pan, S. *ACS Nano*, **2011**, 2, 942-951.

65 Liu, Z.; Liu, Q.; Huang, Y.; Ma, Y.; Yin, S.; Zhang, X.; Sun, W.; Chen, Y. *Adv Mater,* **2008**, 20, 3924-3930.

66 Gupta, V.; Chaudhary, N.; Srivastava, R.; Sharma, G. D.; Bhardwaj, R.; Chand, S. *J Am Chem Soc*, **2011**, 133, 9960-9963.

67 Yu, D.; Park, K.; Durstock, M.; Dai, L. *J Phys Chem Lett,* **2011**, 2, 1113-1118.

68 Stylianakis, M. M. ; Spyropoulos, G. D. ; Stratakis, E. ; Kymakis, E. *Carbon*, **2012**, 50, 5554-5561.

69 Stylianakis, M. M.; Sygletou, M.; Savva, K.; Kakavelakis, G.; Kymakis, E.; Stratakis, E. *Advanced Optical Materials*, **2015**, 5, 658-666.

70 Cho, H. W.; Liao, W. P.; Lin, W. H.; Yoshimura, M.; Wu, J. J.; *Journal of Power Sources,* **2015**, 293, 246-252.

71 Ameri, T.; Khoram, P.; Min, J.; Brabec, C. J. *Adv Mater*, **2013,** 25, 4245-4266.

72 Cheng, P.; Lia, Y.; Zhang, X. *Energy Enviro. Sci,* **2014**, 7, 2005.

73 Jun, G. H.; Jin, S. H.; Lee, B.; Kim, B. H.; Chae, W. S.; Hong, S. H.; Jeon, S. *Energy Environ Sci*, **2013**, 6, 3000–3006.

74 Robaeys, P.; Bonaccorso, F.; Bourgeois, E.; D'Haen, J.; Dierckx, W.; Dexters, W.; Spoltore, D.; Drijkoningen, J.; Liesenborgs, J.; Lombardo, A.; Ferrari, A. C.; Van Reeth, F.; Haenen, K.; Manca, J. V.; Nesladek, *Appl Phys Lett,* **2014**, 105, 083306.

75 Bonaccorso, F.; Balis, N.; Stylianakis, M. M.; Savarese, M.; Adamo, C.; Gemmi, M.; Pellegrini, V.; Stratakis, E.; Kymakis, E.; *Advanced Functional Materials*, **2015**, 25, 3870-3880.

76 Kim, J. K.; Park, M. J.; Kim, S. J.; Wang, D. H.; Cho, S. P.; Bae, S.; Park, J. H.; Hong, B. H. *ACS Nano*, **2013**, 7, 7207-7212.

77 You, J.; Dou, L.; Hong, Z.; Li, G.; Yang, Y. *Prog Polym Sci,* **2013**, 38, 1909.

78 Chueh, C. C.; Li, C. Z.; Jen, A. K. Y. *Energy & Environmental Science*, **2015**, 8, 1160.

79 Kim, J. Y.; Lee, K.; Coates, N. E.; Moses, D.; Nguyen, T. Q.; Dante, M.; Heeger, A. J. *Science,* **2007**, 317, 222.

80 Li, W.; Furlan, A.; Hendriks, K. H.; Wienk, M. M.; Janssen, R. A. J.; *J Am Chem Soc*, **2013**, 135, 5529.

81 Hadipour, A.; de Boer, B.; Wildeman, J.; Kooistra, F. B.; Hummelen, J. C.; Turbiez, M. G. R.; Wienk, M. M.; Janssen, R. A. J.; Blom, P. W. M. *Adv Funct Mater,* **2006**, 16, 1897-1903.

82 De Jong, M. P.; van IJzendoorn, L. J.; de Voigt, M. J. A. *Appl Phys Lett,* **2000**, 77, 2255-2257.

83 Tong, S. W.; Wang, Y.; Zheng, Y.; Ng, M. F.; Loh, K. P. *Adv Funct Mater*, **2011**, 21, 4430-4435.

84 Tung, V. C.; Kim, J.; Cote, L. J.; Huang, J. *J Am Chem Soc*, **2011**, 133, 9262

85 Yusoff, A. R. B. M.; da Silva, W. J.; Kim, H. P.; Jang, J. *Nanoscale,* **2013**, 5, 11051.

86 Chen, Y.; Lin, W. C.; Liu, J.; Dai, L.; *Nano Lett*, **2014**, 14, 1467.

87 Li, C. Z.; Chang, C. Y.; Zang, Y.; Ju, H. X.; Chueh, C. C.; Liang, P. W.; Cho, N.; Ginger, D. S.; Jen, A. K. Y. *Adv Mater,* **2014**, 26, 6262.

88 Lu, L.; Xu, T.; Jung, I. H.; Yu, L. *J Phys Chem C*, **2014**, 118, 22834-22839.

89 Shrotriya, V.; Li, G.; Yao, Y.; Chu, C.; Yang, Y. *Appl Phys Lett*, **2006**, 88, 073508.

90 Jiang, F.; Choy, W. C. H.; Li, X.; Zhang, D.; Cheng, J. *Adv Mater,* **2015**, 27, 2930.

[91] Hains, A. W.; Marks, T. J. *Appl Phys Lett*, **2008**, 92, 023504.

[92] Yip, H. L.; Hau, S. K.; Baek, N. S.; Ma, H.; Jen, A. K. Y. *Adv Mater*, **2008**, 20, 2376.

[93] Chu, T. Y.; Lu, J.; Beaupre, S.; Zhang, Y.; Pouliot, J. R.; Wakim, S.; Zhou, J.; Leclerc, M.; Li, Z.; Ding, J.; Tao, Y. *J Am Chem Soc*, **2011**, 133, 4250.

[94] Jorgensen, M.; Norrman, K.; Krebs, F. C. *Sol Energy Mater Sol Cells*, **2008**, 92, 686.

[95] Li, S. S.; Tu, K. H.; Lin, C. C.; Chen, C. W.; Chhowalla, M. *ACS Nano*, **2010**, 4, 3169.

[96] Yu, J. C.; Jang, J. I.; Lee, B. R.; Lee, G. W.; Han, J. T.; Song, M. H. *ACS Appl Mater Interfaces*, **2014**, 6, 2067.

[97] Chao, Y. H.; Wu, J. S.; Wu, C. E.; Jheng, J. F.; Wang, C. L.; Hsu, C. S. *Adv Energy Mater*, **2013**, 3, 1279-1285.

[98] Paci, B.; Kakavelakis, G.; Generosi, A.; Albertini, V.; Wright, J.; Ferrero, C.; Konios, D.; Stratakis, E.; Kymakis, E. *RSC Advances*, **2015**, 5, 106930-106940.

[99] Yun, J. M.; Yeo, J. S.; Kim, J.; Jeong, H. G.; Kim, D. Y.; Noh, Y. J.; Kim, S. S.; Ku, B. C.; Na, S. I.; *Adv Mater*, **2011**, 23, 4923-4928.

[100] Murray, I. P.; Lou, S. J.; Cote, L. J.; Loser, S.; Kadleck, C. J.; Xu, T.; Szarko, J. M.; Rolczynski, B. S.; Johns, J. E.; Huang, J.; Yu, L.; Chen, L. X.; Marks, T. J.; Hersam, M. C. *J Phys Chem Lett*, **2011**, 2, 3006.

[101] Yeo, J. S. Yun, J. M.; Jung, Y. S.; Kim, D. Y.; Noh, Y. J.; Kim, S. S.; Na, S. I. *J Mater Chem A*, **2014**, 2, 292.

[102] Liu, J.; Xue, Y.; Dai, L. *J Phys Chem Lett,* **2012**, 3, 1928.

[103] Kim, J.; Tung, V. C.; Huang J. *Adv Energy Mater*, **2011**, 1, 1052.

[104] Stratakis, E.; Stylianakis, M. M.; Koudoumas, E.; Kymakis, E. *Nanoscale,* **2013**, 5, 4144.

[105] Li, M.; Ni, W.; Kan, B.; Wan, X.; Zhang, L.; Zhang, Q.; Long, G.; Zuo, Y.; Chen, Y. *Phys Chem Chem Phys*, **2013**, 15, 18973.

[106] Kim, S. H.; Lee, C. H.; Yun, J. M.; Noh, Y. J.; Kim, S. S.; Lee, S.; Jo, S. M.; Joh, H. I.; Na, S. I. *Nanoscale,* **2014**, 6, 7183.

[107] Li, C.; Yang,X.; Zhao, Y.; Zhang, P.; Tu, Y.; Li, Y. *Org Electronics,* **2014**, 15, 2868.

[108] Liu, J.; Xue, Y.; Gao, Y.; Yu, D.; Durstock, M.; Dai, L. *Adv Mater,* **2012**, 24, 2228-2233.

[109] Yang, H. B.; Dong, Y. Q.; Wang, X.; Khoo, S. Y.; Liu, B. *ACS Appl Mater Interfaces,* **2014**, 6, 1092.

[110] Jayawardena, K. D. G. I.; Rhodes, R.; Gandhi, K. K.; Prabhath, M. R. R.; Dabera, G. D. M. R.; Beliatis, M. J.; Rozanski, L. J.; Henley, S. J.; Silva, S. R. P. *J Mater Chem A,* **2013**, 1, 9922.

[111] Beliatis, M. J.; Gandhi, K. K.; Rozanski, L. J.; Rhodes, R.; McCafferty, L.; Alenezi, M. R.; Alshammari, A. S.; Mills, C. A.; Jayawardena, K. D.; Henley, S. J.; Silva, S. R. *Adv Mater,* **2014**, 26, 2078.

[112] Zhang, Y.; Yuan, S.; Li, Y.; Zhang, W.; *Electrochim Acta,* **2014**, 117, 438.

[113] Zhang, Y.; Yuan, S.; Liu, W. *Electrochim Acta,* **2014**, 143, 18.

[114] Qu, S.; Li, M.; Xie, L.; Huang, X.; Yang, J.; Wang, N.; Yang, S. *ACS Nano,* **2013**, 7 ,4070.

[115] Wang, D. H.; Kim, J. K.; Seo, J. H.; Park, I.; Hong, B. H.; Park, J. H.; Heeger, A. J. *Angew Chem Int Ed*, **2013**, 52, 2874-2880.

Experimental Part

Chapter 3

Dispersion behaviour of graphene oxide and reduced graphene oxide

Abstract: The dispersion behaviour of Graphene Oxide (GO) and reduced Graphene Oxide (rGO) has been investigated and compared, with respect to the long-term stability and the dispersion quality. Considering the solvent polarity, the surface tension and the Hansen and Hildebrand solubility parameters, the effect of reduction process on the solubility of GO in eighteen different solvents was examined and analyzed. rGO concentrations up to ~9 μgmL^{-1} in chlorinated solvents, were achieved, demonstrating an efficient solubilization strategy, extending the scope for scalable liquid-phase processing of conductive rGO inks for the development of printed flexible electronics.

3.1 Introduction

Graphene is an atomically thin layer of sp^2-bonded carbon atoms, stacked in a 2D honeycomb lattice, forming the basic building block for carbon allotropes of any dimensionality.[1] Since its isolation as a monolayer, graphene has attracted an extraordinary amount of interest due to its potential application in the fastest growing scientific fields, such as supercapacitors,[2] biosensors,[3] organic photovoltaics[4] and touch panels.[5]

CVD[6] and micromechanical exfoliation of graphite are the most widely used fabrication methods of less defective graphene films. However, the CVD deposition of uniform large area graphene films on arbitrary substrates at low temperatures is not possible and therefore this method is incompatible with roll to roll mass production processes. At the same time, the exfoliated graphene exhibits very low solubility in common organic solvents,[7] due to the essential addition of a stabilizer as the exfoliation liquid medium.[8]

On the other hand, exfoliated GO is the ideal alternative for the production of solution processable graphene, as it can be synthesized in large quantities from inexpensive graphite powder and can readily yield stable dispersions in various solvents.[9] GO is an oxidized graphene sheet having its basal planes decorated mostly with epoxide and hydroxyl groups, in addition to carbonyl and carboxyl groups located at the edges.[10]

The covalent character of C-O bonds disrupts the sp^2 conjugation of the hexagonal graphene lattice, making GO an insulator. Nevertheless, GO can be partially reduced to conductive graphene-like sheets by removing the oxygen-containing groups.[11,12,13] In this way the conjugated structure of graphene can be recovered, resulting in rGO with important electrical properties partially restored.[14]

However, the preparation of dispersed form of graphene for applications in printed flexible electronics is not straightforward, since its stability in various solvents is a critical point. In this context, the solubility of GO in various solvents has been recently examined by several groups.[9,15,16] The previous reported works have focussed on GO dispersibility, without extending the research on dispersion behaviour of its reduced form. Thus the knowledge on how the more conductive rGO can produce stable solutions in common solvents is limited.

In this work, for the first time, the dispersion behaviour of GO and rGO is compared, aiming to get a full insight of how the removal of oxygen containing groups during reduction process affect the dispersion quality of the two nanomaterials. The solubility/dispersibility of rGO is investigated in eighteen different solvents and directly compared with the pristine GO. In this way, critical information is obtained for the formation of conductive rGO inks for the development of printed flexible electronics.[17]

3.2 Experimental section

3.2.1 Preparation of graphene oxide[18]

GO was prepared from graphite powder (Alfa Aesar. ~200 mesh) according to a modified Hummers' method. In more detail, graphite powder (1.0 g) was placed into a mixture of H_2SO_4 (23 mL, 98%) and $NaNO_3$ (0.5 g). The mixture was then stirred and cooled in an ice bath. While maintaining vigorous stirring, $KMnO_4$ (3 g) was then added in portions over a period of 2 h. The reaction mixture was left for 4 h in order to reach room temperature before being heated to 35°C for 30 min. It was then poured into a flask containing deionized water (50 mL) and further heated to 70°C for 15 min. The mixture was then decanted into 250 mL of deionized water and the unreacted $KMnO_4$ was removed by adding 3% H_2O_2. The reaction mixture was then allowed to settle and decanted. The graphite oxide obtained was then purified by repeated centrifugation and redispersed in deionized water until a negative reaction on sulfate ion (with $Ba(NO_3)_2$) was achieved. Finally, the resulting GO was dried at 60°C in a vacuum oven for 48 h before use.

3.2.2 Reduction of graphene oxide[19]

The chemical reduction of GO was performed by exposing the produced GO to N_2H_4 (98% Aldrich) vapors at 40°C. Specifically, the GO powder produced as described in the above section, was placed in a perfectly cleaned glass Petri dish and then inside a larger glass Petri dish, which contained N_2H_4 (1 μL for 10 mg of GO). The drops of N_2H_4 were placed uniformly in the space between the two dishes, around the small Petri dish. The larger dish was covered with a

glass lid, sealed with Parafilm tape, and placed over a hot plate at 40°C for 18 h. Thereafter, the dish was opened and rGO was dried both under a nitrogen stream and by heating to 80°C in vacuum.

3.3 Results and Discussion

For the preparation of GO and rGO dispersions, the products prepared as described in the Experimental Section, were first grounded with a mortar and pestle. In order to compare the dispersion behaviour in the different solvents, the same quantity of GO and rGO powder (~1 mg) was added to a given volume of solvent (~2 mL), with an initial concentration of 0.5 mgmL^{-1}. GO and rGO dispersions were tested in the following organic solvents: (DI) water, acetone, methanol, ethanol, 2-propanol, ethylene glycol, tetrahydrofuran (THF), N,N-dimethylformamide (DMF), N-methyl-2-pyrrolidone (NMP), n-hexane, dichloromethane (DCM), chloroform, toluene, chlorobenzene (CB), o-dichlorobenzene (o-DCB), 1-chloronaphthalene (CN), acetylaceton, diethyl ether. The dispersions were sonicated in an ultrasound bath cleaner (Elmasonic S30H) for 1h and then mildly centrifuged at 500 rpm for 90 min (Alegra X-22) to remove the large aggregates. Afterwards, the supernatant was collected for analysis.

For the estimation of solubility values for GO and rGO in different solvents, UV-Vis spectroscopy was performed on a Shimadzu UV2401PC UV–Vis spectrometer. Using the 2 weeks left suspensions, the dispersibility of GO and rGO in each solvent was examined from the linear relationship between the absorbance (A) and the concentration (C) of a compound in a solution, given by the Lambert–Beer law (A = α l C). It is necessary to determine the absorption coefficient (α), which is related to the absorbance per unit path length A/l and it is an important parameter in characterizing any dispersion. For this purpose, a calibration line was constructed by measuring the absorbance at 660 nm of four GO and rGO solutions with different, low concentrations (**Figure 3.1**). The procedure was repeated for each solvent. The observed values divided by the cuvette length (l=1 cm) were plotted versus the known concentration values, allowing to estimate the absorption coefficient for its suspension. Using the α

values, the maximum solubility of GO and rGO in each solvent could be extracted (**Table 3.1**).
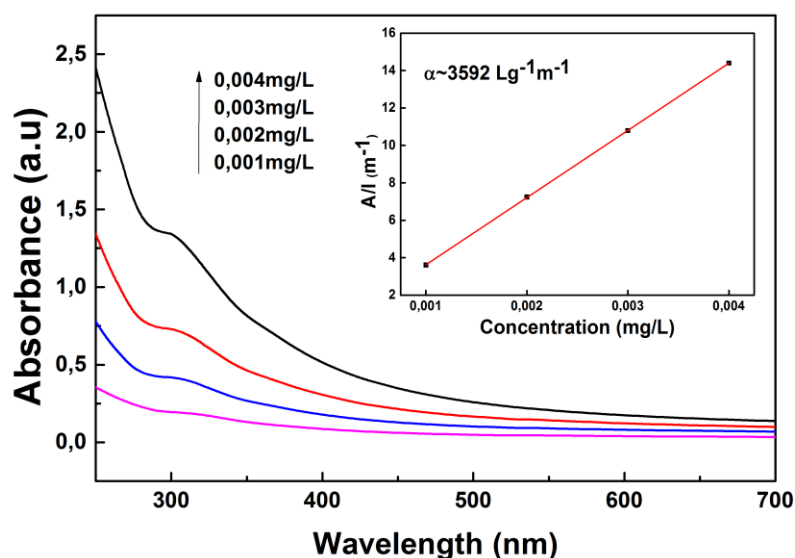
Figure 3.1. UV-Vis spectra of GO dissolved in water at different concentrations. The inset shows the linear relationship between the absorbance per unit path length and the concentration of GO.

Treating GO with hydrazine causes an enormous structural change with the recovery of the conjugated system, through the removal of oxygen containing groups. The morphology, structure and composition of GO and rGO were characterized by Raman spectroscopy, Fourier transform infrared spectroscopy (FT-IR), X-ray diffraction (XRD) and Thermogravimetric Analysis (TGA).

Raman spectroscopy is a powerful tool, which can be used to characterize carbonaceous materials and particularly for distinguishing the disorder in the crystal structures of carbon. In the Raman spectrum of GO and rGO (**Figure 3.2a**) two prominent peaks are clearly visible, corresponding to the so-called D and G bands. In particular the Raman spectrum of GO exhibited a D band peak at 1330 cm^{-1}, that corresponds to the breathing mode of κ-point phonons of A_{1g} symmetry and a G band peak at 1592 cm^{-1}, due to the first-order scattering of the E_{2g} phonons.[20] The corresponding D and G bands in the Raman spectrum of rGO appeared at 1341 cm^{-1} and 1598 cm^{-1}, respectively. The intensity of the D band is related to the size of the in-plane sp^2 domains and the relative intensity ratio (I_D/I_G) is a measure of the extent of disorder.[20] After the reduction

of GO, the intensity ratio (I_D/I_G) was increased significantly and the higher intensity of D band suggests the presence of more isolated graphene domain in rGO compared to GO and removal of oxygen groups from the latter.[21]
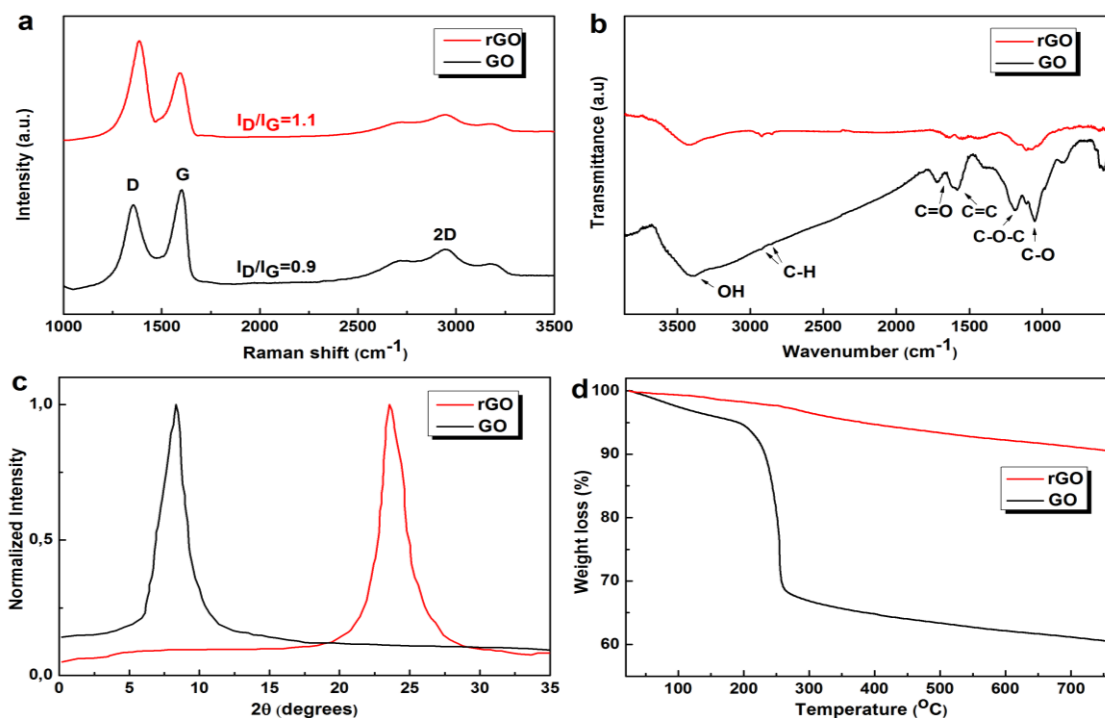
Figure 3.2. Characterization of rGO a) Raman spectra, b) FTIR spectra, c) XRD patterns, d) Decomposition behaviour of GO and rGO.

Figure 3.2b shows the FTIR spectra of GO and rGO. The peaks at ~3400 cm^{-1} (O-H stretching vibrations), at ~1700 cm^{-1} (C=O stretching vibrations), at ~1600 cm^{-1} (skeletal vibrations from unoxidized graphitic domains), at ~1200 cm^{-1} (C-O-C stretching vibrations), at ~1050 cm^{-1} (C-O stretching vibrations) are characteristic for the GO. The removal of oxygen-containing groups during the reduction is confirmed from the decrease (almost disappearance) of the bands of C=O stretching, C-O-C stretching, C-O stretching. The relative decrease in the intensity of O-H stretching band indicates that C-OH still exist, but in lower proportion.

The XRD pattern (**Figure 3.2c**) indicates a larger interlayer spacing in GO than in rGO. Water molecules, as well as the formation of oxygen-containing groups between the layers during the preparation of GO result in a lower angle

reflection peak 2θ= 9.32° (d-spacing ~9.52 Å). The decrease in the interlayer spacing in rGO and the shift of the low peak at higher 2θ angles (23.56°, d-spacing ~3.77 Å) verify the efficient reduction by hydrazine method, due to the more thorough removal of surface functional group.

TGA was used to further assess the level of reduction. Figure 3.2d displays the TGA thermograms that show weight loss as a function of temperature for dried-down GO and rGO. The evaporation of the absorbed water molecules from room temperature to 200°C causes a slight loss in the weight of GO, which is further decreased due to decomposition of oxygen-containing functional groups, losing in total approximately 40% of its mass up to 600°C. On the contrary, rGO displays higher thermal stability, stemming from the deoxygenation during the reduction process.

Table 3.1. Dipole moments, surface tensions and Hildebrand parameters of solvents and GO, rGO solubility values for all solvents studied.

Solvents	Dipole moment	Surface tension (mN/m)	δ_T (MPa$^{1/2}$)	GO Solubility (µg/mL)	rGO Solubility (µg/mL)
Di water	1.85	72.8	47.8	6.6	4.74
Acetone	2.88	25.2	19.9	0.8	0.9
Methanol	1.70	22.7	29.6	0.16	0.52
Ethanol	1.69	22.1	26.5	0.25	0.91
2-propanol	1.66	21.66	23.6	1.82	1.2
Ethylene glycol	2.31	47.7	33	5.5	4.9
Tetrahydrofuran (THF)	1.75	26.4	19.5	2.15	1.44
N,N-dimethylformamide (DMF)	3.82	37.1	24.9	1.96	1.73
N-methyl-2-pyrrolidone (NMP)	3.75	40.1	23	8.7	9.4
n-hexane	0.085	18.43	14.9	0.1	0.61
Dichloromethane (DCM)	1.60	26.5	20.2	0.21	1.16
Chloroform	1.02	27.5	18.9	1.3	4.6
Toluene	0.38	28.4	18.2	1.57	4.14
Chlorobenzene (CB)	1.72	33.6	19.6	1.62	3.4
o-dichlorobenzene (o-DCB)	2.53	36.7	20.5	1.91	8.94
1- chloronaphthalene (CN)	1.55	41.8	20.6	1.8	8.1
Acetylaceton	3.03	31.2	20.6	1.5	1.02
Diethyl ether	1.15	17	15.6	0.72	0.4

Digital pictures were taken to display the dispersion quality of GO and rGO in different solvents, immediately after the sonication (Figure 3.3, 3.4). To identify the degree of sedimentation pictures were again taken a day after. Just after sonication, GO exhibited very good dispersion in NMP, DMF, ethylene glycol, THF and water. These five solvents exhibit significant dipole moment values, although *o*-DCB, which has similar dipole moment (2.53 D) failed to give a stable GO dispersion (Table 3.1). This suggests that solvent polarity is not the only factor for obtaining good dispersibility.[22]

In previous reports, it has been shown that surface tension is an important factor for choosing an effective solvent for graphene and its derivatives.[8,23] The existence of oxygen containing groups in the GO results in higher surface energy, compared with the rGO in which the loss of surface polarity increases its hydrophobicity. By performing wettability and contact angle measurements, the surface energies of GO and rGO have been estimated to be ~62 mNm^{-1} and ~46 mNm^{-1} respectively.[24] Solvents with surface tension similar to the previous values are the most efficient solvents for the dispersion of GO and rGO. Our results (Figure 3.3, 3.4) confirmed this theory, demonstrating improved dispersion behaviour of rGO in *o*-DCB, CN and CB compared with GO.
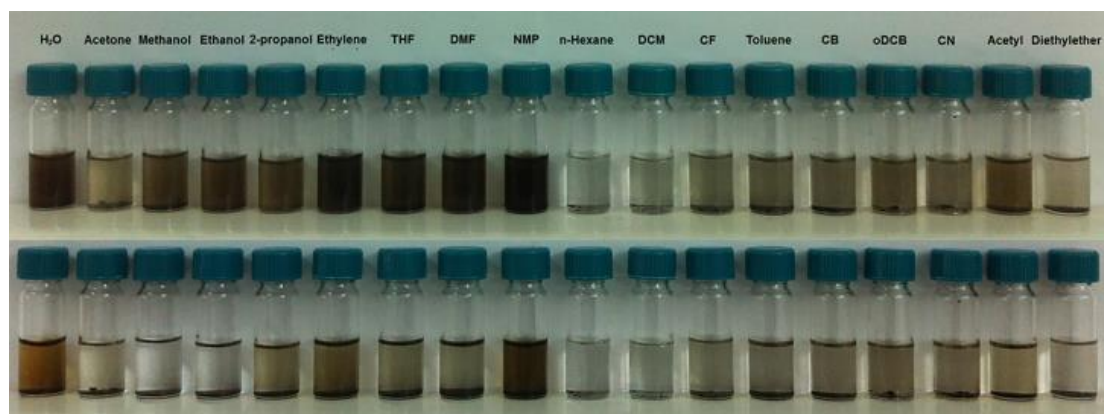
Figure 3.3. Digital picture of GO dispersions in 18 different solvents. Top: immediately after sonication. Bottom: after 24 hours
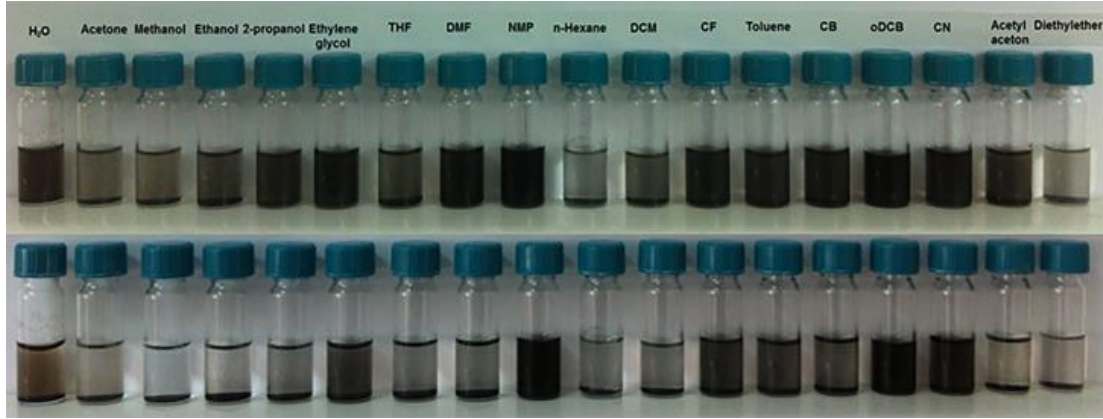
Figure 3.4. Digital picture of rGO dispersions in 18 different solvents. Top: immediately after sonication. Bottom: after 24 hours

Following the Ruoff's et al. approach, the Hansen solubility parameters were used to investigate the dispersion mechanism of GO and rGO.[15] The theory takes into account the dispersion cohesion parameter (δ_D), the polarity cohesion parameter (δ_P), and the hydrogen bonding cohesion parameter (δ_H), which are combined into the equation:

$$\delta_T{}^2 = \delta_D{}^2 + \delta_P{}^2 + \delta_H{}^2$$

to give the Hildebrand solubility parameter (δ_T).[25]

To estimate the Hansen parameters of GO and rGO, the following equation was used:

$$\langle\delta_i\rangle = \frac{\sum_{solv} C \,\delta_{i,solv}}{\sum_{solv} C}$$

where i=D, P, H or T, C is the GO and rGO solubility and $\delta_{i,solv}$ is the ith Hansen parameter in a given solvent.[16] For the studied solvents, the Hansen and Hildebrand parameters for GO were estimated to be $\langle\delta_D\rangle$ ~17.1 MPa$^{1/2}$, $\langle\delta_P\rangle$ ~10 MPa$^{1/2}$, $\langle\delta_H\rangle$ ~15.7 MPa$^{1/2}$ and $\langle\delta_T\rangle$ ~25.4 MPa$^{1/2}$. Our results are in agreement with the previously reported works, verifying that similar parameters values of the GO and the solvent lead to higher solubility.[15] The same model was used to estimate the respective parameters of rGO, which were measured to be $\langle\delta_D\rangle$ ~17.9 MPa$^{1/2}$, $\langle\delta_P\rangle$ ~7.9 MPa$^{1/2}$, $\langle\delta_H\rangle$ ~10.1 MPa$^{1/2}$ and $\langle\delta_T\rangle$ ~22 MPa$^{1/2}$.

Owing to the presence of oxygen containing groups, the GO values for polar and H-bonding components are higher than in the rGO. Similar values of the Hildebrand solubility parameter of solvent and solute is an important criterion for choosing an efficient solvent. This explains the higher solubility values of rGO in chlorinated solvents (DCM, CB, chloroform, o-DCB, CN) in contrast to the GO (**Table 3.2**).

Table 3.2. Physical properties, Hansen and Hildebrand parameters of solvents and GO, rGO solubility values for all solvents studied.

Solvents	Boiling Point (°C)	Polarity	Dipole moment	Surface tension (mN/m)	$\delta_D^\dagger$ (MPa$^{1/2}$)	$\delta_P^\dagger$ (MPa$^{1/2}$)	$\delta_H^\dagger$ (MPa$^{1/2}$)	$\delta_T^\dagger$ (MPa$^{1/2}$)	GO Solubility (µg/mL)	rGO Solubility (µg/mL)
Di water	100	Polar Protic	1.85	72.8	15.5	16	42.3	47.8	6.6	4.74
Acetone	56	Polar Aprotic	2.88	25.2	15.5	10.4	7	19.9	0.8	0.9
Methanol	65	Polar Protic	1.70	22.7	15.1	12.3	22.3	29.6	0.16	0.52
Ethanol	79	Polar Protic	1.69	22.1	15.8	8.8	19.4	26.5	0.25	0.91
2-propanol	82	Polar Protic	1.66	21.66	15.8	6.1	16.4	23.6	1.82	1.2
Ethylene glycol	197	Polar Protic	2.31	47.7	17	11	26	33	5.5	4.9
Tetrahydrofuran (THF)	66	Polar Aprotic	1.75	26.4	16.8	5.7	8	19.5	2.15	1.44
N.N-dimethylformamide (DMF)	153	Polar Aprotic	3.82	37.1	17.4	13.7	11.3	24.9	1.96	1.73
N-methyl-2-pyrrolidone (NMP)	202	Polar Aprotic	3.75	40.1	18	12.3	7.2	23	8.7	9.4
n-hexane	69	Non-polar Aprotic	0.085	18.43	14.9	0	0	14.9	0.1	0.61
Dichloromethane (DCM)	40	Polar Aprotic	1.60	26.5	18.2	6.3	6.1	20.2	0.21	1.16
Chloroform	62	Non-polar	1.02	27.5	17.8	3.1	5.7	18.9	1.3	4.6
Toluene	111	Non-polar Aprotic	0.38	28.4	18	1.4	2	18.2	1.57	4.14
Chlorobenzene (CB)	132	Non-polar	1.72	33.6	19	4.3	2	19.6	1.62	3.4
o-dichlorobenzene (o-DCB)	180	Non-polar	2.53	36.7	19.2	6.3	3.3	20.5	1.91	8.94
1-chloronaphthalene (CN)	250	Polar (weakly)	1.55	41.8	19.9	4.9	2.5	20.6	1.8	8.1
Acetylaceton	139	Polar	3.03	31.2	16.1	11.2	6.2	20.6	1.5	1.02
Diethyl ether	34	Non-polar Aprotic	1.15	17	14.5	2.9	5.1	15.6	0.72	0.4

†Taken from Hansen, C. M. Hansen Solubility Parameters: A User's Handbook; 2nd ed.; CRC Press: Hoboken, 2007

The long-term stability was examined by leaving the suspensions undisturbed for three weeks (**Figure 3.5**). The results clearly displayed that GO retained its excellent solubility in NMP, while there was a slight increase in precipitation of GO in DMF, water and ethylene glycol. It is worth mentioning that the GO showed low but stable dispersibility in non-polar solvents, like toluene, chlorobenzene and o-DCB. Similar to GO, rGO gave very good dispersions in NMP, water and ethyleneglycol, which implies that oxygen-containing functional groups are still present at defect sites. Thus, the relatively stable aqueous solutions of GO and rGO can be attributed to the electrostatic repulsion due to the negatively charged GO and rGO sheets, when dispersed in water.[26] Furthermore, rGO presented greater interaction with non-polar solvents (chloroform, toluene, chlorobenzene) than GO, but only in o-DCB and CN retained its solubility solutions.
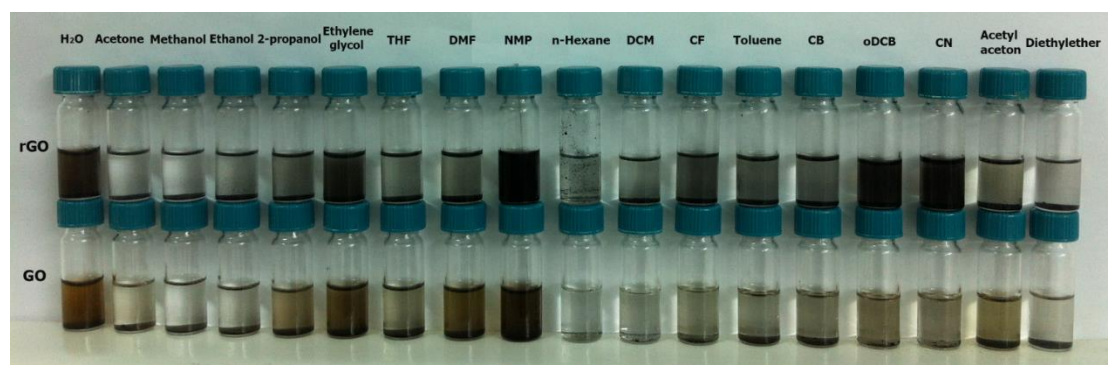
Figure 3.5. Digital picture of GO and rGO dispersions after 2 weeks, showing the long-term stability of different solutions.

3.4 Conclusions

To summarize, we have demonstrated the dispersion behaviour of GO and rGO in eighteen solvents. The Hansen and Hildebrand parameters of GO and for the first time, of rGO, were estimated verifying that efficient solvents are those with similar to the two nanomaterials solubility parameters. The knowledge of these parameters allows both the identification of new solvents for large-scale graphene ink production as well as the prediction of how to dissolve GO and rGO in mixtures of different solvents, none of which can dissolve the nanomaterials by itself.

Solutions of GO in NMP, ethylene glycol and water presented significant long-term stability with solubility values reaching ~8.7 µg/mL for NMP. The dispersion behaviour of GO changed after its reduction, presenting better interaction with solvents like o-DCB (~9 µgmL^{-1}) and CN (~8.1 µgmL^{-1}). The results can be critical in expanding the applications of graphene and its derivatives in a wide variety of applications including the fabrication of graphene-polymer-based composites for further improvement of electrical devices efficiency.

REFERENCES

1 A.K. Geim, K.S. Novoselov, *Nat Mater*, **2007**, 6, 183–191, DOI:10.1038/nmat1849.

2 M.D. Stoller , S J. Park , Y.W. Zhu , J.H. An , R.S. Ruoff , *Nano Lett.*, **2008**, 8, 3498-3502, DOI: 10.1021/nl802558y.

3 C.H. Lu, H.H. Yang, C.L. Zhu, X. Chen, G.N. Chen, *Angewandte Chemie Int. Ed.*, **2009**, 48, 4785-4787, DOI: 10.1002/anie.200901479.

4 E. Kymakis, K. Savva, M.M. Stylianakis, C. Fotakis, E. Stratakis, *Advanced Functional Materials*, **2013**, 23, 2742-2749, DOI: 10.1002/adfm.201202713.

5 S. Bae , H. Kim , Y. Lee , X. Xu, J.-S. Park, Y. Zheng, J. Balakrishnan , T. Lei , H. R. Kim , Y. I. Song , Y.-J. Kim , K. S. Kim, B. Özyilmaz, J.-H. Ahn, B. H. Hong, S. Iijima, *Nat. Nanotech.*, **2010**, 5, 574-578, DOI:10.1038/nnano.2010.132.

6 A. Dato, V. Radmilovic, Z. Lee, J. Phillips, M. Frenklach, *Nano Lett.* **2008**, 8, 2012−2016, DOI: 10.1021/nl8011566.

7 L. Rodríguez-Pérez, M.A. Herranz, N. Martín, *Chem. Commun.*, **2013**, 49, 3721-3735, DOI: 10.1039/C3CC38950B.

8 U. Khan, H. Porwal, A. O'Neill, K. Nawaz, P. May, J.N. Coleman, *Langmuir*, **2011**, 27, 9077−9082, DOI: 10.1021/la201797h.

9 J.I. Paredes, S.V. Rodil, A.M. Alonso, J.M.D. Tascon, *Langmuir*, **2008**, 24, 10560-10564, DOI: 10.1021/la801744a.

10 S. Stankovich, D.A. Dikin, R.D. Piner, K.A. Kohlhaas, A. Kleinhammes, Y. Jia, Y. Wu, S.T. Nguyen, R.S. Ruoff, *Carbon*, **2007**, 45, 1558-1565, DOI: 10.1016/j.carbon.2007.02.034.

11 S. Park, R.S. Ruoff, *Nat. Nanotechnol.*, **2009**, 4, 217-224, DOI:10.1038/nnano.2009.58.

12 I.K. Moon, J. Lee, R.S. Ruoff, H. Lee, *Nat. Commun.*, **2010**, 1, 73-79, DOI: 10.1038/srep01929.

13 H. Feng, R. Cheng, X. Zhao, X. Duan, J. Li, *Nat. Commun.*, 2013, 4, 1539-1546, DOI:10.1038/ncomms2555.

14 S. Eigler, C. Dotzer, A. Hirsch, *Carbon*, **2012**, 50, 3666-3673 DOI:10.1016/j.carbon.2012.03.039.

15 S. Park, J.H. An, I.W. Jung, R.D. Piner, S.J. An, X.S. Li, A. Velamakanni, R.S. Ruoff, *Nano Letters*, **2009**, 9, 1593-1597, DOI: 10.1021/nl803798y.

16 Y. Hernandez, M. Lotya, D.R. Shane, D. Bergin, J.N. Coleman, *Langmuir*, 2010, 26, 3208-3213, DOI: 10.1021/la903188a.

17 F. Torrisi, T. Hasan, W. Wu, Z. Sun, A. Lombardo, T. S. Kulmala, G-W. Hsieh, S. Jung, F. Bonaccorso, P.J. Paul, D. Chu, and A. C. Ferrari, *ACS Nano*, **2012**, 6, 2992–3006, DOI: 10.1021/nn2044609.

18 H.L. Poh, F. Sanek, A. Ambrosi, G. Zhao, Z. Sofer, M. Pumera, *Nanoscale*, **2012**, 4, 3515-3522.

19 H.A. Becerril, J. Mao, Z. Liu, R.M. Stoltenberg, Z. Bao, Y. Chen, *ACS Nano*, **2008**, 2(3), 463-70.

20 Y.Y. Wang, Z.H. Ni, T. Yu, Z.X. Shen, H.M. Wang, *J. Phys. Chem. C*, 2008, 112, 10637-10640, DOI: 10.1021/jp8008404.

21 S. Thakur, N. Karak, *Carbon*, **2012**, 50, 5331-5339, DOI:10.1016/j.carbon.2012.07.023.

22 S. Villar-Rodil, J.I. Paredes, A. Martínez-Alonso, J.M.D. Tascón, *J. Mater. Chem.*, **2009**, 19, 3591–3593, DOI: 10.1039/B904935E.

23 Y. Hernandez, V. Nicolosi, M. Lotya, F.M. Blighe, Z.Y. Sun, S. De, I.T. McGovern, B. Holland, M. Byrne, Y.K. Gun'ko, J.J. Boland, P. Niraj, G. Duesberg, S. Krishnamurthy, R. Goodhue, J. Hutchison, V. Scardaci, A.C. Ferrari, J.N. Coleman, *Nat. Nanotechnol.*, **2008**, 3, 563-568, DOI:10.1038/nnano.2008.215.

24 S.R. Wang, Y. Zhang, N. Abidi, L. Cabrales, L., *Langmuir*, **2009**, 25, 11078-11081, DOI: 10.1021/la901402f.

25 Hansen, C. M. Hansen Solubility Parameters: A User's Handbook; 2nd ed.; CRC Press: Hoboken, **2007**.

26 D. Li, M.B. Muller, S. Gilje, R.B. Kaner, G.G. Wallace, *Nat. Nanotechnol.*, **2008**, 3, 101-105, DOI:10.1038/nnano.2007.451.

Chapter 4

Reduced graphene oxide micromesh electrodes for large area, flexible organic photovoltaic devices

Abstract: A laser-based patterning technique, compatible with flexible, temperature-sensitive substrates, for the production of large area reduced graphene oxide micromesh (rGOMM) electrodes is presented. The mesh patterning can be accurately controlled in order to significantly enhance the electrode transparency with a subsequent slight increase in the sheet resistance and therefore improve the trade-off between transparency and conductivity of rGO layers. In particular, rGO films with an initial transparency of ~20% were patterned, resulting in rGOMMs films with a ~59% transmittance and a sheet resistance of ~565 Ωsq^{-1}, that is significantly lower than the resistance of ~780 Ωsq^{-1}, exhibited by the pristine rGO films at the same transparency. As a proof-of-concept application, rGOMMs were used as the transparent electrodes in flexible organic photovoltaic (OPV) devices, achieving power conversion efficiency (PCE) of 3.05%, the highest ever reported for flexible OPV device incorporating solution processed graphene-based electrodes. The controllable and highly reproducible laser induced patterning of rGO hold enormous promise for both rigid and flexible large scale organic electronic devices, eliminating the lag between graphene-based and indium tin oxide (ITO) electrodes, while providing conductivity and transparency tunability for next generation flexible electronics.

Keywords: Solution processed graphene, Transparent conductive electrode, Laser pattering, Tuning optoelectrical properties, Flexible, large area organic photovoltaics

4.1 Introduction

OPVs is a promising technology for future low cost energy supply due to its ability to employ flexible substrates enabling futuristic applications and mass production technologies such as r2r manufacturing.[1,2,3] Being the first layer of an OPV device that comes in contact with the light, the TCE is a vital determining factor to the device PCE. Recently, OPV devices with efficiencies above 10% were certified, with their operation lifetimes exceeding industrially interesting levels.[4,5] ITO is currently the dominant material used as TCE in rigid optoelectronic devices owing to its high transparency, T_r, in the visible spectrum and its good conductivity.[6] However, considering the employment of OPVs in everyday applications, the electrodes should be inexpensive, lightweight and highly elastic in order to conserve their electrical properties under high stresses. In this context, ITO suffers from considerable limitations. Firstly, it is expensive due to both the scarcity of indium reserves and the sputter deposition line expenses and secondly is not flexible, since its polycrystalline microstructure is brittle and cracks when the layer is bent or stretched repeatedly.[7] On top of that, indium is known to diffuse through the photoactive layer, leading to significant deterioration of the photovoltaic performance.[8,9,10] Therefore, the progress of flexible OPVs is much slower due to the lack of a flexible transparent and high conductive electrode; a r2r compatible substitutive material for ITO with a similar performance, but lower cost is highly desired.

Solution processed carbon nanotubes,[11,12] metallic nanowires[13] and conductive polymers[14] have been utilized as the TCE in organic electronic devices. However, they exhibit relatively high surface roughness or large sheet resistance, R_s, thus reducing the reproducibility rate of the devices.

Ever since the isolation of free standing graphene in 2004,[15] graphene research has experienced a phenomenal growth. Graphene can be produced by several techniques, including micromechanical exfoliation of graphite,[16] sonication-induced exfoliation,[17] thermal- or plasma-enhanced CVD deposition from a carbon feedstock gas,[18] laser-induced exfoliation,[19] and carbon nanotubes unzipping by either laser[20] or chemical treatment.[21]

Graphene exceptional electronic, optical and mechanical properties make it highly attractive, believed to be the next wonder material for optoelectronics

and thus triggering the application of graphene-based materials in the different layers of photovoltaic devices.[22,23,24,25] In particular, the enhanced electrical conductivity, combined with its high transparency in visible and near-infrared spectra,[26] emerged graphene as an ideal low cost ITO substitute.

CVD has been reported as the most successful approach to produce highly transparent and low R_s graphene electrodes.[27] Nonetheless, the grown graphene films have to be transferred onto a target substrate through a complicated process, increasing the manufacturing cost. An alternative low cost approach compatible with r2r mass production is the chemical exfoliation of GO either by ultrasonic dispersion or rapid thermal expansion followed by reduction with proper chemical[28] or photo-assisted routes.[29] The rGO can be easily produced in bulk quantities as graphene ink,[30] taking advantage of its improved soluble character in common solvents.[31] In this context, there was an extensive research effort on the utilization of rGO as the TCE in OPVs.[32,33,34] Nonetheless, the recorded PCEs remain low (~1.0%), mainly due to the low T_r (70%) and high R_s of the rGO films (~1 kΩsq^{-1}), compared to the highly commercialized ITO (90%, 15 Ωsq^{-1}). In the same context, our group has recently demonstrated an efficient laser-based reduction method for fabricating flexible conductive and transparent graphene films that can be spin casted on temperature sensitive substrates. The femtosecond laser treated rGO (LrGO) films with 70% T_r and R_s of 1.6 kΩsq^{-1} were integrated in polymer-fullerene photovoltaic cells, as the TCE leading to an efficiency of 1.1%.[35] Therefore, it is evident that pristine rGO films cannot compete with ITO, due to their extremely high R_s (>1 kΩsq^{-1}) for high transparency values.

One of the most eye catching strategies for increasing the transparency of a TCE material is the employment of a mesh structure with periodic lines, as applied in copper[36] and silver[37] network mats. Their R_s and transparency can be controlled by varying the grid width, spacing, and thickness.[38] In this way, the transparency of the mesh film can be significantly increased compared with the pristine film, while the R_s alternation is minimal; the nanowires network can conduct current even with the presence of large empty spaces. In this context, various patterning techniques were developed, such as lithography with block copolymer,[39] ion beam,[40] plasma etching,[41,42] template method[43] and chemical etching.[44] Most recently, rGO meshes fabricated using standard

photolithography and O_2 plasma methods were utilized as the TCE in OPVs,[45,46] while laser induced patterning of GO[47] has been reported for energy storage[48] and memory applications.[49] However in both cases, the employment of a mask aligner and the additional process step of the photoresist removal by O_2 plasma, induce high cost and complexity in the device fabrication.

In contrast to photolithography patterning, femtosecond (fs) laser patterning[50] has been proposed as a versatile tool for high precision patterning on a wide range of materials[51] and in large scale.[52] The main advantage of the induced fs laser patterning is that it can be applied to temperature sensitive substrates, such as PET, without practically affecting its integrity during processing. In this work, we propose a low cost, high throughput, fully scalable and facile technique for one-step patterning of rGO films on PET or glass substrates based on fs laser irradiation. This technique which can be easily controlled over the entire illuminated area induces minimum thermal damage in the surrounding layers and more importantly is compatible to r2r production processes.[53] Furthermore, direct laser patterning has the advantage of arbitrary designability and reasonably high spatial resolution.[54] By utilizing this methodology, rGOMM are fabricated, enabling to overcome the trade-off between R_s and T_r of pristine rGO layers. The optoelectrical properties of rGO thin films are found to be directly dependent on the interplay between the periodicity and the geometrical characteristics of the mesh pattern structure. ~100 nm thick rGO films with 22.5% T_r can be patterned to form TCEs with significantly increased T_r (up to ~85%), and simultaneous tuning of the film conductivity and sheet resistance. As a proof of concept, we successfully employed the rGOMM as the TCE in small and large active area of PCDTBT:PC_{71}BM based air processed OPV device, achieving PCE values of 3.67% and 3.05% on glass and flexible substrates respectively. To the best of our knowledge, these are the highest PCEs reported for a solution-processed graphene-based TCE in OPVs. This laser-based patterning technique can be considered as a universal strategy in order to fabricate large scale graphene films with controlled electrical and optical properties for various flexible electronic device components.

4.2 Experimental section

4.2.1 Preparation of graphene oxide[55]

GO was prepared from graphite powder (Alfa Aesar. ~200 mesh) according to a modified Hummers' method. In more detail, graphite powder (0.5 g) was placed into a mixture of H_2SO_4 (40 mL, 98%) and $NaNO_3$ (0.375 g). The mixture was then stirred and cooled in an ice bath. While maintaining vigorous stirring, $KMnO_4$ (3.0 g) was then added in portions over a period of 2 h. The reaction mixture was left for 4 h in order to reach room temperature before being heated to 35°C for 30 min. It was then poured into a flask containing deionized water (50 mL) and further heated to 70°C for 15 min. The mixture was then decanted into deionized water (250 mL) and the unreacted $KMnO_4$ was removed by adding 3% H_2O_2. The reaction mixture was then allowed to settle and decanted. The graphite oxide obtained was then purified by repeated centrifugation and redispersed in deionized water until neutralized pH was achieved. Finally, the resulting GO was dried at 60°C in a vacuum oven for 48 h before use.

4.2.2 Preparation of rGO films

GO films were prepared by vacuum filtering the aqueous solutions of GO through mixed cellulose ester membranes (0.025 μm, Millipore). By either varying the filtration volume or the concentration of GO in the solution, films with varied thicknesses and thus different transparencies can be produced. In this case, the initial concentration of the GO solution used for film preparation was 5 mgL^{-1}. Aliquots of the GO solution was further diluted in water, sonicated to achieve exfoliated sheets of GO and filtrated. The GO-coated membrane was cut into the desired sizes, immersed in deionized water to be wetted and placed with the film side down onto the substrate (PET and glass) surface. The GO film was allowed to dry and adhere to the substrate at room temperature under a 1 kg weight. After 5 h the membrane was removed, leaving the GO films on the substrates, which were dried in a 60°C oven. The process is highly repeatable and the films are well adhered to glass and plastic substrates. The reduction of GO films can be performed by exposing them to Hydriodic acid

(55%)/Acetic acid (HI/AcOH) vapour.[56] In detail, the as prepared PET/GO and glass/GO films were placed on a stand inside a small desiccator that contained a mixture of HI (2.0 mL) and AcOH (5.0 mL). The desiccator was sealed and placed in an oil bath at 40°C for 24 h. The films were then washed with methanol and dried and dried at 60 °C in an oven. For the R_s improvement the prepared rGO films were subjected to additional chemical treatment, by dipping them in a HNO_3 bath for 1 h, followed by cleaning and drying the surface under nitrogen steam.[53,57]

4.2.3 Fabrication of rGO nanomesh

The rGO films were mounted on a computer controlled motorized X-Y translation stage. During the irradiation, the rGO films were scanned in two orthogonal directions (X and Y) in a fully controlled manner across a focused excimer laser beam (fluence ~ 0.4 Jcm^{-2}, beam size 0.02 mm^2, pulse width 0.5 ps, repetition rate 1 Hz, emission wavelength 248 nm). The dependence of the transparency of the rGO films with the mesh periodicity was examined by controlling the movement step of X-Y stage. As a result of laser irradiation, part of the irradiated material was ablated in order to achieve higher transparency. By increasing the number of laser pulses, greater amount of the irradiated material was removed.

4.2.4 Device fabrication and measurements

PCDTBT and $PC_{71}BM$ was purchased from Solaris Chem. PCDTBT:$PC_{71}BM$ were dissolved in 1,2-dichlorobenzene: Chlorobenzene (3:1) (o-DCB:CB) in a 1:4 (4 mg:16 mg) ratio and stirred for at least 72 h at 80°C before used. The ITO-based photovoltaic devices were fabricated on 20 mm by 15 mm ITO coated PET substrates with R_s of 100 Ωsq^{-1} (Sigma Aldrich). The rGOMM electrodes were prepared on flexible PET (Goodfellow) substrates (20 mm × 15 mm) with 90 μm thickness. The impurities were removed from the substrates through a 3-step ultrasonication cleaning process (deionized water with soap, aceton, IPA). As a buffer layer, PEDOT:PSS, purchased from Heraeus, was spin-cast from an aqueous solution on the rGOMM and ITO-coated electrodes with a layer thickness of the layer was 20 nm and 30 nm respectively , followed

by baking for 15 min at 120°C inside a nitrogen-filled glove box. The PCDTBT:PC$_{71}$BM photoactive layer was subsequently deposited by spin-coating the blend solution at 1000 rpm on top of PEDOT:PSS layer until the thickness reaches approximately 70 nm, followed by drying at 60°C for about 5 min under inert condition. Titanium suboxide (TiO$_x$), used as the electron transport layer, was prepared according to a literature method.[6] TiO$_x$ was dissolved in methanol (1:200) and then spin-coated to a thickness of approximately 10 nm (6000 rpm, 40 s) in air.[58] The samples were heated at 80 °C for 1 min in air. Lastly, 100 nm of Al was deposited through a shadow mask by thermal evaporation on the devices. The whole device fabrication occurred in ambient conditions.

The performances of the devices were measured at room temperature with an Air Mass 1.5 Global (A.M. 1.5 G) solar simulator at an intensity of 100 mW cm^{-2}. A reference monocrystaline silicon solar cell from Newport was used to calibrate the light intensity. All measurements were carried out in air immediately after device fabrication without encapsulation process.

4.3 Results and Discussion

The as prepared, using the modified Hummers' method.[55] GO was dispersed in water to form stable aqueous solutions. Vacuum filtration technique was used to deposit uniform layers of GO on top of mixed cellulose ester membrane. The thickness and the homogeneity of the GO films can be accurately controlled by simply varying either the concentration of the GO solution or the filtration volume. The prepared GO films were transferred on glass and PET substrates for further treatment. To restore the conjugated structure of graphene and improve the films conductivity, chemical reduction is performed by exposing the GO films to hydriodic acid/Acetic acid (HI/AcOH).[56] **Figure 4.1** presents the X-ray photoelectron spectroscopy (XPS) survey spectra of GO and rGO, indicating that most oxygen-containing groups are effectively removed during HI/AcOH reduction.
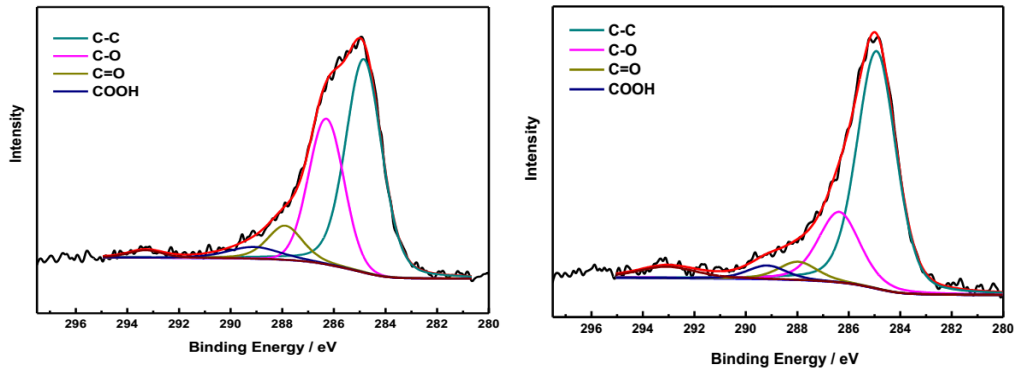
Figure 4.1. High-resolution XPS C1s spectra for a) GO and b) rGO (HI-AcOH).

HNO$_3$ has been widely used as p-type dopant to improve the conductivity and charge transfer efficiency of carbon structures.[53,57] **Figure 4.2a** presents the correlation of R$_s$ and T$_r$ at 550 nm of rGO films to their thicknesses. Both T$_r$ and R$_s$ decrease with increasing film thickness, highlighting the inherent trade-off between the two factors. The R$_s$ as a function of transmittance before and after HNO$_3$ treatment is demonstrated in **Figure 4.2b**. It is clear that R$_s$ shifts to lower values (~27% decrease) after additional treatment by dipping the prepared rGO films in a HNO$_3$ bath (65%) for 1 h.

Figure 4.2. a) Transmittance and sheet resistance of rGO thin films as a function of thickness. b) Plot of sheet resistance vs transmittance at 550 nm before and after doping with nitric acid.

The selective laser patterning of rGO on top of glass or PET (**Figure 4.3**) was performed with the delivery of UV ultra-short laser pulses (248 nm, 500 fs) with 1 Hz repetition rate. Unlike previous studies,[59] the proposed process is

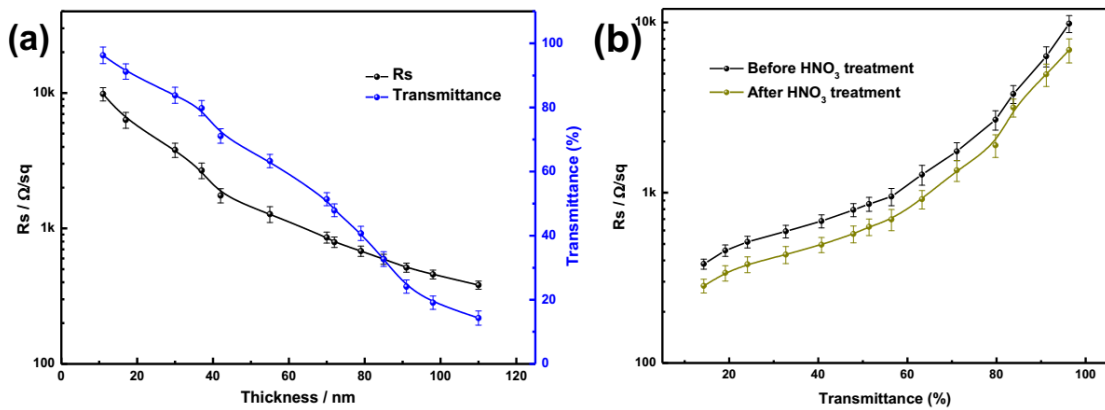one-step and does not require time-consuming and labor-intensive lithography; no complex masks, post-processing, or clean room facilities are required. Even though it is a point-by-point patterning technique, the processing rate can be significantly increased using high repetition lasers sources and multiple beam interference irradiation schemes.[60] Besides this, it is fully automated technique, allowing processing of the rGO layers according to pre-programmed patterns. In our experiments the rGO mesh periodicity, the number of pulses per pit, as well as the neck width of the mesh could be readily controlled.
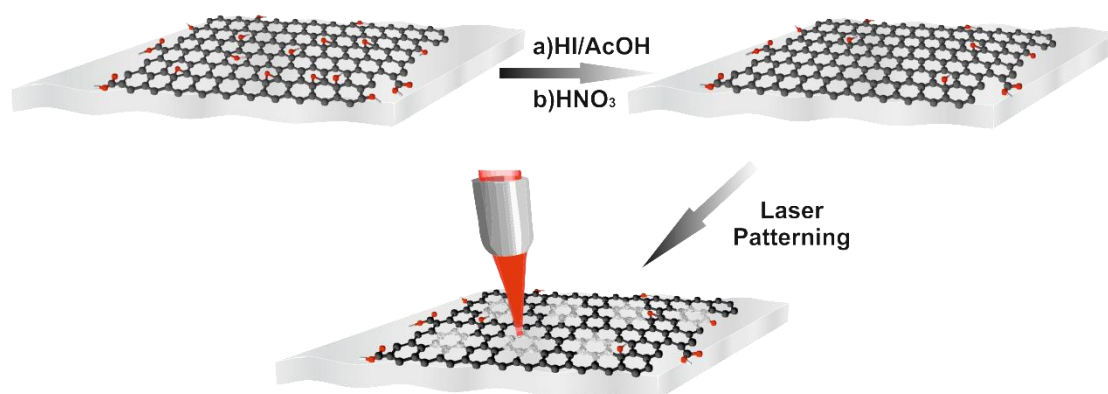
Figure 4.3. Schematic illustration of the rGO mesh electrodes preparation.

The physical processes (**Figure 4.4**) that follow fs laser-matter interactions are various and occur in different timescales. Specifically the laser pulse energy is initially absorbed by the electrons and is transferred to the lattice over a picosecond timescale. Within a few nanoseconds a shock wave is propagating away from the electron plasma. On the microsecond timescale the thermal energy diffuses out of the focal volume. The heat generation can be finely controlled by several factors including layer absorption properties, laser power, number of pulses per spot and beam profile. For a certain beam and above a minimum laser energy value, single-shot ablation can be observed that causes permanent structural changes. In our case, the excimer laser beam used had a rectangular intensity profile and its energy per pulse was adjusted with the aid of a half-wave plate. Besides this, the focusing optics defined the focal volume and thus the mesh pattern size (the latter is also defined by the number of laser pulses)[61] and its symmetry.[62] It was observed that, the minimum laser fluence required to partially remove rGO was 386 mJcm^{-2}; this fluence was

enough to attain a strong optical contrast between the processed and non-processed area, observed by optical microscopy. Upon increasing the laser pulse energy or the number of pulses per irradiating spot (exposure time), the irradiance is increased and consequently the ablated depth.
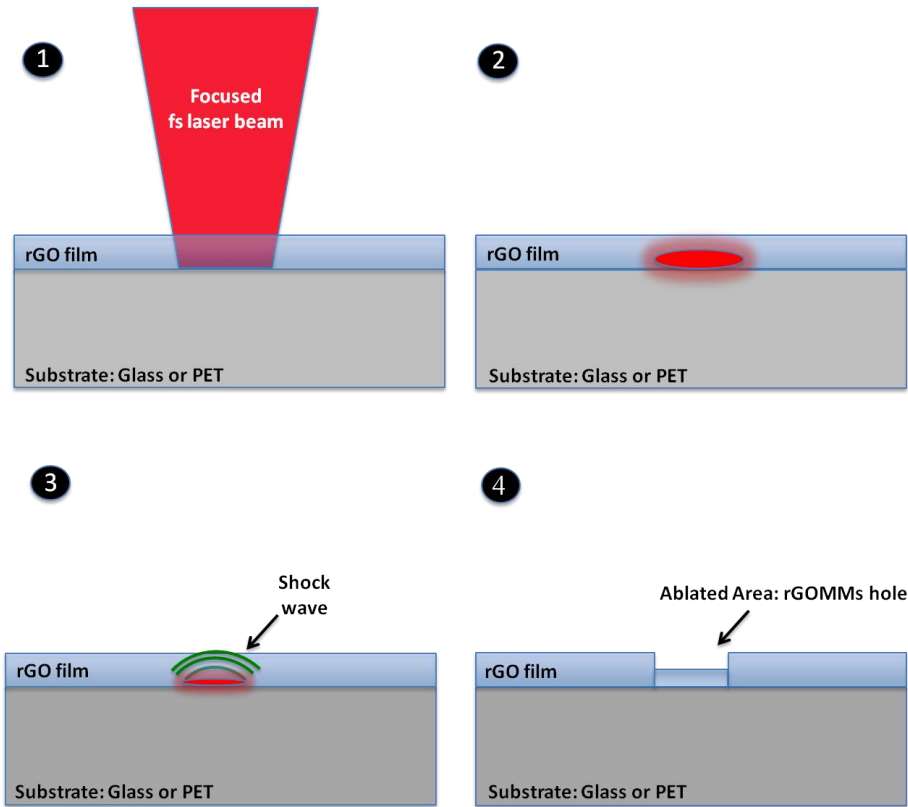
Figure 4.4. Cross section schematic of rGO film partially ablation 1) Irradiation with an UV focused fs laser pulse, 2) Absorption of the laser pulse energy 3) Due to sample heating a shock wave is generating and 4) ablates the film layer.

It is found that the ablation or pit depth is a key factor that determines the transparency and sheet resistance of laser patterned rGO layers. Besides this, the number of fs laser pulses needed to achieve the optimum trade-off between T_r and R_s is determined by the rGO layer thickness (initial T_r) and the substrate over which the film has been deposited. As Kymakis et al. previously demonstrated, the primary advantage of utilizing fs laser irradiation lies in the ability of in-situ controlled epidermal treatment giving rise to minimum induced thermal effect on the supporting substrate.[61] This, in-turn, enables for selective removal of the rGO material without practically affecting the integrity, even of thermally sensitive substrates underneath. It further allows the progressive

removal of rGO upon using a series of pulses. This is in contrast to our experimental observation that the use of longer pulse duration gives rise to, uncontrolled, explosive ablation of the thin layer, causing the merge of neighbouring mesh features, as well as thermal distortion of flexible substrate due to heat the accumulation effects. Both effects were found to be detrimental to the conductivity of the treated rGO layers.
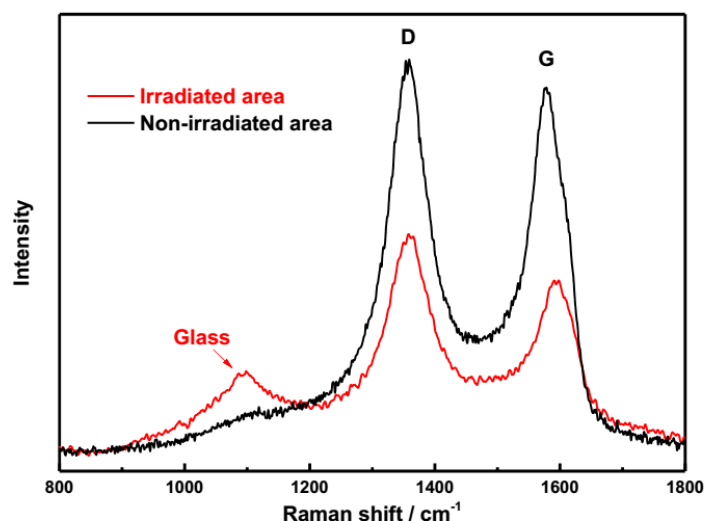
Figure 4.5 Raman spectra of rGO irradiated (red line) and non-irradiated areas (black line). In the case of irradiated areas the laser ablation of rGO in some areas is so intense that the glass substrate peak appears.

The effectiveness of laser patterning has been examined on the frame of the composition and surface morphology differences between the pristine and irradiated areas. The former were investigated through Raman spectroscopy, whereas the latter were examined by AFM. The progressive material removal induced upon increasing the number of irradiation pulses, N, is demonstrated by the Raman spectra of the pristine and laser patterned regions of the rGO mesh on glass, using N=2 and N=3 laser pulses of the threshold fluence respectively (**Figure 4.5**). The appearance of the D (1359 cm^{-1}) and G (1578 cm^{-1}) peaks in the irradiated area for N=2 but with decreased intensity, demonstrates the partial etching of rGO from the irradiated areas. At the same time a Raman peak at 1045 cm^{-1} corresponding to the glass substrate becomes more pronounced. On the contrary, for N=3 the rGO peaks disappear, indicating the complete removal of the rGO layer. AFM was employed to

115

observe the difference in the surface morphology of irradiated and non-irradiated areas on the rGO films. **Figurec 4.6** demonstrates a quite homogeneous and smooth surface for the non-irradiated area, with a root-mean-square (rms) roughness value of 1.59 nm. Following laser treatment with N=2, the rms roughness was increased to 6.99 nm due to the abrupt ablation process.
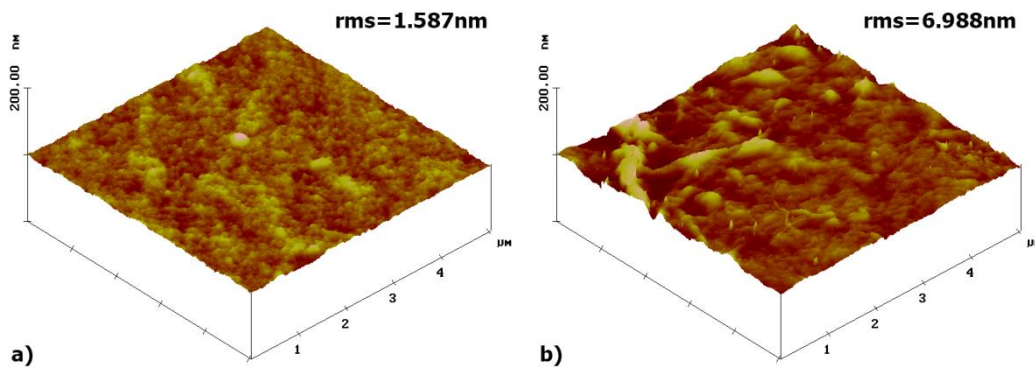
Figure 4.6. AFM images of a) non-irradiated and b) irradiated area in rGO film showing that roughness is increased after laser ablation.

Figure 4.7 presents scanning electron microscopy (SEM) images of the laser generated rGO mesh patterns obtained upon irradiation with N=2 at the threshold fluence. The bright spots in the illumination area reveal the partial ablation of the rGO layer, which is in agreement with the respective Raman spectra. In addition, the observed mesh pattern spatially shape variations are mainly due to small laser pulse energy fluctuations. Regarding the optimum neck width of the mesh, it should be as small as possible in order to reduce the losses due to light shadowing effects on the one hand and to retain the sheet conductivity on the other.
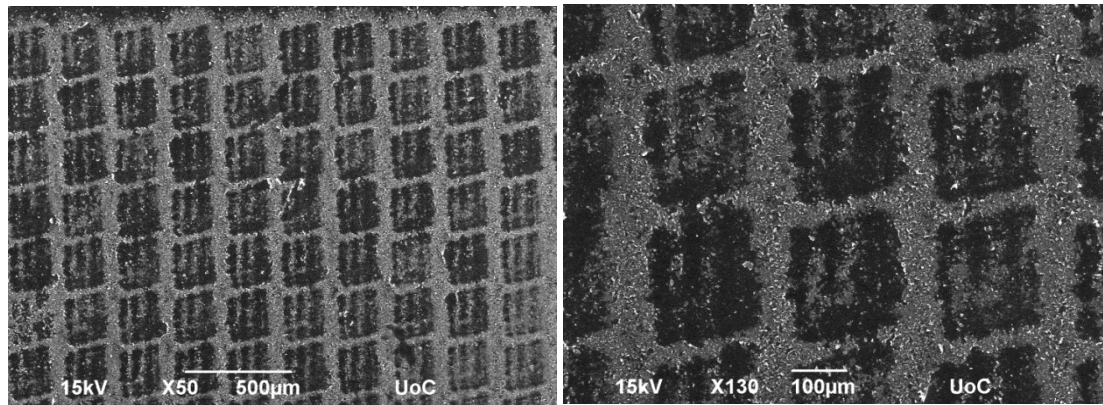
Figure 4.7. SEM images of the laser induced mesh patterns. The samples has been irradiated with N=2 fs pulses of 386 mJcm^{-2} fluence. The laser generated mesh has a period of 250 μm and the transparency has increased by ~48%.

One of the key challenges in rGO microelectronic devices applications is to tune the relation of T_r and R_s in a controllable manner.[63] The attractiveness of the technique proposed here is that it permits such fine tuning via variation of the irradiation dose (energy, number of pulses) and/or the periodicity and thus the neck width of the mesh. For instance, **Figures 4.8a-d** demonstrate the progressive increase of T_r upon variation of the periodicity, D, of the rGOMMs pattern using the threshold fluence. Although the initial T_r of the rGO layer was ~20% it was significantly improved to ~85% for D~213 μm (**Figure 4.8d**). At the same time, as shown in **Figure 4.8e**, the layer conductance slightly decreases, which is highly desirable for TCE applications. It should be noted here that, regardless of the substrate used, the lowest conductance changes can be only achieved provided that a continuous rGO film is realized after the laser patterning process, i.e. without complete removal of the irradiated areas.

The cost effectiveness of the presented laser patterning technique can be supported by the following: (a) it does not require any strict operational conditions or complex facilities, compared to other techniques like e-beam and ion beam lithography,[64] (b) it provides high flexibility for arbitrary graphene oxide patterning since it is noncontact and computer driven, (c) it is maskless in contrast to other patterning techniques,[65] (d) the use of fs laser pulses make it compatible with flexible, low cost substrates, (e) it is a one-step and not time-consuming process, (f) it is operated under open air and room temperature conditions, and (g) the fabrication setup is simple and easily controllable.

Finally, the laser-assisted maskless patterning is easily reproducible since its key parameters, laser irradiance and micromesh periodicity, can be controlled with high precision.
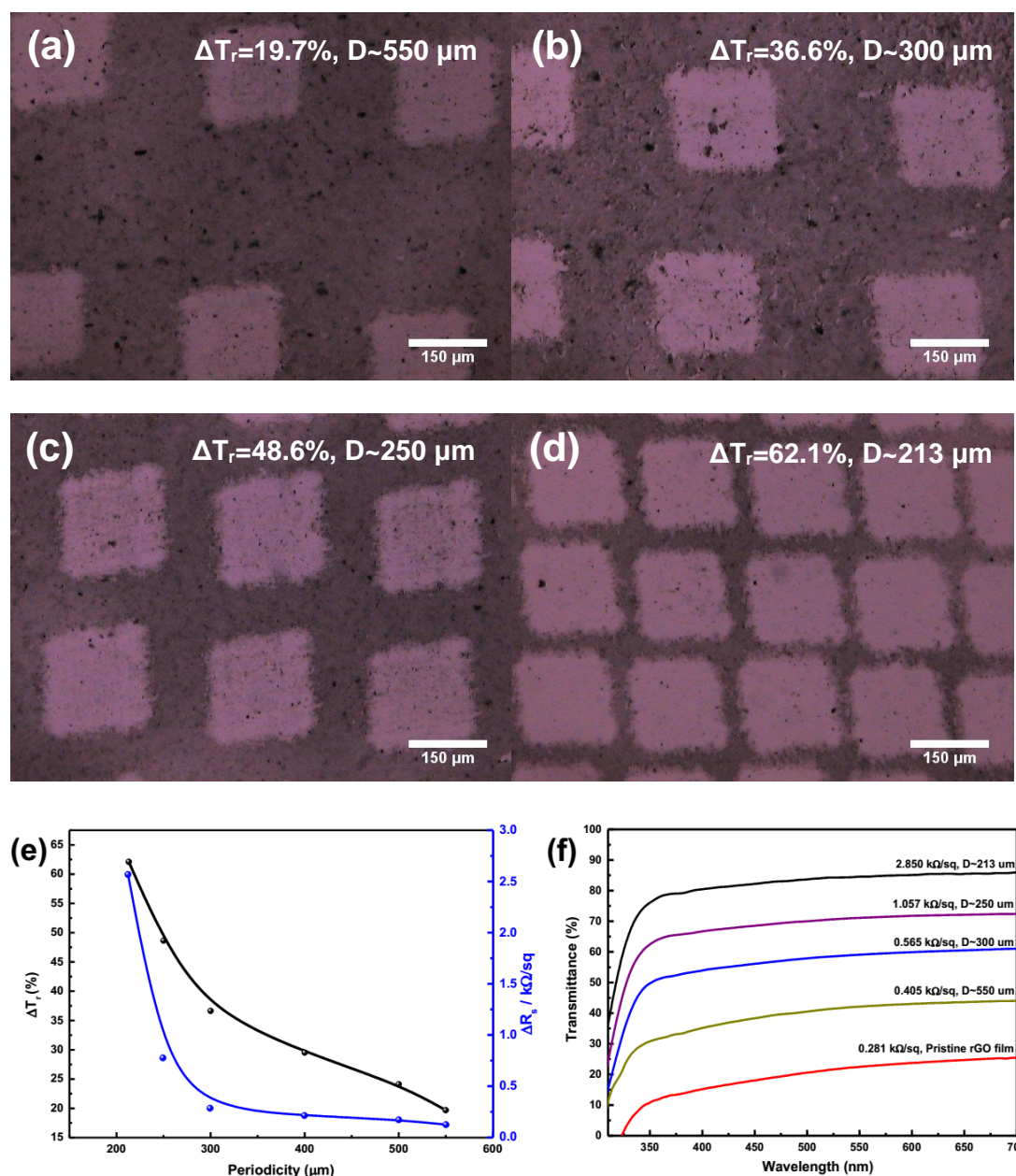
Figure 4.8 Optical microscopy images of laser-generated rGOMMs demonstrating the effect of the mesh periodicity on the film transmittance. Transparency was increased by a) ΔT_r=19.7%, b) ΔT_r=36.6%, c) ΔT_r=48.6%, d) ΔT_r=62.1% with ~550 µm, ~300 µm, ~250 µm and ~213 µm periodicity respectively. e) Transmittance difference at 550 nm (ΔT_r) and sheet resistance difference (ΔR_s) as a function of the periodicity (D) of the laser-induced rGOMM. The starting values for the pristine rGO layer were T_r 22.5% and R_s~281 Ωsq^{-1}. f) Optical transmittance spectra of rGOMMs with different periodicities, demonstrating also the R_s values of the rGO film after the laser patterning.

118

Compared with previously established patterning techniques, the presented laser-based method exhibits unique advantages. It is a one-step method, since no grid-like patterning masks,[66] or any further transfer steps, are required. In addition, there is no need of any photoresistive material[67] or prepatterned elastomeric stamps,[68] while the use of fs laser pulses allows the pattering of microsize holes on top of flexible, temperature sensitive, and low cost materials. Finally, its operation can be performed under ambient and it is fully automated, since all the patterning parameters-mesh period and laser parameters-are precisely controlled by a specially designed software. The main disadvantage of the proposed laser technique is related with the finer mesh dimensions attainable, which are optical diffraction-limited. As a result, the technique can provide micrometer- or at most submicrometer-sized patterns, contrary to nanosized features that can be achieved by other competitive methods.[39]

As a proof of the potential application of the proposed method for the fabrication of high performance transparent electrodes, we applied the rGOMM layers as the bottom TCE layer in flexible OPV devices, aiming to identify the optimum combination of T_r and R_s leading to the best PCE. For this purpose we have used the rGOMM meshes demonstrated in **Figures 4.8e** and **4.8f**. Devices were fabricated on PET substrates and the performance of OPV devices with PCDTBT:PC$_{71}$BM photoactive blends deposited on rGOMMs was compared with those deposited on ITO. The OPV devices structure employed is schematically presented in **Figure 4.9a**, with holes collected in the TCE electrode and electrons in the Al metal electrode. **Figure 4.9b** presents the illuminated J-V characteristics for the best performed OPV device incorporating rGOMM as TCE, compared with the control ITO-based one, while **Table 4.1** summarizes the averaged photovoltaic parameters of the whole series of OPV devices measured. While, the standard deviations of all measured quantities are presented in **Figure 4.10**.
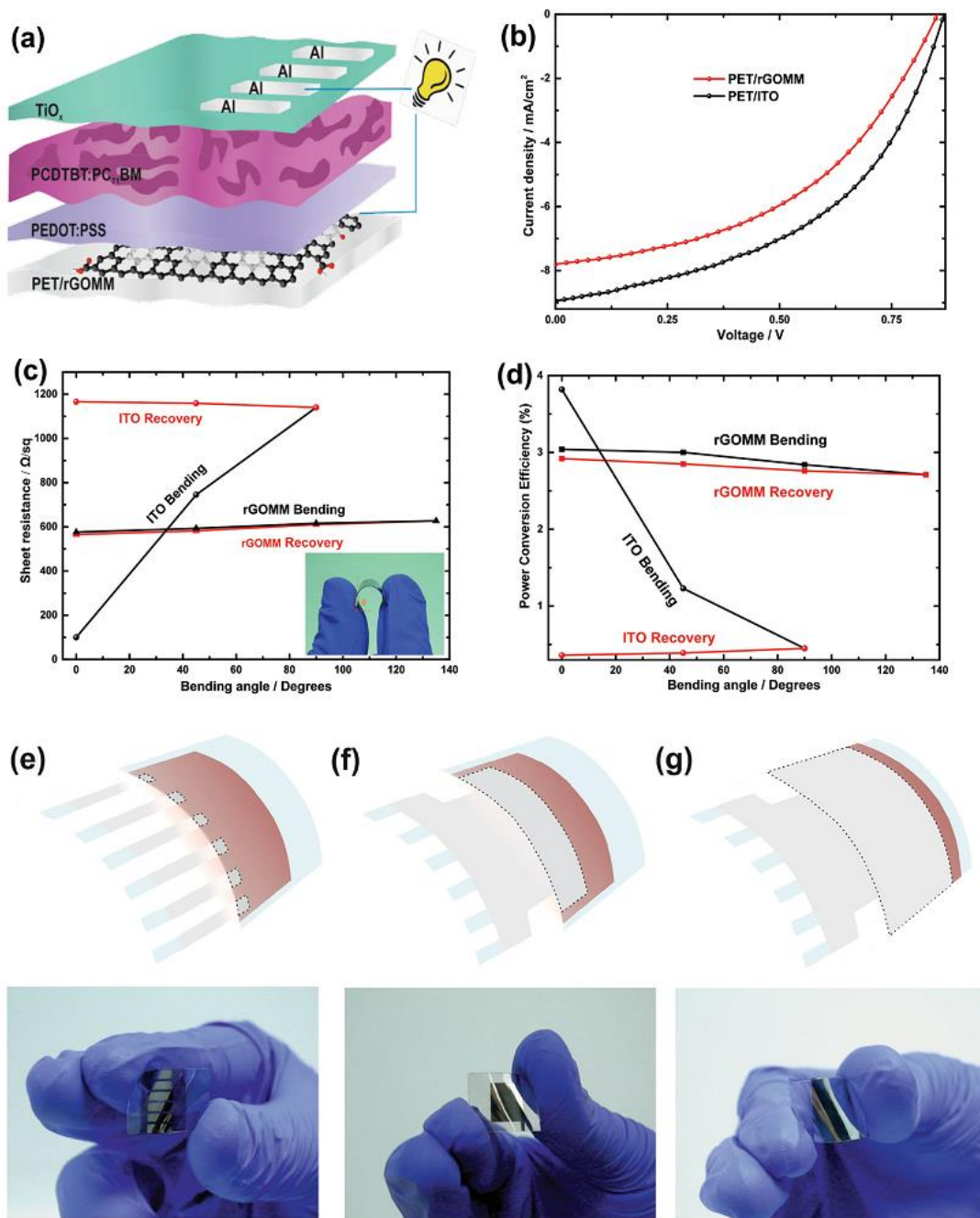
Figure 4.9. a) Schematic illustration of BHJ OPV device with the laser-induced rGOMM as TCE. b) The illuminated current-voltage (J-V) curves of the solar cells with rGOMM (red) and ITO (black) as TCE. c) Sheet resistance vs device bending angle of rGOMM- and ITO-based OPV cells. The inset photo represents a rGOMM-based device subjected to bending. d) PCE of rGOMM- and ITO-based flexible devices under and after bending at certain angles. Schematic illustration and photographs of devices exhibiting increased active areas; e) 4 mm^2, f) 50 mm^2 and g) 135 mm^2.

Table 4.1. Averaged photovoltaic parameters[*] of the solar cells incorporating rGO, rGOMMs and ITO as TCE.

PET/rGOMM (T, R_s)	J_{sc} (mA/cm^2)	V_{oc} (mV)	FF (%)	PCE (%)
22.5%, 281 Ω/sq (pristine rGO film)	4.51	837	47.2	1.78
42.2%, 405 Ω/sq	6.52	843	46.4	2.55
59.1%, 565 Ω/sq	7.81	848	45.9	3.05
71.1%, 1057 Ω/sq	3.72	840	42.3	1.32
84.6%, 2850 Ω/sq	2.37	832	37.6	0.74
PET/ITO	8.93	864	49.5	3.82

[*]Average photovoltaic characteristics for OPV devices with different TCEs. To account for experimental errors, the reported averages for each case are taken for 10 identical devices, consisting of six cells each.
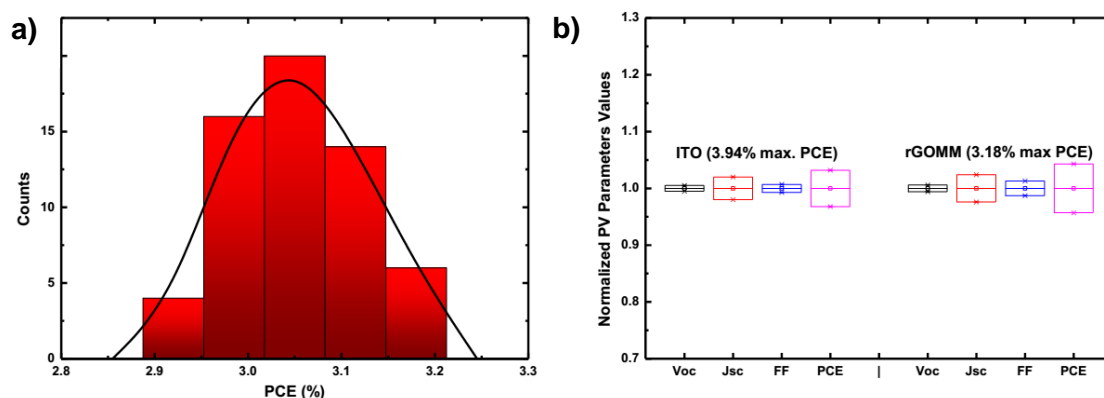
Figure 4.10. a) Histogram of average efficiencies for 60 cells. b) Standard deviations for the photovoltaic parameters values.

It can be clearly observed that the open circuit voltage (V_{oc}) remains almost constant for all devices, which is reasonable, considering that its value is derived by the energy levels offset between the HOMO of PCDTBT and LUMO of PC$_{71}$BM. On the other hand, a tradeoff between the photocurrent (J_{sc}) and fill factor (FF) is observed. In particular, the J_{sc} is increased as the T_r of the rGOMM layer becomes higher, up to the limit that R_s remains in the same order of magnitude compared to the starting material. The FF is mainly affected from the R_s of TCE, thus is constantly decreased as the mesh structure becomes

denser. As can also be seen by the 3D graph of **Figure 4.11**, the optimum photovoltaic parameters for the rGOMM-based devices were extracted for $T_r \approx 59.1\%$ and $R_s \approx 565$ Ωsq^{-1}, with a resulting PCE of 3.05%. Furthermore, OPV devices incorporating rGO films with different thicknesses and therefore different T and R_s pairs were also fabricated and characterized (**Table 4.2**). In this way, a direct comparison of the PV performance of the optimum devices, utilizing unpatterned rGO and patterned rGOMM films, can take place.

Table 4.2. Averaged photovoltaic parameters of the solar cells incorporating different (T, R_s) rGO and rGOMM as TCE.

	(T, R_s)	J_{sc} (mA/cm^2)	V_{oc} (mV)	FF (%)	PCE (%)
rGO	22.5%, 281 Ω/sq	4.51	837	47.2	1.78
	60.3%, 819 Ω/sq	5.92	834	42.5	2.12
	69.7%, 1235 Ω/sq	6.73	835	40.1	2.25
rGOMM	59.1%, 565 Ω/sq	7.81	848	45.9	3.05

It can be clearly seen that the performance of the rGOMM-based devices is superior to the devices, which utilize rGO films, mainly due to the difference in R_s, which has a strong effect on the devices FF. In particular, the unpatterned rGO-based device exhibits a maximum PCE of 2.12%, while the rGOMM-based device exhibits a PCE of 3.05%. Also, the device which utilizes rGO as the TCE with approximately the same transparency as the rGOMM film (60.3% and 59.1%, respectively) exhibits an even lower PCE of 2.12%, due to the significant difference in the R_s of the TCE. Therefore, the laser patterning technique clearly enables us to improve the tradeoff between T_r and R_s of the rGO films, since patterned films with the same transparency as the unpatterned rGO films exhibit much higher conductivity values.
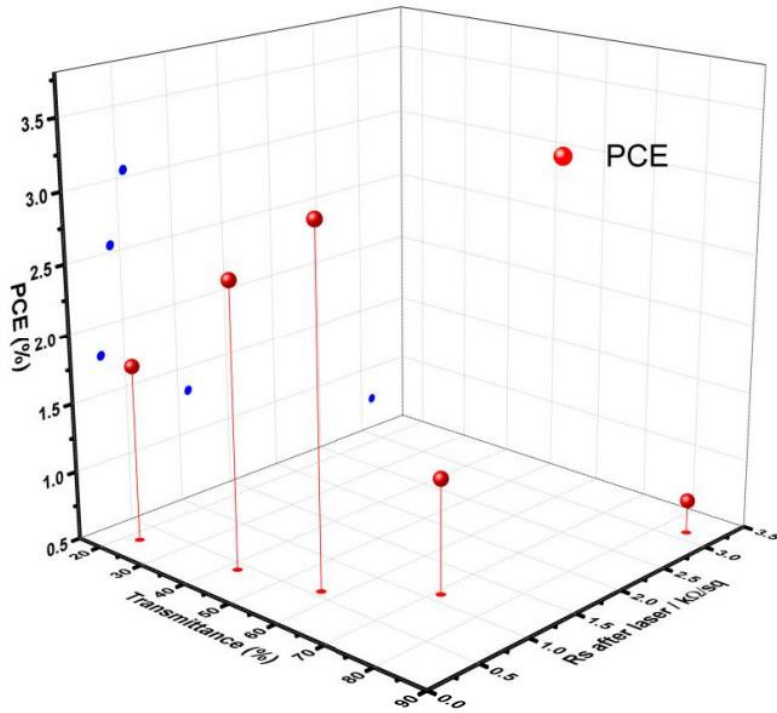
Figure 4.11. 3D graph for the variation in power conversion efficiency in flexible devices with respect to the transmittance and sheet resistance of the produced rGOMMs films.

Table 4.3. Summary of the averaged photovoltaic parameters for optimum rGOMM and ITO electrodes with different device active area.

	Device Area (mm^2)	J_{sc} (mA/cm^2)	V_{oc} (mV)	FF (%)	PCE (%)
rGOMM	4	7.81	848	45.9	3.05
	50	5.44	846	38.9	1.79 (41.1%↓)
	135	3.87	831	33.2	1.07 (64.9%↓)
ITO	4	8.93	864	49.5	3.82
	50	6.31	862	42.5	2.31 (39.5%↓)
	135	4.48	848	36.3	1.38 (63.2%↓)

Another important benefit of the flexible rGOMM electrode on PET substrate is its high durability under extreme bending conditions and its ability to retain its electrical properties. This capability is very important for every flexible electronic device. Indeed, as shown in **Figure 4.9c** the R_s change upon 90°bending is

negligible, as it does not change more than 8%, while the overall change is ≈11% up to a bending angle of 135°. Following the reverse route, the R_s returns near to its initial value, showing a slight increase (less than 2%). This implies that no appreciable change in the TCE structure occurs during bending. This excellent flexibility is advantageous over the conventional ITO, which showed a rapid increase in its R_s value under identical bending conditions (also shown in **Figure 4.9c**). This behavior can be attributed to the well-reported cracking effect of ITO that gives rise to a catastrophic electrical failure.[69]

An important motivation for using solution-processed rGOMM electrodes is to realize highly flexible OPVs that can be used for compact roll-type solar modules. A similar behavior with above findings is observed in **Figure 4.9d** where the photovoltaic performance with respect to the device bending history is presented. Indeed, the rGOMM-based device almost retains its initial photovoltaic performance after extreme bending conditions, a result that is highly desired for flexible organic electronic applications. On the contrary, ITO-based devices showed a remarkable different behavior; the device could operate only up to 45° bending, but with a significant deterioration in its performance, while it is completely destroyed after 90° bending, without the ability of retaining its initial PCE values.

Another important issue investigated in this work was whether our proposed method can be applicable to large area OPV devices (**Figure 4.9e-g**). This is crucial for the future development of this technology and its subsequent upscaling from single cells to solar modules. For this purpose, rGOMM- and ITO-based devices with increasing active area were fabricated and tested. As it can be clearly observed in **Table 4.3**, the deterioration in the photovoltaic performance measured for both rGOMM- and ITO-based devices was practically the same, i.e. for 135 mm^2 active area PCE reduction measured was 63.2% for ITO and 64.9% for rGOMM, respectively. It can be concluded that the proposed electrode patterning method can be effectively applied to large area photovoltaic cells without compromising the photovoltaic efficiency.

The contribution of our work in the graphene-based TCE technology reported to date is illustrated in **Figure 4.12**. The figure indicates the PCE values of OPV devices fabricated on solution-processed graphene-based TCE reported in the literature, together with the corresponding values of rGOMM-based devices

reported here. Devices on rigid as well as flexible substrates are taken into account. It is more than clear that the proposed laser patterning technique produces high quality rGOMM electrodes and could potentially mitigate the lag between graphene-based and ITO-based TCEs.
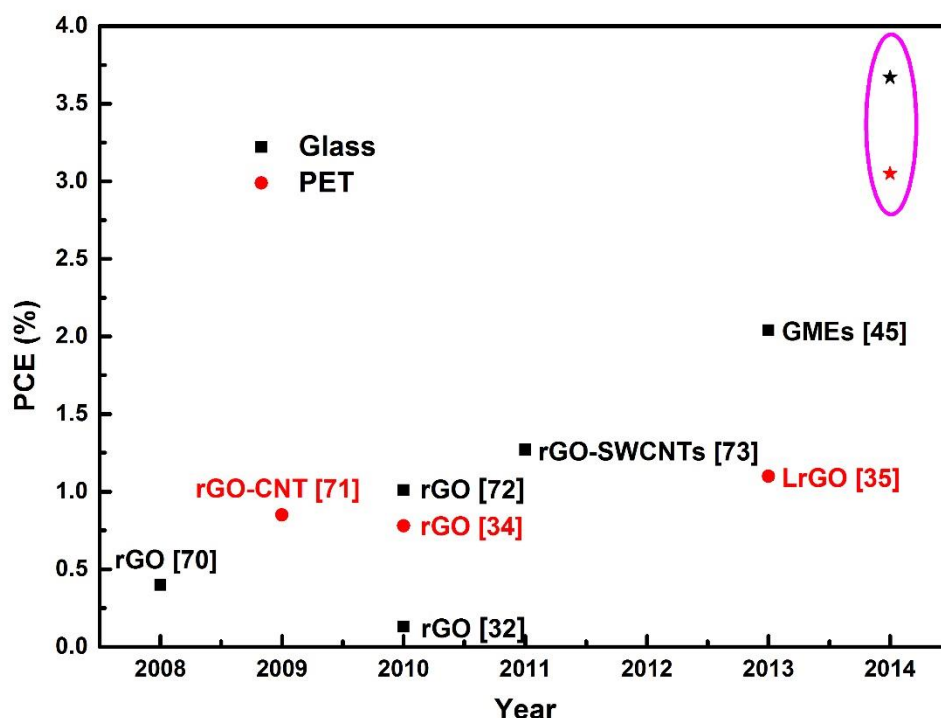
Figure 4.12. OPVs performance of OPV cells based on solution processed graphene-based TCEs reported to date in the literature.[58,60,61,45,70,71,72,73] Black squares stand for rigid devices, while red circles for devices on flexible substrates. Stars illustrate the contribution of this work to the PCE improvement.

4.4 Conclusion

In conclusion, the successful development of a direct fs laser writing technique to fabricated pattern rGO mesh TCEs has been demonstrated. The technique enables the accurate control of rGO micromesh geometrical features on top of rigid (glass), as well as flexible (PET) substrate. As a result, the conductivity and transparency of the treated rGO films can be finely tuned and tailored for the specific application. Using this technique, it is shown that rGO electrode transparency can be readily changed from ≈20% to up to ≈85%, with only a slight increase in the respective R_s value. To demonstrate the application

and the potential applicability of the proposed technique in the field of flexible transparent electronics, OPV devices that host the laser-induced rGOMMs films as the TCE electrode were fabricated, exhibiting superior performance compared to the ones that incorporate pristine rGO TCEs. The devices displayed a PCE of 3.05%, which is the highest reported to date for flexible OPV devices incorporating solution-processed graphene-based electrodes. Due to their chemical stability, mechanical flexibility, high transparency, and conductivity, along with their scalable production through solution processing and subsequent laser patterning, rGOMMS are excellent potential candidates for a wide range of new applications with tunable optoelectrical properties, including flexible electronic OPVs, perovskite solar cells, organic light emitting diodes, and photosensors, as well as traditional electronic devices based on rigid substrates.

REFERENCES

[1] N. S. Sariciftci, L. Smilowitz, A. J. Heeger, F. Wudl, *Science* **1992**, *258*, 1474.

[2] G. Yu, J. Ga, J. C. Hummelen, F. Wudl, A. J. Heeger, *Science* **1995**, *270*, 1789.

[3] G. Li, R. Zhu, Y. Yang, *Nat. Photonics* **2012**, *6*, 153.

[4] M. A. Green, K. Emery, Y. Hishikawa, W. Warta, E. D. Dunlop, *Prog. Photovolt: Res. Appl.* **2014**, *22*, 701.

[5] M. C. Scharber, N. S. Sariciftci, Prog Polym Sci. **2013**, 38, 1929.

[6] S. H. Park, A. Roy, S. Beaupre, S. Cho, N. Coates, J. S. Moon, D. Moses, M. Leclerc, K. Lee, A. J. Heeger, *Nat. Photonics* **2010**, *3*, 297.

[7] D. S. Hecht, L. Hu, G. Irvin, *Adv. Mater.* **2011**, *23*, 1482.

[8] a) J. B. Wu, M. Agrawal, H. A. Becerril, Z. N. Bao, Z. F. Liu, Y. S. Chen, P. Peumans, *ACS Nano* **2010**, *4*, 43 b) W. J. da Silva, H. P. Kim, A. R. b. M. Yusoff, J. Jang, *Nanoscale* **2013**, *5*, 9324.

[9] B. Paci, G. Kakavelakis, A. Generosi, G. Wright, C. Ferrero, D. Konios, E. Stratakis, E. Kymakis, *Submitted.*

[10] B. Paci, D. Bailo, V. Albertini, J. Wright, C. Ferrero, G. D. Spyropoulos, E. Stratakis, E. Kymakis, *Advanced Materials* **2013,** *25*, 4760.

[11] T. P. Tyler, R. E. Brock, H. J. Karmel, T. J. Marks, M. C. Hersam, *Adv. Energy Mater.* **2011**, *1*, 785.

[12] E. Kymakis, E. Stratakis, E. Koudoumas, C. Fotakis, *IEEE Trans. Electron Devices* **2011**, *58*, 860.

[13] S. De, T. M. Higgins, P. E. Lyons, E. M. Doherty, P. N. Nirmalraj, W. J. Blau, J. J. Boland, J. N. Coleman, *ACS Nano* **2009**, *3*, 1767.

[14] S. I. Na, S. S. Kim, J. Jo, D. Y. Kim, *Adv. Mater.* **2008**, *20*, 4061.

[15] K. S. Novoselov, A. K. Geim, S. V. Morozov, D. Jiang, Y. Zhang, S. V. Dubonos, I. V. Grigorieva, A. A. Firsov, *Science* **2004**, *306*, 666.

[16] K. S. Novoselov, D. Jiang, F. Schedin, T. J. Booth, V. V. Khotkevich, S. V. Morozov, A. K. Geim, *Proc. Natl. Acad. Sci.* U.S.A. **2005**, 102, 10451

[17] Y. Hernandez, V. Nicolosi, M. Lotya, F. M. Blighe, Z. Sun, S. De, I. T. McGovern, B. Holland, M. Byrne, Y. K. Gun'Ko, J. J. Boland, P. Niraj, G. Duesberg, S. Krishnamurthy, R. Goodhue, J. Hutchison, V. Scardaci, A. C. Ferrari, J. N. Coleman, *Nat. Nanotechnol.* **2008**, 3, 563 .

[18] a) X. Li, Y. Zhu, W. Cai, M. Borysiak, B. Han, D. Chen, R. D. Piner, L. Colombo, R. S. Ruoff, *Nano Lett.* 2009, 9, 4359 ; b) K. S. Kim, Y. Zhao, H. Jang, S. Y. Lee, J. M. Kim, K. S. Kim, J. H. Ahn, P. Kim, J. Y. Choi, B. H. Hong, *Nature* **2009**, 457, 706 .

[19] a) P. Kumar, RSC Adv. 2013, 3, 11987 ; b) U. Maitra, H. Matte, P. Kumar, C. N. R. Rao, *Chimia* **2012**, 66, 941 .

[20] P. Kumar, L. S. Panchakarla, C. N. R. Rao, *Nanoscale* **2011**, 3, 2127 .

[21] D. V. Kosynkin, A. L. Higginbotham, A. Sinitskii, J. R. Lomeda, A. Dimiev, B. K. Price, J. M. Tour, *Nature* **2009**, 458, 872 .

[22] M. M. Stylianakis, M. Sygletou, K. Savva, G. Kakavalakis, E. Kymakis, E. Stratakis, *Adv. Opt. Mater.* **2014**, DOI:10.1002/adom.201400450

[23] E. Stratakis, K. Savva, D. Konios, C. Petridis, E. Kymakis, *Nanoscale* **2014**, 6, 6925.

[24] Z. Yin, J. Zhu, Q. He, X. Cao, C. Tan, H. Chen, Q. Yan, H. Zhang, *Adv. Energy Mater.* **2014**, *4*, 1300574.

[25] G. Kakavelakis, D. Konios, E. Stratakis, E. Kymakis, *Chemistry of Materials* **2014**, *26*, 5988.

[26] F. Bonaccorso, Z. Sun, T. Hasan, A. C. Ferrari, *Nat. Photonics* **2010**, *4*, 611.

27 B. Bae, H. Kim, Y. Lee, X. F. Xu, J. S. Park, Y. Zheng, J. Balakrishnan, T. Lei, H. R. Kim, Y. I. Song, Y. J. Kim, K. S. Kim, B. Ozyilmaz, J. H. Ahn, B. H. Hong, S. Iijima, *Nat. Nanotechnol.* **2010**, *5*, 574.

28 S. Park, J. An, J. R. Potts, A. Velamakanni, S. Murali, R. S. Ruoff, *Carbon* **2011**, *49*, 3019.

29 a) P. Kumar, K. S. Subrahmanyam, C. N. R. Rao, *Intl. Jour. Nanosci.* **2011**, *10*, 559; b) P. Kumar, B. Das, B. Chitara, K. S. Subrahmanyam, K. Gopalakrishnan, S. B. Krupanidhi, C. N. R. Rao, *Macromol. Chem. Phys.* **2012**, *213*, 1146 c) E. Kymakis, C. Petridis, T. D. Anthopoulos, E. Stratakis, *IEEE Journal of Selected Topics in Quantum Electronics* **2014**, *20*, art. no. 6573325.

30 F. Bonaccorso, A. Lombardo, T. Hasan, Z. Sun, L. Colombo, A. C. Ferrari, *Mater. Today* **2012***, 15,* 564.

31 D. Konios, M. M. Stylianakis, E. Stratakis, E. Kymakis, *J. Col. Interf. Sci.* **2014**, *430*, 108.

32 Y. Xu, G. Long, L. Huang, Y. Huang, X. Wan, Y. Ma, Y. Chen, *Carbon* **2010**, *48*, 3308.

33 E. Kymakis, E. Stratakis, M. M. Stylianakis, E. Koudoumas, C. Fotakis, *Thin Solid Films* **2011**, *520*, 1238.

34 Z. Yin, S. Sun, T. Salim, S. Wu, X. Huang, Q. He, Y. M. Lam, H. Zhang, *ACS Nano* **2010**, *4*, 5263.

35 E. Kymakis, K. Savva, M.M. Stylianakis, C. Fotakis, E. Stratakis, *Adv. Funct. Mater*. **2013**, *23*, 2742.

36 H. Wu, L. Hu, M. W. Rowell, D. Kong, J. J. Cha, J. R. McDonough, J. Zhu, Y. Yang, M. D. McGehee, Y. Cui, *Nano Letters* **2010**, *10*, 4242.

37 J. van de Groep, P. Spinelli, A. Polman, *Nano Letters* **2012**, *12*, 3138.

38 J. Zou, H. L. Yip, S. K. Hau, A. K. Y. Jen, *Appl. Phys. Lett.* **2010**, *96*, 203301.

39 J. Bai, X. Zhong, S. Jiang, Y. Huang, X. Duan, X., *Nature Nanotech.* **2010**, *5*, 190.

40 N. E. Sosa, J. Liu, C. Chen, T. J. Marks, M. C. Hersam, *Adv. Mater.* **2009**, *21*, 721.

41 L. Zhang, S. Diao, Y. Nie, K. Yan, N. Liu, B. Dai, Q. Xie, A. Reina, J. Kong, Z. Liu, *J. Am. Chem. Soc.* **2011**, *133*, 2706.

42 Z. Zeng, X. Huang, Z. Yin, H. Li, Y. Chen, Q. Zhang, J. Ma, F. Boey, H. Zhang, *Adv. Mater.* **2012**, *24*, 4138.

43 Z. L. Wang, D. Xu, H. G. Wang, Z. Wu, X. B. Zhang, *ACS Nano* **2013**, *7*, 2422.

44 Y. Zhu, S. Murali, M. D. Stoller, K. J. Ganesh, W. Cai, P. J. Ferreira, A. Pirkle, R. M. Wallace, K. A. Cychosz, M. Thommes, D. Su, E. A. Stach, R. S. Ruoff, R. S., *Science* **2011**, *332*, 1537.

45 Q. Zhang, X. Wan, F. Xing, L. Huang, G. Long, N. Yi, W. Ni, Z. Liu, J. Tian, Y. Chen, *Nano Research* **2013**, *6*, 478.

46 A. R. b. M. Yusoff, S. J. Lee, F. K. Shneider, W. J. da Silva, J. Jang, *Adv. Energy Mater.* **2014**, *4*, 1301989.

47 P. Kumar, K. S. Subrahmanyam, C. N. R. Rao, *Mater. Exp,* **2011**, *1*, 252.

48 M. F. El-Kady , R. B. Kaner *, Nat. Commun.* **2013**, *4*, 1475 .

49 H. Tian, H.-Y. Chen, T.-L. Ren,C. Li, Q.-T. Xue, M. A. Mohammad, C. Wu, Y. Yang, H.-S P. Wong, *Nano Lett.* **2014**, *14*, 3214.

50 A. Y. Vorobyev, C. Guo, *Laser Photonics Rev.* **2013**, *7*, 385.

51 E. Stratakis, *Science of Advanced Materials* **2012**, *4*, 407.

52 B. N. Chichkov, C. Momma, S. Nolte, F. Von Alvensleben, A. Tunnermann, *Applied Physics A* **1996**, *63*, 109.

53 M. F. El-Kady, R. B. Kaner, *ACS Nano* **2014**, *8*, 8725.

54 Y. L. Zhang, Q. D. Chen, H. Xia, H. B. Sun, *Nano Today* **2010**, *5*, 435.

55 D. Li , M. B. Muller , S. Gilje , R. B. Kaner , G. G. Wallace , Nat. Nanotechnol. **2008**, 3, 101 .

56 I. K. Moon , J. Lee , R. S. Ruoff , H. Lee , **Nat. Commun. 2010**, 1, 73 .

57 S. Das , P. Sudhagar , E. Ito , D.-Y. Lee , S. Nagarajan , S. Y. Lee , W. S. Kang , W. Choi , *J. Mater. Chem.* **2012**, 22, 20490 .

58 G. Kakavelakis , E. Stratakis , E. Kymakis , *Chem. Commun.* 2014**,** 50, 5285 .

[59] S. Pang, H. N. Tsao, X. Feng, K. Mullen, *Adv. Mater.* **2009**, *21*, 3488.

[60] H. B. Jiang, Y. L. Zhang, D. D. Han, H. Xia, J. Feng, Q. D. Chen, Z. R. Hong, H. B. Sun, *Adv. Funct. Mater.* **2014**, *24*, 4595.

[61] S. M. Eaton, *Optics Express* **2005**, *13*, 4708.

[62] R. Osellane, *Journal of Optical Society of America B* **2003**, *20*, 1559.

[63] Y. C. Li, T. F. Yeh, H. C. Huang, H. Y. Chang, C. Y. Lin, L. C. Cheng, C. Y. Chang, H. Teng, S. J. Chen, *Optics Express* **2014**, *22*, 19726.

[64] J. B. Park, W. Xiong, Y. Gao, M. Qian, Z. Q. Xie, M. Mitchell, Y. S. Zhou, G. H. Han, L. Jiang, Y. F. Lu, *Appl. Phys. Lett.* **2011**, 98, 123109 .

[65] a) T. Kim, H. Kim, S. W. Kwon, Y. Kim, W. K. Park, D. H. Yoon, A.-R. Jang, H. S. Shin, K. S. Suh, W. S. Yang, Nano Lett. **2012**, 12, 743 ; b) J. W. Bai, X. Zhong, S. Jiang, Y. Huang, X. F. Duan, *Nat. Nanotechnol.* **2010**, 5, 190

[66] J. S. Oh, S. H. Kim, T. Hwang, H.-Y. Kwon, T. H. Lee, A. H. Bae, H. R. Choi, J. D. Nam, *J. Phys. Chem. C* **2013**, 113, 663 .

[67] Y.-Q. Bie, Y.-B. Zhou, Z.-M. Liao, K. Yan, S. Liu, Q. Zhao, S. Kumar, H.-C. Wu, G. S. Duesberg, G. L. W. Cross, J. Xu, H. Peng, Z. Liu, D.-P. Yu, *Adv. Mater.* **2011**, 23, 3938 .

[68] Q. He, H. G. Sudibya, Z. Yin, S. Wu, H. Li, F. Boey, W. Huang, P. Chen, H. Zhang, *ACS Nano* **2010**, 4, 3201 .

[69] M. N. Saleh, G. Lubineaou, *Solar Energy Mater. Solar Cells* **2015**, 139, 199 .

[70] J. B. Wu, H. A. Becerril, Z. N. Bao, Z. F. Liu, Y. S. Chen, P. Peumans, *Appl. Phys. Lett.* **2008**, *92*, 263302.

[71] V. C. Tung, L. M. Chen, M. J. Allen, J. K. Wassei, K. Nelson, R. B. Kaner, Y. Yang, *Nano Lett.* **2009**, *9*, 1949.

[72] J. Geng, L. Liu, S. B. Yang, S. C. Youn, D. W. Kim, J. S. Lee, J. K. Choi, H. T. Jung, *J. Phys. Chem. C* **2010**, *114*, 14433.

[73] J. H. Huang, J. H. Fang, C. C. Liu, C. W. Chu, *ACS Nano* **2011**, *5*, 6262.

Chapter 5

Improving the efficiency of organic photovoltaics by tuning the work-function of graphene oxide hole transporting layers

Abstract: A facile, fast, non-destructive and r2r compatible photochemical method for the simultaneously partial reduction and doping of graphene oxide (GO) films through ultraviolet laser irradiation in the presence of Cl_2 precursor gas is demonstrated. The photochemical chlorinated GO-Cl films were fully characterized by XPS measurement, in which the grafting of chloride to the edges and the basal plane of GO was confirmed. By tuning the laser exposure time, it is possible to control the doping and reduction levels and therefore to tailor the work function (WF) of the GO-Cl layers from 4.9 eV to a maximum value of 5.23 eV. These WF values match the HOMO level of most polymer donors employed in OPV devices. Furthermore, high efficiency PCDTBT:PC_{71}BM based OPVs with GO-Cl as the HTL were demonstrated with PCE of 6.56 % which is 17.35% and 19.48% higher than the pristine GO and PEDOT:PSS based OPVs devices respectively. The performance enhancement was attributed to more efficient hole transportation due to the energy levels matching between the GO-Cl and the polymer donor.

5.1 Introduction

OPV devices utilizing polymer:fullerene BHJs have been widely studied due to their promising advantages over their traditional inorganic Si based counterparts, including low cost fabrication on light weight, large area and flexible substrates and use of r2r mass production techniques.[1,2] Recently, the research effort has been focused to the interface engineering of OPVs and especially to the introduction of buffer layers with electron blocking properties between the BHJ active layer and the transparent ITO electrode, in order to reduce recombination and leakage of current at the photoactive layer-electrode interface.[3,4]

The highly doped PEDOT:PSS is the most regularly used HTL material for organic BHJ solar cells, because of its solution process ability, high WF, sufficient conductivity, and high optical transparency in the visible-NIR regime.[5] However, here are several drawback issues leading to OPV failure, which are directly related to the PEDOT:PSS. The acidic and hygroscopic nature of PEDOT:PSS corrodes both the ITO electrode[6] and the processing equipment[7] at elevated temperatures, and can introduce water into the active layer, degrading the performance and long-term stability of the OPV device.[8] In addition, the strong anisotropy in the conductivity of the spin coated PEDOT:PSS films originating from their lamellar structure, leads to inhomogeneous charge extraction in some locations and dead spots in others.[9] To overcome these drawbacks, several types of materials have been explored to serve as HTLs in BHJ solar cells, mainly focussing on metal oxide inorganic semiconductors.[10,11,12] However, the oxides are deposited using cost-intensive high vacuum techniques that are incompatible with low-cost solution-processable and r2r large area manufacturing of OPVs. So, it is obvious that the development of low cost and simply processable HTL materialscompatible with OPV materials and r2r techniques is urgently demanded.

In this context, solution processable carbon nanotubes[13] and graphene based materials[14] were used as the HTL. In particular, spin coated GO derivatives have been studied as promising alternatives to PEDOT:PSS, due to their optical transparency, mechanical flexibility and compatibility with r2r production.[15,16] GO is a graphene sheet modified with oxygen functional groups

in the form of epoxy and hydroxyl groups on the basal plane and various other types, such as carboxylic acid groups at the edges.[17] It can be produced by exfoliation of inexpensive graphite powders with strong oxidizing reagents.[18] The availability of reactive groups on both the basal plane and the GO sheets enables the manipulation of the size, shape and relative fraction of the sp^2 hybridized domains of GO, allowing the tailoring of its optoelectronic properties.[19,20]

However, the obtained performances are only comparable with the PEDOT:PSS based devices and not superior as would be expected due to the GO film higher transparency across the whole visible spectrum. The main barrier to higher performance enhancement is the WF of the as prepared GO film. The measured WFs are in the range of 4.7-4.9 eV[21,22] and do not match the HOMO of the most commonly used electron donor materials in state-of-the-art BHJ OPV devices, as in the PEDOT:PSS case (>5.1 eV).[23] Therefore, tuning of the GO WF with the polymer HOMO is needed. In this pathway, oxygen plasma treated and sulfated GO with increased WFs of 4.8 and 5.2 eV respectively were successfully utilized as the HTLs in OPVs.[24,25] Moreover, it was recently demonstrated that spin coated GO films can be in situ non-thermal reduced by femtosecond pulsed laser beam irradiation.[26]

In this work, a novel approach of WF tuning of GO HTLs is demonstrated, based on laser-induced doping of GO. In particular, pulsed laser irradiation of ultrathin GO films in the presence of a dopant Cl_2 precursor gas, was employed for the simultaneous reduction and doping of GO. It is shown that the laser induced chloride atoms substitute the GO defects into both the edges as well as in the plane of the GO lattice.[27] In this way, the WF of irradiated layers can be tuned as a function of the laser exposure time. This process leads to a significant increase of the photocurrent and hence of the OPV devices performance mainly due to an increase in the hole mobility of the respective devices.

5.2 Experimental section

5.2.1 Preparation of GO films

Graphite oxide was synthesized by the modified Hummers method and exfoliated to give a brown dispersion of GO under ultrasonication.[28] GO solution in ethanol (0.5 mgml^{-1}) was dropped after an oxygen plasma treatment for 2 min in order to make the ITO surface hydrophilic. The GO solution was maintained for a waiting period of 2 min and was then spun at 3000 rpm for 30 s, followed by 30 min baking at 100 °C inside a nitrogen -filled glove box. The thickness of the films was analogous to the number of spinning repetitions; a film thickness of 3.4 nm was obtained with two successive coatings.

5.2.2 Photochemical doping and reduction of GO films

The as-spun GO layers on ITO/glass substrates were subjected to irradiation by a KrF excimer laser source emitting 20 ns pulses of 248 nm at 1Hz repetition rate that was translated onto the film area. For uniform exposure of the whole sample to laser radiation, a top-flat beam profile of 20×10 mm^2 was obtained using a beam homogenizer. The whole process took place into a vacuum chamber at 50 Torr Cl_2 gas pressure maintained through a precision micro valve system. Different combinations of laser powers (P) and number of pulses (N_P) were tested in an effort to optimize the photochemical functionalization processes. In a typical experiment, the sample was irradiated at a constant P with Np = 10, 20, 30, 40, 50, 60, 120, 600 and 1200, corresponding to different photochemical reaction times.

5.2.3 Device fabrication

The photovoltaic devices reported were fabricated on 15 mm by 15 mm ITO glass substrates with a sheet resistance of 15 Ωsq^{-1}. The impurities are removed from the ITO glass through a 3-step cleaning process. GO with different thicknesses were spin casted as described previously. Next, a photoactive layer consisting of a PCDTBT:PC$_{71}$BM (1:4 wt.% ratio, 80 nm thick) blend was spin coated on the HTL from a 1:4 ratio dichlorobenzene:

chlorobenzene solution at 1000 rpm. The solution was stirred for at least 72 h at 80°C before used. Next a TiO_x electron transporting interlayer was dissolved in methanol (1:200) and then spin-coated to a thickness of approximately 10 nm (6000 rpm, 40 s). Finally, a 100 nm thick Al layer was deposited by thermal evaporation through a shadow mask to define an active area of 6 mm^2.

5.2.4 Microscopic and spectroscopic characterization

The by UV-VIS absorption spectra of the samples were recorded using a Shimadzu UV-2401 PC spectrophotometer over the wavelength range of 400-1000 nm. The morphology of the surfaces was examined by field emission scanning electron microscopy (FE-SEM; JEOL JSM-7000F) and by atomic force microscopy (AFM; Digital Instruments NanoScope IIIa). X-ray photoelectron spectroscopy (XPS) measurements were carried out in a Specs LHS-10 Ultrahigh Vacuum (UHV) system. The XPS spectra were recorded at room temperature using unmonochromatized AlKa radiation under conditions optimized for maximum signal (constant ΔE mode with pass energy of 36 eV giving a full width at half maximum (FWHM) of 0.9 eV for the Au 4f7/2 peak). The analyzed area was an ellipsoid with dimensions 2.5 x 4.5 mm^2. The XPS core level spectra were analysed using a fitting routine, which allows the decomposition of each spectrum into individual mixed Gaussian-Lorentzian components after a Shirley background subtraction. The ultraviolet photoelectron spectroscopy (UPS) spectra were obtained using HeI irradiation with hv = 21.23 eV produced by a UV source (model UVS 10/35). During UPS measurements the analyser was working at the Constant Retarding Ratio (CRR) mode, with CRR = 10. The WF was determined from the UPS spectra by subtracting their width (i.e. the energy difference between the analyzer Fermi level and the high binding energy cutoff), from the HeI excitation energy. For these measurements a bias of -12.30 V was applied to the sample in order to avoid interference of the spectrometer threshold in the UPS spectra. All the WF values obtained by UPS were calibrated with scanning kelvin probe microscopy (SKPM) measurements. The relative error is 0.02 eV.

5.3 Results and Discussion

5.3.1 Characterization of photochlorinated GO films

The photochlorinated GO (GO-Cl) was investigated by XPS,UPS, and AFM. **Figure 5.1** compares typical XPS spectra of the pristine GO and GO-Cl films. It can be clearly seen that the intensity of the O1s peak relative to that of C1s is reduced while the characteristic Cl2p, due to chloride bonds, appears after the photoclorination process. The XPS results clearly indicate that simultaneous photoreduction and Cl doping of the GO nanosheets take place. **Figures 5.1b** present in high resolution the respective C1s peaks of GO and GO-Cl, consisting of three kinds of components assigned to C-O (hydroxyl and epoxy), C=O (carbonyl), and C-(O)-O (carboxyl) functional groups.[19] Upon photochlorination, the C-O/C-C intensity ratio decreases from 1.09 to 0.60 while the Cl2p/C1s intensity ratio becomes equal to 0.17. In particular, the C1s spectrum of as-prepared GO sheets shows an additional peak at higher binding energies, corresponding to large amounts of sp^3 carbon with C-O bonds, carbonyls (C=O), and carboxylates (O-C=O).[29] **Figure 5.1c** shows the high-resolution Cl2p spectra of the GO-Cl film, confirming the Cl_2 doping in the GO lattice. The Cl2p spectra can be fitted in two non-equivalent chlorine sites from the A) 3/2 and B) 1/2 levels. The more intense peak A was close to 200 eV corresponding to Cl-C covalent bonds at the edges, while the less intense peak B at 201.7 eV corresponds to the Cl-C=O groups.[30] The above findings indicate enhancement of the doping efficiency upon increasing the number of the GO oxygen groups, suggesting that Cl-doping most likely occurs at the edges and defect sites.[31,32]
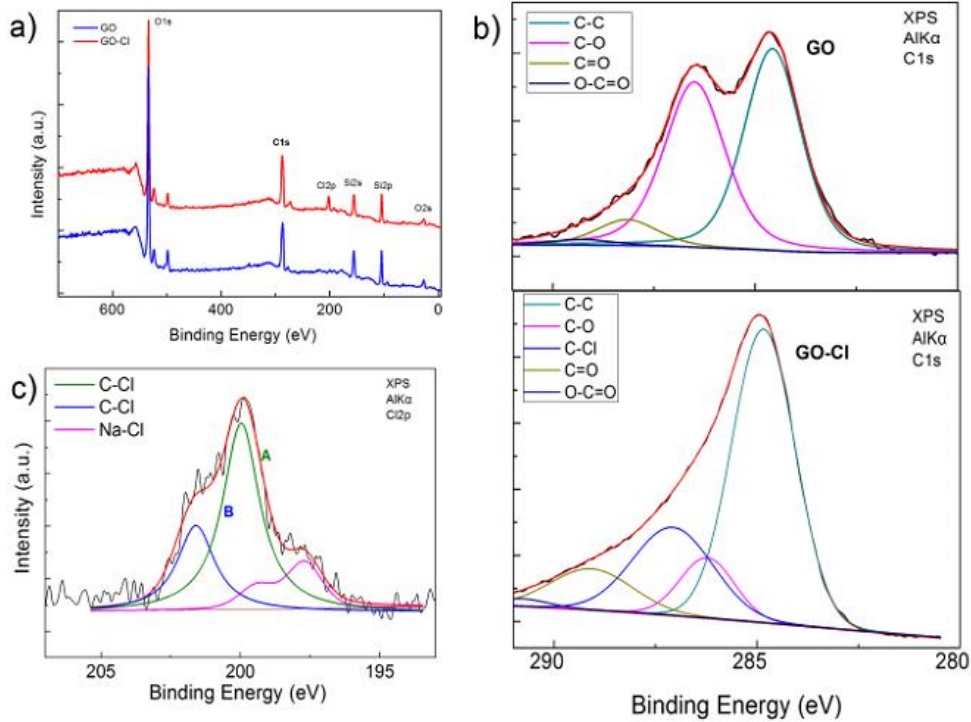
Figure 5.1. a) XPS survey spectra. b) High-resolution XPS C1s spectra. c) High-resolution Cl2p XPS of GO and GO-Cl films.

Tuning of the laser source key parameters can lead to a respective tuning of Cl_2 doping level of the GO. In particular, this can take place upon increasing the laser power (P) ranging from 10 to 50 mW or the number of pulsed (N_p) at a certain P, giving rise to a corresponding decrease of the doping level. **Figure 5.2a** shows that the I(C-C)/I(C-O) ratio, which corresponds to the GO reduction degree, increases upon increasing the N_p, while the I(Cl2p)/I(C1s) ratio, which corresponds to Cl_2 doping, decreases. The maximum introduction of Cl-groups attained was ~11.3 atom% as estimated by the ratio of the Cl2p to the C1s peak areas after considering the atomic sensitivity factors for Cl2p and C1s.The WF of the respective GO-Cl layers was determined by UPS, and SKPM for N_p values of 1-60 and are presented in **Figure 5.2b**. It was observed that the WF rises with increased exposure, and tends to saturate at 5.23 eV for N_p=60. As can be extracted (**Figure 5.2c**) from UPS measurement, this value is much higher than the respective WFs measured for GO (4.9 eV). The maximum WF is obtained at the point, which both the reduction and the doping rates start to significantly increase and decrease respectively. Therefore, as it can be also seen from the inset of **Figure 5.2b**, the WF increase is most likely due to a

synergetic effect of the chloride doping and the partial reduction processes. It is evident that laser radiation causes partial reduction of the GO sheets while at the same time chlorine molecules split into highly reactive radicals and react with the GO lattice via a free radical addition reaction. Under these conditions, tuning of the GO WF can be achieved by the formation of surface $C^{\delta+}$-$Cl^{\delta-}$ dipoles with different electronegativity (2.55 for C compared to 3.16 for Cl).
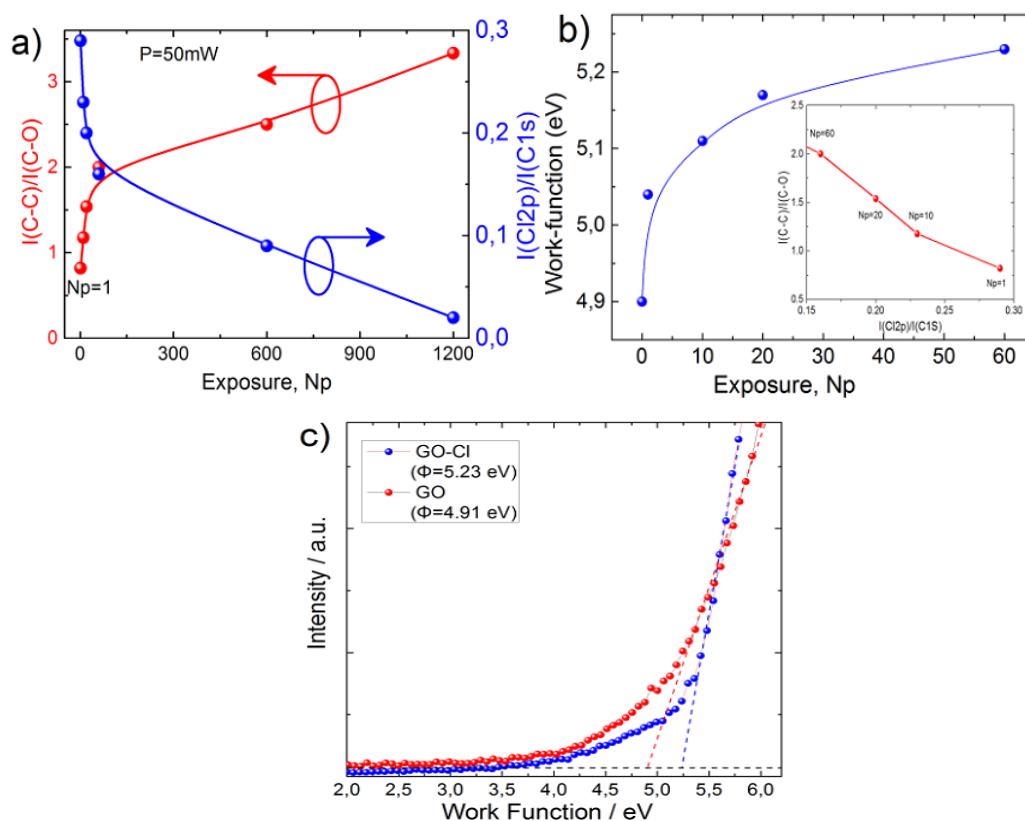
Figure 5.2. a) GO reduction and doping levels as a function of N_p. b) WF of GO-Cl films as a function of the N_p exposure. The inset shows the dependence of Cl_2 doping (I(Cl2p)/I(C1S)) with the reduction degree ((I(C-C)/I(C-O)). c) Work function of GO and GO-Cl films extracted from UPS spectra (Np=60).

As shown in **Figure 5.3a**, such dipoles can be formed by chlorine atoms in Cl-C covalent bonds at the edges and/or Cl–C=O groups located outside the graphene basal plane.[33,34] The induced polar character of C-Cl bonds is responsible for the downward shift of the Fermi level in the valence band of GO-Cl, and the subsequent increase in the WF from 4.9 eV in GO to 5.23 eV in GO-Cl (**Figure 5.3b**).[34,35] In addition, the charge rearrangement by the electron drawing towards chlorine atoms, increase the number of hole charge carriers

in the conjugated sp^2 network of GO-Cl, enhancing its p-type behavior.[36] Therefore, the strength of the out of plane dipole moment in the GO, and thus the WF can be tuned by a) the variation of the overall oxygen content, realized by partial reduction and b) the replacement of oxygen atoms with chloride ones with higher electronegativity upon doping.
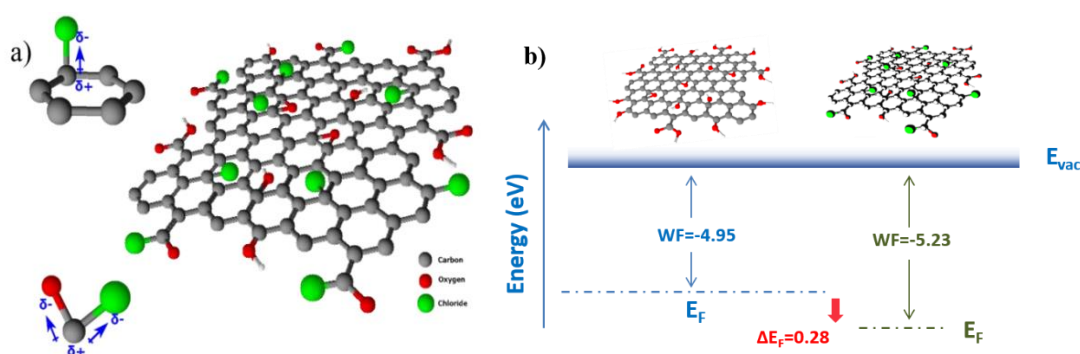
Figure 5.3. a) 3D chemical structure of the photochlorinated GO, illustrating the formation of dipoles by chlorine atoms in Cl-C covalent bonds at the edges and/or Cl-C=O groups located outside the graphene basel plane. b) Schematic energy level diagram showing the effect of polar C-Cl bonds on the WF.

5.3.2 Photovoltaic performance

To explore the effects of the photochlorination of the GO layer on device performance, OPVs with the conventional device structure glass/ITO/HTL/polymer:PC$_{71}$BM/TiO$_x$/Al, where fabricated. The HTL layers compared were PEDOT:PSS, GO and GO-Cl. The device structure and the energy level diagrams of the different materials used in the fabrication are shown in **Figure 5.4a** and **5.4b**.
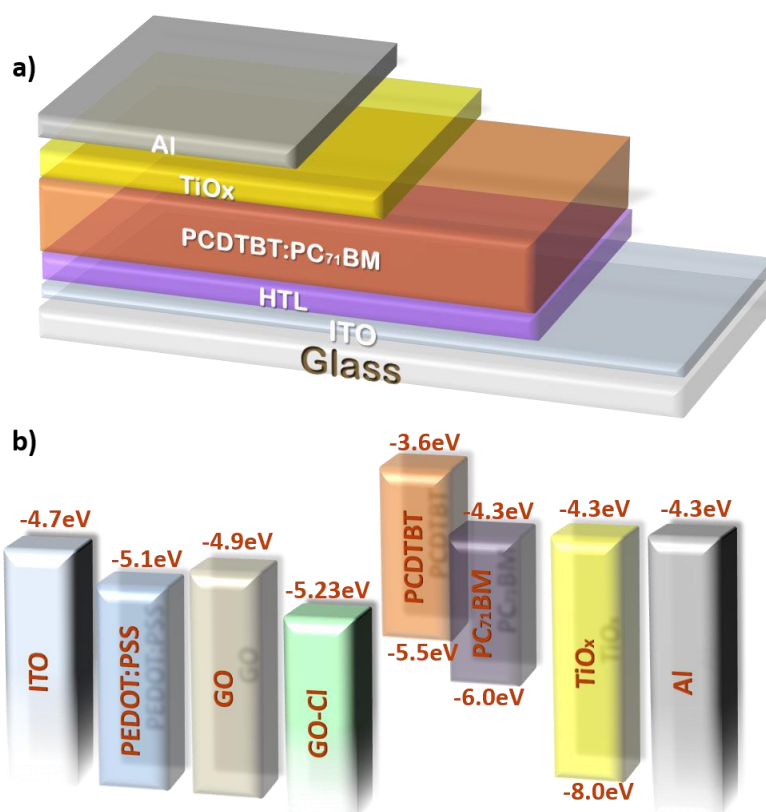
Figure 5.4. a) Schematic illustration of the BHJ OPV device with GO-Cl HTL. b) The energy level diagram depicting the relevant energy levels under flat band conditions of all materials used in the OPV cells studied and not the actual interfaces.

Before analyzing the photovoltaic characteristics, it is important to describe the functionality of the HTL during the device operation. The solar light irradiates the photoactive layer through the HTL/ITO electrode side, while the active layer absorbs photons to produce excitons. The photo-excited excitons dissociate at the polymer-fullerene interface into electrons in the LUMO of the fullerene acceptor, and holes in the HOMO of the polymer donor. Therefore, the HOMO level of the polymer donor should be ideally equal to the WF of the HTL, so that the holes can be readily transported to the ITO electrode through the HTL. In this context, OPV devices incorporating the PCDTBT donor material with HOMO of 5.3 eV were utilized, in order to examine the influence of the GO-Cl HTL WF on the photovoltaic characteristics. Reference devices incorporating the PEDOT:PSS and pristine GO as the HTL were also fabricated for comparison. It should be noted that the optimum thickness of the GO film is found to be around 3.4 nm for both GO and GO-Cl HTLs. This finding is in disparity with the first report of GO based HTLs, where the GO thin films with a

thickness of 2 nm gave the highest efficiency,[15] but in agreement with our previous studies[13] and recent studies of plasma treated GO HTLs, in which the same spinning conditions of the GO films, resulted in 1 and 3 nm thin films on mica and ITO substrates respectively.[24] This effect may also be caused by the different lateral dimensions of GO flakes employed.
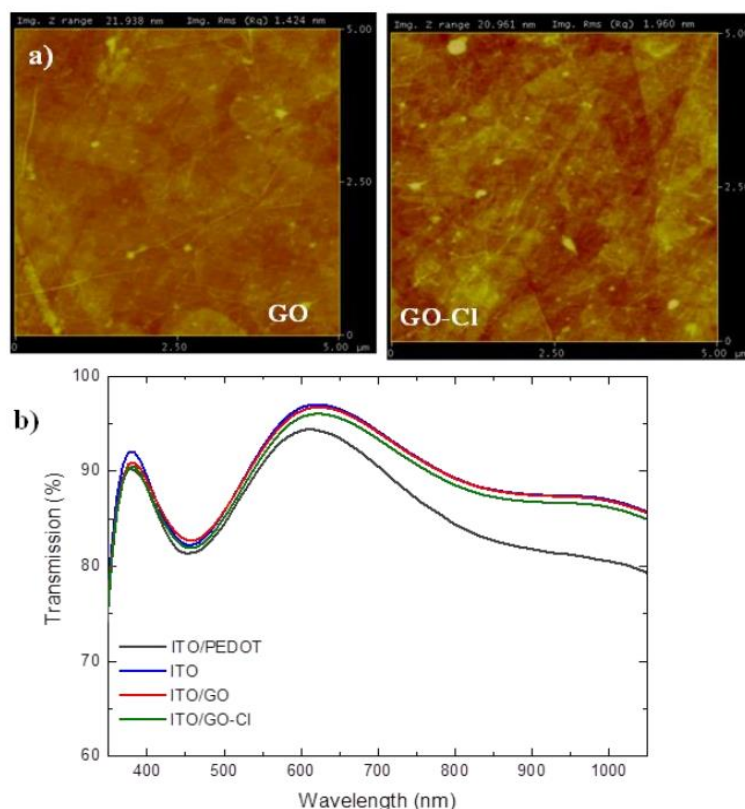
Figure 5.5. a) 5µm x 5µm AFM images of the GO (left) and the GO-Cl layer (right) with RMS roughness of 1.424 and 1.96 nm on ITO/glass substrates. b) Transmission spectra of GO and GO-Cl films spin coated on ITO/glass. The spectra of ITO glass coated with PEDTO:PSS are also shown.

Finally it is important to note that the mean roughness of both GO and GO-Cl HTLs is comparable as indicated by AFM measurements (**Figure 5.5**). This suggests that the photochlorination process does not significantly affect the HTL film morphology. **Figure 5.6** shows the typical illuminated current density-voltage (J-V) curves of the PCDTBT:PC$_{71}$BM OPV devices with PEDOT:PSS, GO and GO-Cl (prepared at different exposure times) as the HTLs. As it can be seen in the J-V curves and the summarized photovoltaic parameters in **Table 5.1**, device performance is significantly enhanced by the photochlorination of the GO film and strongly depends on the WF of the GO-Cl layer. Indeed, the

increase of the WF of GO-Cl films from 4.9 to 5.23 eV leads to a PCE of 6.56% which is 17.35% and 19.48% higher than the pristine GO and PEDOT:PSS based OPVs devices respectively. The PCE enhancement achieved via the GO film photochlorination is primarily a result of increased J_{sc}, which is proportional to the WF increase of the GO-Cl films.
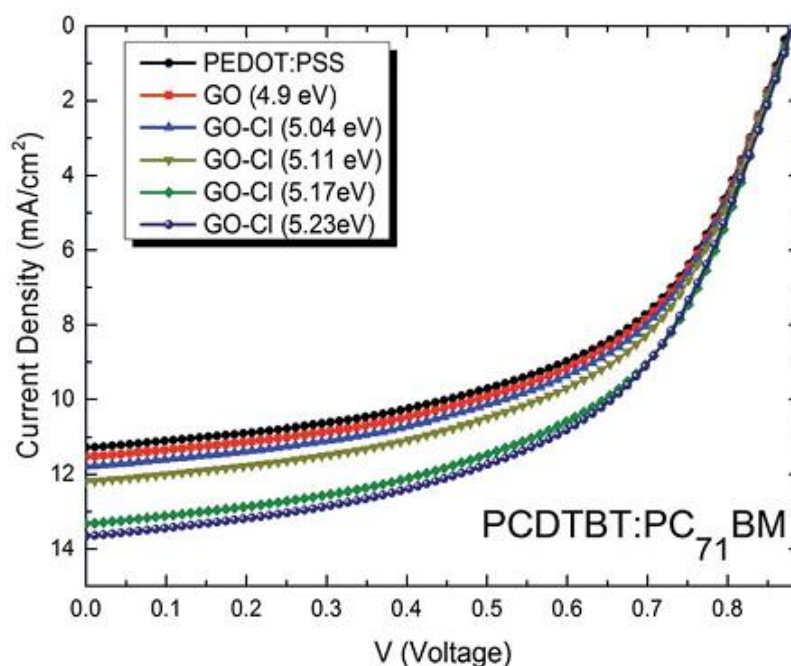
Figure 5.6. J-V characteristics of PCDTBT:PC$_{71}$BM photovoltaic devices with different HTLs under simulated A.M. 1.5, 100 mWcm^{-2} solar irradiation.

This J_{sc} increase cannot be attributed to enhanced optical transmittance, since there was practically no difference in transparency between the pristine and photochlorinated GO HTLs (**Figure 5.5b**). Also, it should be noted that, the pristine GO based OPV slightly outperforms the PEDOT: PSS due to a small increase of J_{sc}. Such increase may be attributed to the improved hole transportation due to the 2D nature of the HTL. Our results suggest that the photocurrent enhancement can be explained by an improvement on the hole transport efficiency facilitated by the perfect match of GO-Cl WF with the HOMO level of the polymer. To validate this presumption, hole-only devices with the structure: ITO/HTL/PCDTBT:PC$_{71}$BM/MoO$_3$/Au were fabricated for all different types of devices. The hole mobility was estimated from the J-V characteristics

at low voltage region, where the current is described by the Mott-Gurney square law:[37]

$$J_{SCLC} = \frac{9}{8}\varepsilon_0\varepsilon_r\mu_e\frac{(V-V_{bi})^2}{d^3}$$

where J_{SCLC} is the current density of SCLC, ε_r is the relative permittivity of the organic active layer, ε_0 is the permittivity of free space, V is the applied voltage, V_{bi} is the built-in voltage, μ_e is the electron mobility, and d is the thickness of the active layer.[38]

Table 5.1. Summary of the photovoltaic parameters of the fabricated OPVs with PCDTBT:PC$_{71}$BM active layer using different HTLs (The data was averaged from ten devices).

HTL	J_{sc} (mA/cm^2)	V_{oc} (V)	FF (%)	PCE (%)
PCDTBT:PC$_{71}$BM				
PEDOT:PSS	11.27	0.88	55.3	5.49
GO 4.9 eV	11.52	0.88	55.1	5.59
GO-Cl 5.04 eV	11.78	0.88	55.1	5.71
GO-Cl 5.11 eV	12.19	0.88	55.2	5.92
GO-Cl 5.17 eV	13.32	0.88	55.1	6.46
GO-Cl 5.23 eV	13.65	0.88	54.7	6.56

It should be noted that the obtained hole mobilities refer to the complete device including the active and the HTLs. The hole mobilities of the devices prepared with PEDOT:PSS, GO and GO-Cl (5.23 eV) as the HTLs, respectively are calculated from the currents in the square law region to be 9.64×10^{-5}, 1.2×10^{-4} and 2.35×10^{-4} cm^{2}V^{-1}s^{-1} respectively. Therefore, it is more than clear that the hole mobility increases as the GO-Cl WF increases, leading to higher PCEs due to improve hole transport. Further support of the enhancement effect of GO-Cl HTLs is the observation that OPV devices incorporating GO HTLs that were laser irradiated without the presence of chloride, exhibit PCEs comparable with that of devices incorporating pristine GO HTLs. Moreover, the dark current

density in reverse bias of the OPVs with GO-Cl is one order of magnitude lower than that of the OPVs with pristine GO HTLs, resulting in a higher diode rectification ratio and therefore better hole collection and electron blocking behaviour. Therefore, it can be concluded that only the simultaneous partial reduction and chlorination of the GO films, lead to increased WF, and hence PCE.

All the above clearly demonstrate that tuning of the GO-Cl WF with respect to the energy levels of the polymer donor is the main performance enhancement factor. Optical or morphological side effects can be neglected, since the measured roughness and optical transmission of the pristine and the photochlorinated GO layers are comparable. The OPVs with GO-Cl as the HTL exhibit significant higher lifetime stability when exposed to continuous solar illumination in air compared with OPVs using PEDOT:PSS. OPVs were tested under prolonged irradiation without any encapsulation. While OPVs with PEDOT:PSS as the HTL die after 20 h, OPVs fabricated with GO or GO-Cl HTLs preserve more than 70% and 50% of its initial PCE for over 25 h and 45 h respectively.[39] This result is due to the fact that PEDOT:PSS is spin coated from highly acidic suspension (pH~1), which erodes ITO and causes indium migration into the photoactive layers. Also, water molecules can readily penetrate into the hygroscopic PEDOT:PSS layer, resulting in degraded device performance.[40] Thus, the GO-Cl does not only enhance the device PCE but also act against fast degradation of the device, offering a superior alternative HTL material. Finally, it is important to note that the presented technique ensures low cost, since it is a room temperature process and applicable to flexible and light-weight substrates, and therefore compatible with large industrial r2r manufacturing of OPVs. A GO ink is printed onto flexible plastic foils using standard industrial inkjet printers, then the GO film can be in situ photochlorinated using a scanning laser beam. Furthermore, the technique can be applied to other organic electronic devices, in which tuning of the graphene ink electronic properties is desirable.

5.4 Conclusion

In summary, ultraviolet laser irradiation in a chlorine gas medium was successfully employed as a facile and catalyst-free approach to prepare photochlorinated GO films with controllable reduction and doping levels, and thus WF. In effect, the resultant GO-Cl has been demonstrated to be an excellent HTL material for OPVs, significantly outperforming the reference PEDOT:PSS and pristine GO HTLs. This is attributed to its increased WF which perfectly matches with the HOMO level of the PCDTBT, ensuring an ohmic contact at the interface. This new technique can employ other dopants for not only the increase but also the decrease of the GO work function, aiming to its use as the electron transport layer, opening new avenues for the development of an all graphene based OPVs.

REFERENCES

[1] H. Y. Chen, J. H. Hou, S. Q. Zhang, Y. Y. Liang, G. W. Yang, Y. Yang, L. P. Yu, Y. Wu, G. Li, *Nature Photon.*, **2009**, 3, 649

[2] G. Zhao, Y. He, Y. Li, *Adv. Mater.*, **2010**, 22, 4355.

[3] R. Steim, F.R. Koglera, C.J. Brabec*, J. Mater. Chem.*, **2010**, 20, 2499.;

[4] H. L. Yip and A. K. Y. Jen, *Energy Environ. Sci.*, **2012**, 5, 5994-6011

[5] F. Zhang, M. Ceder, O. Inganas, *Adv. Mater.*, **2007**, 19, 1835

[6] H. Yan, P. Lee, N. R. Armstrong, A. Graham, G. A. Evmenenko, P. Dutta, T. J. Marks, *J. Am. Chem. Soc.*, **2005**

[7] X. H. Yang, F. Jaiser, B. Stiller, D. Neher, F. Galbrecht, U. Scherf, *Adv. Funct. Mater.*, **2006**, 16, 2156

[8] F. So, D. Kondakov, *Adv. Mater.*, **2010**, 22, 3762

[9] A. W. Hains, T. J. Marks*, Appl. Phys. Lett.*, **2008**, 92, 1.

[10] A. Garcia, G. C. Welch, E. L. Ratcliff, D. S. Ginley, G. C. Bazan, D. C. Olson, *Adv. Mater.* **2012**, 24, 5368

[11] R. Po, C. Carbonera, A. Bernardi and N. Camaioni, *Energy Environ. Sci.*, **2011**, 4, 285-310.

[12] M. Vasilopoulou, A. Soultati, D.G. Georgiadou, T. Stergiopoulos, L.C. Palilis, S. Kennou, N.A. Stathopoulos, D. Davazoglou, P. Argitis, *J. Mater. Chem. A*, **2014**, 2, 1738.

[13] E. Kymakis, M.M. Stylianakis, G.D. Spyropoulos, E. Stratakis, E. Koudoumas, C. Fotakis, *Sol. Energy Mater. Sol. Cells*, **2012**, 96, 298.

[14] J. Liu, M. Durstock, L. Dai., *Energy Environ. Sci.*, **2014**, 7, 1297

[15] S. S. Li, K. H. Tu, C. C. Lin, C. W. Chen, M. Chhowalla, *ACS Nano* **2010**, 4, 3169

[16] H. P. Kim, A. R. M. Yusoff, J. Jang, *Sol. Energy Mater. Sol. Cells*, **2013**, 110, 87

[17] W.W. Cai, R. D. Piner, F. J. Stadermann, S. Park, M. A. Shaibat, Y. Ishii, D. X. Yang, A. Velamakanni, S. J. An, M. Stoller, J. H. An, D. M. Chen, R. S. Ruoff, *Science*, **2008**, 321, 1815.

[18] W. S. Hummers and R. E. Offeman*, J. Am. Chem. Soc.*, **1958**, 80, 1339

[19] D. R. Dreyer, S. J. Park, C. W. Bielawski, R. S. Ruoff, *Chem. Soc. Rev.*, **2010**, 39, 228

[20] P. Matyba, H. Yamaguchi, M. Chhowalla, N. D. Robinson, L. Edman, *ACS Nano*, **2010**, 5, 574

[21] J. Liu, Y. Xue, Y. Gao, D. Yu, M. Durstock, L. Dai, *Adv. Mater.* **2012**, 24, 2228.

[22] B. R. Lee, J. W. Kim, D. Kang, S. Ko, H. J. Lee, J. Y. Kim, H. S. Shin, M. H. Song, *ACS Nano*, **2012**, 6, 2984

[23] C. L. Chochos, S. A. Choulis, *Prog. Polym. Sci.*, **2011**, 36, 1326

[24] D. Yang, L.Y. Zhou, L.C. Chen, B. Zhao, J. Zhang , C. Li, *Chem. Commun.* **2012**, 48, 8078

[25] J. Liu, Y. H. Xue, L. M. Dai, *J. Phys. Chem. Lett.* **2012**, 3, 1928

[26] E. Kymakis, K. Savva, M.M. Stylianakis, C. Fotakis, E. Stratakis, Adv. Funct. Mater., **2013**, 23, 2742

[27] B. Li, L. Zhou, D. Wu, H. Pang, K. Yan, Y. Zhou, Z. Liu, *ACS Nano*, **2011**, 5, 5957

[28] D. Li, M.B. Müller, S. Gilje, R.B. Kaner, G.G. Wallace, *Nat. Nanotechnol.*, **2008**, 3, 101.

[29] S. Stankovich, D. A. Dikin, R.D. Piner, K.A. Kohlhaas, A. Kleinhammes, Y. Jia, Y. Wu, S.T. Nguyen, R.S. Ruoff, *Carbon*, **2007**, 45, 1558.

[30] D.-W. Wang, K.-H. Wu , I.R. Gentle, G.Q. Lu ,*Carbon* **2012**, 50, 333

[31] X. Wang, X. Li, L. Zhang, Y. Yoon, P.K. Weber, H. Wang, J. Guo, H. Dai, *Science*, **2009**

[32] J.L. Bahr, J.P. Yang, D.V. Kosynkin, M.J. Bronikowski, R.E. Smalley, J.M. Tour, *J. Am. Chem. Soc.*, **2001**, 123, 6536.

[33] P.V. Kumar, M. Bernardi, J.C. Grossman, *ACS Nano*, **2013**, 7, 1638

[34] J.-Y. Kim, W. H. Lee, J. W. Suk, J. R. Potts, H. Chou, I. N. Kholmanov, R. D. Piner, J. Lee, D. Akinwande and R. S. Ruoff, *Adv. Mater.*, **2013**, 16, 2308

[35] K.C. Kwon, K.S. Choi, Y. Kim, *Adv. Funct. Mater.* **2012**, 22, 4724

[36] J.K. Wassei, K.C. Cha, V.C. Tung, Y. Yang, R. B. Kaner, *J. Mater. Chem.*, **2011**, 21, 3391

[37] M. Y. Chiu, U. Jeng, C. H. Su, K. S. Liang, K. H. Wei, *Adv. Mater.*, **2008**, 20, 2573

[38] V. Shrotriya, E. H.-E. Wu, G. Li, Y. Yao, Y. Yang, *Appl. Phys. Lett.*, **2006**, 88, 064104

[39] E. Stratakis, M.M. Stylianakis, E. Koudoumas, E. Kymakis, *Nanoscale*, **2013**, 5, 4144.

[40] M. Jørgensen, K. Norrman and F. C. Krebs, Sol. *Energy Mater.Sol. Cells*, **2008**, 92, 686

Chapter 6

Ternary organic solar cells with reduced graphene oxide-Sb_2S_3 hybrid nanosheets as the cascade material

Abstract: We demonstrate that the efficiency of a $PCDTBT$:$PC_{71}BM$ bulk heterojunction solar cell can be improved from 5.53% to 6.81% by incorporating reduced graphene oxide-antimony sulfide (rGO-Sb_2S_3) hybrid nanosheets as the third component, hybrid as the cascade material, we combine the ultra-conductive multi charge transfer paths provided by graphene with the favourable arrangement of the material energy bands due to the presence of Sb_2S_3 nanocrystals. The higher LUMO energy level of rGO-Sb_2S_3 relative to $PC_{71}BM$, results in an increase of the open circuit voltage upon increasing the rGO-Sb_2S_3 concentration, while the photocurrent and fill factor are enhanced due to the presence of more exciton dissociation interfaces and more efficient charge transport.

6.1 Introduction

Organic solar cells (OSCs) have recently attracted much attention due to their indubitable advantages for manufacturing low cost, light weighted, flexible photovoltaic devices.[1,2,3] The PCE of OSCs has already approached 10% for single junction devices,[4] making them a very promising option for cost effective and highly efficient solar energy harvesting and conversion technology. BHJ OSCs consist of a blend layer of a conjugated polymer as the electron donor and a fullerene derivative as the electron acceptor. A tightly bound Frenkel exciton is created into the polymer and subsequently dissociated at the donor-acceptor interface creating a free electron and a free hole due to ionization of the charge transfer state. Ideal polymer donor materials should have low energy band gap (~1.5 eV), strong and broad absorption in the visible and near IR regions, and high hole mobility to transport holes effectively. A successful acceptor material is characterized by high electron affinity and electron mobility to accept and transport electrons towards cathode. Moreover polymer energy bands should be adaptable to the electron acceptor material energy levels. After exciton dissociation at the donor-acceptor interface, free electrons and holes are moving towards the positive and negative electrode respectively, overwhelming the energy barriers between the successive layers.

A strategy adopted to facilitate the energy cascade procedure is the introduction of a third component into the photoactive binary layer, resulting in the formation of a ternary blend structure device.[5,6] The basic motivation behind this approach is the insertion of a material having its HOMO and LUMO between the HOMO and LUMO of the polymer and the fullerene. This material can act either as a secondary donor or acceptor material, offering an extra interface for exciton dissociation and charge transfer. Among others, carbon derivatives such as Indene-C60 bisadduct (ICBA) have been used as the third component into ternary blends.[7] Nonetheless, a promising perspective is the utilization of a graphene derivative as the additive exploiting graphene special properties.[8] Graphene is a novel crystalline carbon allotrope with high charge carrier mobility,[9] high mechanical strength[10] and great surface area,[11] characterized by high optical transparency, electrical conductivity and mechanical flexibility. These features and especially the tremendous carrier

mobility via the graphene one-atom thick, honeycomb lattice, emerged it as a highly attractive material for several optoelectronic applications.[12] Towards the fabrication of all-carbon devices, graphene has already been used in every structural unit of OSCs.[13,14,15,16,17] However, the introduction of graphene as the third component in BHJ devices remains a great challenge. Despite the fact that rGO, a graphene derivative, has suitable work-function value and the electron transfer from the polymer is energetically favorable, the lack of an appropriate bandgap makes rGO nanosheets acting mainly as carrier traps in the BHJ. Therefore, pristine rGO cannot be considered as an energy cascade material for ternary OSCs.

In this context, many researchers have investigated the synthesis of graphene-inorganic nanocrystals derivatives in a way of designing energetically favorable materials for solar cells applications.[18,19] Regarding the field of BHJ solar cells, few approaches have presented the employment of such materials as additives[20] or electron acceptors.[21,22] On the other hand, semiconductor nanocrystals are very promising materials for light harvesting applications due to their unique electrical and optical properties, arising from the quantum confinement effect.[23] The band gap of semiconductor nanoparticles can be tuned by controlling their particle size and so by adjusting the experimental parameters of nanocrystals synthesis, one can modify their size and consequently their properties. Among others, metal chalcogenide nanocrystals such as CdS, CdSe, ZnS and PbS have been widely used in third generation photovoltaic applications as sensitizers.[24,25] The efficiency of the respective solar cells, has approached 9%[26] offering major advantages, such as, hot carriers utilization and multi electron generation. Among others, crystalline Sb_2S_3 (stibnite) is a novel material recently used in photovoltaic applications.[27] As a chalcogenide nanocrystal, it is characterized by high absorption coefficient, intrinsic large dipole moment, convenient band gap tuning and solution processability.[28,29] It is particularly attractive as an efficient light absorber because of its suitable band gap (~1.7 eV), strong absorption coefficient (1.8×10^5 cm^{-1} in the visible region) and its relatively environment-friendly characteristics. Therefore it has been widely explored in solid state sensitized solar cells based on CuSCN,[30] P3HT,[31,32] PCPDTBT,[27] spiroMEOTAD[33] as hole transport materials.

The utility of semiconductor nanocrystals in solar cell applications depends primarily on the ability of charge transfer from a photoexcited nanocrystal before the trapping and recombination of the charge carriers. Most of the studies on individual nanocrystals have proved that such phenomena occur at an ultra-fast time scale. Accordingly, carrier recombination takes place before electrons get transferred to the acceptor molecules, leading to the limited use of these materials for solar cell applications.[34] It is thus essential to retard the electron-hole recombination within the semiconductor nanocrystals. In this context, the unique structure and excellent electronic properties of graphene and especially its high mobility, make it a competitive alternative for electron-transport matrices in semiconductor nanocrystals systems.[35] For example, it is shown that the combination of rGO with semiconductor nanocrystals can assist towards overcoming conductivity problems inhered in nanocrystals, via substituting electron hopping with ballistic electron transport through graphene sheets.[36]

This study proposes the introduction of rGO-Sb_2S_3 nanosheets as an additive into the active layer of an OSC, leading to the formation of a ternary OSC device. The photoactive layer of the control device comprises of PCDTBT as the donor material and $PC_{71}BM$ as the acceptor one. Antimony sulfide presents favorable energy band levels with respect to PCDTBT and $PC_{71}BM$, while rGO can assist to overcome the conductivity problems inhered in the isolated nanocrystals, as mentioned above. Therefore, rGO-Sb_2S_3 hybrids combine the advantages of the individual materials, and could potentially enhance the energy cascade transfer into the active layer. Besides this, Sb_2S_3 acts as a secondary light-harvesting antenna in the visible spectral region, enhancing the light absorption of the active layer, while rGO offers highly conductive multi charge transfer percolation paths, suitable for ballistic electron transport to the LUMO of $PC_{71}BM$. Using GO as the starting material, an easy solvothermal synthetic route under high-pressure conditions was followed that provides the ability to control the dimensions and shape of the nanocrystals. During the process, the reduction of GO and the growth of the nanocrystals occurred simultaneously. The introduction of rGO-Sb_2S_3 into air processed PCDTBT:$PC_{71}BM$-based devices gave rise to a remarkable enhancement of the PCE by 23%, reaching a value of 6.81%.

6.2 Experimental section

6.2.1 Preparation of graphene oxide[37]

GO was prepared from graphite powder (Alfa Aesar. ~200 mesh) according to a modified Hummers' method. In more detail, graphite powder (0.5 g) was placed into a mixture of sulfuric acid, H_2SO_4 (40 mL, 98%) and sodium nitrate, $NaNO_3$ (0.375 g). The mixture was then stirred and cooled in an ice bath. While maintaining vigorous stirring, potassium permanganate, $KMnO_4$ (3.0 g) was added in portions over a period of 2 h. The reaction mixture was left for 4 h to reach room temperature before being heated to 35°C for 30 min. It was then poured into a flask containing deionized water (50 mL) and further heated to 70°C for 15 min. The mixture was then decanted into 250 mL of deionized water and the unreacted $KMnO_4$ was removed by adding 3% hydrogen peroxide, H_2O_2. The reaction mixture was then allowed to settle and decanted. The obtained graphite oxide was purified by repeated centrifugation and redispersion in deionized water until neutralized pH was achieved. Finally, the resulting GO was dried at 60°C in a vacuum oven for 48 h before use.

6.2.2 rGO-Sb_2S_3 synthesis

GO was dispersed in ethylene glycol with concentration of 0.1 mgmL^{-1}, followed by ultrasonication for 1.5 h. Then antimony (III) chloride, $SbCl_3$ (0.0652 mg) was added in an aliqutot (20 mL) of the solution and the mixture was vigorously stirred for 1 h at room temperature. Subsequently, the solution was transferred into a 70 mL polytetrafluoroethylene (PTFE) lined stainless steel autoclave, followed by the addition of thiourea (0.0652 mg). A teflon magnet was added and the autoclave was sealed and heated at 180°C for 8 h, followed by cooling at room temperature. The product was centrifuged and washed thoroughly with water and ethanol, before being vacuum dried at 60°C for 3 h. Finally, thermal treatment of the produced material was carried out at 300°C in a N_2 filled tube furnace for 3 h.

6.2.3 PCDTBT:PC$_{71}$BM and PCDTBT:PC$_{71}$BM:rGO-Sb$_2$S$_3$ blends preparation

The PCDTBT:PC$_{71}$BM solution was prepared according to the following procedure: PCDTBT and PC$_{71}$BM (1:4 w/w), both purchased from Solaris Chem, were dissolved in a mixture of chlorobenzene (CB) and o-dichlorobenzene (o-DCB) (1:3 v/v) and stirred overnight at 70°C. rGO-Sb$_2$S$_3$ nanosheets were also dissolved into o-DCB followed by utrasonication for 1 h. Finally, the PCDTBT:PC$_{71}$BM solutions were mixed with different amounts of rGO-Sb$_2$S$_3$ (0.10%, 0.20%, 0.25%, 0.30%, 0.40% v/v) to obtain the final blends.

6.2.4 Device fabrication

The reported photovoltaic devices were fabricated on 20 mm by 15 mm ITO glass substrates with a sheet resistance of 10 Ωsq^{-1}. The impurities were removed from the ITO glass through a 3-step ultrasonication cleaning process (deionized water with 10% soap, aceton, IPA). After cleaning, the substrates were spin-casted with a PEDOT:PSS layer at 6000 rpm for 60 s, obtaining a 30 nm film. The films were baked for 20 min at 120°C inside a nitrogen-filled glove box to dry any residual moisture. All photoactive layers (PCDTBT:PC$_{71}$BM and PCDTBT:PC$_{71}$BM:rGO-Sb$_2$S$_3$) were subsequently deposited on top of the PEDOT:PSS layer by spin-coating at 1000 rpm, until the thickness reached approximately 80 nm determined by cross-sectional SEM images. The cells were dried at 60°C for 1 min and subsequently a 10 nm titanium suboxide (TiO$_x$) layer, synthesized as described elsewhere,[38] was spin coated on top of the photoactive layer. Finally, a 100 nm Al top electrode was deposited through a shadow mask by thermal evaporation to complete device architecture creating an active area of 0.04 cm^2.

The performances of the devices were measured at room temperature with an Air Mass 1.5 Global (A.M. 1.5 G) solar simulator at an intensity of 100 mW cm^{-2}. A reference monocrystaline silicon solar cell from Newport was used to calibrate the light intensity. All measurements were carried out in air immediately after device fabrication without encapsulation process.

6.2.5 Characterization

The samples were characterized by Raman spectrometer at room temperature using a Nicolet Almega XR Raman spectrometer (Thermo Scientific) with a 473 nm laser as excitation sources. Fourier transform infrared (FT-IR) spectra were measured on a BRUKER FT-IR spectrometer IFS 66v/F (MIR). UV-vis absorption spectra were recorded using a Shimadzu UV-2401 PC spectrophotometer over the wavelength range of 200-800 nm. Cyclic voltammetry measurements were carried out with an Autolab potentiostat PGSTAT128N. X-ray diffraction patterns were collected on a Panalytical Expert Pro X-ray diffractometer, using Cu Kα radiation (k = 1.5406 A˚). The morphology of the surfaces was examined by field emission scanning electron microscopy (FE-SEM JEOLJSM-7000F), while transmission electron microscopy (TEM) images were taken using a JEM-2100 LaB6 ultra-high-resolution electron microscope. Current-voltage (J-V) and mobility measurements were performed at room temperature using an Agilent B1500A Semiconductor Device Analyzer. For photovoltaic characterization under light conditions the devices were illuminated with 100 mWcm^{-2} power intensity of white light with an Air Mass 1.5 Global (A.M. 1.5 G) solar simulator through the glass/ITO side. External quantum efficiencies (EQE) were measured by the QE-R system (Enli Technolog, Taiwan). All measurements were performed in air immediately after the device fabrication.

6.3 Results and Discussion

Figure 6.1 shows schematically the possible formation mechanism of the rGO-Sb_2S_3 material. The GO sheets are negatively charged, containing hydroxyl, epoxy and carboxylic acid anchoring groups on the basal plane and the edges, thereby highly react with Sb^{3+} ions. The oxygen groups act as the anchor sites to facilitate the subsequent in situ formation of nanostructures attaching to the surface and edges of GO sheets. Thiourea was added as the sulfur source, contributing the S^{-2} ions that attach to Sb^{3+} ions. After several hours of reaction, nucleation and growth, the Sb_2S_3 nanocrystals were formed

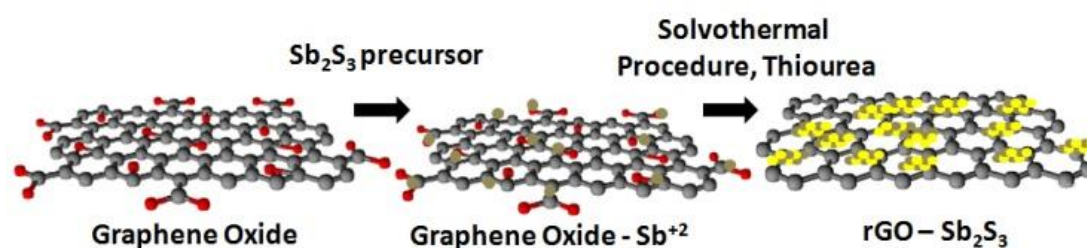while at the same time GO was reduced. Without the use of GO only Sb$_2$S$_3$ spheres are obtained.[39]

Figure 6.1. Schematic illustration of rGO-Sb$_2$S$_3$ preparation process.

Figure 6.2a shows the absorption spectra of GO and rGO-Sb$_2$S$_3$. The absorption band of GO is located mainly in a short wavelength region, while the absorption of rGO-Sb$_2$S$_3$ is enhanced and slightly shifted to longer wavelength due to the presence of Sb$_2$S$_3$ which presents a strong absorption in the visible region.[40] Both the initial and functionalized materials were characterized by FT-IR spectroscopy. The spectrum of GO (indicated by black color) in **Figure 6.2b** demonstrates the presence of peaks at ~3400 cm^{-1} (O-H stretching vibrations), at ~1717 cm^{-1} (C=O stretching vibrations), at ~1615 cm^{-1} (skeletal vibrations from unoxidized graphitic domains), at ~1180 cm^{-1} (C-O-C stretching vibrations), at ~1050 cm^{-1} (C-O stretching vibrations) are characteristic for the GO. Moreover, the a peaks at 2917 cm^{-1} and 2853 cm^{-1} are present, corresponding to the aliphatic C-H stretching. In the obtained rGO-Sb$_2$S$_3$ derivative (indicated by red color), the characteristic peaks correspond to the oxygen containing bonds of GO, have been reduced or eliminated due to the reduction process during the solvothermal procedure. The observed band at ~1566 cm^{-1} can be attributed to the skeletal vibration of C=C in graphene sheets, confirming the recovery of the sp^2 hybrid carbon skeleton. This fact further indicates the successful reduction of GO.
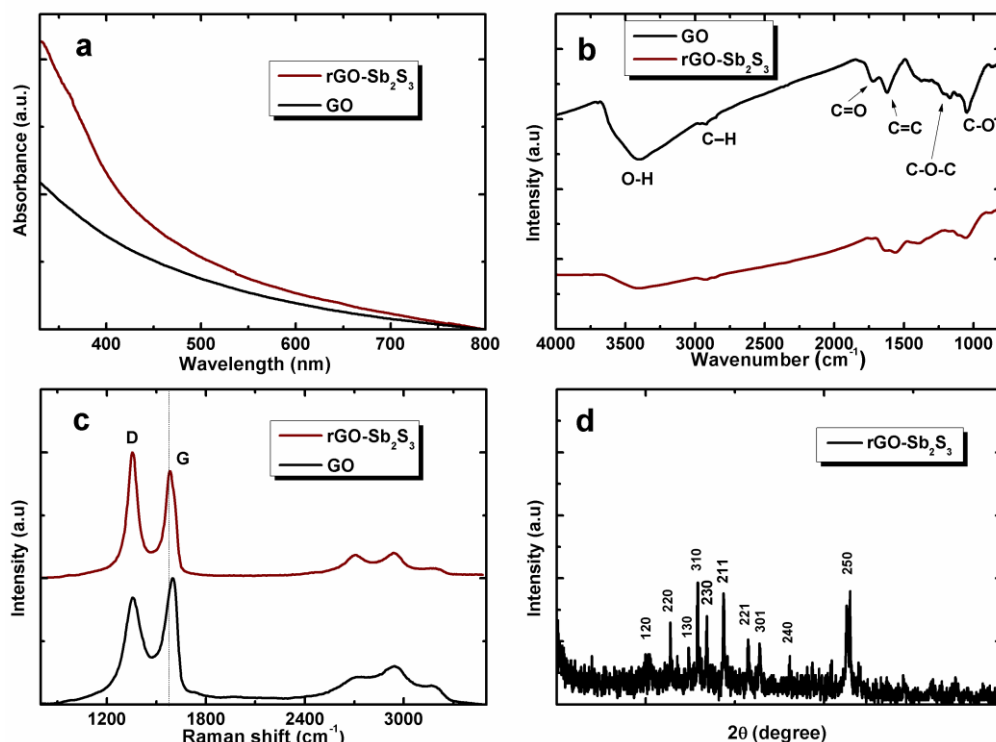
Figure 6.2. a) UV/Vis absorption spectra of GO and rGO-Sb$_2$S$_3$ solutions. b) FT-IR spectra of GO and rGO-Sb$_2$S$_3$. c) Raman spectra of GO and rGO-Sb$_2$S$_3$. d) XRD pattern of rGO-Sb$_2$S$_3$.

The Raman spectra (**Figure 6.2c**) also confirms the reduction of GO. Pristine GO exhibits two prominent peaks at about 1357 cm^{-1} and 1597 cm^{-1}, the so-called D and G peaks, corresponding to the breathing mode of κ-point phonons of A$_{1g}$ symmetry and the first-order scattering of the E$_{2g}$ phonons, respectively. rGO-Sb$_2$S$_3$ exhibits the same peaks, but the slight red shift of G peak, from 1597 cm^{-1} to 1583 cm^{-1} can be attributed the restoration of the sp^2 carbon.[41] In addition, the I$_D$/I$_G$ ratio increased from 0.86 in GO to 1.06 in rGO-Sb$_2$S$_3$, due to the introduction of in-plane defects during the reduction. This further suggests that GO had been reduced to rGO, which is consistent with the FT-IR spectra.

In order to clarify the structure of rGO-Sb$_2$S$_3$, XRD measurement was conducted. As it can be seen in **Figure 6.2d** all the diffraction peaks of rGO-Sb$_2$S$_3$ coincide with those of Sb$_2$S$_3$ and correspond to the orthorhombic phase of crystalline Sb$_2$S$_3$, stibnite (JCPDS 42-1393).[42] Moreover there are no other significant diffractions, characteristic of possible impurities, such as antimony oxide, indicating the presence of pure Sb$_2$S$_3$ with high crystallinity. The

nanomorphology of rGO-Sb$_2$S$_3$ nanosheets was investigated through microscopic characterization.

Figure 6.3a shows SEM image of GO with the characteristic wrinkles, indicating the presence of few layered graphene structure. Following the solvothermal reduction, rGO-Sb$_2$S$_3$ sheets get entangled and creased (**Figure 6.3b**). **Figure 6.3c** shows a TEM image of rGO-Sb$_2$S$_3$, where 5-10 nm Sb$_2$S$_3$ nanocrystals are dispersed on the surface of rGO sheets. In order to tune the shape and size of Sb$_2$S$_3$, the temperature and time of the solvothermal reaction was controlled. In low reaction times, 2 or 3 h, Sb$_2$S$_3$ spheres are formed, while for longer reaction times, 12 h and more, the shape changes in rod-like structures.[43] Temperature is also crucial as the particle size ascends by increasing the temperature of the solvothermal procedure.[44] The presence of Sb$_2$S$_3$ was also confirmed by Energy Dispersive X-Ray (EDX) spectroscopy (**Figure 6.3d**).
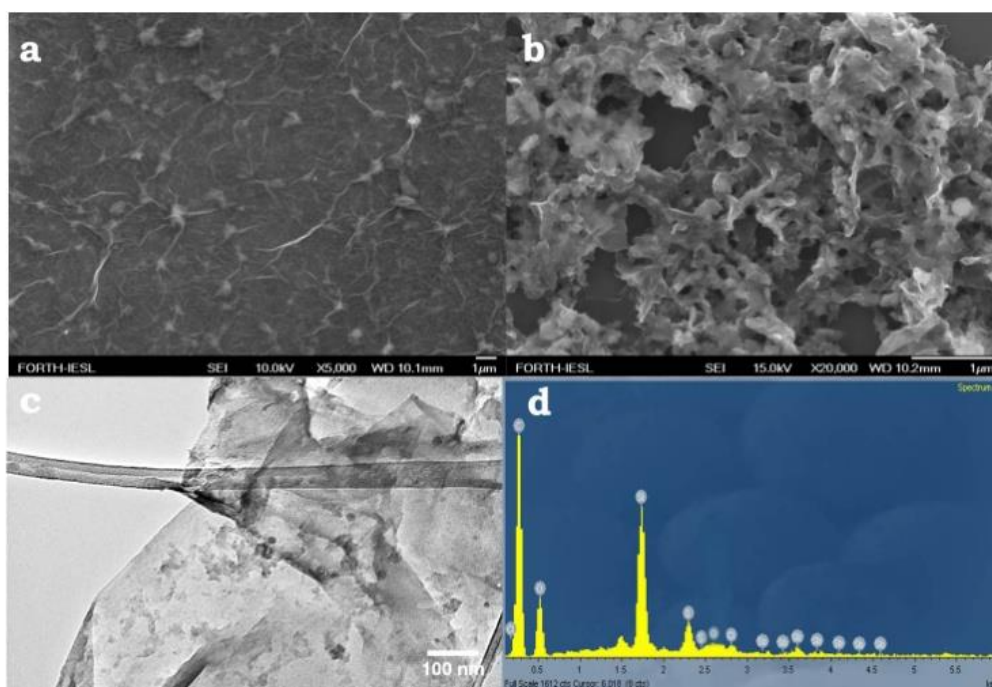
Figure 6.3. a) SEM image of GO. b) SEM image of rGO-Sb$_2$S$_3$ nanosheets. c) TEM image of rGO-Sb$_2$S$_3$. d) EDX spectrum of rGO-Sb$_2$S$_3$.

Figures 6.4a and **6.4b** presents the device architecture and the energy levels of the components of the devices. As depicted, the excitons created into PCDTBT can diffuse to both PCDTBT:rGO-Sb$_2$S$_3$ and PCDTBT:PC$_{71}$BM interfaces. Moreover, the conduction band of rGO-Sb$_2$S$_3$ is located between the

LUMO levels of PCDTBT and $PC_{71}BM$, acting as energy intermediate step, so that the electrons can be transferred towards the cathode through this energetic cascade pathway. In addition, electron-hole pairs are also created in the rGO-Sb_2S_3 component. In particular, under light irradiation, electrons are excited from the valence band to the conduction band of the semiconductor and then transferred to the graphene sheets. Once graphene is combined with the semiconductor nanoparticles, it acts as an electron collector and transporter, separating the photogenerated electron-hole pairs effectively, lengthening the lifetime of the charge carriers.[45] Although efficient electron-hole pair dissociation and electron collection are still big challenges for nanostructures like Sb_2S_3, the high carrier mobility of graphene can facilitate electron transport thereby decreasing the probability for carrier recombination.[46] These facts are expected to enhance the electron and hole mobilities of the devices.
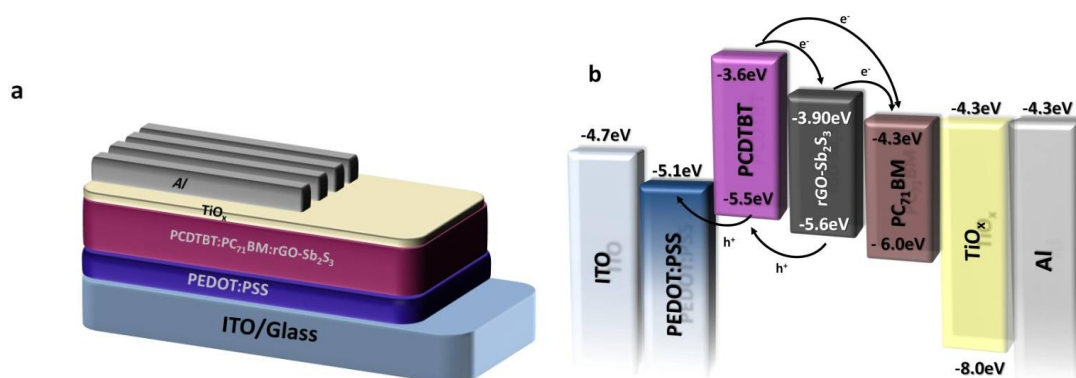
Figure 6.4. a) Schematic illustration of the sandwich-type BHJ solar cell. b) Energy level diagram of the ternary OSC showing the energy bands of the components.

The obtained material, rGO-Sb_2S_3 was electrochemically characterized by cyclic voltammetry (CV) to determine the energy levels.[47] The measurements were conducted in a three electrode apparatus, using a Pt foil as the counter electrode and a Ag/AgCl electrode as the reference one. The voltammetric behavior of rGO-Sb_2S_3 in acetonitrile (CH_3CN) using 0.1 M tetrabutylammonium hexafluorophosphate (TBAPF6) as the electrolyte is illustrated in **Figure 6.5a**.

Figure 6.5. a) Cyclic voltammogram of rGO-Sb$_2$S$_3$ in CH$_3$CN using 0.1 M TBAPF6 as electrolyte. Scan rate was set at 10 mV sec^{-1}. The inset focuses on the oxidation peak of rGO-Sb$_2$S$_3$. b) UV/Vis absorption spectra of PCDTBT:PC$_{71}$BM blends with and without rGO-Sb$_2$S$_3$.

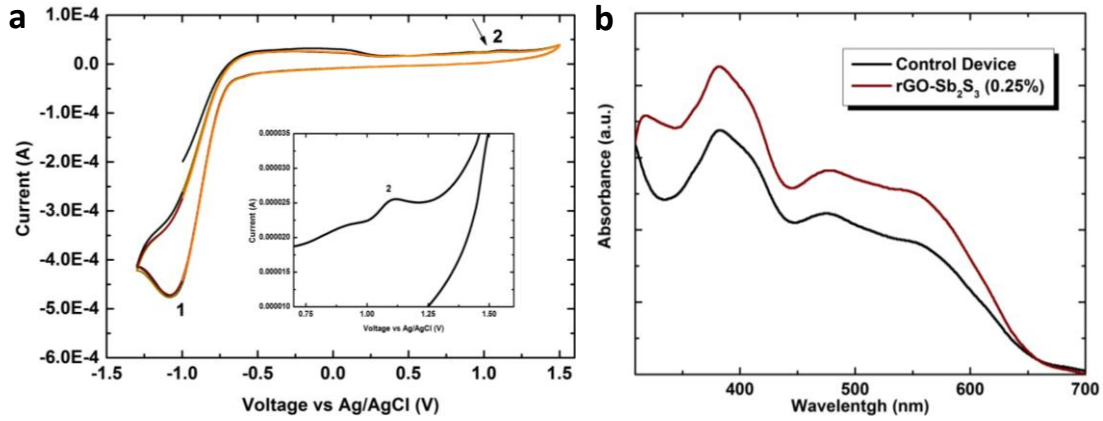A clear reduction peak and an indistinguishable but existing (as depicted in the inset) oxidation peak at -1.07 V and 1.05 V respectively are presented. It is important that the peaks remained unchanged after several measurement cycles, indicating that the peaks correspond to the conduction and valence bands of the material and not to possible oxidation or reduction interactions between the material and the electrolyte. For the calculations, the onsets of oxidation (+0.96 V) and reduction (-0.74 V) peaks are used. The bands were calculated upon the formulas:[48]

$$E_{val} = -(E_{[onset,ox]} - E_{1/2(ferrocene)} + 5.1) \text{ (eV) and,}$$

$$E_{con} = -(E_{[onset,red]} - E_{1/2(ferrocene)} + 5.1) \text{ (eV)}$$

Ferrocene was used as external standard. The cyclic voltammogram of ferrocene shows two peaks at 0.40 and 0.52 V, hence the $E_{1/2(ferrocene)}$ is equal to 0.46. Thus the valence band of rGO–Sb$_2$S$_3$ is located at -5.60 eV, while the conduction band is -3.90 eV. The value of the band gap (1.7 eV) is similar with that of nanostructured Sb$_2$S$_3$,Σφάλμα! Δεν έχει οριστεί σελιδοδείκτης. but the bands are both downshifted due to the presence of rGO and the energy interaction between the two materials.

Figure 6.5b presents the absorption spectra of PCDTBT:PC$_{71}$BM films with and without the presence of rGO-Sb$_2$S$_3$ (0.25%). It is clear that even the

addition of a small amount of rGO-Sb_2S_3 nanosheets enhances the light harvesting of the active layer compared to the reference film. This enhancement is larger at wavelengths below 650 nm, as Sb_2S_3 absorbs light strongly in this region. The effect of rGO-Sb_2S_3 in the performance of BHJ solar cells was investigated by altering the additive content into the photoactive layer. **Figure 6.6a** demonstrates the current density-voltage (J-V) curves of PCDTBT: $PC_{71}BM$ based cells, under A.M. 1.5 G (100 mWcm^{-2}) light intensity illumination, in the presence and absence of rGO-Sb_2S_3.
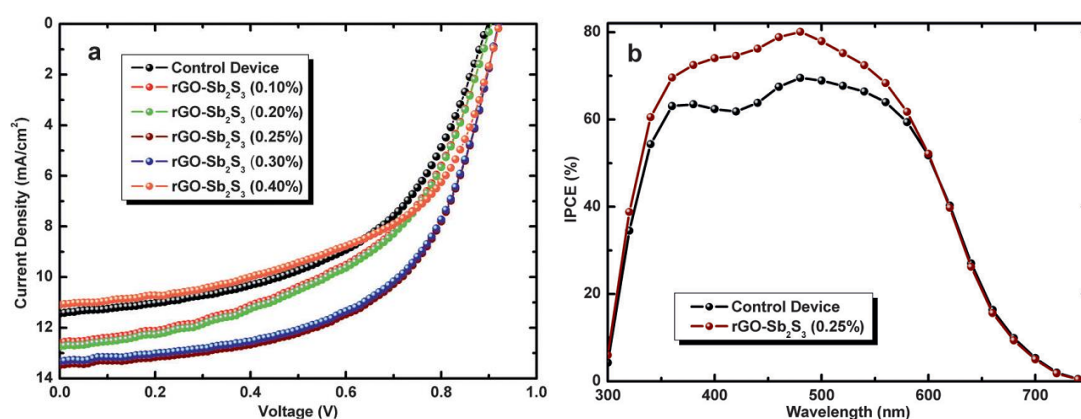

Figure 6.6. a) J-V characteristics under 1 sun illumination (100 mWcm^{-2}) for devices with different concentrations of rGO-Sb_2S_3. b) IPCE spectra for the control device and the one containing rGO-Sb_2S_3.

Table 6.1. Average photovoltaic characteristics for OSC devices with different rGO-Sb_2S_3 contents as additives. To account for experimental errors, the reported averages for each case are taken for 10 identical devices, consisting of six cells each.

rGO-Sb_2S_3 (%)	J_{sc} (mA/cm^2)	V_{oc} (mV)	*FF* (%)	PCE (%)
0	11.42±0.18	898±6	54.2±0.4	5.53±0.15 (5.58)
0.10	12.59±0.25	904±6	53.1±0.4	6.03±0.18 (6.21)
0.20	12.75±0.32	904±5	53.2±0.4	6.11±0.19 (6.30)
0.25	13.47±0.33	919±7	55.0±0.5	6.81±0.19 (7.00)
0.30	13.34±0.30	919±7	55.1±0.5	6.74±0.17 (6.91)
0.40	11.09±0.20	922±5	54.5±0.4	5.52±0.15 (5.57)

Table 6.1 summarizes the photovoltaic characteristics of the tested OSCs. The reference cell yielded a PCE of 5.53%, with a J_{sc} of 11.42 mAcm^{-2}, a V_{oc} of 898 mV and a FF of 54%. Several devices were fabricated and measured by varying the amount of rGO-Sb_2S_3 from 0.1% to 0.4% v/v, with the superior device being the one containing 0.25% v/v rGO-Sb_2S_3. Specifically the PCE increased from 5.53% to 6.81%, presenting an improvement of 23%, attributed to the increase of the J_{sc} and V_{oc}. With respect to the J_{sc}, the increase is caused by enhanced charge carrier separation, transportation and collection, as well as better light utilization (**Figure 6.7**). In addition, the improvement of V_{oc} due to the ternary structure of the blend makes crucial contribution to the PCE increase. V_{oc} is proportional to the energy difference between the HOMO of the donor and the LUMO of the acceptor material and the presence of rGO-Sb_2S_3 actually enlarges this difference.

Table 6.2. Average photovoltaic characteristics for OSC devices with different rGO contents as additives. To account for experimental errors, the reported averages for each case are taken for 10 identical devices, consisting of six cells each.

rGO (%)	J_{sc} (mA cm^{-2})	V_{oc} (mV)	FF (%)	PCE (%)
0	11.42±0.16	898±6	54.2±0.4	5.43±0.15 (5.58)
0.10	11.35±0.26	832±6	48.1±0.4	4.35±0.18 (4.53)
0.20	10.21±0.30	832±5	46.2±0.4	3.92±0.18 (4.10)
0.50	9.99±0.35	820±7	43.0±0.5	3.52±0.20 (3.72)
1.00	9.55±0.31	800±6	35.1±0.5	2.68±0.15 (2.83)

To further enhance our hypothesis about the rGO-Sb_2S_3 electron cascade effect, PCDTBT:PC_{71}BM OSCs, incorporating only rGO, were also fabricated and characterized. The photovoltaic characteristics are summarized in **Table 6.2**. It can be clearly seen that the addition of pristine rGO in the active layer, results in PCE deterioration. This effect is partially attributed to the decrease of the J_{sc} implying that rGO favors the recombination of electron-hole pairs. In addition, V_{oc} declines, possibly due to the disruption of the active layer morphology, since PCDTBT is amorphous and rGO cannot act as a crystallinity improvement agent, as in the case of P3HT.[49] This deterioration is expected, since rGO establishes an energetically favorable offset between the polymer and the fullerene only for electron transport, and not for hole transport. Therefore, the lack of a bandgap makes the rGO nanosheets act as recombination centers in the BHJ, and not as an electron cascade material. Finally the incident photon-to-current efficiency (IPCE) of the fabricated devices was measured (**Figure 6.6b**). The results are consistent with the J-V curves and the increased J_{sc} measured.
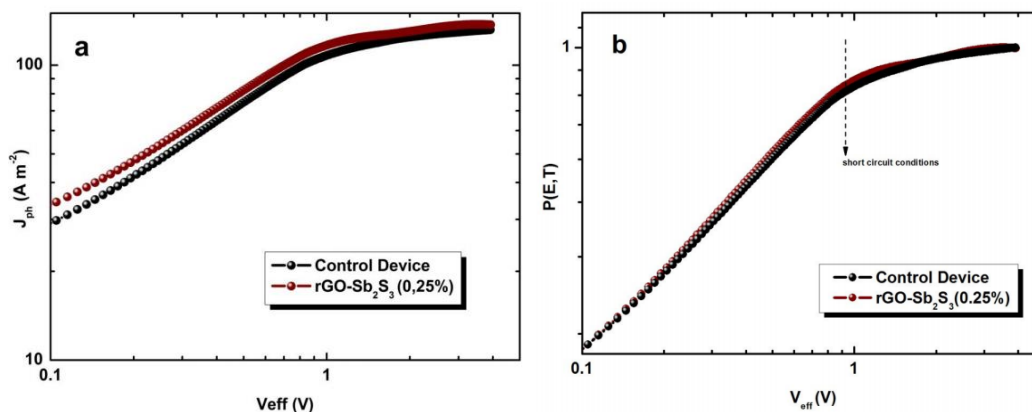
Figure 6.7. a) Photocurrent density (J_{ph}) versus effective voltage (V_{eff}) curves. b) Exciton dissociation probabilities P(E,T) versus V_{eff} curves.

To gain further insight into the mechanism responsible for the enhanced performance, the photocurrent densities of devices with and without rGO–Sb_2S_3 were measured and the results were plotted (**Figure 6.7a**) versus the effective voltage (V_{eff}). The maximum exciton generation rate (G_{max}) and exciton dissociation probabilities P(E,T) of the OSCs can be extracted from the plots. J_{ph} can be measured using the equation $J_{ph}=J_{il}-J_d$, where J_{il} and J_d are the current density under illumination and in the dark respectively. V_{eff} can be calculated as $V_{eff}= V_0-V_a$, where V_0 is the voltage when $J_{ph}=0$ and V_a is the applied bias voltage.[50] If we assume that the saturated J_{sc} is defined by the total amount of the absorbed photons and all the photogenerated excitons are dissociated into free charge carriers, then G_{max} can be calculated by the formula $J_{sat}=eG_{max}L$, where e is the electron charge and L is the thickness of the active layer (in this case 80 nm). The values of G_{max} as calculated from the **Figure 6.7a**, are $0.96*10^{-28}$ $s^{-1}m^{-3}$($J_{sat}=132$ Am^{-2}) for the reference and $1.03*10^{-28}$ $s^{-1}m^{-3}$ ($J_{sat}=123$ Am^{-2}) for the rGO-Sb_2S_3 device. G_{max} increased after the addition of rGO-Sb_2S_3, suggesting increased light absorption in rGO-Sb_2S_3-based device, in good agreement with the increased absorption from UV/Vis absorption spectra.[51] The P(E,T) values can be calculated from J_{ph}/J_{sat} ratio. Under the J_{sc} condition, P(E,T) value (**Figure 6.7b**) increased from 80% in the reference device to 84% in the rGO-Sb_2S_3 device.
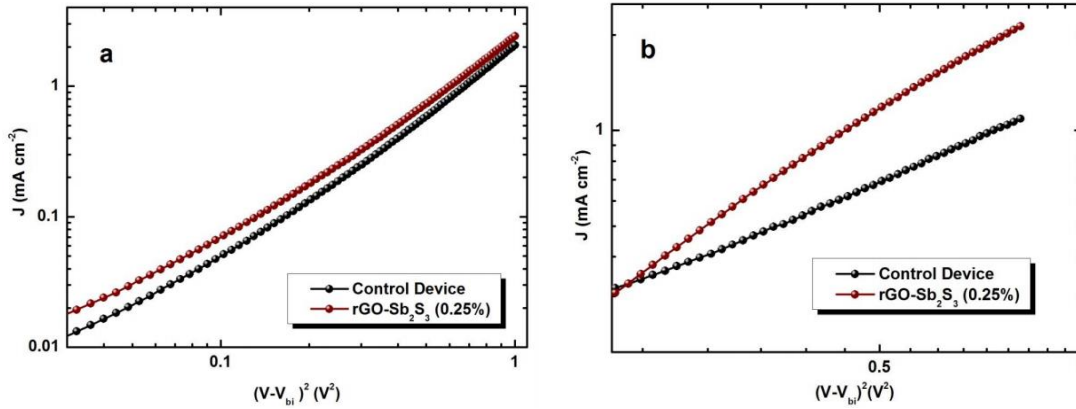
162

Figure 6.8. J-V^2 characteristics under dark conditions for a) electron -only and b) hole-only devices with and without rGO-Sb$_2$S$_3$.

The increased value of J$_{sc}$ was also investigated through electron and hole mobilities measurements (**Figure 6.8**). For that purpose electron- and hole-only devices were fabricated with the following structure: ITO/PEDOT/Active layer/Au for the hole-only and ITO/Al/Active layer/TiO$_x$/Al for the electron only device respectively. The values calculated were improved for both electron and hole mobilities. Calculations were based on Mott-Gurney equation:

$$J_{SCLC} = \frac{9}{8}\varepsilon_0\varepsilon_r\mu_e\frac{(V - V_{bi})^2}{d^3}$$

in which e$_r$ is the relative dielectric constant, e$_0$ is the permittivity of free-space, μ is the charge carrier mobility, V is the applied voltage, V$_{bi}$ is the built-in potential and dis the thickness of the active layer. The mobility values for the reference OSCs were μ$_e$=5.81*10^{-5} cm^{2}s^{-1}V^{-1} for the electron and μ$_h$=3.92*10^{-5}cm^{2}s^{-1}V^{-1} for the hole mobility while for the rGO-Sb$_2$S$_3$-based cells the values were μ$_e$=6.51*10^{-5}cm^{2}s^{-1}V^{-1} for the electron and μ$_h$=6.05 *10^{-5}cm^{2}s^{-1}V^{-1} for the hole mobility, respectively. The mobilities were not only increased, especially the hole mobility, but also imbalanced. This is a crucial improvement because hole transport is considered as a factor that limits the photocurrent generation, since the hole mobility of the electron donors is much lower than the electron mobility of the acceptors. Also the mobilities imbalance indicates the effective dissociation of charge carriers, avoiding trapping of electrons near the back electrode.[49] Both electron and hole mobility increases should be attributed to rGO-Sb$_2$S$_3$ and specifically to the presence of two exciton dissociation

interfaces, the existence of multiple, highly conductive pathways created in the active layer and the unencumbered charge carrier percolation in the cell, guaranteed by the well-matched energy levels with PCDTBT and PC$_{71}$BM.

Also, the effect of the incorporation of the hybrid rGO-Sb$_2$S$_3$ on the stability of the OSCs was investigated. OSCs were tested in open circuit mode under continuous solar illumination (100 mWcm^{-2}) and without encapsulation, in order toallow humidity to directly affect their performance. The aging in binary and ternary OSCs after 24 h of continuous solar illumination was detected to be approximately 42% and 44%, respectively, of the initial PCE. Furthermore, in both OSCs the degradation rate was almost saturated after ~100 h of solar illumination. Therefore, rGO-Sb$_2$S$_3$ incorporation does not have an effect a strong effect on the stability.

6.4 Conclusion

In conclusion, rGO-Sb$_2$S$_3$ nanocrystals were synthesized and utilized as the cascade material in ternary BHJ solar cell based on a PCDTBT:PC$_{71}$BM donor–acceptor pair. GO was used as the starting material and by following a simple and fully controllable solvothermal procedure, simultaneous reduction and decoration of graphene sheets with Sb$_2$S$_3$ nanocrystals was achieved. The energy bands of the rGO-Sb$_2$S$_3$ matched those of PCDTBT donor and PC$_{71}$BM acceptor materials, resulting in V$_{oc}$ increase. In addition, the photocurrent and the FF were increased due to the balanced charge transport and enhanced light absorption owing to the dispersion of the rGO-Sb$_2$S$_3$ nanosheets inside the photoactive layer. The graphene sheets offer instantaneous charge transfer, hindering the recombination phenomena in the inorganic nanocrystals. The PCE improvement was significant and reached a total of 23%, establishing graphene-based inorganic nanocrystals as a very promising material towards efficient ternary blend structures.

REFERENCES

[1] D. H. Wang, J. H. Kim, J. H. Seo, I. Park, B. H. Hong, J. H. Park, A. J. Heeger, *Angew. Chem. Int. Ed.* **2013**, *52*, 2874.

[2] G. Zhao, Y. He, Y. Li, *Adv. Mater.* **2010**, 22, 4355.

[3] C. C. Chen, W. H. Chang, K. Yoshimura, K. Ohya, J. You, J. Gao, Z.Hong, Y. Yang, *Adv.Mater.* **2014**, *26*, 5670.

[4] Z. He, C. Zhong, S. Su, M. Xu, H. Wu, Y. Cao, *Nat. Photonics* **2012**, 6, 591.

[5] F. Goubard, G. Wantz, *Polym. Int.*2014, 63, 1362.

[6] T. Ameri, P. Khoram, J. Min, C. J. Brabec, *Adv. Mater.* **2013**, 25, 4245.

[7] P. Cheng, Y. Lia, X. Zhang, Energy Environ. Sci. **2014**, 7, 2005.

[8] K. S. Novoselov, A. K. Geim, S. V. Morozov, D. Jiang, Y. Zhang, S. V. Dubonos, I. V. Grigorieva, A. A. Firsov,*Science*, **2004**, 306, 666.

[9] F. Chen, J. L. Xia, N. J. Tao, *Nano Lett.*, **2009**, 9, 2571.

[10] J.-U. Lee, D. Yoon, H. Cheong, *Nano Lett.*, **2012**, 12, 4444.

[11] S. Stankovich, D. A. Dikin, G. H. B. Dommett, K. M. Kohlhaas, E. J. Zimney,E. A. Stach, R. D. Piner, S. T. Nguyen, R. S. Ruoff, Nature, **2006**, 442, 282.

[12] D. Jariwala, V. K. Sangwan, L. J. Lauhon, T. J. Marks, M. C. Hersam, *Chem.Soc. Rev.* **2013**, 42, 2824.

[13] E. Kymakis, K. Savva, M. M. Stylianakis, C. Fotakis, E. Stratakis, *Adv. Funct.Mater.* 2013, 23, 2742.

[14] E. Stratakis, K. Savva, D. Konios, C. Petridis, E. Kymakis, *Nanoscale* 2014, 6, 6925

[15] M. M. Stylianakis, M. Sygletou, K. Savva, G. Kakavelakis, E. Kymakis, E. Stratakis, *Adv. Opt. Mater.* **2015**, 5, 658

[16] G. Kakavelakis, D. Konios, E. Stratakis, E. Kymakis, Chem. Mater. **2014**, 26, 5988.

[17] D. Konios, C. Petridis, G. Kakavelakis, M. Sygletou, K. Savva, E. Stratakis, E. Kymakis,*Adv. Funct. Mater.* **2015**, 25, 2213

[18] P. Wang, T. F. Jiang, C. Z. Zhu, Y. M. Zhai, D. J. Wang, S. J. Dong, *Nano Res.* **2010**, 3, 794.

[19] A. Cao, L. Zhen, S. Chu, M. Wu, Z. Ye, Z. Cai, Y. Chang, S. Wang, Q. Gong, Y. Liu,*Adv. Mater.* **2010**, 22, 103.

[20] K. Yuan, L. Chen, L. Tan, Y. Chen, *Chem. Eur. J.* **2014**, 20, 6010.

[21] M. Eck, C. Van Pham, S. Zufle, M. Neukom, M. Sessler, D. Dcheunmann, E. Erdem, S. Weber, H. Borchert, B. Ruhstaller, M. Kruger,*Phys. Chem. Chem. Phys.* **2014**, 16, 12251.

[22] S. W. Tong, N. Mishra, C. L. Su, V. Nalla, W. Wu, W. Ji, J. Zhang, Y. Chan,K. P. Loh,*Adv. Funct. Mater.* **2014**, 24, 1904

[23] S. Baskoutas, A. F. Terzis, *J. Appl. Phys.* **2006**, 99, 013708.

[24] N. Balis, V. Dracopoulos, K. Bourikas, P. Lianos, *Electrochim. Acta* **2013**, 91, 246.

[25] G. Sfyri, S. Sfaelou, K. S. Andrikopoulos, N. Balis, G. A. Voyiatzis, P. Lianos, *J. Phys. Chem. C* **2014**, 118, 16547.

[26] C. H. M. Chuang, P. R. Brown, V. Bulovic ´, M. G. Bawendi, *Nat. Mater.* **2014**, 13, 796

[27] Y. C. Choi, D. U. Lee, J. H. Noh, E. K. Kim, S. I. Seok, *Adv. Funct. Mater.* **2014**, 24, 3587.

[28] M. Shim, P. Guyot-Sionnest, *J. Chem. Phys.***1999**, 111, 6955

[29] W. W. Yu, L. Qu, W. Guo, X. G. Peng, *Chem. Mater.* **2003**, 15, 2854

[30] J. A. Christians, D. T. Leighton, Jr., P. V. Kamat, *Energy Environ. Sci.* **2014**, 7, 1148

[31] J. A. Chang, S. H. Im, Y. H. Lee, H. J. Kim, C. S. Lim, J. H. Heo, S. I. Seok, *Nano Lett.* **2012**, 12, 1863.

[32] J. A. Chang, J. H. Rhee, S. H. Im, Y. H. Lee, H. J. Kim, S. I. Seok, Md. K. Nazeeruddin, M. Gratzel,*Nano Lett.* **2010**, 10, 2609.

[33] S. J. Moon, Y. Itzhaik, J. H. Yum, S. M. Zakeeruddin, G. Hodes, M. Gratzel,*J. Phys. Chem. Lett.* **2010**, 1, 1524 – 1527.

[34] B. Rajbanshi, S. Sarkar, P. Sarkar, *J. Mater. Chem. C,* **2014**, 2, 8967.

[35] H. X. Wang, Q. Wang, K. G. Zhou, H. L. Zhang, *Small*, **2013**, 9, 1266

[36] P. V. Kamat, *J. Phys. Chem. Lett.* **2013**, 4, 908.

[37] D. Konios, M. M. Stylianakis, E. Stratakis, E. Kymakis, *J. Colloid Interface Sci.* **2014**, 430, 108.

[38] G. Kakavelakis, E. Stratakis, E. Kymakis, *Chem. Commun.* **2014**, 50, 5285.

[39] W. Tao, J. Chang, D. Wua, Z. Gao, X. Duan, F. Xu, K. Jiang, *Mater. Res.Bull.* **2013**, 48, 538

[40] S. Ito, S. Tanaka, K. Manabe, H. Nishino, *J. Phys. Chem. C*, **2014**, 118, 16995.

[41] S. Stankovich, D. A. Dikin, R. D. Piner, K. A. Kohlhaas, A. Kleinhammes, Y.Jia, Y. Wu, S. T. Nguyen, R. S. Ruoff,*Carbon*, **2007**, 45, 1558.

[42] P. Christian, P. O'Brien, J. Mater. Chem., **2005**, 15, 4949.

[43] P. Roy, S. K. Srivastava, B. B. Nayak, A. K. Saxena, *Cryst. Growth Des*. **2008**, 8, 2019.

[44] T. S. Senthil, N. Muthukumarasamy, M. Kang, *Mater. Charact*., **2014**, 95,164.

[45] Q. Li, B. Guo, J. Yu, J. Ran, B. Zhang, H. Yan, J. R. Gong, *J. Am. Chem. Soc.* **2011**, 133, 10878.

[46] J. Chen, F. Xu, J. Wu, K. Qasim, Y. Zhou, W. Lei, L. T. Sun, Y. Zhang, *Nanoscale*, **2012**, 4, 441.

[47] G. B. Markad, S. Battu, S. Kapoor, S. K. Haram, *J. Phys. Chem. C*, **2013**, 117,20944

[48] C. M. Cardona, W. Li, A. E. Kaifer, D. Stockdale, G. C. Bazan, *Adv. Mater.*, **2011**, 23, 2367.

[49] P. Robaeys, F. Bonaccorso, E. Bourgeois, J. D'Haen, W. Dierckx, W. Dexters, D. Spoltore, J. Drijkoningen, J. Liesenborgs, A. Lombardo, A. C. Ferrari, F. Van Reeth, K. Haenen, J. V. Manca, M. Nesladek, *Appl. Phys. Lett*. **2014**, 105, 083306

[50] J. L. Wu, F. C. Chen, Y. S. Hsiao, F. C. Chien, P. Chen, C. H. Kuo, M. H.Huang, C. S. Hsu, *ACS Nano*, **2011**, 5, 959

[51] L. Lu, T. Xu, W. Chen, J. M. Lee, Z. Luo, I. H. Jung, H. Park II., S. O. Kim, L. Yu, *Nano Lett.*, **2013**, 13, 2365.

Chapter 7

Enhancement of the Efficiency and Stability of Organic Photovoltaic Devices via the Addition of a Lithium-Neutralized Graphene Oxide Electron-Transporting Layer

Abstract: Lithium-neutralized graphene oxide (GO-Li) was spin coated between the photoactive layer and the metal oxide electron-transporting layer (ETL) as an additional interlayer in organic photovoltaic devices. The introduction of GO-Li leads to a superior interface between the ETL and the photoactive layer. Combined with the reduced work function (WF) of GO-Li (4.3 eV), which is a perfect match with the fullerene acceptor material LUMO level, PCDTBT:PC$_{71}$BM based air-processed devices with a GO-Li layer exhibited a significant enhancement in their power conversion efficiency (PCE) from 5.51 to 6.29% (14.2% increase over that of comparable devices without the graphene-based interfacial layer). Furthermore, the GO-Li device exhibited stability higher than that of the device without the interlayer due to the fact that the GO-Li acts as an internal shield against humidity, protecting the air sensitive polymers and improving the lifetime of the devices.

Keywords: Graphene Oxide, Organic Photovoltaics, Buffer layer, Work Function

7.1 Introduction

OPV devices based on donor−acceptor BHJ structure hold tremendous potential for low-cost, large-scale fabrication on flexible substrates, presenting great compatibility with r2r manufacturing.[1,2,3] Over the past few years, there has been significant progress in the performance of polymer BHJ solar cells because of the intensive effort in the development of new photoactive materials, morphological structures, and fabrication techniques that facilitated enhanced PCE exceeding 9% for single-junction OPVs[4,5,6] and >10% for tandem OPVs.[7,8]

As is well-known, the efficiency of OPVs is highly dependent on the charge extraction efficiency, and therefore, potential barriers at photoactive layer−electrode interfaces have to be minimized. Ideally, there should be sufficient Ohmic contact between the photoactive layer and the electrodes, with the WF of the anode matching the HOMO of the donor material (a conjugated polymer) and the WF of the cathode matching the LUMO of the acceptor material (usually fullerene). To this end, the incorporation of an ETL between the photoactive layer and the cathode can lead to improved charge transport and charge extraction in the device, playing a key role in enhancing the PCE. Additionally, the ETL improves the stability of the device by acting as a shield against the penetration of humidity into the active layer, retarding degradation of BHJ OPVs.[9,10,11]

Graphene, an atomically thin layer of sp^2-bonded carbon atoms, stacked in a 2D honeycomb lattice, has attracted great interest in the scientific community for its extraordinary electrical and optical properties, its mechanical flexibility, and its tunable WF, which give rise to its utilization as various components in novel optoelectronic devices.[12,13,14,15,16,17,18] The extensive research on the production of solution processable graphene by exfoliation of graphite into GO, has allowed the functionalization and processing of graphene flakes with various methods, triggering the large-scale production of graphene-based devices.[19,20] However, designing GO-based materials with controllable electronic properties for application in high-performance devices remains a challenge.

Current state-of-the-art materials for ETLs include certain metalfluorides,[21] n-type semiconductors (e.g. ZnO),[22] and n type organic semiconductors (e.g.

bathocuproine),[23] with TiO$_x$ being by far the most commonly used material.[24] The demand for low-cost and simply processable ETL materials compatible with OPV materials and r2r fabrication techniques has stimulated the scientific interest in graphene. Graphene-based materials have been studied as promising buffer layers by exploiting the tunable character of their WF.

Both as yielded GO and its derivatives, functionalized or doped with molecules to increase the WF, are ideal for application in hole transport layers.[25,26,27] Most recently, our group demonstrated that GO WF can be tuned by ultraviolet laser irradiation in the presence of chlorine gas.[28] By tuning the laser exposure time, we are able to control the doping and reduction levels and therefore to tailor the WF of the chlroninated GO layer from 4.9 eV to a maximal value of 5.23 eV. In this way, hole transportation is enhanced because of the perfect energy matching of the GO-Cl and the polymer donor. Similarly, sulfated and fluorine-functionalized GO with increased WF were also employed as the HTL in OPVs.[29,30] Alternatively, the WF of GOs can be effectively reduced, allowing electrons to efficiently travel to the cathode and thus triggering its use as ETL.[31,32,33]

So far, the highest efficiency with graphene-based ELTs was obtained by Heeger and co-workers,[31] who developed a stamping process to directly transfer stretchable graphene onto the BHJ layer prior to the top cathode deposition. The PCE of the device based on a GO/TiO$_x$ ETL was increased by 6.8% compared to that of the pure TiO$_x$ ETL-based device. The improvement was attributed to the decrease in the electron injection barrier in the BHJ device. However, monolayer graphene is first synthesized by CVD on a copper foil and then transferred to the top of the active layer by stamping, a non-compatible process with r2r mass production of flexible OPVs. On top of that, oxidized metal particles formed during the etching process may become trapped between the graphene and the substrate interface during the transfer step, contaminating the whole device. Another important issue in the transfer process is the possibility of formation of cracks and tearing of graphene, while the complicated, time-consuming stamping technique creates issues concerning the efficiency of the transfer for large area applications. Therefore, a low-cost, high-throughput, facile, and r2r compatible method for incorporating graphene-based ETLs is highly desirable.

In this study, we first report a r2r compatible graphene-based interfacial ETL for low-cost and large-scale integration. We have rationally designed and prepared a simple and fast functionalization of GO with Li alkali metal, resulting in the effective reduction of the WF of GO. The GO-Li exhibits a WF of 4.3 eV, which perfectly matches the LUMO level of fullerene acceptor material leading to improved electron extraction. As a proof of concept, we successfully developed a GO-Li/TiO$_x$ ETL using the solution-processed GO-Li and applied it in a PCDTBT:PC$_{71}$BM-based air processed OPV device, achieving a PCE of 6.29% compared to devices without the GO-Li interlayer, which exhibit a PCE of 5.51%. In addition, the interfacial GO-Li layer serves as an effective oxygen and moisture diffusion barrier resulting in the long-term stability of the device.

7.2 Experimental section

7.2.1 Preparation of graphene oxide[34]

GO was prepared from graphite powder (Alfa Aesar. ~200 mesh) according to a modified Hummers' method. In more detail, graphite powder (0.5 g) was placed into a mixture of sulfuric acid, H$_2$SO$_4$ (40 mL, 98%) and sodium nitrate, NaNO$_3$ (0.375 g). The mixture was then stirred and cooled in an ice bath. While maintaining vigorous stirring, potassium permanganate, KMnO$_4$ (3.0 g) was added in portions over a period of 2 h. The reaction mixture was left for 4 h to reach room temperature before being heated to 35°C for 30 min. It was then poured into a flask containing deionized water (50 mL) and further heated to 70°C for 15 min. The mixture was then decanted into 250 mL of deionized water and the unreacted KMnO$_4$ was removed by adding 3% hydrogen peroxide, H$_2$O$_2$. The reaction mixture was then allowed to settle and decanted. The obtained graphite oxide was purified by repeated centrifugation and redispersion in deionized water until neutralized pH was achieved. Finally, the resulting GO was dried at 60°C in a vacuum oven for 48 h before use.

7.2.2 Preparation of graphene oxide functionalized with lithium (GO-Li)[32]

The chemical functionalization of GO with lithium was performed using an aqueous solution of the previously prepared GO (1.5 mg mL^{-1}, 40 mL). Li$_2$CO$_3$ (200 mg) was then added, and the solution was stirred and heated for 1 h. The polyvinylidene fluoride membrane (0.45 μm) was used to filter and collect the solid, which was then dissolved in water (20 mL). The process of solution and filtration was repeated twice.

7.2.3 Preparation of the titanium suboxide (TiO$_x$) solution

Titanium(IV) isopropoxide {Ti[OCH(CH$_3$)$_2$]$_4$, 5 mL}, 2-methoxyethanol (CH$_3$OCH$_2$CH$_2$OH, 20 mL), and ethanolamine (H$_2$NCH$_2$CH$_2$OH, 2 mL) were added to a three-neckflask under a nitrogen atmosphere. The solution was then stirred for 1 h at room temperature, followed by heating at 80°C for 1 h and 120°C for an additional 1 h. The solution was then cooled to room temperature, and 10 mL of isopropanol (IPA) was added.

7.2.4 Device fabrication and measurements.

PCDTBT and PC$_{71}$BM was purchased from Solaris Chem. PCDTBT and PC$_{71}$BM were dissolved in a 3:1 1,2-dichlorobenzene/chlorobenzene mixture in a 1:4 (4 mg:16 mg) ratio and stirred for at least 72 h at 80°C before being used. The photovoltaic devices reported were fabricated on 20 mm×15 mm ITO glass substrates with a sheet resistance of 10 Ωsq^{-1}. The impurities were removed from the ITO glass through a three-step ultrasonication cleaning process (deionized water with 10% soap, acetone, and IPA). As a buffer layer, PEDOT:PSS, purchased from Heraeus, was spin cast from an aqueous solution on the ITO substrate at 6000 rpm for 60 s, and the average thickness of the layer was 40 nm, followed by baking for 15 min at 120°C inside a nitrogen-filled glovebox. All photoactive layers were subsequently deposited by spin coating the blend solution at 1000 rpm on top of the PEDOT:PSS layer until the thickness reached approximately 70 nm, which was determined from cross-sectional scanning electron microscopy images (not shown), followed by drying at 60°C for~5 min under inert conditions. Then the electron extraction layers were coated by spin casting the solutions on top of the active layer. The TiO$_x$

171

interlayer was dissolved in methanol (1:200) and then spin coated to a thickness of approximately 10 nm (6000 rpm, 40 s) in air. GO and GO-Li interlayers were deposited through spin coating at 2000 rpm for 60 s and both controlled to be 2±0.3 nm thick. The samples were heated at 80°C for 1 min in air. Lastly, 100 nm of Al was deposited through a shadow mask by thermal evaporation on the devices. The area of each device was 4 mm^2, as determined by the overlap of the ITO and the evaporated Al.

The performances of the devices were measured at room temperature with an Air Mass 1.5 Global (A.M. 1.5 G) solar simulator at an intensity of 100 mW cm^{-2}. A reference monocrystalline silicon solar cell from Newport was used to calibrate the light intensity. All measurements were taken in air immediately after device fabrication without the encapsulation process. For the degradation tests, the best performance cell of each photovoltaic device (10 devices fabricated for each case) was chosen and the photovoltaic degradation performances of the 10 tested cells were averaged. In addition, the degradation measurements were taken under ambient conditions without encapsulation.

7.3 Results and Discussion

The GO as synthesized by the Hummers method was doped with lithium alkali metal using Li_2CO_3 as a precursor. The functionalization of GO with lithium was confirmed using XPS and FTIR spectroscopy, while the change in the electronic structure in the functionalized GO was investigated by UPS. The bonding type in GO-Li was characterized by XPS. **Figure 7.1a** shows the XPS C1s spectra of GO and GO-Li. The peaks for GO are assigned to four components that correspond to carbon atoms in different functional groups: the nonoxygenated C at 285 eV (C=C/C−C), the hydroxyl/epoxy groups at 287 eV (C−OH/C−O), the carbonyl groups at 288 eV (C=O), and the carboxylate carbon at 289 eV (O=C−OH).[35] Compared to the C 1s spectrum of pristine GO, that of GO-Li clearly exhibited a decreased intensity for peak(s) corresponding to the hydroxyl/epoxy and carboxylate carbon groups, indicating a partial reduction of GO upon the addition of a Li alkali metal.[36]
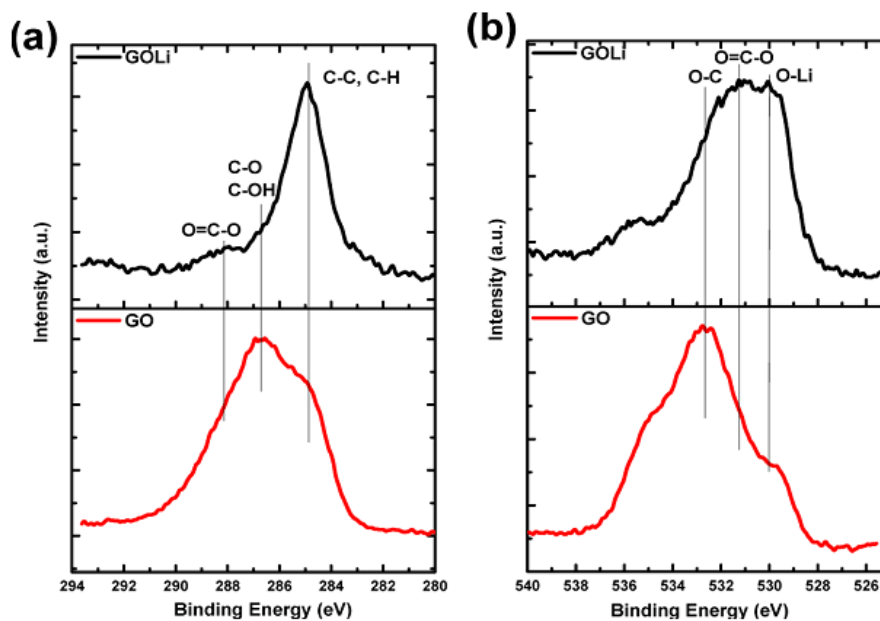
Figure 7.1. High-resolution XPS a) C1s and b) O1s spectra of GO and GO-Li.

In addition, Li and O interactions are identified at 530.1 eV in the XPS O1s spectrum (**Figure 7.1b**) and can be verified by the formation of a new binding energy peak and the overall broadening of the O1s peak.[37,38] **Figure 7.2** shows the FTIR spectra of GO and GO-Li. The peaks at ~3400 cm^{-1} (O−H stretching vibrations), ~1700 cm^{-1} (C=O stretching vibrations), ~1600 cm^{-1} (skeletal vibrations from unoxidized graphitic domains), ~1200 cm^{-1} (C−O−C stretching vibrations), and ~1050 cm^{-1} (C−O stretching vibrations) are characteristic of GO. The intensity of the O−H stretching peak was markedly decreased, and a new peak at ~510 cm^{-1} was observed, arising from the O−Li bond.[39]
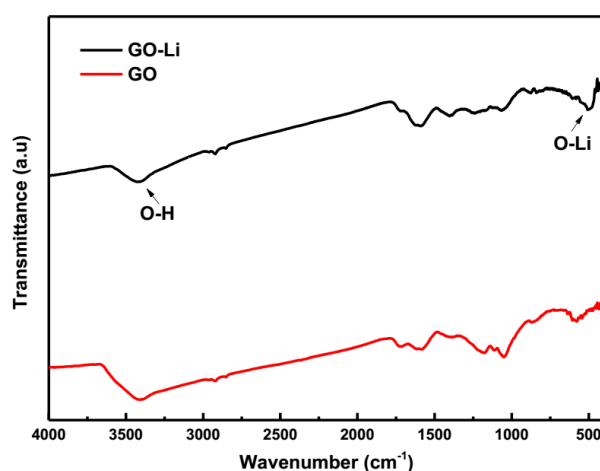

Figure 7.2. FTIR spectra of GO and GO-Li

Prior to the use of GO-Li as the ETL in OPVs, its WF was measured with UPS. The WF of GO and GO-Li can be calculated from the secondary electron energy threshold as:

$$WF = hv - E_F - E_{cutoff}$$

where hv is the He(I) excitation energy, E_F the Fermi level, and E_{cutoff} the high-binding energy cutoff (**Figure 7.3a**). In contrast to our previous work,[28] in which the introduction of the highly electronegative chlorine atoms induces $C^{\delta+}Cl^{\delta-}$ dipoles that are responsible for the downward shift of the Fermi level toward the valence band, the replacement of -H in the carboxyl groups of GO with Li atoms can effectively reduce the WF of GO from 5.0 to 4.3±0.1 eV. Lithium has a low electronegativity and a low WF (2.9 eV).
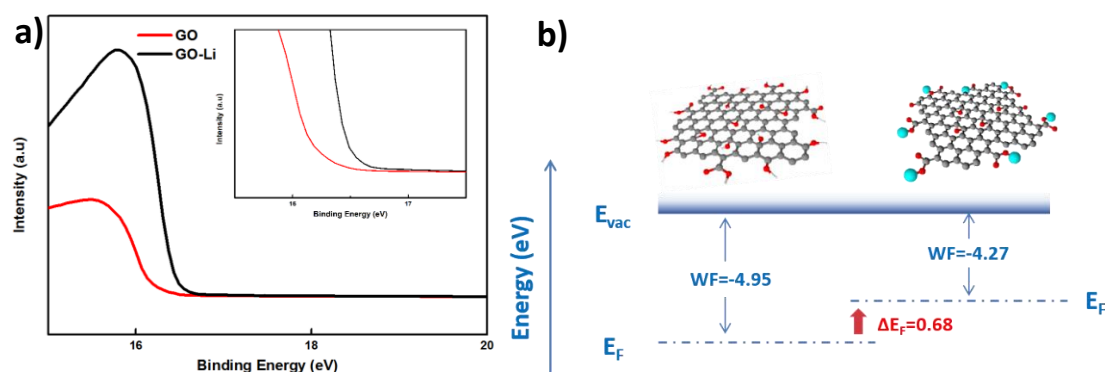

Figure 7.3. UPS a) secondary cutoff region for GO and GO-Li (expanded view of the secondary cutoff region features). b) Energy diagram showing the Fermi level of GO (left) and its shifting after the functionalization with Li alkali metal (right).

When bonded in GO, Li atoms lose their valence electrons to the GO plane, and the resulting positive Li^+ induces dipoles.[40] This transfer of charge from the metal to the GO plane shifts the Fermi level toward the vacuum, yielding a difference in the Fermi level between the two materials of 0.67 eV, which is responsible for the decrease in WF (**Figure 7.3b**).[41] The WF of GO-Li displays a better match with the LUMO level of $PC_{71}BM$ (4.3 eV) (**Figure 7.4a**), triggering its use as an interlayer material for efficient electron extraction.
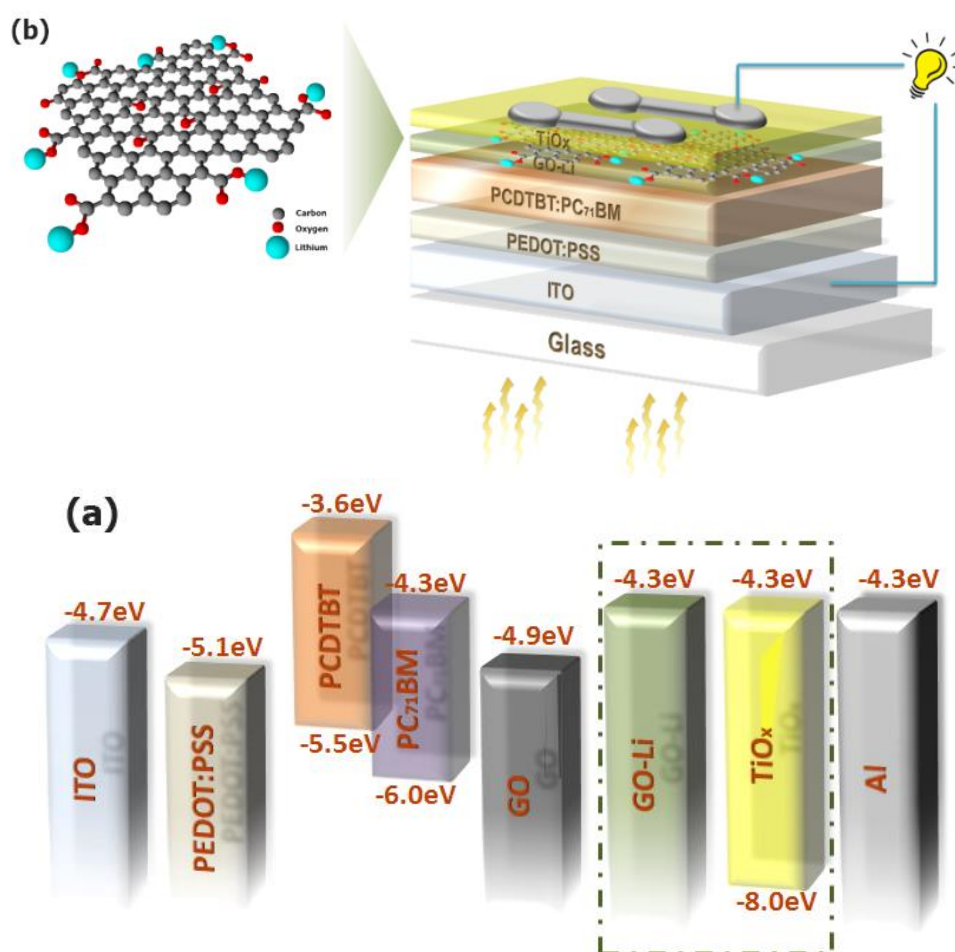
Figure 7.4. a) Energy level diagram depicting the revalent energy levels under flat conditions of all materials used in OPV cells studied and not the actual interfaces. b) Schematic illustration of the BHJ OPV device with GO-Li/TiO$_x$ as the ETL.

To assess the viability of GO-Li as the ETL in OPVs, we employed three different device architectures (**Figure 7.4b**) based on the same active layer (PCDTBT:PC$_{71}$BM) and varying only the respective ETL (TiO$_x$, GO/TiO$_x$, and GO-Li/TiO$_x$). AFM images (**Figure 7.5**) display the surface morphology of PCDTBT:PC$_{71}$BM films with and without the ETL layers. Clearly, the morphology of the GO-Li modified active layer surface (**Figure 7.4c**) is quite homogeneous and smooth, with a rms roughness value of 0.57 nm. The incorporation of GO-Li as an interlayer between the active layer and the TiO$_x$ planarizes the active layer surface roughness, facilitating the TiO$_x$ coating. The GO-Li/TiO$_x$ bilayer structure exhibited a smooth surface with a rms roughness of 0.70 nm compared to that of bare TiO$_x$ (0.89 nm).
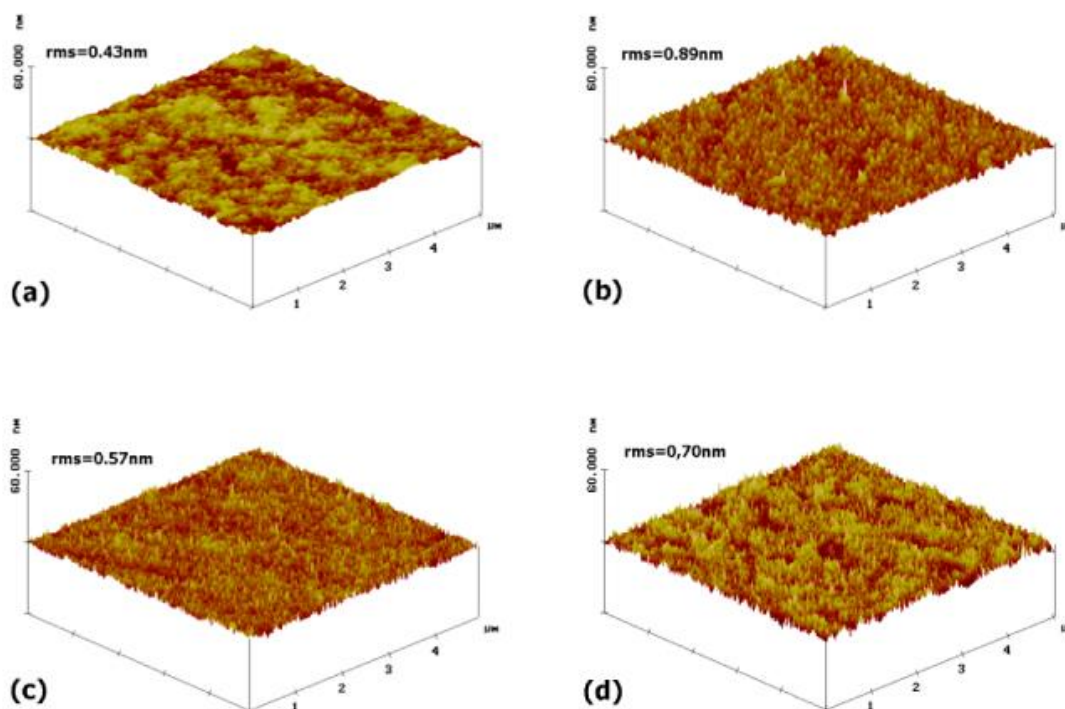
Figure 7.5. AFM micrographs and root-mean-square values of the PCDTBT: PC$_{71}$BM active layer a) without ETL, b) with TiO$_x$, c) with GO-Li, or d) with GO-Li/TiO$_x$ as the ETL.

The active layer surface modification was also confirmed with the contact angle measurement. As shown in **Figure 7.6**, the contact angle of the active layer surface (PCDTBT:PC$_{71}$BM without and with GO-Li) was measured to investigate the changes to the surface after the deposition of the additional interfacial layer. The contact angle of the PCDTBT:PC$_{71}$BM layer was 93.1±1.2, because of its hydrophobic property. In contrast, the contact angle of the PCDTBT:PC$_{71}$BM/GO-Li layer was 72.3±0.4°. The images clearly demonstrate the improvement in the surface wettability of the PCDTBT:PC$_{71}$BM active layer, resulting in a better film forming property, in full agreement with AFM measurements.
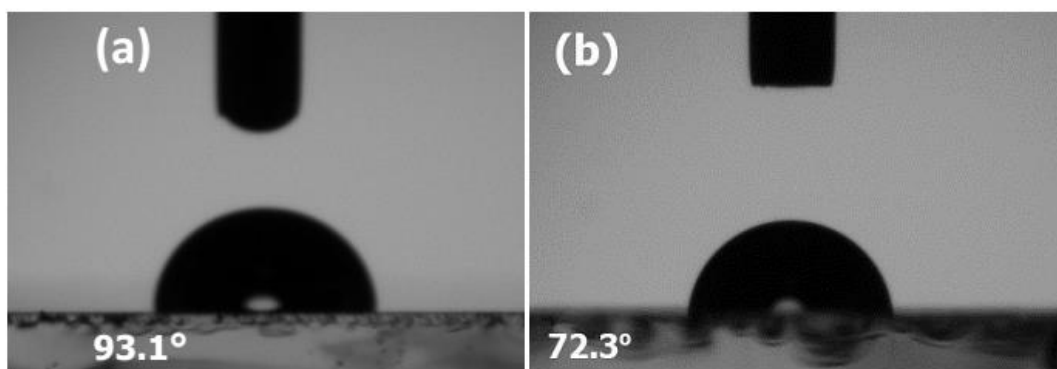
Figure 7.6. Contact angle images of (a) PCDTBT:PC$_{71}$BM and (b) PCDTBT:PC$_{71}$BM/ GO-Li.

In addition, the hydrophilic -COO$^-$ groups of GO-Li improve the wettability between the hydrophobic organic active layer surface and the buffer layer. Therefore, the introduction of a GO-Li layer not only reduces the interface potential barrier and contact resistance but also forms a better interfacial contact, facilitating the movement of the electrons to the cathode. It should be noted that the pristine GO film presents a similar contact angle value (71.9°); however, the presence of an energy barrier between the LUMO level of the fullerene and the pristine GO WF interrupts the efficient electron transport to the metal cathode.

Figure 7.7. J−V characteristics of PCDTBT:PC$_{71}$BM photovoltaic devices with different ETLs.

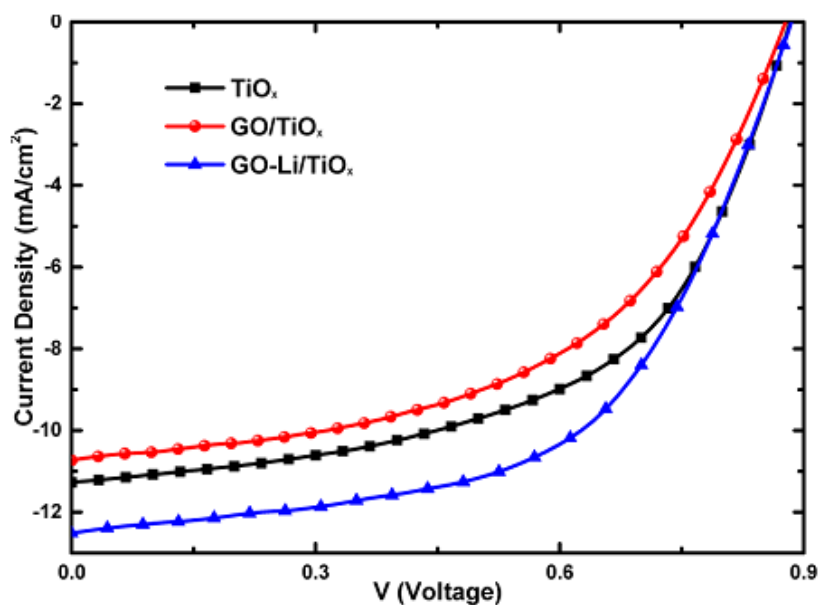**Figure 7.7** shows the illuminated (100 mWcm^{-2}) current density−voltage (J−V) curves of the PCDTBT:PC$_{71}$BM-based OPV devices with TiO$_x$, GO/TiO$_x$, or GO-Li/TiO$_x$ as the ETL. The averaged photovoltaic characteristics obtained from 10 identical devices, consisting of six cells each (60 I−V curves in total), are summarized in **Table 7.1** and indicate that the incorporation of GO-Li as an interfacial layer between the active layer and the TiO$_x$ ETL significantly increases the device efficiency by~14.2% compared to that of the bare TiO$_x$ ETL device. In particular, the later yielded a PCE of 5.51%, with a J$_{sc}$ of 11.28 mAcm^{-2}, a V$_{oc}$ of 878 mV, and a FF of 55.6% compared to the GO-Li/TiO$_x$ bilayer ETL-based device that yielded a significantly enhanced PCE of 6.29%, with a J$_{sc}$ of 12.51 mAcm^{-2}, a V$_{oc}$ of 890 mV, and an FF 56.5%.

Table 7.1. Summary of the Averaged Photovoltaic Parameters of the Fabricated OPVs.

ETL	J$_{sc}$ (mA/cm^2)^a	V$_{oc}$ (mV)^a	FF (%)^a	PCE (%)^a	R$_s$ (Ωcm^2)
TiO$_x$	11.28±0.20	878±3	55.6±0.4	5.51±0.15 (5.66)	18.18
GO/TiO$_x$	10.73±0.19	883±5	51.6±0.3	4.89±0.14 (5.03)	19.68
GO-Li/TiO$_x$	12.51±0.35	890±6	56.5±0.5	6.29±0.28 (6.57)	16.95

^{a} Average photovoltaic characteristics and standard deviations for OPV devices with different ETLs. The numbers in parentheses represent the values obtained for the champion OPV cells. To account for experimental errors, the reported averages and deviations for each ETL are taken for 10 identical devices, consisting of six cells each.

In addition, devices were prepared by replacing the GO-Li interfacial layer with pristine GO to better clarify the effect of WF tuning in device efficiency. Significant decreases in J$_{sc}$ of~15% and in FF of~9% were observed, which can be attributed to the energy barrier of 0.6 eV between the LUMO level of the acceptor material (4.3 eV) and the GO WF (4.9 eV) (**Figure 7.4a**). For ideal electron transport, the LUMO level of the acceptor material should be absolutely equal to the WF of the ETL. Therefore, as the WF of GO-Li perfectly matches the LUMO of PC$_{71}$BM and TiO$_x$ ETL, the electrons are transported without an energy barrier to the cathode. The enhancement of J$_{sc}$ can be attributed to the improved electron transportation due to the two-dimensional nature of the GO-Li interfacial ETL. The planarizing role of GO-Li (**Figure 7.5**) creates a perfect

interface between the ETL and the cathode, leading to an improved Ohmic contact and therefore minimizing the contact resistance at the interface (**Table 7.1**, R_s, obtained by the inverse slop of the I−V curve at the far forward characteristics where the curve becomes linear).

A number of experiments were performed to investigate the effect of GO-Li film thickness on the PCE of the devices. A series of GO-Li thin films were prepared with average thicknesses of 1.3±0.2, 2.0±0.3, and 3.1±0.2 nm. The different thicknesses GO-Li films were utilized as the interfacial ETL in PCDTBT:PC$_{71}$BM devices. The J_{sc}, V_{oc}, FF, and PCE values for each set of devices (over 5 devices with 6 photovoltaic cells were fabricated for each set) are summarized in **Table 7.2**. It can be clearly seen that the performance of the GO-Li based device depends strongly on the GO-Li layer thickness, with the 2±0.3 nm film being the optimum thickness. The inhomogeneous film formed in lower than 2 nm thicknesses results in lower PCE compared with the optimum thicknesses devices, while on the contrary the thicker GO-Li film leads to increased R_s in the device.

Table 7.2. Photovoltaic performance of OPV devices with different GO-Li thicknesses

GO-Li thickness (nm ±0.1)	J_{sc} (mA/cm^2)	V_{oc} (mV)	FF (%)	PCE (%)
0	11.28	878	55.6	5.51
1.3	11.84	880	54.8	5.71
2.0	12.51	890	56.5	6.29
3.1	10.97	887	49.7	4.84

It should also be noted that the OPV devices utilizing GO-Li as the sole ETL, in the absence of a TiO$_x$ layer, exhibited performance that was poorer than that of the TiO$_x$ device (PCE of 5.04%). Although the WF of GO-Li perfectly matches the LUMO level of PC$_{71}$BM and the electron extraction is conducted in the absence of a potential barrier, the main reason for the reduced PCE in sole GO-Li devices is the lack of optical spacing ability of TiO$_x$. TiO$_x$ acts as an optical spacer, which redistributes the electric field inside the devices, resulting in an enhanced photocurrent.[23] By combining the ideal electron transport of GO-Li

and the optical spacing ability of TiO_x, we demonstrated a novel ETL bilayer with strong electron extraction performance.

To gain additional insight into the mechanism responsible for the enhanced performance of the devices, we measured the electron-only space-charge-limited current density (SCLC) for devices with structure: ITO/Al/PCDTBT:PC_{71}BM/ETL/Al with bilayer GO-Li/TiO_x and individual TiO_x as ETLs (**Figure 7.8a**). The SCLC is modeled using the Mott−Gurney equation:[42]

$$J_{SCLC} = \frac{9}{8} \varepsilon_0 \varepsilon_r \mu_e \frac{(V - V_{bi})^2}{d^3}$$

where J_{SCLC} is the current density of SCLC, ε_r is the relative permittivity of the organic active layer, ε_0 is the permittivity of free space, V is the applied voltage, V_{bi} is the built-in voltage, μ_e is the electron mobility, and d is the thickness of the active layer.

Table 7.3. Electron and hole mobilities of the devices with TiO_x and GO-Li/TiO_x as ETL

Electron Only Device Structure	μ_e (cm^2/Vs)
ITO/Al/PCDTBT:PC_{71}BM/TiO_x/Al	$2.28\ 10^{-4}$
ITO/Al/PCDTBT:PC_{71}BM/ GO-Li/TiO_x /Al	$3.19\ 10^{-4}$

Thus, by fitting this equation to the experimental data, we calculated the electron mobilities of the devices (**Table 7.3**). The addition of the GO-Li as an interfacial layer between the photoactive layer and TiO_x increases the electron mobility of the device compared to that of the TiO_x ETL from 2.28×10^{-4} to 3.19×10^{-4} cm^{2}V^{-1}s^{-1}. This improvement in mobility is responsible for the increase in J_{sc} and for the reduction in contact resistance (from 18.18 Ω for the TiO_x ETL to 16.95 Ω for the GO-Li/TiO_x ETL). As expected, the insertion of the GO-Li has no effect on hole mobility, because no modifications related to the anode have been made. The observed increase in electron mobility does not unbalance the device charge extraction capacity, because the electron/hole mobility ratio is slightly altered.
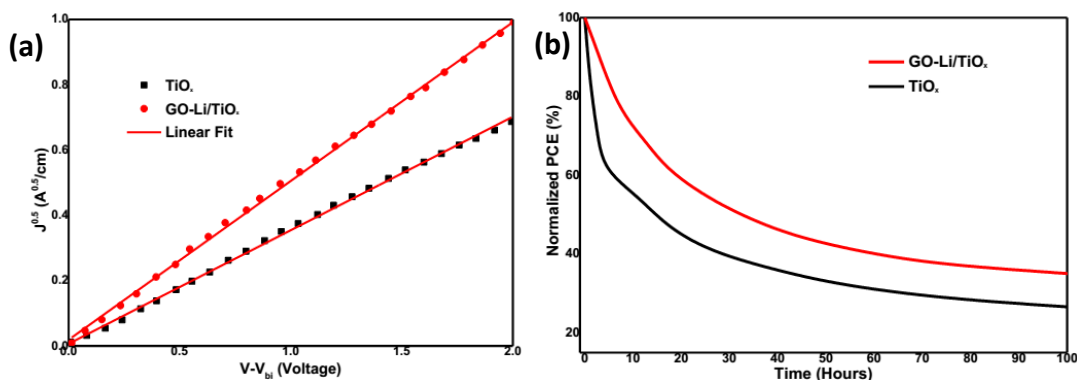
Figure 7.8. a) Electron mobilities of the devices with TiO_x (black symbols) and GO-Li/TiO_x (red symbols) as ETL. b) Stability of the PCE as a function of exposure solar irradiation time.

To gain further insight into the origin of the enhanced J_{sc} in the device, one-dimensional transfer matrix formalism based on optical modeling calculations assuming monochromatic light propagating normal to the device layers was conducted;[43,44] experimentally measured refractive indices and extinction coefficients were used. **Figure 7.9** presents the simulated optical electric field distribution, $|E^2|$, as a function of wavelength in the OPV devices without and with the GO-Li layer. The optical constants of the PCDTBT:$PC_{71}BM$ layer were obtained from previous reports.[45] As shown in **Figure 7.9**, the optical electric field amplitude is slightly enhanced for the device with the GO-Li interfacial layer, compared with that of the device with only the TiO_x. The highest optical electric field amplitudes are 2.77 and 1.6 Vm^{-1} for the device with GO-Li/TiO_x and TiO_x as the ETL, respectively. We can conclude that the addition of the GO-Li interfacial layer increases the electric field amplitude in the photoactive layer, and therefore, more photocurrent is generated in the devices. This effect acts in synergy with the observed reduced series resistance and electron mobility. Therefore, the enhancement in PCE upon the addition of a GO-Li interfacial layer can be attributed to the observed reduced series resistance, increased electron mobility, and enhanced electric field in the device.

Apart from the improved PCE, the incorporation of GO-Li as the ETL affects the device stability. To be more precise, the extra layer of GO-Li acts as an oxygen and moisture barrier that protects the active layer against degradation. OPV devices were tested in open circuit mode with continuous solar illumination (100 $mWcm^{-2}$) and without encapsulation, to allow humidity to directly affect

their performance. **Figure 7.8b** clearly demonstrates that the lifetime of the devices is significantly improved, revealing another vital advantage of the induced graphene-based interfacial ETL. In addition, the GO-Li acts as a surface smoothing layer in combination with the TiO_x layer forming an excellent Ohmic contact between the photoactive layer and the Al cathode, resulting in a significantly reduced degradation rate. A critical point to be considered is that during prolonged solar irradiation, a further photoreduction of the GO-Li layer may take place, as in the case of femtosecond laser-induced reduction of the GO,[46] leading to a more stable interface between the photoactive layer and the Al electrode. The aging in the PCDTBT:PC_{71}BM/TiO_x device after continuous solar illumination for 24 h was detected to be approximately 42% of the initial PCE. On the contrary, in the PCDTBT:PC_{71}BM/GO-Li/TiO_x device, the degradation rate on the same time scale is much slower, preserving approximately 56% of its initial PCE. In both devices, the degradation rate was almost saturated after solar illumination for~100 h. In particular, the single-layer ETL (TiO_x) device demonstrated ~27% of its initial PCE compared to the device using a bilayer ETL (GO-Li/TiO_x) that retained ~35% of its initial PCE value, exhibiting improved stability.
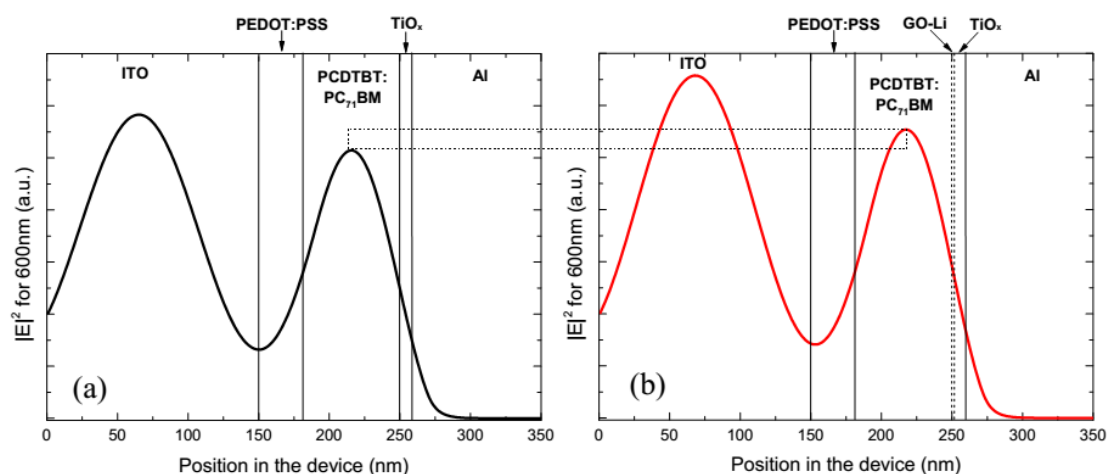

Figure 7.8. Calculated distribution of the normalized modulus squared of the optical electric field $|E^2|$ inside an OPV device: a) glass-ITO (150 nm)/PEDOT:PSS (40 nm)/PCDTBT:PC_{71}BM (70 nm)/TiO_x (10 nm)/Al(100 nm) and b) glass-ITO (150 nm)/PEDOT:PSS (40 nm)/PCDTBT:PC_{71}BM (70 nm)/ GO-Li (2 nm)/TiO_x (10 nm)/Al (100 nm) for a wavelength of 600 nm.

7.4 Conclusion

In summary, we developed a high-throughput, facile strategy for reducing the WF of solution-processed GO with Li alkali metal. The resultant GO-Li has been used in a graphene-based bilayer buffer structure (GO-Li/TiO$_x$) that significantly outperformed the reference device without the additional GO-Li layer, achieving an increase in the PCE of ~14.2%. The results demonstrated a bifunctional role of GO-Li serving both as an interfacial engineering material, improving the Ohmic contact between the ETL and the cathode and the electric field amplitude of the device, and as an extra protection layer against the oxygen and humidity providing better device stability during prolonged illumination. This facile, low-cost method for WF tuning of solution-processed GO is highly desirable as it can significantly facilitate the practical use of this unique material, for developing all-carbon, r2r compatible OPVs. In addition, the solution processable character of GO-Li can boost the scaleup by the development of graphene-based printable inks for large area r2r fabrication. While spin coating is incompatible with r2r processing, the transfer of doctor blading to a r2r pilot line is a straightforward process. In this context, 2 nm thick graphene-based layers can be easily deposited by doctor blading. This new technique demonstratesthe utilization of graphene oxide as a universal buffer layer for both electron and hole transport through fine WF tuning.

REFERENCES

[1] Sariciftci, N. S.; Smilowitz, L.; Heeger, A. J.; Wudl, F. *Science* **1992**, 258, 1474.

[2] Yu, G.; Ga, J.; Hummelen, J. C.; Wudl, F.; Heeger, A. J.*Science* **1995**, 270, 1789.

[3] Li, G.; Zhu, R.; Yang, Y.*Nat. Photonics,* **2012**, 6, 153.

[4] Park, S. H.; Roy, A.; Beaupre, S.; Cho, S.; Coates, N.; Moon, J. S.; Moses, D.; Leclerc, M.; Lee, K.; Heeger, A. J.*Nat. Photonics,* **2010**, 3, 297.

[5] He, Z.; Zhong, C.; Huang, X.; Wong, W.-Y.; Wu, H.; Chen, L.; Su, S.; Cao, Y. *Adv. Mater.,* **2011**, 23, 4636.

[6] Liu, S. J.; Zhang, K.; Lu, J. M.; Zhang, Z.; Yip, H. L.; Huang, F.; Cao, Y.*J. Am. Chem. Soc.* **2013**, 135, 15326.

[7] You, J. B.; Dou, L. T.; Yoshimura, K.; Kato, T.; Ohya, K.; Moriarty, T.; Emery, K.; Chen, C. C.; Gao, J.; Li, G.; Yang, Y.*Nat. Commun.***2013**, 4, 1446−1455.

[8] Dou, L. T.; You, J. B.; Yang, J.; Chen, C. C.; He, Y. J.; Murase, S.; Moriarty, T.; Emery, K.; Li, G.; Yang, Y. *Nat. Photonics,* **2012**, 6, 180.

[9] Seo, J. H.; Kim, H.; Cho, *S.Phys. Chem. Chem. Phys.***2012**, 14, 4062.

[10] You, J.; Chen, C.-C.; Dou, L.; Murase, S.; Duan, H.-S.; Hawks, S. A.; Xu, T.; Son, H. J.; Yu, L.; Li, G.; Yang, Y.*Adv. Mater.,* **2012**, 24, 5267.

[11] Jørgensen, M.; Norrman, K.; Gevorgyan, S. A.; Tromholt, T.; Andreasen, B.; Krebs, F. C.*Adv. Mater,* **2012**, 24, 580.

[12] Bao, Q.; Loh, K. P.*ACS Nano,***2012**, 6, 3677.

[13] Yu, D. S.; Yang, Y.; Durstock, M.; Baek, J.-B.; Dai, L. M.*ACS Nano,***2010**, 4, 5633.

[14] Loh, K. P.; Bao, Q.; Ang, P. K.; Yang, J.*J. Mater. Chem.*, **2010**, 20, 2277.

[15] Guo, C. X.; Guai, G. H.; Li, C. M.*Adv. Energy Mater,* **2011**, 1, 448.

[16] Wöbkenberg, P. H.; Eda, G.; Leem, D.-S.; de Mello, J. C.; Bradley, D. D. C.; Chhowalla, M.; Anthopoulos, T. D.*Adv. Mater.* **2011**, 23, 1558.

[17] Kymakis, E.; Savva, K.; Stylianakis, M. M.; Fotakis, C.; Stratakis, E.*Adv. Funct. Mater.*, **2013**, 23, 2742.

[18] Loh, K. P.; Bao, Q.; Eda, G.; Chhowalla, M. *Nat. Chem.* **2012**, 2, 1015.

[19] Zhang, L.; Liang, J.; Huang, Y.; Ma, Y.; Wang, Y.; Chen, Y. *Carbon,* **2009**, 47, 3365

[20] Bonaccorso, F.; Sun, Z.Opt. *Mater. Express***2014**, 9, 63

[21] Steim, R.; Koglera, F. R.; Brabec, C. J. J. *Mater. Chem.* **2010**, 20, 2499.

[22] Yip, H.-L.; Hau, S. K.; Baek, N. S.; Ma, H.; Jen, A. K.-Y.*Adv. Mater.***2008**, 20, 2376.

[23] Chu, T.-Y.; Lu, J.; Beaupre, S.; Zhang, Y.; Pouliot, J.-R.; Wakim, S.; Zhou, J.; Leclerc, M.; Li, Z.; Ding, J.; Tao, Y.*J. Am. Chem. Soc.* **2011**, 133, 4250

[24] Kim, J. Y.; Kim, S. H.; Lee, H. H.; Lee, K.; Ma, W.; Gong, X.; Heeger, A. J.*Adv. Mater.*, **2006**, 18, 572.

[25] Murray, I. P.; Lou, S. J.; Cote, L. J.; Loser, S.; Kadleck, C. J.; Xu, T.; Szarko, J. M.; Rolczynski, B. S.; Johns, J. E.; Huang, J.; Yu, L.; Chen, L. X.; Marks, T. J.; Hersam, M. C.*J. Phys. Chem. Lett.* **2011**, 2, 3006.

[26] Kim, S.-H.; Lee, C.-H.; Yun, J.-M.; Noh, Y.-J.; Kim, S.-S.; Lee, S. L.; Jo, S. M.; Joh, H.-I.; Na, S. I. *Nanoscale,* **2014**, 6, 7183.

[27] Yang, D.; Zhou, L. Y.; Chen, L. C.; Zhao, B.; Zhang, J.; Li, C. *Chem. Commun.*, **2012**, 48, 8078.

[28] Stratakis, E.; Savva, K.; Konios, D.; Petridis, C.; Kymakis, E. *Nanoscale,* **2014**, 6, 6925.

[29] Liu, J.; Xue, Y. H.; Dai, L. M.*J. Phys. Chem. Lett.*, **2012**, 3, 1928.

[30] Kim, S.-H.; Lee, C.-H.; Yun, J.-M.; Noh, Y.-J.; Kim, S.-S.; Lee, S.; Jo, S. M.; Joh, H.-I.; Na, S.-I. *Nanoscale,* **2014**, 6, 7183.

[31] Wang, D. H.; Kim, J. K.; Seo, J. H.; Park, I.; Hong, B. H.; Park, J. H.; Heeger, A. J.*Angew. Chem., Int. Ed.* **2013**, 52, 2874.

[32] Liu, J.; Xue, Y.; Gao, Y.; Yu, D.; Durstock, M.; Dai, L. *Adv. Mater.***2012**, 24, 2228.

[33] Beliatis, M. J.; Gandhi, K. K.; Rozanski, L. J.; Rhodes, R.; McCafferty, L.; Alenezi, M. R.; Alshammari, A. S.; Mills, A. C. A.; Jayawardena, K. D. G. I.; Henley, S. J.; Silva, S.; Ravi, P. *Adv. Mater.* **2014**, 26, 2078.

[34] Poh, H. L.; Sanek, F.; Ambrosi, A.; Zhao, G.; Sofer, Z.; Pumera, M.*Nanoscale* **2012**, 4, 3515.

[35] Dreyer, D. R.; Park, S.; Bielawski, C. W.; Ruoff, R. S.*Chem. Soc. Rev.***2010**, 39, 228.

[36] Park, S.; An, J.; Piner, R. D.; Jung, I.; Yang, D. X.; Velamakanni, A.; Nguyen, S. T.; Ruoff, R. S.*Chem. Mater.* **2008**, 20, 6592.

[37] Verma, P.; Maire, P.; Nová k, P.*Electrochim. Acta* **2010**, 55, 6332

[38] Beamson, G.; Briggs, D. High Resolution XPS of Organic Polymers: The Scienta ESCA 300 Database; John Wiley & Sons: Chichester, U.K., **1992**.

[39] Nakamoto, K. Infrared and Raman Spectra of Inorganic and Coordination Compounds, 4th ed.; John Wiley & Sons: New York, **1986**.

[40] Lang, N. D.*Phys. Rev. B,***1971**, 4, 4234.

[41] Zhao, J.; Han, J.; Lu, J. P.*Phys. Rev. B***2002**, 65, 193401.

[42] Shrotriya, V.; Yao, Y.; Li, G.; Yang, Y.*Appl. Phys. Lett.*, **2006**, 89, 063505.

[43] Pettersson, L. A. A.; Lucimara, S. R.; Inganas, O.*J. Appl. Phys.* **1999**, 86, 487.

[44] Burkhard, G. F.; Hoke, E. T.; McGehee, M. D. *Adv. Mater.* **2010**, 22, 3293.

[45] Nickel, F.; Sprau, C.; Klein, M. F. G.; Kapetana, P.; Christ, N.; Liu, X.; Klinkhammer, S.; Lemmer, U.; Colsmann, A. *Sol. Energy Mater. Sol. Cells*, **2012**, 104, 18.

[46] Kymakis, E.; Savva, K.; Stylianakis, M. M.; Fotakis, C.; Stratakis, *E.Adv. Funct. Mater*, **2013**, 23, 2742.

Chapter 8

High efficient organic photovoltaic devices utilizing work-function tuned graphene oxide derivatives as the anode and cathode charge extraction layer

Abstract: The effective utilization of work function (WF) tuned solution processable graphene-based derivatives as both hole and electron transport layers in organic photovoltaic (OPV) devices is demonstrated. The systematic tuning of functionalized graphene oxide (GO) WF took place by either photochlorination for WF increase, or lithium neutralization for WF decrease. In this way, the WF of the photochlorinated GO layer was perfectly matched with the HOMO level of two different polymer donors, enabling excellent hole transport. While the WF of the lithium functionalized GO was perfectly matched with the LUMO level of the fullerene acceptor, enabling excellent electron transport. The utilization of these graphene-based hole and electron transport layers in PTB7:PC$_{71}$BM active layer devices, led to ~19% enhancement in power conversion efficiency (PCE) compared to the reference graphene free device, resulting in the highest reported PCE for graphene-based buffer layer OPVs of 9.14%. The proposed techniques open new paths towards novel material and interface engineering approaches for a wide range of new applications, including flexible electronics, OPVs, perovskite solar cells, organic light emitting diodes, and photosensors, as well as traditional electronic devices.

Keywords: Organic photovoltaic, Graphene derivatives, Work function tuning, Graphene-based buffer layers

8.1 Introduction

During the past decade, OPV devices based on the BHJ blend have attracted great interest due to their potential for low fabrication cost but, more importantly their versatility for large-scale fabrication on flexible substrates.[1,2,3,4] Despite the numerous studies on OPVs, their PCE compared to the silicon and other inorganic materials based photovoltaic technologies remains relatively low (~10%).[5] Aiming to improve the competitiveness of OPVs, extensive research effort has been devoted to the interface engineering of devices and especially to the introduction of charge extracting interlayers between the BHJ layer and the electrodes.[6,7]

In contrast to inorganic PVs where surface doping is responsible for Ohmic contacts, OPVs require alternative strategies in terms of the interface engineering. The introduction of buffer layers with electron and hole blocking (or transport) properties between the donor:acceptor active layer and the anode and cathode respectively, can effectively reduce recombination and current leakage generated at the photoactive layer-electrode interface and enhance the open circuit voltage (V_{oc}) of the device.[8] A number of HTL materials for OPVs have been used, including transition metal oxides (e.g. MoO_3, NiO)[9,10] and self-assembled organic molecules,[11,12] with the PEDOT:PSS being the current state-of-art material. On the other hand, the most regularly used electron transport layer (ETL) materials include certain metal fluorides,[13,14] n-type inorganic (e.g. TiO_x, ZnO)[15,16] and organic (e.g. bathocuproine)[17] semiconductors. However, there are several drawbacks concerning the current state-of-the-art buffer layers, leading to decreased OPV stability, arising, for example, from the acidic and hygroscopic character of PEDOT:PSS[18] or the sensitiveness of sol-gel prepared TiO_x to moisture, and also the increased manufacturing cost, since some metal oxides and metal fluorides require high vacuum thermal deposition and therefore are incompatible with r2r processes and thus with flexible photovoltaics. In addition, the majority of the aforementioned materials do not allow their WF tuning,[19] preventing the direct energy match with the numerous active layer donors and acceptors and urging the need for universal, tuned WF buffer layer materials.

Recently, GO, a graphene sheet functionalized with oxygen groups (e.g. epoxy, hydroxyl, carboxyl), and its derivatives have been investigated as alternatives HTLs and ETLs.[20,21,22,23,24] The availability of the reactive groups on GO sheets enables its further functionalization with molecules, manipulating in this way its optoelectronic properties.[25,26] In addition, the solution processable character of GO[27] and its derivatives is in accordance with the r2r mass fabrication processes, that are often cited as the advantage of OPVs compared to conventional photovoltaic technologies. More importantly, its tunable WF character makes GO an ideal precursor for creating new materials with WF values perfectly matching the HOMO level of the donor material (a conjugated polymer) and the LUMO level of the acceptor material (usually fullerene derivative). So far, only one study have investigated the photovoltaic performance of devices incorporating simultaneously GO derivatives as HT and ET layers, demonstrating 16% increase in the PCE.[28] Nevertheless, the lack of WF tunability of the produced GO derivatives limits its application on only the well-studied P3HT:$PC_{61}BM$ based cell, since hole or electron transport is not energetically possible with the current cutting edge active layers, such as PTB7:$PC_{71}BM$. Therefore low-cost, high-throughput, facile and r2r compatible methods for WF tuning of the GO buffer layers, which will allow their application in high efficient BHJ OPVs are highly desirable.

In this work, a novel, all graphene-based buffer layer OPV device is realized, investigating the effect of the simultaneously utilization of two different solution processable functionalized GOs as cathode and anode buffer layers, on the PCE of the device. The two r2r compatible graphene-based materials, previously prepared by our group, the first one through laser-induced doping of GO with chloride (GO-Cl) leading to a WF increase from 4.9 to 5.16 eV and 5.23 eV and the second one after a simple and fast functionalization of GO with Li alkali metal (GO-Li) leading to a WF decrease from 4.9 to 4.3 eV, exploited unique electron and hole blocking (or transport) properties respectively. The increased WF of GO-Cl and on the other hand the reduced surface potential of GO-Li provide a direct match with the HOMO level of the donor PTB7 and the LUMO level of the acceptor $PC_{71}BM$ respectively, leading to enhanced photovoltaic performance, outperforming by ~19% the reference graphene free device. To our knowledge, the achieved PCE is the highest reported for all

graphene based buffer layers OPV devices, opening new paths to develop a new generation of low cost, high efficient, solution processable all-carbon solar cells.

8.2 Experimental section

8.2.1 Preparation of graphene oxide[29,30]

GO was prepared from purified natural graphite powder (Alfa Aesar, ~200 mesh) according to a modified Hummers' method. Specifically, graphite powder (0.5 g) was placed into a cold mixture of concentrated H_2SO_4 (40 mL, 98%) and $NaNO_3$ (0.375 g) under vigorous stirring for 1 h, in an ice bath. $KMnO_4$ (3 g) was slowly added into the reaction mixture over 1 h. The mixture was then stirred at room temperature for 4 h. Thereafter, the reaction mixture was allowed to reach room temperature before being heated to 35°C for 30 min, forming a thick paste. It was then poured into a beaker containing 50 mL of deionized water and further heated to 90°C for 30 min. 200 mL of distilled water was added, followed by a slow addition of H_2O_2 (3 mL, 30%), turning the color of the solution from dark brown to yellow. The reaction mixture was then allowed to settle down and decanted. The graphite oxide obtained was then purified by repeated high-speed centrifugation (4200 rpm, 3 min) and redispersing in deionized water to neutralize the pH (~10 times needed). Finally, the resulting GO was dried at 60°C in a vacuum oven for 48 h.

8.2.2 Preparation of photochlorinated graphene oxide (GO-Cl) films[23]

The as-spun GO layers on ITO/glass substrates were subjected to irradiation by a KrF excimer laser source emitting 20 ns pulses of 248 nm at 1 Hz repetition rate that was translated onto the film area. For uniform exposure of the whole sample to laser radiation, a top-flat beam profile of 20×10 mm^2 was obtained using a beam homogenizer. The whole process took place into a vacuum chamber at 50 Torr Cl_2 gas pressure maintained through a precision micro valve system. Different combinations of laser powers (P) and number of pulses (N_P) were tested in an effort to optimize the photochemical functionalization

processes. In a typical experiment, the sample was irradiated at a constant P with N_p=10, 20, 30, 40, 50, 60, 120, 600 and 1200, corresponding to different photochemical reaction times.

8.2.3 Fabrication of graphene oxide functionalized with lithium (GO-Li)[24]

The chemical functionalization of GO with lithium was performed using an aqueous solution of the previously prepared GO (1.5 mg mL^{-1}, 40 mL). Li_2CO_3 (200 mg) was then added, and the solution was stirred for 1 h. A polyvinylidene fluoride membrane (0.45 μm) was used to filter and collect the solid, which was then dissolved in water (20 mL). The process of solution and filtration was repeated twice.

8.2.4 Preparation of the titanium suboxide (TiO$_x$) solution:[31]

Titanium(IV) isopropoxide {Ti[OCH(CH$_3$)$_2$]$_4$, 5 mL}, 2-methoxyethanol (CH$_3$OCH$_2$CH$_2$OH, 20 mL), and ethanolamine (H$_2$NCH$_2$CH$_2$OH, 2 mL) were added to a three-neck flask under a nitrogen atmosphere. The solution was then stirred for 1 h at room temperature, followed by heating at 80°C for 1 h and 120°C for an additional 1 h. The solution was then cooled to room temperature, and 10 mL of methanol was added.

8.2.5 Device fabrication and measurements

PCDTBT:PC$_{71}$BM were dissolved in 1,2-dichlorobenzene:chlorobenzene (3:1) with a 1:4 (4 mg:16 mg) ratio. A PTB7:PC$_{71}$BM 1:1.5 (10 mg:15 mg) ratio was dissolved in chlorobenzene, followed by the addition of 1,8-diiodooctane (DIO) to give overall DIO amount of 3%. The photovoltaic devices reported were fabricated on 20 mm by 15 mm ITO glass substrates with a sheet resistance of ~20 Ω sq^{-1}. The impurities were removed from the ITO glass through a three-step cleaning process (detergent deionized water, aceton, isopropanol). Before the deposition of the HTL, the substrates were placed inside a ultraviolet ozone cleaner in order to remove the organic contamination and increase the surface hydrophilicity of ITO-coated substrates. The PEDOT:PSS (Al 4083) HTL, purchased from Heraeus, was spin-cast from an

aqueous solution on the ITO substrate at 6000 rpm for 60 s and the average thickness of the layer was 30 nm, followed by baking for 15 min at 120°C inside a nitrogen-filled glove box. All photoactive layers were subsequently deposited by spin-coating the blend solutions at 1000 rpm on top of PEDOT:PSS, GO and GO-Cl layers. Then the electron extraction layers were coated by spin casting the solutions on top of the active layers. The TiOx interlayer was dissolved in methanol (1:200) and then spin coated to a thickness of approximately 10 nm (6000 rpm, 40 s) in air. GO and GO-Li interlayers were deposited through spin coating at 2000 rpm for 60 s and both controlled to be 2±0.3 nm thick. The devices with PCDTBT:PC$_{71}$BM blend were then heated at 80 °C for 1 min in air, while the PTB7:PC$_{71}$BM-based devices were dried inside a vacuum antichamber with dynamic vacuum for ≈15 min. Lastly, 100 nm of Al was deposited, at a standard rate of 1.5 Ås^{-1}, through a shadow mask by thermal evaporation on the devices through a shadow mask to define an active area of 4 mm^2 for each device.

The performances of the devices were measured at room temperature with an Air Mass 1.5 Global (A.M. 1.5 G) solar simulator at an intensity of 100 mWcm^{-2}. A reference monocrystalline silicon solar cell from Newport was used to calibrate the light intensity. The external quantum efficiency measurements were conducted immediately after device fabrication using an integrated system (Enlitech, Taiwan) and a lock-in amplifier with a current preamplifier under short-circuit conditions. The light spectrum was calibrated using a monocrystalline photodetector of known spectral response. The OPV devices were measured using a Xe lamp passing through a monochromator and an optical chopper at low frequencies (~200 Hz) in order to maximize the signal/noise (S/N) ratio. The spot size of the insident monochromatic light was absolute equal with device active area

8.3 Results and Discussion

8.3.1 Work function tuning

The as synthesized through the modified Hummers method GO was used as the pristine material to perform the functionalization and the subsequent WF tuning. In particular, the as-spun GO layers on ITO/glass substrates were subjected to irradiation by a KrF excimer laser source emitting 20 ns pulses of 248 nm at 1 Hz repetition rate in the presence of chlorine (Cl_2) precursor gas. To implement and investigate the GO WF tuning, different N_P was used, increasing from 1 to 65. **Figure 8.1a** presents the GO WF change with respect to the applied N_P. It is clear that the WF increases as the exposure is more intense, and tends to saturate at 5.23 eV for N_P=60, because after this point the level of reduction tends to be very important in the tradeoff between the reduction and doping. In particular, the polar character of C-Cl bonds induced by the formation of surface $C^{\delta+}$-$Cl^{\delta-}$ dipoles owing to the different electronegativity between carbon and chloride (2.55 for C compared to 3.16 for Cl) is responsible for the Fermi level downward shift towards the valence band of GO-Cl, and the subsequent increase in the WF.[32,33] Thus, this simultaneous chloride doping[20] and the partial reduction process[34] gives the possibility of wide a WF tuning allowing the use of GO-Cl as a universal HTL in different optoeletronic devices. **Figure 8.1b** demonstrates such dipoles formation in the C-Cl covalent bonds at the edges and/or Cl-C=O groups located outside the graphene basal plane.[32]
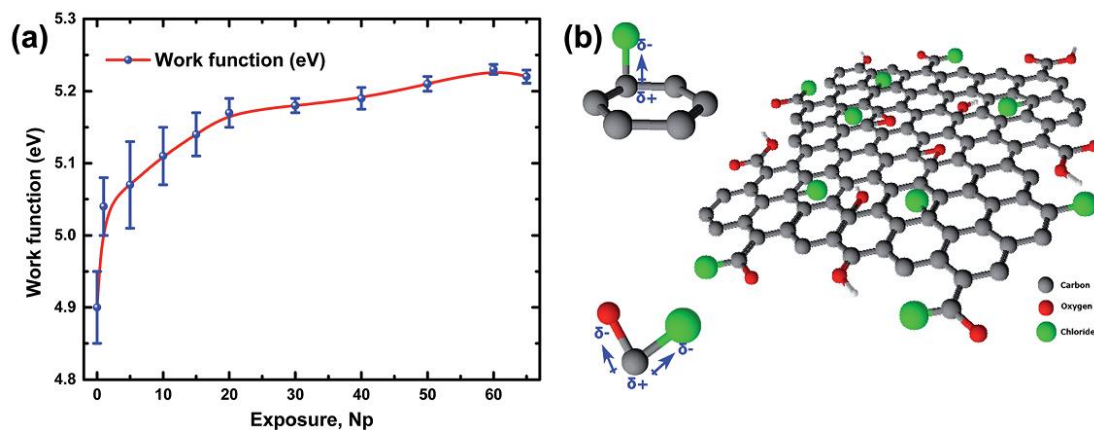
Figure 8.1. a) Work function tuning of GO-Cl films as a function of the N_p exposure. b) 3D chemical structure if the photochlorinated GO, illustrating the formation of $C^{\delta+}$-$Cl^{\delta-}$ dipoles.

In contrast to laser induced chloride doping of GO, the replacement of -H in the carboxyl groups of GO with Li atoms can effectively reduce the WF of GO. The GO doping was performed using lithium carbonate (Li_2CO_3) as a precursor. Lithium has low electronegativity value and low WF (2.9 eV). When bonded in GO, Li atoms lose their valence electrons to the GO plane, with the resulted positive Li^+ inducing dipoles.[35] The generated charge transfer from the metal to the GO plane lead to an upward shift of the Fermi level toward the vacuum, yielding a difference in the Fermi level between the two materials of 0.68 eV, which is responsible for the WF decrease to ~4.3±0.1 eV, establishing GO-Li as an ideal candidate ETL material for OPVs, since its WF perfect matches the LUMO level of the state of the art electron acceptor materials ($PC_{71}BM$). **Figure 8.2** summarizes our findings on GO functionalization to produce GO-based materials with tunable WF (increased or decreased) values with respect to the pristine materials to be used in a variety of optoelectronic applications.
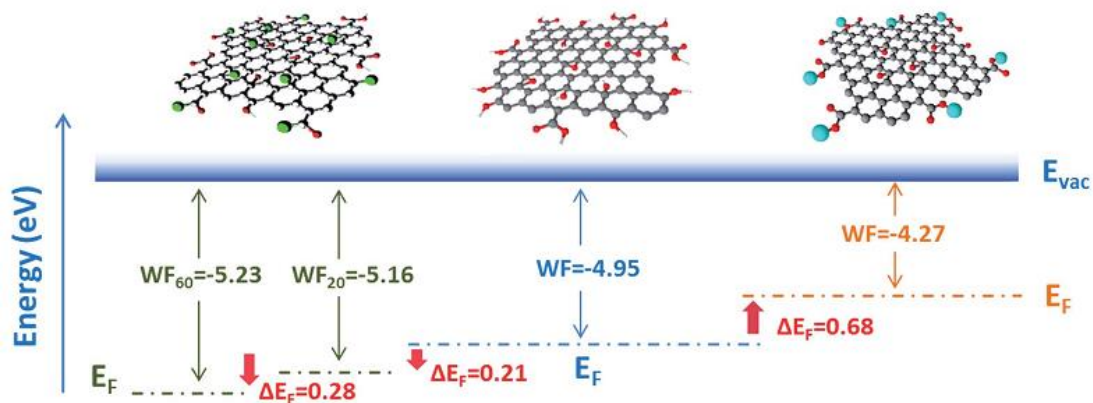
Figure 8.2. Energy diagram showing the Fermi level of GO (middle) and its shifting after the functionalization with Cl (left) and Li alkali metal (right). In the case of photochlorination different WF values can be achieved by controlling the number of pulses (in this case N_p=20 or 60).

8.3.2 Photovoltaic performance

To assess the viability of the proposed GO WF tuning methods in optoelectronic applications, different structures of PCDTBT:PC$_{71}$BM and PTB7:PC$_{71}$BM-based OPV devices were fabricated. More particular, the effects by the incorporation of GO-Cl (with different WF values) as HTL and the GO-Li as ETL on device performance were investigated and compared with the state of the art buffer layer materials (PEDOT:PSS and TiO$_x$ as HTL and ETL respectively). The device structure and the energy level diagrams of the different materials used in this study are shown in **Figure 8.3**.
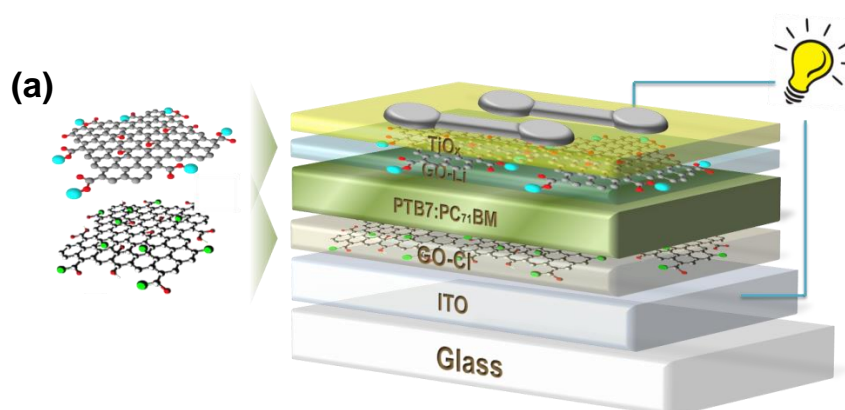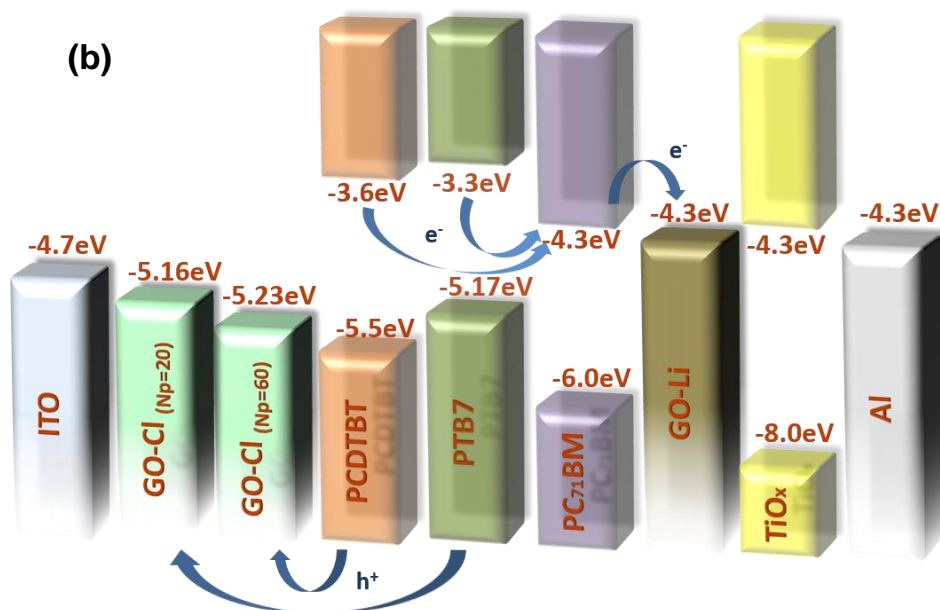
Figure 8.3. a) Schematic illustration of the BHJ OPV device with GO-Cl as the HTL and GO-Li/TiO$_x$ as the ETL. b) Energy level diagram depicting the relevant energy levels under flat conditions of all materials used in OPV cells studied and not the actual interfaces.

The averaged photovoltaic characteristics obtained from 10 identical devices, consisting of 6 cells each (60 current density-voltage (J-V) curves in total) are summarized in **Table 8.1**, indicate that the incorporation of GO-Cl as HTL and GO-Li as ETL significantly increases the PTB7-based device efficiency by ~12% and ~8% compared to the reference device (PEDOT:PSS as HTL and TiO$_x$ as ETL). As depicted in **Figure 8.3b,** the proposed laser induced technique for WF tuning, allowed to produce universal graphene-based HT material with desirable electronic properties. In particular, OPV devices with two different polymer donors a) PCDTBT with HOMO of 5.5 eV and b) PTB7 with HOMO of 5.17 eV were fabricated to clarify the effect of the use of GO-Cl with different WF values on photovoltaic performance. **Figure 8.4a** demonstrates the typical illuminated (100 mW cm^{-2}) J-V curves of the PCDTBT:PC$_{71}$BM OPV devices incorporating PEDOT:PSS, GO and GO-Cl with different WF as HTLs. A significant enhancement in the photovoltaic performance upon the increase of GO-Cl WF values can be observed, leading to a PCE of 6.56% for GO-Cl (5.23 eV) compared to the references devices with PEDOT:PSS (5.49%) and GO (5.59%) HTLs, which can be attributed to

the improved hole transport as verified by the hole mobility measurements.[20] The universal applicability of the proposed method is demonstrated by the fact that the less laser exposed GO-Cl sample exhibiting WF of 5.16 eV (N_p=20) was used as HTL in PTB7:PC$_{71}$BM devices achieving a record PCE of 8.28% for graphene-based HTL devices (**Figure 8.4b**). This difference in optimum WF value for GO-Cl applied in the two different photoactive blends can be explained by the induced offset between the two donors HOMO level and the WF of the GO-Cl. In particular, for PTB7-based devices using 20 pulses for GO chlorination induces a ~0.01eV energy barrier between the HOMO of the PTB7 and the WF of GO-Cl, while in the PCDTBT case, the corresponding minimum energy barrier is 0.27 eV (**Figure 8.4c**). Therefore, it can be concluded that the ability to fine tune the GO-Cl WF with respect to the polymer-donor energy levels offers a facile route to boost the OPV PCEs.

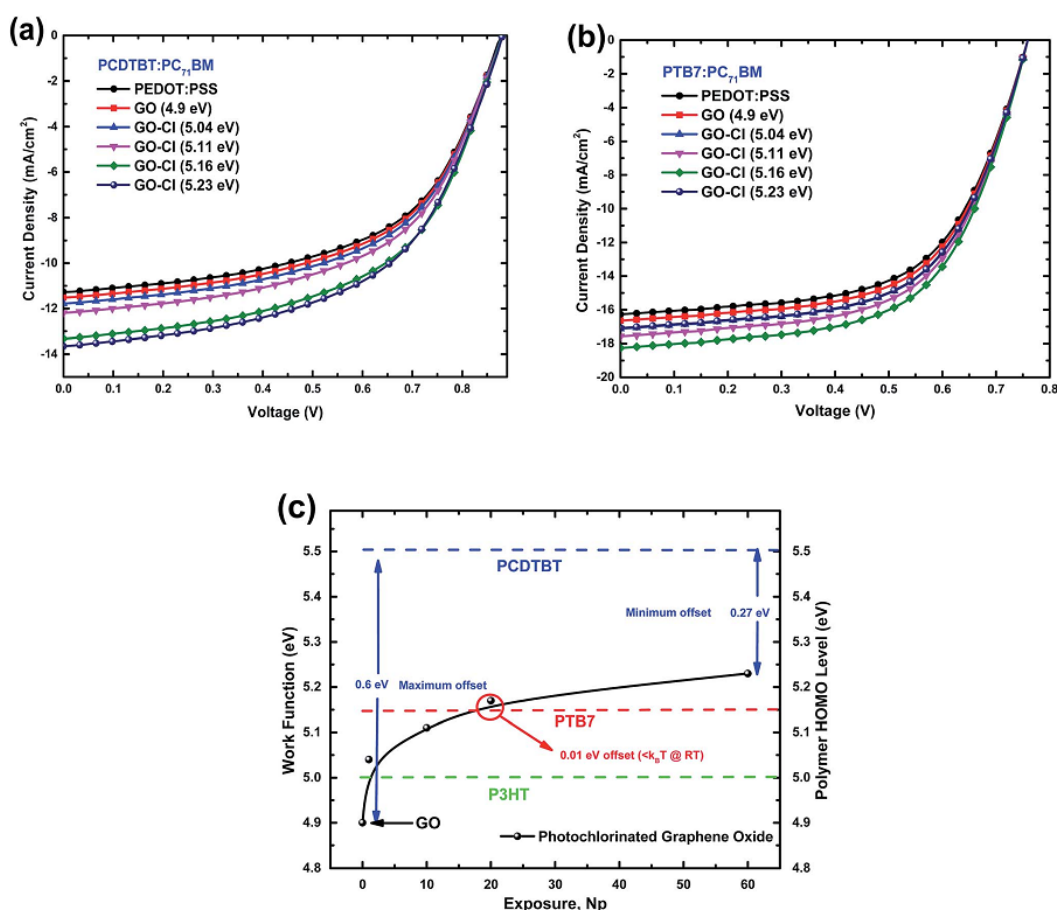**Figure 8.4.** J-V characteristics of a) PCDTBT:PC$_{71}$BM and b) PTB7:PC$_{71}$BM-based photovoltaic devices incorporating different HTLs, but the same TiO$_x$ ETL. c) Graph demonstrating the WF tuning of GO-Cl films as a function of the Np exposure and the

relevant energy offset between the photochlorination treated films and the polymer donor HOMO level.

Figure 8.5 shows the illuminated J-V curves of the PCDTBT:PC$_{71}$BM and PTB7:PC$_{71}$BM-based OPV devices with TiO$_x$, and GO-Li/TiO$_x$ as ETLs. The reference PCDTBT:PC$_{71}$BM-based device incorporating TiO$_x$ ETL yielded a PCE of 5.53%, with a J$_{sc}$ of 11.28 mAcm^{-2}, and V$_{oc}$ of 882 mV, and a FF of 55.6%, compared to the GO-Li/TiO$_x$ bilayer ETL based device that yielded a significantly enhanced PCE of 6.25%, with J$_{sc}$ of 12.51 mAcm^{-2}, V$_{oc}$ of 884 mV, and FF 56.5%. In addition, PCDTBT-based devices were prepared by replacing the GO-Li interfacial layer with GO to better clarify the effect of WF tuning in device efficiency. In this case, a significant decrease of the J$_{sc}$ by ~15% and of the FF by ~9% was observed, which can be attributed to the energy offset of 0.6 eV between the LUMO level of the acceptor material (4.3±0.1 eV) and the GO WF (4.95±0.1 eV). For ideal electron transport, the LUMO level of the acceptor material should be absolute equal to the WF of the ETL. Therefore, as the GO-Li WF perfectly matches the LUMO of PC$_{71}$BM and TiO$_x$ ETL, the electrons transport to the cathode is conducted without energy barrier. The J$_{sc}$ enhancement can be attributed to the improved electron transportation due to the 2D nature of the GO-Li interfacial ETL. Atomic force microscopy measurements have also verified that GO-Li has a planarizing role,[24] creating a perfect interface between the TiO$_x$ ETL and the cathode, leading to an improved Ohmic contact and therefore minimizing the contact resistance at the interface.[24] In this context OPV devices were fabricated using PTB7 as polymer donor. After the introduction of GO-Li between the active layer and the TiO$_x$ the device PCE was increased from 7.4% to 7.98%, mainly due to a significant increase in the J$_{sc}$ which is maybe caused by the improve electron extraction as in the case of PCDTBT based devices.[24]
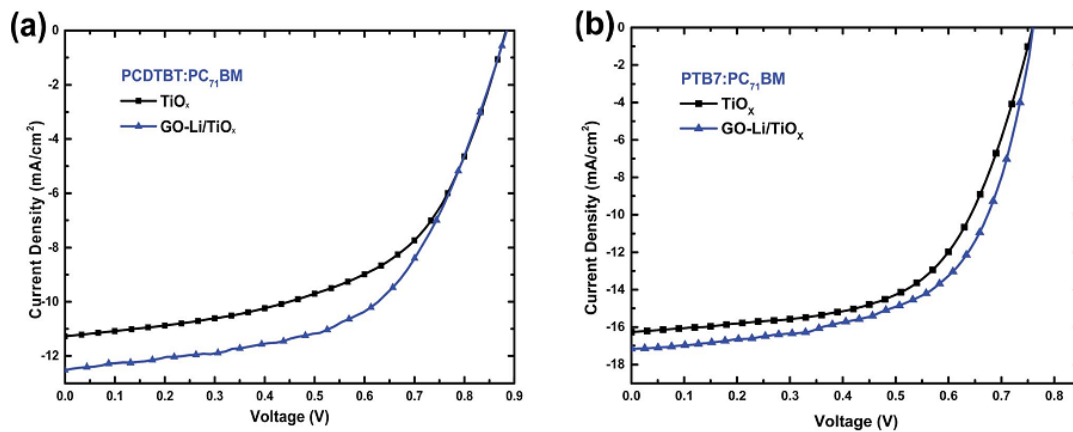
Figure 8.5. J-V characteristics of a) PCDTBT:PC$_{71}$BM and b) PTB7:PC$_{71}$BM-based photovoltaic devices incorporating different ETLs, but the same PEDOT:PSS HTL.

To further support the excellent hole and electron extraction capabilities of GO-Cl and GO-Li respectively, OPV devices incorporating graphene-based materials as both HT and ET layers were fabricated. For this purpose, both the performance of the reference device with the configuration of glass/ITO/PEDOT:PSS/PCDTBT:PC$_{71}$BM or PTB7:PC$_{71}$BM/TiO$_x$/Al and the one structured as glass/ITO/GO-Cl/PCDTBT:PC$_{71}$BM or PTB7:PC$_{71}$BM/GO-Li/TiO$_x$/Al were investigated.
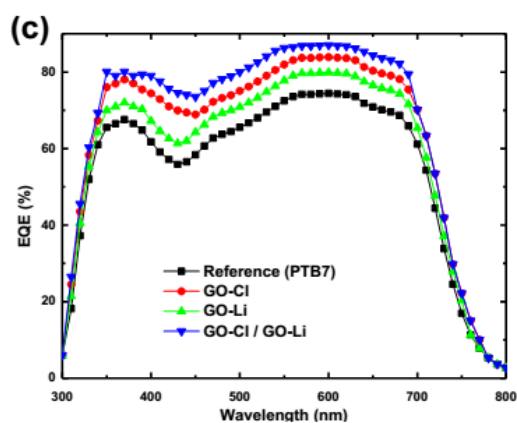

198
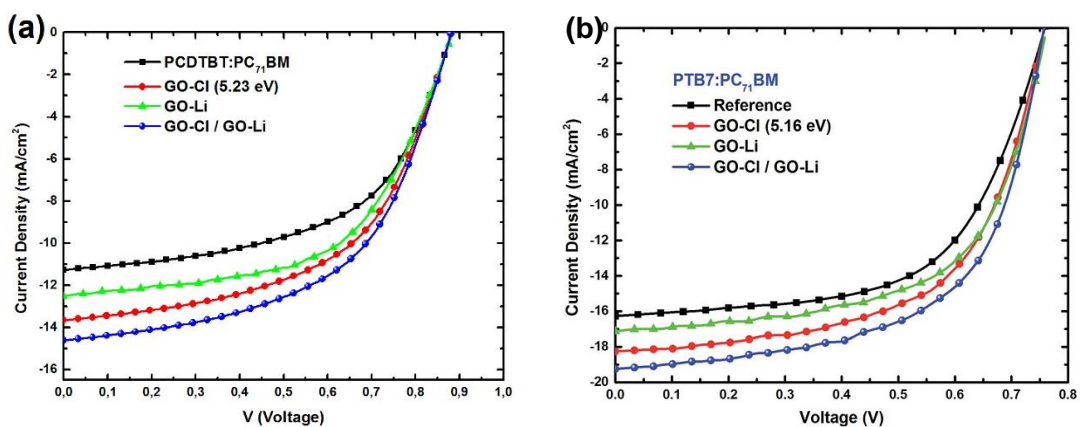
Figure 8.6. J-V characteristics of a) PCDTBT:PC$_{71}$BM, b) PTB7:PC$_{71}$BM-based photovoltaic devices and c) IPCE spectra for the devices using different combinations of hole and electron transport layers of PTB7 based OPV devices.

    Figure 8.6 depicts the J-V curves for the tested devices. Clearly, in both BHJ active layer there is a significant J$_{SC}$ improvement (28% for PCDTBT and 18% for PTB7-based devices) upon the addition of graphene-based interlayers. On the one hand, this is because of the WF match between GO-Li and the LUMO level of PC$_{71}$BM, with the GO-Li modified electrode forming an Ohmic contact with the PCDTBT:PC$_{71}$BM and PTB7:PC$_{71}$BM active layer for improved electron extraction. On the other hand, the WF tuning of GO-Cl produces HTL materials that match the HOMO level of PCDTBT and PTB7 ensuring an Ohmic contact at the interface for efficient hole extraction. However, the alignment of the GO HTL WF to the polymer HOMO, through photochlorination, does not result to a change in the V$_{oc}$. The maximum V$_{oc}$ of bulk heterojuction OPV devices typically results from the polymer donor and fullerene acceptor interface gap, that is the energy difference between the HOMO of the polymer and the LUMO of the fullerene.[36,37] In this way, charge transfer leads the WFs of the ETL and the HTL to be pinned to the LUMO of the fullerene and the HOMO of the polymer respectively.[38] Therefore, the V$_{oc}$ is unaffected, since regarding the WF of the GO-Cl HTL employed, a Fermi level pinning of the HTL WF to the HOMO of the polymer donor takes place, in full agreement with previous works.[39,40] On top of that the actual interface between the HTL and the active layer does not change upon the WF tuning process, since the photochlorination takes place on the spin-coated GO films and does not cause any morphological changes. As a result, both graphene-based buffer layers

OPV devices significantly outperformed the reference ones, leading to a PCE improvement of 30% for PCDTBT and 19% for PTB7-based devices and to a record PCE of 9.14% for graphene-based buffer layer devices.
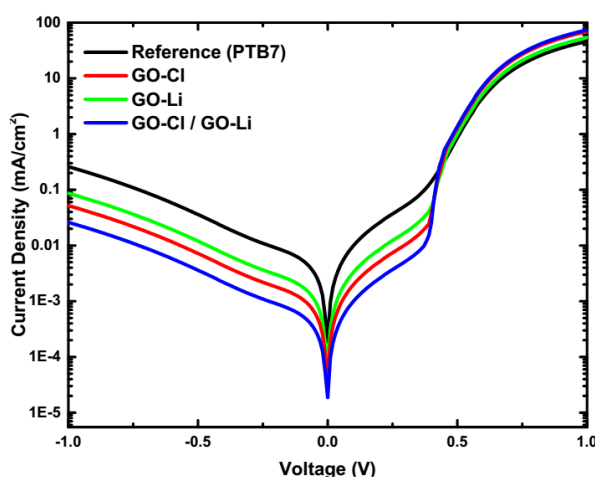

Figure 8.7. Dark J-V characteristics of PTB7:PC$_{71}$BM-based photovoltaic devices incorporating graphene-based HT and ET layers.

The dark J-V curves (**Figure 8.7**) also show excellent diode characteristics with very low leakage current and high rectification ratio for the combination of both HT and ET graphene based devices (forward to reverse factor higher than 10^3) exhibiting that the injected current density in the dark (0.5–1.0 V) is higher than that of the reference device. This is in full agreement with the assumed reduced injection barrier. In order to get an insight for the responsible mechanism of the enhanced device performance, the IPCE curves (**Figure 8.6c**) of the devices with different buffer layer combinations was measured and compared with the pristine one. The pristine device exhibits a maximum IPCE of ~69%, while the GO-Cl/GO-Li based devices exhibit an enhanced maximum of ~86% using PTB7 as donor material. This significant and broad enhancement is in agreement with increased J_{sc} observed in the J-V measurements. It should also be noted that, the J_{sc} calculated by integrating the IPCE spectrum with the A.M. 1.5G spectrum, for the pristine and the GO-Cl/GO-Li based PTB7-PC$_{71}$BM devices are 15.75 and 18.51 mAcm^{-2} respectively. The actual J_{sc} measured from J-V curves were 4% larger than the IPCE calculated values, indicating good accuracy of the OPV measurement. It should be noted that the J-V curves were firstly recorded inside the glove box

in encapsulated OPV devices, and moved outside the glove box for the IPCE measurements.

Table 8.1. Summary of the averaged photovoltaic parameters of the fabricated OPVs. Devices with two different polymer donors a) PCDTBT with HOMO of 5.5 eV and b) PTB7 with HOMO of 5.15 eV were fabricated. PEDOT:PSS, GO and GO-Cl with different WF values were used and compared with respect to their HTL performance in PCDTBT:PC$_{71}$BM and PTB7:PC$_{71}$BM-based photovoltaic devices incorporating the same TiO$_x$ ETL. In addition, TiOx, GO/TiOx and GO-Li/TiOx were used and compared with respect to their ETL performance in PCDTBT:PC$_{71}$BM and PTB7:PC$_{71}$BM-based photovoltaic devices incorporating the same PEDOT:PSS HTL. Finally, combo OPV devices incorporating GO-Cl and GO-Li/TiO$_x$ as HT and ET layers respectively were fabricated and compared with the reference device incorporating PEDOT:PSS and TiO$_x$ as buffer layers.

HTL	J_{sc} (mA cm^{-2})	V_{oc} (V)	FF (%)	PCE (%)
PCDTBT:PC$_{71}$BM				
PEDOT:PSS	11.28±0.12	0.880±0.02	55.6±0.3	5.51 (5.61)
GO	11.52±0.15	0.880±0.02	55.1±0.4	5.59 (5.71)
GO-Cl (5.04 eV)	11.78±0.14	0.880±0.02	55.1±0.3	5.71 (5.82)
GO-Cl (5.11 eV)	12.19±0.17	0.880±0.02	55.2±0.5	5.92 (6.07)
GO-Cl (5.16 eV)	13.32±0.15	0.880±0.02	55.1±0.5	6.46 (6.61)
GO-Cl (5.23 eV)	13.65±0.19	0.880±0.02	55.3±0.4	6.57 (6.79)
PTB7:PC$_{71}$BM				
PEDOT:PSS	16.27 ±0.23	0.760±0.03	59.8±0.6	7.40 (7.60)
GO	16.65±0.21	0.760±0.03	59.7±0.5	7.56 (7.74)
GO-Cl (5.04 eV)	17.13±0.18	0.760±0.02	59.6±0.5	7.78 (7.93)
GO-Cl (5.11 eV)	17.58±0.25	0.760±0.03	59.6±0.6	7.97 (8.19)
GO-Cl (5.16 eV)	18.30±0.27	0.760±0.02	59.9±0.8	8.28 (8.52)
GO-Cl (5.23 eV)	17.09±0.19	0.760±0.03	59.5±.05	7.73 (7.91)
ETL	J_{sc} (mA cm^{-2})	V_{oc} (V)	FF (%)	PCE (%)
PCDTBT:PC$_{71}$BM				
TiO$_x$	11.28±0.12	0.882±0.02	55.6±0.3	5.53 (5.61)
GO/TiO$_x$	10.73±0.19	0.883±0.05	51.6±0.3	4.89 (5.03)
GO-Li/TiO$_x$	12.51±0.35	0.884±0.05	56.5±0.5	6.25 (6.57)

	PTB7:PC$_{71}$BM			
TiO$_x$	16.27±0.23	0.760±0.03	59.8±0.6	7.39 (7.60)
GO/TiO$_x$	15.32±0.31	0.757±0.02	54.8±0.8	6.35 (6.60)
GO-Li/TiO$_x$	17.16±0.25	0.759±0.02	61.2±0.5	7.98 (8.17)
Combo	**J$_{sc}$ (mA cm^{-2})**	**V$_{oc}$ (V)**	**FF (%)**	**PCE (%)**
	PCDTBT:PC$_{71}$BM			
PEDOT:PSS & TiO$_x$	11.28±0.12	0.878±0.02	55.6±0.3	5.51 (5.61)
GO-Cl & GO-Li/TiO$_x$	14.48±0.13	0.880±0.01	56.3±0.5	7.17 (7.31)
	PTB7:PC$_{71}$BM			
PEDOT:PSS & TiO$_x$	16.27±0.23	0.760±0.03	59.8±0.6	7.39 (7.60)
GO-Cl & GO-Li/TiO$_x$	19.28±0.31	0.760±0.02	60.5±0.7	8.83 (9.14)

*Average photovoltaic characteristics and standard deviations for the different structured OPV devices. The numbers in parentheses represent the values obtained for the champion OPV cells. To account for experimental errors, the reported averages and deviations for each ETL are taken for 10 identical devices, consisting of six cells each.

The increased value of J$_{sc}$ was also investigated through electron and hole mobility measurements (**Figure 8.8**). For that purpose electron- and hole-only devices were fabricated with the following structure: ITO/HTL/Active layer/ETL/Au for the hole-only and ITO/Al/HTL/Active layer/ETL/Al for the electron only device respectively. The values calculated were improved for both electron and hole mobilities. Calculations were based on Mott–Gurney equation:

$$J_{SCLC} = \frac{9}{8} \, \varepsilon_r \varepsilon_0 \mu \, \frac{(V - V_{bi})^2)}{d^3}$$

in which ε$_r$ is the relative dielectric constant, ε$_0$ is the permittivity of free-space, m is the charge carrier mobility, V is the applied voltage, V$_{bi}$ is the built-in potential and d is the thickness of the active layer. The mobility values for the reference OPV device were μ$_e$=7.86 x 10^{-5} cm^2 V^{-1} s^{-1} for the electron and μ$_h$ = 1.30 x 10^{-4} cm^2 V^{-1} s^{-1} for the hole mobility while for the GO-Cl / GO-Li based cells the values were μ$_e$=1.59 x 10^{-4} cm^2 V^{-1} s^{-1} for the electron and μ$_h$ = 1.91 x 10^{-4} cm^2 V^{-1} s^{-1} for the hole mobility, respectively. The mobilities were not only increased, especially the electron mobility, but also balanced which is a very

important factor in order to prevent charge accumulation in the device. Before further analyzing our results we should first shed light in the functional mechanism taking place. Because holes are collected at the front electrode in the conventional device structure, and taking into account that the most of the excitons are created near by the front contact the holes mobilities should have slightly lower value compared to the electron mobility. Thus, this is the reason that PTB7 based OPV devices ($\mu_h > \mu_e$) have lower PCE values in the conventional structure compared to the inverted one and in our case this is maybe the reason for the lower PCE enhancement of PTB7 compared to PCDTBT ($\mu_h > \mu_e$). In this context, this is a crucial improvement because electron transport is considered as a factor that limits the photocurrent generation in the conventional PTB7 based devices, since the electron mobility is much lower than the hole mobility. Both electron and hole mobility increases should be attributed on the one hand to GO–Li planaring role[24] and perfect energy levels matching and on the other hand to perfect WF tuning of GO after the photochlorination process. As a result, when we combined GO-Cl HTL and GO-Li interfacial layer the μ_h/μ_e ratio was significantly reduced, from 1.65 to 1.20 as it is observed in **Table 8.2**. We can thus assume, that if we use the inverted structure with the proposed graphene based buffer layers the improvement in the PCE could be much higher than in the conventional structure used here.
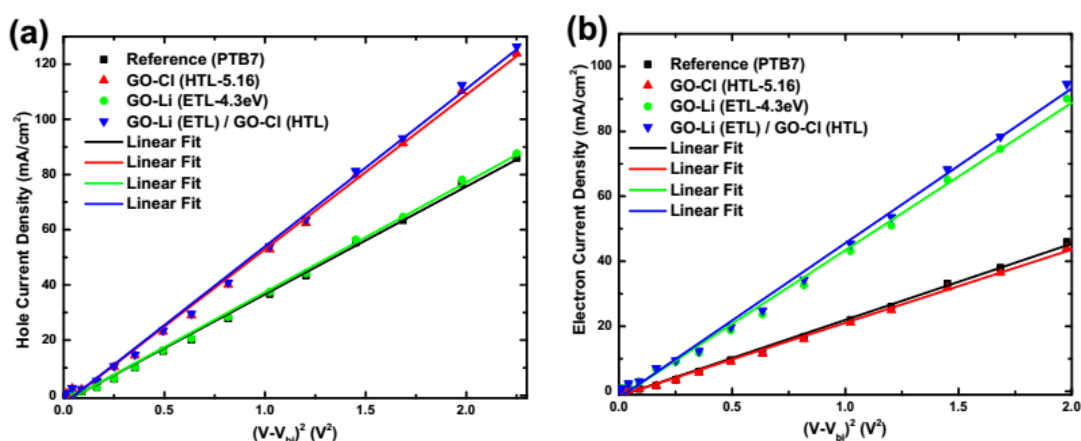

Figure 8.8. J-V^2 characteristics under dark conditions of the fabricated devices for the calculation of a) hole and b) electron mobilities using the Mott–Gurney equation.

Table 2. Electron and hole mobilities of the reference and the device with graphene based buffer layers.

HTL / ETL	μ_h (cm^2 V^{-1} s^{-1})	μ_e (cm^2 V^{-1} s^{-1})	Ratio (μ_h / μ_e)
	PTB7:PC$_{71}$BM		
PEDOT:PSS / TiO$_x$	1.30 x 10^{-4}	7.86 x 10^{-4}	1.65
GO-Cl / GO-Li	1.91 x 10^{-4}	1.59 x 10^{-4}	1.20

In order to examine and confirm our findings (increased J_{sc} and balanced mobilities) we studied the charge recombination kinetics at short circuit for the reference and for the devices with graphene based buffer layers. The J_{sc} can be correlated to illumination intensity (I_{light}) by,

$$J_{sc} = \propto I_{light}^n \ (n \le 1)$$

At short circuit, the bimolecular recombination should be minimum (n < 1) for maximum carrier sweep out. Any deviation from a < 1 implies bimolecular recombination.[41] **Figure 8.9** shows J_{sc} vs. I fitted using the power law described above. The fitting of the data yield a=0.870 for reference device, which can be attributed to bimolecular recombination. After the introduction of GO-Cl and GO-Li, a is 0.968, which imply that bimolecular recombination is significantly reduced.
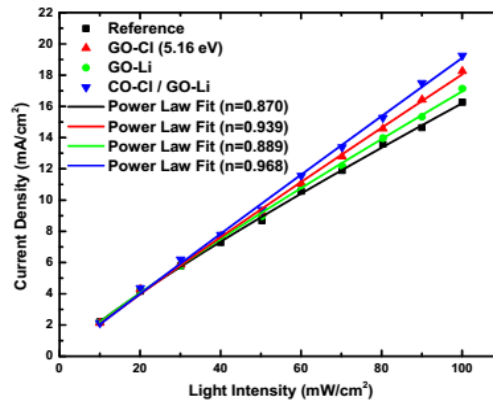

Figure 8.9. Measured J_{sc} of PTB7:PC$_{71}$BM BHJ OPVs using different combination of buffer layer plotted against light intensity (symbol) and fitted power law (line) yield n.

To gain further insight into the origin of the enhanced J_{sc} in the device, one-dimensional transfer matrix formalism based on optical modeling calculations

assuming monochromatic light propagating normal to the device layers was conducted.[42] **Figure 8.10** presents the simulated optical electric field distribution, $|E^2|$, as a function of wavelength in the reference OPV device and using different combinations of buffer layer as reported previously. The optical constants of the PCDTBT:PC$_{71}$BM layer were obtained from previous reports.[43] As shown in **Figure 8.10**, the optical electric field amplitude is significantly enhanced for the device with the GO-Li interfacial layer and GO-Cl as HTL, compared with that of the reference device with only the TiO$_x$ as ETL and with PEDOT:PSS as HTL. The highest optical electric field amplitudes are 0.745 and 0.619 for the dual graphene based buffer device and reference, respectively. This electric field enhancement is directly attributed to the better refractive index (*n*) matching in the sandwich devices using graphene based buffer layer compared to the reference sandwich. In particular, for the reference device PEDOT:PSS n value is ~1.5, PTB7:PC$_{71}$BM is ~1.9 and TiO$_x$ ~2.5 and for the graphene based buffer layer device GO-Cl *n* value is ~1.9, PTB7:PC$_{71}$BM is ~1.9 GO-Li is ~2 and TiO$_x$ is ~2.5. In this way, an important part of the incident electric field is reflected at the interface between PEDOT:PSS and active layer while in the case of GO-Cl due to the perfect *n* matching the interface parasitic reflection is minimum. Also, GO-Li *n* matches with the *n* of active layer and TiO$_x$ acting as a bridge gradually allowing the electric field to pass through the device and thus increasing its intensity.[44] We can conclude that the addition of the graphene based buffer layers increases the electric field amplitude in the photoactive layer, and therefore, more photocurrent is generated in the devices. This effect acts in synergy with the observed balanced charge mobilities. Therefore, the enhancement in PCE upon the addition of a GO-Li interfacial layer and GO-Cl HTL can be attributed to the observed reduced recombination at the interfaces, balanced charge mobilities, and enhanced electric field in the device.
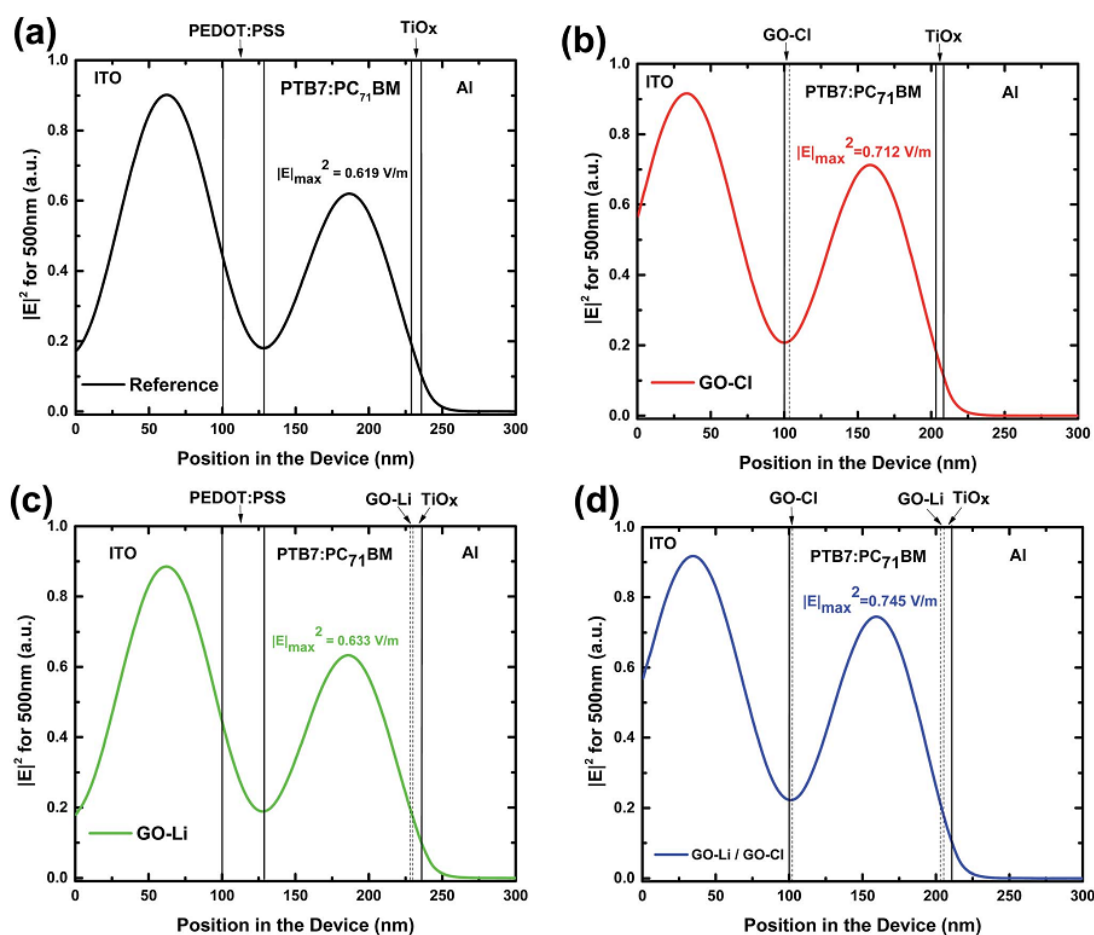
Figure 8.10. Calculated distribution of the normalized modulus squared of the optical electric field $|E^2|$ inside an OPV device: a) ITO (100 nm)/PEDOT:PSS (35 nm)/PTB7:PC$_{71}$BM (100 nm)/TiO$_x$ (10 nm)/Al (100 nm), b) ITO (100 nm)/GO-Cl (2 nm)/PTB7:PC$_{71}$BM (100 nm)/TiO$_x$ (10 nm)/Al (100 nm), (c) ITO (100 nm)/PEDOT:PSS (35 nm)/PTB7:PC$_{71}$BM (100 nm)/GO-Li(2 nm)/TiOx (10 nm)/Al (100 nm) and (d) ITO (100 nm)/GO-Cl (2 nm)/PTB7:PC$_{71}$BM (100 nm)/ GO-Li (2 nm)/TiO$_x$ (10 nm)/Al (100 nm) for a wavelength of 500 nm.

8.4 Conclusion

In summary, this work demonstrates how the WF tuning of the buffer layers can affect the performance of OPV devices. Two facile, fast, non-destructive and r2r compatible methods are briefly presented, which allowed the WF fine tuning of graphene-based derivatives to develop universal buffer layers that direct match the energy levels of the polymer donor and electron acceptor in the state-of-the art OPVs. OPVs with a GO-Cl as HTL exhibited a PCE of

8.28%, much higher than those of reference devices with GO (7.56%) or PEDOT:PSS (7.40%), while the incorporation of GO-Li as ET interlayer between the active layer and the TiO_x optical spacer led to a PCE of 7.98% which was significantly increased compared to the reference one (7.40%). The excellent hole and electron extraction capabilities of GO-Cl and GO-Li were combined to an all graphene-based buffer layer OPV device which exhibited a PCE of 9.14% (8.83% average), significantly outperforming the reference one by ~19%. The described methods can contribute to novel interface engineering approaches, creating graphene- and other 2D materials-based derivatives as excellent potential candidates for a wide range of new applications with tunable optoelectrical properties, including flexible electronic OPVs, perovskite solar cells, organic light emitting diodes, and photosensors, as well as traditional electronic devices.

REFERENCES

[1] B. C. Thompson, J. M. J. Frechet, *Angew. Chem., Int. Ed.*, **2007**, **47**, 58

[2] B. Azzopardi, C. J. M. Emmott, A. Urbina, F. C. Krebs, J. Mutale, J. Nelson, *Energy Environ. Sci.*, **2011**, **4**, 3741

[3] G. Li, R. Zhu, Y. Yang, *Nat. Photonics*, **2012**, **6**, 153

[4] J. Adams, G. D. Spyropoulos, M. Salvador, N. Li, S. Strohm, L. Lucera, S. Langner, F. Machui, H. Zhang, T. Ameri, M. M. Voigt, F. C. Krebs, C. J. Brabec, *Energy Environ. Sci.*, **2015**, **8**, 169

[5] J. B. You, L. T. Dou, K. Yoshimura, T. Kato, K. Ohya, T. Moriarty, K. Emery, C. C. Chen, J. Gao, G. Li, Y. Yang, *Nat. Commun*, **2013**, **4**, 1446

[6] R. Steim, F. R. Koglera, C. J. Brabec, *J. Mater. Chem.*, **2010**, **20**, 2499

[7] H. Ma, H. L. Yip., F. Huang, A. K. Y. Jen, *Adv. Funct. Mater.*, **2010**, **20**, 1371

[8] C.-Z. Li, C.-Y. Chang, Y. Zang, H.-X. Ju, C.-C. Chueh, P.-W. Liang, N. Cho, D. S. Ginger and A. K. Y. Jen, *Adv. Mater.,* **2014**, **26**, 6262

[9] V. Shrotriya, G. Li, Y. Yao, C. Chu, Y. Yang, *Appl. Phys. Lett.*, **2006**, **88**, 073508

[10] M. D. Irwin, D. B. Buchholz, A. W. Hains, R. P. H. Chang, T. J. Marks, *Proc. Natl. Acad. Sci. U.S.A.*, **2008**, **105**, 2783

[11] H. Yan, P. Lee, N. R. Armstrong, A. Graham, G. A. Evmenenko, P. Dutta, T. J. Marks, *J. Am. Chem. Soc.*, **2005**, **127**, 3172

[12] A. W. Hains, T. J. Marks, *Appl. Phys. Lett.*, **2008**, **92**, 023504

[13] X. Jiang, H. Xu, L. Yang, M. Shi, M. Wang, H. Chen, Sol. Energy Mater. Sol. Cells, **2009**, **93**, 650

[14] C. J. Brabec, S. E. Shaheen, C. Winder, N. S. Sariciftci, *Appl. Phys. Lett.*, **2002**, **80**, 1288

[15] J. Y. Kim, S. H. Kim, H. H. Lee, K. Lee, W. Ma, X. Gong, A. J. Heeger, *Adv. Mater.*, **2006**, **18**, 572

[16] H. L. Yip, S. K. Hau, N. S. Baek, H. Ma, A. K.Y. Jen, *Adv. Mater.*, **2008**, **20**, 2376

[17] T.Y. Chu, J. Lu, S. Beaupre, Y. Zhang, J.R. Pouliot, S. Wakim, J. Zhou, M. Leclerc, Z. Li, J. Ding, Y. Tao, *J. Am. Chem. Soc.*, **2011**, **133**, 4250

[18] M. Jorgensen, K. Norrman, F. C. Krebs, *Sol. Energy Mater. Sol. Cells*, **2008**, **92**, 686

[19] L. Lu, T. Xu, I. H. Jung, L. Yu, *J. Phys. Chem. C*, **2014**, **118**, 22834-22839

[20] S.-S. Li, K.-H. Tu, C.-C. Lin, C.-W. Chen, M. Chhowalla, *ACS Nano*, **2010**, **4**, 3169-3174

[21] J. Liu, Y. Xue, L. Dai, *J. Phys. Chem. Lett.*, **2012**, **3**, 1928-1933

[22] J.-S. Yeo, J.-M. Yun, Y.-S. Jung, D.-Y. Kim, Y.-J. Noh, S.-S. Kim, S.-I. Na, *J. Mater. Chem. A*, **2014**, **2**, 292-298

[23] E. Stratakis, K. Savva, D. Konios, C. Petridis, E. Kymakis, *Nanoscale,* **2014**, **6**, 6925-6931

[24] G. Kakavelakis, D. Konios, E. Stratakis, E. Kymakis, *Chem. Mater.*, **2014**, **26** , 5988-5993

[25] T.-Y. Chu, S.-W. Tsang, J. Zhou, P. G. Verly, J. Lu , S. Beaupré, M. Leclerc, Y. Tao*, Sol. Energy Mater. Sol. Cells*, **2012**, **96**, 155

[26] C. A. Amb, S. Chen, K. R. Graham, J. Subbiah, C. E. Small, F. So, J. R. Reynolds, *J. Am. Chem. Soc.* **2011**, **133**, 10062

[27] D. Konios, M. M. Stylianakis, E. Stratakis, E. Kymakis, *Journal of Colloid And Interface Science*, **2014**, **430**, 108

[28] J. Liu, Y. Xue, Y. Gao, D. Yu, M. Durstock, L. Dai, *Adv. Mater.* **2012**, **24**, 2228-2233.

[29] H. L. Poh, F. Sanek, A. Ambrosi, G. Zhao, Z. Sofer and M. Pumera,*Nanoscale*, **2012**, 4, 3515.

[30] W. S. Hummers and R. E. Offeman,J. Am. Chem. Soc., **1958**, 80, 1339.

[31] D. Konios, C. Petridis, G. Kakavelakis, M. Sygletou, K. Savva, E. Stratakis, E. Kymakis, *Adv. Funct. Mater.,* **2015**, **25**, I 2213.

[32] J.-Y. Kim, W. H. Lee, J. W. Suk, J. R. Potts, H. Chou, I. N. Kholmanov, R. D. Piner, J. Lee, D. Akinwande, R. S. Ruoff, *Adv. Mater.*, **2013**, **16**, 2308

[33] K. C. Kwon, K. S. Choi, Y. Kim, *Adv. Funct. Mater.*, **2012**, **22**, 4724

[34] L. Huang, Y. Liu, L.-C. Ji, Y.-Q. Xie, T. Wang, W.-Z. Shi, *Carbon*, **2011**, **49**, 2431-2436.

[35] N. D. Lang, *Phys. Rev. B*, **1971**, 4, 4234

[36] B. P. Rand, D. P. Burk, S. R. Forrest, *Phys. Rev. B,* **2007**, **75**, 115327

[37] L.-M. Chen, Z. Xu, Z. Hong, Y. Yang, .*J. Mater. Chem.,* **2010**, **20**, 2575-2598

[38] K. X. Steirer, P. F. Ndione, N. E. Widjonarko, M. T. Lloyd, J. Meyer, E. L. Ratcliff, A. Kahn, N. R. Armstrong, C. J. Curtis, D. S. Ginley, J. J. Berry, D. C. Olson, *Adv. Energy Mater.,* **2011**, **1**, 813−820

[39] V. Shrotriya, G. Li, Y. Yao, C.-W. Chu, Y. Yang, *Appl. Phys. Lett.*, **2006**, **88**, 073508

[40] B. R. Lee, J.-W. Kim, D. Kang, D. W. Lee, S.-J. Ko, H. J. Lee, C.-L. Lee, J. Y. Kim, H. S. Shin, M. H. Song, *ACS Nano,* **2012**, **6**, 2984–2991

[41] I. Riedel, J. Parisi, V. Dyakonov, L. Lutsen, D. Vanderzande, C. Hummelen, *Adv. Funct. Mater.,* **2004**, **14**, 38

[42] G. F. Burkhard, E. T. Hoke, M. D. McGehee, *Adv. Mater.,* **2010**, **22**, 3293

[43] X. Li, X. Ren, F. Xie, Y. Zhang, T. Xu, B. Wei, W. C. H. Choy, *Adv. Opt. Mater.,* **2015**, **3**, 1220

[44] D. H. Wang, J. K. Kim, J. H. Seo, I. Park, B. H. Hong, J. H. Park, A. J. Heeger, *Angew. Chem. Int. Ed.* **2013**, **52**, 2874-2880

Conclusions and Perspectives

In this dissertation, the design and development of novel solution-processed graphene-based materials was presented. A simple technique to improve and simultaneously tune the optoelectronic properties of graphene based TCFs, by using a fs laser was developed. Taking advantage of the rGO solution processability and chemical stability, rGO micromeshes were patterned on flexible substrate and incorporated in OPV devices. In addition, a fast, non-destructive and r2r compatible photochemical method for the fabrication of chlorinated graphene oxide (GO-Cl) films with an increased WF of 5.23 eV and a facile process for lithium alkali metal functionalized graphene oxide with reduced WF, from 4.9 eV to 4.3 eV, were presented. Finally, graphene-inorganic nanocrystals hybrid materials were demonstrated as electron cascade materials as a promising way towards improving the performance of OPVs. The graphene-based concepts presented here might be extended to other material combinations, holding great promise both for the improvement of OPVs efficiency as well as other optoelectronic applications.

The outstanding properties of graphene and other 2D semiconducting nanomaterials have generated immense interest for both conventional semiconductor technology as well as the nascent flexible nanotechnology. Although dramatic progress has been made, the utilization of other 2D materials, apart from graphene, in optoelectronics and especially OPVs and the recently presented Perovskite solar cells is still at premature stage, taking into consideration that graphene, who is the most established 2D, is relatively a new material, as compared with the periods taken from discovery to commercialization for fullerenes, or carbon nanotubes.

Regarding TCE applications, the solution processable rGO based layers exhibit much lower conductivity than ITO. Therefore applications only in flexible OPVs should be meaningful. In this context, the development of hybrids between solution processable 2D nanosheets with state-of-the-art metal nanowires, or carbon nanotubes or the adaption of a micromesh structure can be considered promising alternative approaches. On the other hand, the utilization of CVD grown graphene, which exhibits high conductivity and transparency as the transparent electrode of OPVs is visible. However, special

attention should be paid on the synthesis methods, targeting in improving the graphene quality and considerably reduce the cost. Moreover, compatible in-situ doping techniques with the r2r fabrication process of OPVs should be developed. Therefore, the overall goal should be the optimization of the synthesis process of large area graphene layers in rigid and flexible substrates with controlled morphology, bandgap and purity. Moreover, the need of a complex transfer of graphene films on flexible substrates hinders their application in flexible OPVs. Regarding the application of CVD graphene as the non-transparent back electrode is more straightforward, however proper functionalization should take place in order to tune the hydrophobic surface of graphene in order be effectively deposited on top of the photoactive layer.

The most promising application in OPVs so far, is the utilization of WF tuned GO derivatives, Molybdenum disulfide (MoS_2) and tungsten disulfide (WS_2) as buffer layers in binary OPVs for both hole and electron transport, or interlayers in tandem OPVs. Recent results demonstrated their superiority from state-of-the-art buffer layers, such as the PEDOT:PSS and metal oxides (MOs), in both performance and stability. Due to their solution processability, WF tunability and mechanical stability, they can directly be incorporated in r2r OPV fabrication lines, replacing traditional vacuum deposited materials. Also, taking account the plethora of 2D materials, other 2D materials, such as tungsten diselenide (WSe_2), molybdenum ditelluride ($MoTe_2$) and molybdenum diselenide ($MoSe_2$) should be proper functionalized and tested as either HTL or ETL. In this aspect, a key challenge is the upscaling of this technology, by printing 2D based large area, homogeneous films with a few nanometers thickness without pinholes or defects.

Finally, another attention-grabbing application is the use of solution processable 2D nanosheets as energy cascade materials in ternary OPVs. In this application, proper functionalization routes of the 2D nanosheets should be employed in order to engineer their energy levels to perfectly match with the energy levels of newly designed high efficient polymers. Also 2D based hybrids can be used, in order to extend the absorption spectra of the photoactive layer to the near-IR region.